

# Nonlinear free-surface flows, waterfalls and related free-boundary problems

Elle Patricia McLean

*Supervisors:*

Dr. Robert Bowles, Prof. Jean-Marc Vanden-Broeck and Prof. Frank Smith

A dissertation submitted in partial fulfillment  
of the requirements for the degree of  
Doctor of Philosophy  
of  
University College London

Department of Mathematics  
University College London

March 2023

## **Declaration**

I, Elle Patricia McLean, confirm that the work presented in this thesis is my own. Where information has been derived from other sources, I confirm that this has been indicated in the thesis.

## Abstract

Many works have considered two-dimensional free-surface flow over the edge of a horizontal plate, forming a waterfall, and with uniform horizontal flow far upstream. The flow is assumed to be steady and irrotational, whilst the fluid is assumed to be inviscid and incompressible. Gravity is also taken into account. In particular, amongst these works, numerical solutions for supercritical flows have been computed, utilising conformal mappings as well as a series truncation and collocation method. Here, an extension to this work is presented where a more appropriate expression is taken for the assumed form of the complex velocity. The justification of this lies in the behaviour of the flows far downstream and the wish to better encapsulate the parabolic nature of such a free-falling jet. New numerical results will be presented, demonstrating the improved shape of the new free-surface profiles. Further adjustments to the method are presented which lead to enhanced coefficient decay. The aforementioned adjustments are also applied to other supercritical flows (such as weir flows) and similar improvements to the jet shape can be observed. Flows that are still horizontal upstream but instead negotiate a convex corner and then run along an angled supporting bed (i.e. spillway flows) are also surveyed. New spillway problems and results are presented, where the spillway's angled wall is more complex than a linear path; and, again, series truncation and collocation are utilised. Finally, a wake model for potential flow past a finite plate, perpendicular to the oncoming flow and below a free surface, is pursued. The approach here is to adopt a closure model of horizontal flow far downstream and use the boundary integral equation method to obtain a solution numerically. Related free-boundary problems are included to progress from a case of zero-gravity, unbounded flow to the full problem.

## Impact Statement

Within the area of free-surface flows research, the investigations into waterfall flows presented in this study are very beneficial. The numerical approach of series truncation and collocation is utilised but its implementation is improved upon by taking more suitable forms for the complex velocity ansatz and by refining the numerical method (smoothing and using the ‘*A*-method’ as introduced in §2.4) to obtain better solutions that allow for the extrapolation of the results. Hence, this improves the computational efficiency of the approach. This particular section of work has been disseminated through publication in the Journal of Fluid Mechanics; and has been presented and discussed at numerous talks both locally (within the Department of Mathematics at University College London) and more widely at conferences such as the British Applied Mathematics Colloquium. Further benefit can arise from this work since the developments of the method can be applied to other potential flow problems that involve jets. This means it is applicable to a wide variety of practical examples such as flow from a nozzle or breaking-wave flows.

Again, within the research area of free-surface flows, the work presented here on spillways and waterfalls with complex geometry upstream is valuable since we demonstrate the versatility of the series truncation and collocation method, beyond its previous usage in the literature. For example, we are able to consider curved spillway walls and waterfalls that follow stepped walls upstream. Such potential flows (where the fixed, curvilinear boundaries are defined piecewise) can be difficult to solve, but the aforementioned numerical approach enables us to tackle these problems. Moreover, physical examples of spillways and waterfalls often involve complex geometries upstream. Hence, there is scope and reason for investigation of further related free-surface flow problems utilising this approach and the adjustments to the method discussed in this thesis.

Finally, the work presented here on cavity and wake flows past a plate normal to the undisturbed stream is motivated by flow around a submerged rowing blade. Design in industry is often heavily influenced by experimental investigations. However, having a fundamental theoretical understanding of flows is crucial to avoid flawed design elements. The models studied in the present work can be built upon to more closely model the flow past a rowing blade, hence its applicability to sports science research.



## UCL Research Paper Declaration Form:

### referencing the doctoral candidate's own published work(s)

*Please use this form to declare if parts of your thesis are already available in another format, e.g. if data, text, or figures:*

- *have been uploaded to a preprint server*
- *are in submission to a peer-reviewed publication*
- *have been published in a peer-reviewed publication, e.g. journal, textbook.*

*This form should be completed as many times as necessary. For instance, if a student had seven thesis chapters, two of which having material which had been published, they would complete this form twice.*

1. **For a research manuscript that has already been published** (if not yet published, please skip to section 2):

- (a) **What is the title of the manuscript?**

Improved calculations of waterfalls and weir flows

- (b) **Please include a link to or doi for the work:**

<https://doi.org/10.1017/jfm.2022.305>

- (c) **Where was the work published?**

Journal of Fluid Mechanics

- (d) **Who published the work?**

Cambridge University Press

- (e) **When was the work published?**

27/04/2022

- (f) **List the manuscript's authors in the order they appear on the publication:**

E. McLean, R. Bowles, B. Scheichl and J.-M. Vanden-Broeck

- (g) **Was the work peer reviewed?**

Yes

- (h) **Have you retained the copyright?**

Yes

- (i) **Was an earlier form of the manuscript uploaded to a preprint server (e.g. medRxiv)? If ‘Yes’, please give a link or doi**

If ‘No’, please seek permission from the relevant publisher and check the box next to the below statement:

☐ *I acknowledge permission of the publisher named under 1d to include in this thesis portions of the publication named as included in 1c.*

2. **For a research manuscript prepared for publication but that has not yet been published** (if already published, please skip to section 3):

- (a) **What is the current title of the manuscript?**
- (b) **Has the manuscript been uploaded to a preprint server?** (e.g. medRxiv; if ‘Yes’, please please give a link or doi)
- (c) **Where is the work intended to be published?** (e.g. journal names)
- (d) **List the manuscript’s authors in the intended authorship order:**
- (e) **Stage of publication** (e.g. in submission) :

3. **For multi-authored work, please give a statement of contribution covering all authors** (if single-author, please skip to section 4):

The research manuscript was prepared by McLean with drafts reviewed by the remaining three authors. The content of the article was discussed between the four authors. Initial investigations into the development of the complex velocity ansatz for the waterfall from the form utilised in the work of Dias and Tuck [1991] were carried out by Bowles and Scheichl. More detailed justification for this development was provided by McLean. Each author separately wrote the code for their own routine for solving the system in order to compare and validate the results. Analysis of the numerical results, the comparisons with the solutions of Clarke [1965] and Dias and Tuck [1991], and the application of the revised expression for the jet singularity in the finite-depth weir case were completed by McLean with supervision from Bowles and Vanden-Broeck.

4. **In which chapter(s) of your thesis can this material be found?**

This material can be found in chapters 2 and 3.

5. **e-Signatures confirming that the information above is accurate** (this form should be co-signed by the supervisor/ senior author unless this is not appropriate, e.g. if the paper was a single-author work):

**Candidate:**



**Date:** 09/03/2023

**Supervisor/Senior Author signature** (where appropriate):



**Date:** 29/03/2023

# Contents

<b>Introduction</b>	<b>10</b>
<b>1 Spillway flows</b>	<b>24</b>
1.1 Simple spillway . . . . .	24
1.1.1 Reproduction . . . . .	24
1.1.2 Alternative mapping . . . . .	35
1.2 Curved wall corner . . . . .	43
1.3 Stepped wall . . . . .	53
1.4 Parabolic wall . . . . .	66
1.5 Stepped wall to horizontal channel . . . . .	71
<b>2 Waterfall flows</b>	<b>84</b>
2.1 Reproduction . . . . .	84
2.2 Large- $\phi$ analysis: flow far downstream . . . . .	89
2.3 Improved calculation . . . . .	94
2.4 Further numerical investigations . . . . .	98
<b>3 Application of three-term jet singularity</b>	<b>107</b>
3.1 Finite-depth, supercritical weir flows . . . . .	107
3.2 Finite-depth, subcritical weir flows . . . . .	117
3.3 Steps upstream of waterfall . . . . .	124
3.4 Obstacle upstream of waterfall . . . . .	131
<b>4 Zero-gravity cavity and wake flows</b>	<b>138</b>
4.1 Cavity of infinite extent . . . . .	139
4.2 Cavity horizontal closure . . . . .	142
4.2.1 Analytic method (reproduction) . . . . .	142
4.2.2 Finite Hilbert transform method . . . . .	148
4.2.3 Matrix inversion method . . . . .	154

<b>5</b>	<b>Gravitational cavity and wake flows</b>	<b>158</b>
5.1	Cavity horizontal closure . . . . .	158
5.1.1	Plate perpendicular to flow . . . . .	158
5.1.2	Plate at arbitrary angle of attack . . . . .	174
5.2	Wake horizontal closure with free surface . . . . .	177
<b>6</b>	<b>Conclusions and future work</b>	<b>193</b>
	<b>References</b>	<b>196</b>

# Introduction

Free-surface flow is the subject of this study. Spillways, waterfalls and flows past submerged obstacles are the overarching problems that will be investigated. A spillway is a hydraulic structure that has numerous intended functions such as energy dissipation, water treatment and flood release [Chanson, 1994]. Often they are built into, or near to, a dam. In this case, their purpose of releasing water from a dam in a controlled manner means that understanding the fluid flow of spillways is paramount. Figure 1 shows some examples of spillways. Typically, spillway structures start with a water basin and then there is a declining wall either all of the way down to or part of the way down to a water basin below. Clearly, the term spillway in (engineering) literature corresponds to a range of very different characteristic flows. Throughout this study, the term ‘spillway’ will refer to the structure of a horizontal bed followed by an angled supporting bed. Evidently this description does not apply to all of the structures shown in figure 1. We will use the term ‘waterfall’ for flow over the trailing edge of a horizontal plate, forming a gravity-driven free jet. Figure 2a demonstrates a waterfall where the flow in any cross-section (away from the sides of the channel) is essentially the same and so such a three-dimensional problem can be suitably approximated as two-dimensional. Similarly, a weir flow is analogous to a waterfall except that the fluid negotiates a region of raised bed, or lip, before falling freely under gravity. Figure 2b illustrates such weir flows. Finally, the flows past submerged obstacles are self-explanatory and examples are depicted in figure 3 that will be investigated here. We will study wake and cavity flows past a finite plate that is normal or oblique to the oncoming flow. The particular motivation for this problem is the behaviour of flow around a rowing blade but, given the simplified schematic of the flow, the problem is applicable to other scenarios.

There is much engineering research conducted on spillway, waterfall and weir flows. This largely concerns experimental investigations with interest in energy dissipation, hydrodynamic forces acting upon the structures and discharge coefficients. The varying possible purposes (releasing excess flood waters, an aesthetic water feature, serving as fish ladders, etc.) and constraints (geometry, topography, material availability, etc.) have led to a wide range of these hydraulic structures that exhibit different flow behaviours. For example, if energy dissipation is prioritised, common choices



(a) A spillway flow, by StillWorksImagery. Adapted from Pixabay.  
(Pixabay License  
<https://pixabay.com/service/terms/#license>).



(b) Srisaillam Dam Spillway, photographed by Chintohere. Adapted from Wikimedia Commons.  
Public Domain.



(c) A photograph of a cascade spillway flow, taken by wfmillar. Adapted from Wikimedia Commons.  
(Creative Commons License CC BY-SA 2.0  
<https://creativecommons.org/licenses/by-sa/2.0/>).



(d) Kouris Reservoir Spillway, photographed by Xaris333. Adapted from Wikimedia Commons.  
(Creative Commons License CC BY-SA 4.0  
<https://creativecommons.org/licenses/by-sa/4.0/deed.en>).

Figure 1: Spillway examples.

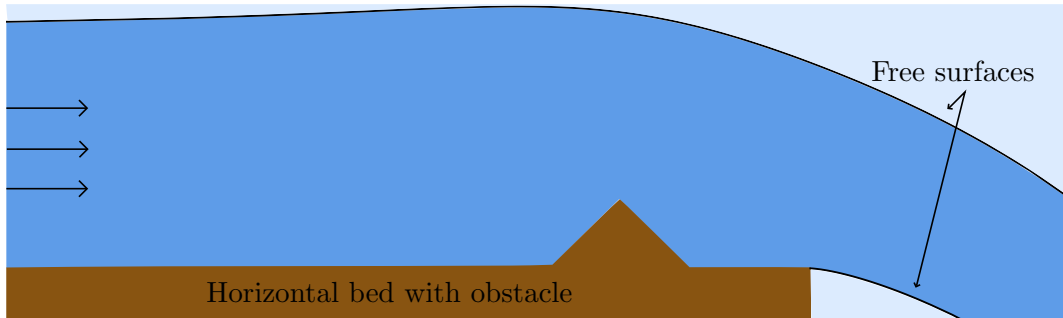


(a) A photograph of a waterfall flow from a city fountain, taken by Mirek Durma. Adapted from Pixabay.  
(Pixabay License  
<https://pixabay.com/service/terms/#license>).

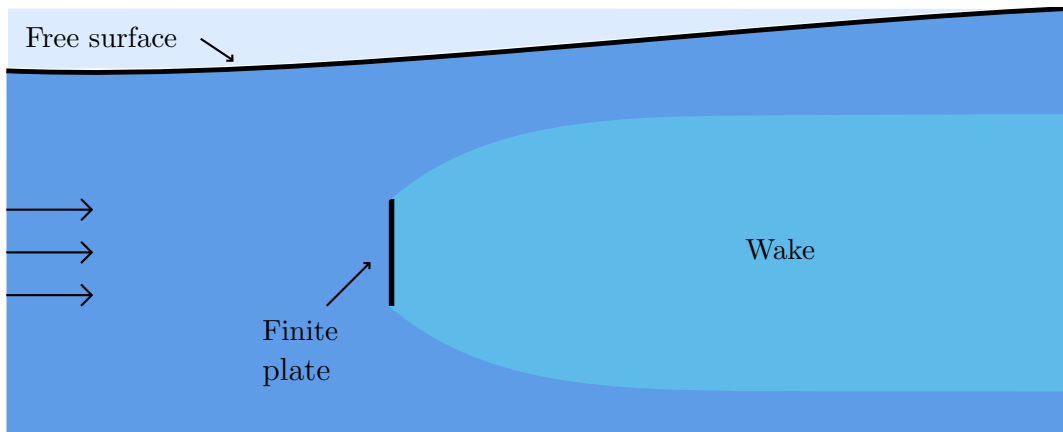


(b) A weir flow, photographed by Ardfern. Adapted from Wikimedia Commons.  
(Creative Commons License CC BY-SA 3.0  
<https://creativecommons.org/licenses/by-sa/3.0/deed.en>).

Figure 2: Waterfall and weir flows.



(a) Waterfall flow with a submerged obstacle upstream.



(b) Flow past a finite plate normal to the flow.

Figure 3: Flows past submerged obstacles.



include constructing a flip bucket (e.g. figure 1b) from which a high velocity jet takes off and impinges into a downstream plunge pool; having a stilling basin downstream where a hydraulic jump is created; or constructing a stepped spillway where either nappe or skimming flows occur [Chanson, 1994]. For clarity, in the case of the stepped spillway, nappe flow is a series of free-falling flows over the edge of each step; and skimming flow ‘skims’ over the edges of the steps as a stream which is supported by recirculating vortices beneath it. Furthermore, the hydrodynamic forces are of importance for investigating or predicting the potential damage caused to the structures as (in some cases more than others) it is imperative for the structures not to fail. Finally, computing the discharge coefficient is useful when comparing theoretical predictions for the flow with experimental results, and so aids design work further. A particular use of weirs is in determining the flow rate of a channel, the calculation of which involves the discharge coefficient. Overall, it is clear that experimental investigations of these hydraulic structures are valuable.

It is also necessary to understand the spillway, waterfall and weir flows theoretically. As already mentioned, the varying specifications for the aforementioned hydraulic structures lead to a wide variety of flows. Upstream, we could have a fluid basin or channel which can be shallow or deep. Downstream, we have the same possibilities. The flows can be laminar or turbulent, depending on the physical parameters involved. This means that the flows can involve jets, aeration, air bubble entrainment or hydraulic jumps, to name a few possibilities. This is indeed a wide range. In the investigations presented here, the concern will be with steady, laminar flows. Many works have considered such flows. For example, Kistler and Scriven [1994] study the effects of viscosity on sheet flow falling from the edge of an inclined plate — one of many investigations into the ‘teapot effect’. In another case, the effect of compressibility on a jet falling from a vertical pipe is considered by Christodoulides et al. [2010]. However, in the present study, the assumptions will be such that we have potential flow which is suitable for many applications. Regardless, differences between observable results and those obtained via the approximation of potential flow theory can also offer insight.

For flow past obstacles, there is much available in the literature regarding experimental results since there are many applications for such research in industry. Since the flow depicted in figure 3a

can be classed as a waterfall flow with a disturbance upstream (and it will be tackled in much the same way as the waterfall and weir flows in this study), for now we focus on discussing investigations relevant to flow past an obstacle in a uniform stream, i.e. figure 3b. We will consider both wake flows and cavity flows in the present study due to the similarities between them. As discussed in detail and with comparisons made to cavitating flows by Wu [1972], a (fully established) wake flow is characterised by a dividing streamline that separates from the obstacle in the stream to bound a region of slow recirculating fluid close behind the obstacle where the pressure is nearly constant and less than the pressure in the far-field, followed by turbulent flow which diminishes due to mixing and dissipation, and leading to regaining the undisturbed stream flow and recovery of the pressure. Similarly, a (fully-developed or super-) cavitating flow is as described above but with a cavity (a vapour-filled bubble) forming close behind the obstacle — still a region of slow recirculation — and the occurrence (and type) of cavitation is dependent on the cavitation number. This cavitation number is a nondimensional parameter that involves the difference between the pressure within the cavity and in the far-field. Note that when the cavitation number falls below a critical value, small air bubbles begin to form; whereas even smaller cavitation numbers correspond to the formation of the single cavitation bubble as already described. For wake flows, instead of referring to the cavitation number, we use the term ‘wake underpressure coefficient’ to refer to the nondimensional parameter which involves the difference between the pressure within the wake and in the far-field. Similarly to the cavitation number with respect to cavitating flows, the wake underpressure coefficient characterises the wake flow.

Returning to the point of the existence of many experimental studies of wake and cavitating flows forming behind an obstacle, we note the work of Fage and Johansen [1927] concerning wake flow in air; and the works of Parkin [1958], Silberman [1959] and Dawson [1959] regarding these flows in water. Coefficients of drag and lift are obtained, and Wu [1962] computes and compares theoretical results with the available experimental data from the aforementioned studies. The work of Wu [1962] concerns a wake forming behind a flat plate in potential flow with the effects of gravity neglected and the analytic results compare well with those of physical simulations. Of greater relevance to the full problem of interest in the present study (c.f. figure 3b) are the experimental

investigations of Dawson [1959] into cavitating flow close to the free surface. Dawson [1959] looks into the effect of several factors on the cavitating flow, such as depth of submergence, angle of attack and cavitation number on various quantities, such as the coefficient of drag and the cavity length. For instance, one particular observation is that the experimental cavity length decreases with greater proximity to the free surface. However, Dawson [1959] does comment that some of the results do not agree very well with existing theoretical approximations or other experiments. There are unanswered fundamental questions regarding a wake or cavity that forms behind a finite plate normal or oblique to the oncoming flow and close to the free surface, under the assumptions necessary for potential flow with the effects of gravity included. These will be explored in the present work.

As already discussed, many of the flows covered in this thesis are well-studied, both classically and more recently. So, what justifies investigating all of these free-surface flows together here? Under certain assumptions, the method of solution can be very similar and advancements made for one problem can be applied to other relevant flows. In particular, here the flow is assumed to be steady and irrotational, whilst the fluid is assumed to be inviscid and incompressible. Two-dimensional flow under the aforementioned assumptions allows for the application of potential flow theory. Exact solutions are obtainable in the absence of gravity through use of analytic techniques such as utilising conformal mappings to map between the physical and complex potential planes. However, the effects of gravity are included in the problems discussed here and so numerical techniques will also be employed.

First, we will begin with spillway flow (see chapter 1). As explained earlier, this is where the fluid negotiates a convex corner and then runs along an angled supporting bed. More specifically, in the case presented here, we have uniform horizontal flow upstream before running along the sloping wall. Under the assumptions already listed, we have potential flow and numerical solutions for supercritical flows have already been computed for this problem by Vanden-Broeck and Keller [1986]. Note that wave-free solutions are the focus of the present work. The method utilised to obtain these numerical solutions will be presented as it will be repeatedly called-upon in subsequent problems. The method, in short, is as follows. Given the assumptions of the flow, we look to find

a solution to Laplace’s equation and the boundary conditions. Local analysis of singularities of the flow enables us to remove such singularities from a series representation for the solution. For a good numerical solution, we expect to find that the coefficients of the series decay rapidly for a converged series representation. In order to actually implement such a method, the series is truncated after a certain number of terms and mesh points along the boundaries of the flow are introduced. The boundary conditions are then imposed at the mesh points and we can solve the system of equations numerically by iteration. Clearly, due to the truncation involved, the series is preferred to be rapidly convergent. It follows that a good numerical solution is characterised by being largely independent of the truncation, i.e. the solution should not change greatly as more terms are included in the series representation. Therefore, in analysing the solutions obtained via this series truncation and collocation method, we will look for quick decay of the coefficients and for the last few coefficients to be very small, typically of order  $10^{-4}$  or less. We will regularly plot the coefficients against the reciprocal of the index of the coefficient. A ‘decaying tail’ signifies good convergence. A lack of this decaying tail signifies bad convergence and suggests that a singularity of the flow has been incorrectly or insufficiently removed from the series representation.

Following the presentation of this spillway with basic geometry, new spillway cases will then be investigated with a similar approach. This will include a curved corner; a stepped wall; and a parabolic wall. Few alterations are made to the method described for the standard spillway case in order to apply it to these more arbitrarily-shaped spillways. A key question that is explored is whether the assumed form for the downstream jet singularity is suitable and sufficient. Note that this is investigated further in a later chapter which is focused on waterfall flow. Then, the problem of a stepped wall down to a horizontal channel will also be considered. Related to this are the investigations into free-surface flow over a semi-infinite step in the bed of a channel by King and Bloor [1987] and Binder et al. [2008], where a boundary integral equation approach is utilised. Here, in the present study, we find that an exact solution for the zero-gravity case can be obtained using conformal mappings. However, in the case of gravitational flow that is supercritical both up- and downstream, we encounter problems in forming an appropriate ansatz for the complex velocity. Numerical solutions are presented for this problem but analysis of the quality of solution

is given which suggests further investigation is required.

We then turn our attention to waterfall flows (see chapter 2). Recall that this is where the flow is uniform and horizontal far upstream and two free surfaces form a gravity-driven free jet far downstream. Numerous studies have dealt with these fundamental potential flows over the edge of a plate numerically. Here, we note some of the most seminal works of this kind. Solutions have been obtained by Chow and Han [1979], Smith and Abd-el-Malek [1983], and Goh and Tuck [1985] using finite difference methods or integral equations. Furthermore, Clarke [1965] uses the method of matched asymptotic expansions to find the free surfaces for the waterfall flow: an expansion that is valid downstream based on the thinness of the jet is matched with an expansion that is valid upstream based on a parameter related to the inverse square Froude number. Most importantly, Dias and Tuck [1991] advantageously utilise conformal mappings and the efficient series truncation and collocation method — leading to more easily obtainable results. This work will be discussed in terms of its method and results. The method of Dias and Tuck [1991], although used to study waterfalls, implicitly imposes such a spillway flow as a downstream asymptote. So, could a form specifically derived for a waterfall jet-flow downstream lead to better solutions? It will become clear that a more appropriate expression for the assumed form of the complex velocity can benefit the numerical solutions. The rigorous justification of this improvement lies in the representation of the waterfall flow far downstream, where we should look to capture the physically relevant parabolic downfall (c.f. figure 2a). Then, this extension will be presented. New numerical results will be illustrated which, at first glance, are very similar to free-surface profiles obtained through use of the complex velocity form of Dias and Tuck [1991]. However, profiles that have been extrapolated further downstream are also presented, demonstrating the improvement in the shape of the new free-surface profiles. Comparisons with the asymptotic solutions found by Clarke [1965] will be made, validating these numerical solutions — in particular for flows with larger Froude numbers. Further adjustments to the method and the form of the complex velocity will then be presented. These points can lead to improved numerical solutions by enhancing the decay of the coefficients that are obtained through the series truncation and collocation method.

A similar approach is also presented for including more terms of the expansion for the down-

stream jet singularity in the case of supercritical, finite-depth weir flows (see chapter 3) — again, further developing the complex velocity ansatz utilised by Dias and Tuck [1991]. A weir flow is analogous to a waterfall except that the fluid negotiates a region of raised bed, or lip, before falling freely under gravity. The influence on the flow of the height of this lip is of interest. As with the waterfall, the new free-surface profiles are very similar to those of Dias and Tuck [1991]. However, extrapolating the free surfaces to reach further downstream highlights the improvement to the shape of the jet. The different types of solutions (Dias and Tuck [1991] refer to waterfall-type and solitary-wave-type solutions) are still retained through employing the revised ansatz. Following this, we will then apply the improved form to subcritical, finite-depth weir flows. It will be shown that the one-parameter family of solutions obtained by Dias and Tuck [1991] for the subcritical, finite-depth weir is unchanged. As in the supercritical case, extrapolated free-surface profiles show the improvement to the downstream free-falling jet. Then, we consider the problem of waterfalls with upstream obstacles: a stepped bed and a triangular obstacle. These examples show the need for the correct form for the jet downstream, due to the effect the obstacles have on the conserved horizontal momentum flux of the flow and (in turn) on the jet downstream. Note that these flows can also be tackled using a boundary integral method instead, as calculated by Yoon and Semenov [2011] for flows under the same assumptions with an arbitrarily-shaped weir wall. The alternative approach of Yoon and Semenov [2011] still leads to numerical solutions, but it is the opinion of the author that a solution is more-readily available if series truncation and collocation is utilised instead, provided the singularities of the flow can be suitably captured.

There are many other studies of similar two-dimensional, free-surface flows with two free surfaces forming a jet downstream. These studies include jets emerging from a nozzle by Dias and Christodoulides [1991]; breaking wave flows by Dias and Tuck [1993]; and flow which rises along the bow of a ship and falls back down as a jet by Dias and Vanden-Broeck [1993]. These works also use the approach of conformal mappings with series truncation and collocation. Furthermore, since the parabolic nature of the jet is not incorporated into the form for the complex velocity, as discussed above for the waterfall and weir flows of Dias and Tuck [1991], the present work has great relevance to these other problems.

Finally, a wake model for potential flow past a finite plate, perpendicular to the oncoming flow and below a free surface, is pursued. Note that the assumptions required for potential flow are reasonable here — in particular, neglecting the viscous effects is appropriate since we know the locations of detachment points of the cavity or wake boundaries from the object, i.e. the two ends of the plate in this case [Brennen, 1995]. The approach here is to adopt a closure model of horizontal flow far downstream and use the boundary integral equation method to obtain a solution numerically. Related free-boundary problems are included to progress from a case of zero-gravity, unbounded flow to the full problem. We will begin with consideration of the problem of a cavity of infinite extent forming behind the plate that is normal to the flow (see chapter 4). Here, we neglect the effects of gravity, the pressure within the cavity is ambient and the assumptions on the flow are still such that we have potential flow. As discussed by Batchelor [2010], free-streamline theory and the method of solution that will be described are commonly attributed to Kirchhoff [1869] and Helmholtz [1868]. Very briefly, conformal mappings are utilised to find a closed-form exact solution. Note that the boundary of the cavity asymptotes to a parabola. It is also worth mentioning that a similar approach can be employed in the case where the flat plate is at an arbitrary angle to the stream. Again, a closed-form solution is obtained and is presented by Rayleigh [1876]. Note that, whilst the calculations in chapter 4 and section 1 of chapter 5 of this thesis will be with reference to a cavity forming behind the plate, the calculations are also applicable to the case of a wake forming instead.

To develop the problem, we look to incorporate a closure model. This is required since potential flow theory does not allow for complex processes within the cavity to be incorporated into the calculations [Brennen, 1995]. We assume constant pressure throughout the cavitation bubble and so we cannot simply join up the two cavity boundaries with a stagnation point at their intersection since the pressure at this point would not be consistent [Franc and Michel, 2004]. It follows that we adopt some form of closure of the cavitation bubble downstream. Here, we take a horizontal wall closure model, often referred to as the open-wake model. This simply means that the boundaries of the cavity become parallel to the undisturbed stream at some point downstream. The idea for this model is suggested by Joukowski [1890] in terms of the introduction of a point along a free

streamline before which we impose the usual dynamic boundary condition and after which the streamline continues in some way to downstream infinity. This undetermined way of continuing the free streamlines downstream is taken as the streamlines being parallel to the undisturbed stream by Roshko [1954]. Wu [1956] and Mimura [1958] also employ the open-wake model in solving for more generalised obstacle shapes: Wu [1956] formulates the problem for a general curved barrier whilst providing explicit solutions for a circular arc and a flat plate; and the work of Mimura [1958] concerns an inclined flat plate. Here, we present the method and solution for the flat plate normal to the flow, using different conformal mappings to those utilised by the works already discussed but arriving at the same results. Additional methods for solution are also presented: an analytic approach where the Cauchy integral formula is utilised to obtain an integral equation which is solved by inverting a finite Hilbert transform; and a numerical approach where the aforementioned integral equation is discretised and the system can be solved by matrix inversion. The purpose of including these methods is to show their use in the current problem and, therefore, their capacity for use in other suitable potential flow problems. Note that the pressure is assumed to be constant throughout the bubble but now it is not ambient (as opposed to the earlier case of the cavity of infinite-extent). Interestingly, if the cavitation number is the fixed parameter, then the closure points for the flow are found as part of the solution, i.e. the flow is dependent only on the cavitation number. It should be acknowledged that we have a symmetric problem and so the closure is at the same point (in terms of velocity potential or horizontal distance from the vertical plate) on each free streamline.

When the flat plate is instead inclined so that it is at an arbitrary angle of attack, we then have an asymmetric problem and a further constraint should be imposed since we then have two unknown closure points (i.e. one on each free streamline). Wu [1956] and Mimura [1958] impose that the velocity potential is the same on both free streamlines at the closure points. This constraint is again later used in the work of Wu [1962] where the closure model is altered slightly so that, instead of imposing that the free streamlines become parallel to the stream at the closure points, it is assumed that after the closure points the pressure continuously returns from the pressure within the cavity to the pressure of the free stream. The validation of these choices comes from



comparison with experimental data and we note that these comparisons are really only of interest in the local neighbourhood of the plate since the closure models are artificial by construction and not designed for realistic representation of the flow far downstream.

Before moving on to discuss the development of the problem to involve the effects of gravity, here, we first briefly mention a solution presented by Gurevich [1965] for the zero-gravity problem of the flat plate normal to the stream, with the flow bounded above by a wall. It should be mentioned that this solution is formed with reference to work by Bonder [1936] and the wall bounding the stream is instead below. Again, a closed-form solution is obtainable using conformal mappings. The result is that the magnitude of the drag on the flat plate is independent of the position of the plate relative to the wall and is of the same magnitude as that obtained for the cavity of infinite extent in an unbounded stream — a potentially surprising result.

Finally, we discuss the effects of gravity on the wake flow that forms due to a finite-length, flat plate submerged in a uniform horizontal stream (see chapter 5). There are many works concerning free-surface flow past submerged obstacles where the assumptions are such that we have potential flow and gravity is included. For example, Dias and Vanden-Broeck [1989] seek wave-free solutions for flow past a triangular obstacle that lies on the bed of the channel; Vanden-Broeck and Dias [1991] find wave-free solutions for flow past a submerged, inclined flat plate; and Semenov and Wu [2020] solve for flow past a submerged cylindrical body. However, these investigations do not include a wake or cavity forming behind the obstacle. Of great relevance to the flow of interest in the present study (c.f. figure 3b) is the work of Faltinsen and Semenov [2008] where a closed cavity-wake model is used for the flow past a hydrofoil close to the free surface. Boundary integral equations are obtained and solved numerically. It should be noted that Faltinsen and Semenov [2008] propose a more mathematically complex closure: it is assumed that a curvilinear contour closes the upper boundary of the cavity; the upper and lower boundaries meet at some point downstream to physically close the cavity; and the shape of the closure of the lower boundary is found from the solution. It is found that, as the depth of submergence decreases or gravity increases, there is a decrease in the length of the cavity. Faltinsen and Semenov [2008] state that this closure model is proposed to more realistically simulate the potential flow at the end of

the cavity. There is good agreement with experimental results but this is also the case with the employment of more simple closure models, at least in terms of quantities relevant to the local neighbourhood of the plate. Recall that modelling the flow around rowing blades is the initial motivation for this work, where the forces acting on the plate are of most physical importance. Therefore, it is reasonable to utilise an open-wake closure model here.

We will begin by including gravity along the cavity boundaries that form behind a plate that is normal to the undisturbed infinite stream. Here, similarly to the case with zero-gravity, we use the Cauchy integral formula and Bernoulli condition along the boundaries to obtain integral equations to be solved numerically for the flow speed and angle. Note that this is an asymmetric problem and so the earlier discussion of extra constraints due to the point of closure on each cavity boundary is relevant here. We will examine three reasonable options for this extra equation: the usual assumption of equal velocity potential at the two closure points; an interpolation formula for the flow angle at some point along a cavity boundary; or a constraint on the flow angle along the boundaries derived to explicitly impose that the dividing streamline is parallel to the free stream far upstream. Results are presented that support the use of the latter condition. Free-surface profiles will be given to demonstrate the dependencies of the solution on the Froude and cavitation numbers. The problem will then be generalised to model flow past a finite-length, flat plate that is instead at an arbitrary angle of attack. A particular result that we will see is that for a given angle of attack, a solution cannot be obtained for every set of the specified parameters (i.e. the Froude and cavitation numbers). This will be explored in the case of the plate set normal to the undisturbed flow.

The final problem presented here will be that of the finite-length plate submerged below the free surface, as depicted in figure 3b. As in the previous cases, the plate is normal to the undisturbed stream but now we will limit the model to only consider the formation of a wake behind the body (i.e. the assumptions will not be justified for a cavitating flow). The effects of gravity will be included in the model along the free surface. However, it is reasonable to not include gravity along the boundaries of the wake — justification for this will be provided. Note also that we seek a wave-free solution. Similarly to before, we employ the open-wake model and we obtain integral

equations that are discretised in order to solve the system numerically, including solving for the unknown shape of the wake boundaries and free surface. Analogous to the problem studied here are ploughing flows as investigated by Tuck and Vanden-Broeck [1998]. The difference is that the ploughing flows concern flow around a solid block that is submerged in a uniform horizontal stream: the top and bottom sides of the object in the ploughing flows case contrast with the upper and lower wake boundaries of the present study. The approach used here is similar to that utilised by Tuck and Vanden-Broeck [1998]. As in the earlier cavity and wake problems, knowledge of the behaviour of the flow far upstream will be imperative. Examples of free-surface profiles will be given and the effects of various factors (including the Froude number and wake underpressure coefficient) will be discussed.

Concluding remarks will then be presented, summarising some of the notable results and the improvements to the numerical approaches utilised in the various problems. Finally, we will indicate areas for future work. Amongst other points, we will give suggestions for further applications of the improvements to the method for flows involving gravity-driven jets, along with ideas for developing the investigations into wake flow past a plate normal to the stream.

# 1 Spillway flows

## 1.1 Simple spillway

We consider the flow of an inviscid and incompressible fluid over a spillway (c.f. figure 4a). The flow is steady, two-dimensional and irrotational; and the effects of gravity will be included. Far upstream, we have a uniform horizontal stream of constant velocity and depth. The fluid flows along a flat bed and then along an angled wall, forming a jet downstream. In working with a general angle, say  $\beta$ , between the two walls of the spillway, it follows that this work can also be used to consider a fluid being poured over a wedge-shaped lip (c.f. figure 4b), on the important assumption that the flow remains attached. A numerical approach will be used to analyse these flows: conformal mappings will be utilised with the aim of obtaining an expression for the physical flow in terms of the associated complex potential, which can be achieved through use of the series truncation and collocation technique, as in work on this flow by Vanden-Broeck and Keller [1986].

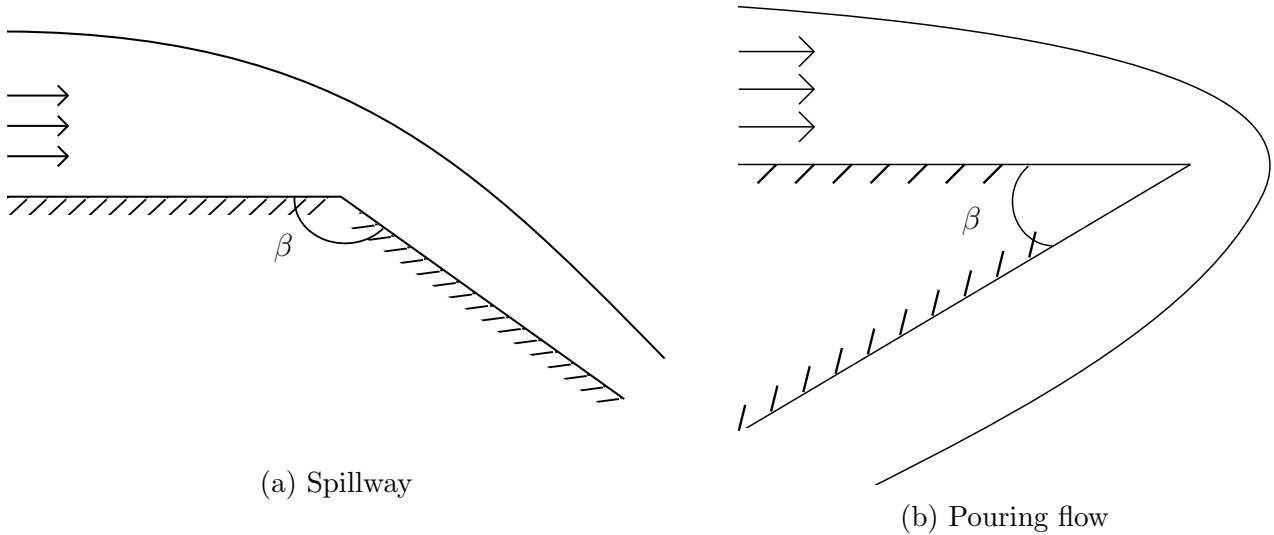


Figure 4:  $z$ -planes for spillway and pouring flows

### 1.1.1 Reproduction

The reproduction of this method serves to demonstrate the general approach that will be utilised in many subsequent problems presented here; and comparisons to this work will be made later.

We define the Froude number

$$F = \frac{U}{\sqrt{gH}}, \quad (1.1)$$

where  $U$  is the far-upstream velocity,  $g$  is the acceleration due to gravity and  $H$  is the far-upstream depth of the flow. In the calculations here, we are concerned with  $F > 1$ , i.e. supercritical flow. We will assume constant atmospheric pressure and denote it by  $P_a$ . In particular, we assume that the pressure along the free surface is this constant atmospheric pressure. We non-dimensionalise with respect to the far-upstream depth and velocity and so we have unit depth and velocity far upstream. Figure 5a depicts the  $z$ -plane of the spillway problem, where  $z$  is the complex variable defined by  $z = x + iy$ . Note that the origin is set to be at the corner  $C$  of the spillway walls. Throughout the flow, the Bernoulli condition gives that

$$\frac{1}{2}q^2 + \frac{y}{F^2} + p = \frac{1}{2} + \frac{1}{F^2}, \quad (1.2)$$

where  $q$  is the magnitude of the velocity; and  $p = (P - P_a)/(\rho U^2)$  where  $P$  and  $\rho$  denote the dimensional pressure and density. For brevity, we will refer to  $p$  as the pressure. Recalling that we assume  $P = P_a$  on the free surface, then along  $IJ$  we have

$$\frac{1}{2}q^2 + \frac{y}{F^2} = \frac{1}{2} + \frac{1}{F^2}. \quad (1.3)$$

The earlier stated assumptions for the fluid and flow mean that the flow satisfies Laplace's equation and so we can utilise potential flow theory. Therefore, we now introduce the complex potential,  $f$ , which is defined by  $f = \phi + i\psi$ , where  $\phi$  is the velocity potential and  $\psi$  is the streamfunction. We set  $\phi = 0$  at the corner  $C$ ;  $\psi = 0$  along the wall  $ICJ$ ; and  $\psi = 1$  along the free surface  $IJ$ . Figure 5b shows the  $f$ -plane, which is an infinite strip of width 1, where  $0 \leq \psi \leq 1$ . Note that  $f$  is an analytic function of  $z$ ; and that, in the flow domain, the velocity potential  $\phi$  satisfies Laplace's equation.

We aim to map the flow region to a unit semi-circle in an intermediate complex plane, so we

introduce the  $t$ -plane which is defined by

$$f = \frac{2}{\pi} \log \frac{1+t}{1-t}. \quad (1.4)$$

This maps the infinite strip of the  $f$ -plane to the upper-half of a unit semi-circle in the  $t$ -plane. The interior of the infinite strip maps into the interior of the semi-circle, whilst the free surface  $IJ$  maps to the arc of the semi-circle; and the walls of the spillway map to the diameter of the semi-circle along the real-axis of the  $t$ -plane (c.f. figure 5c).

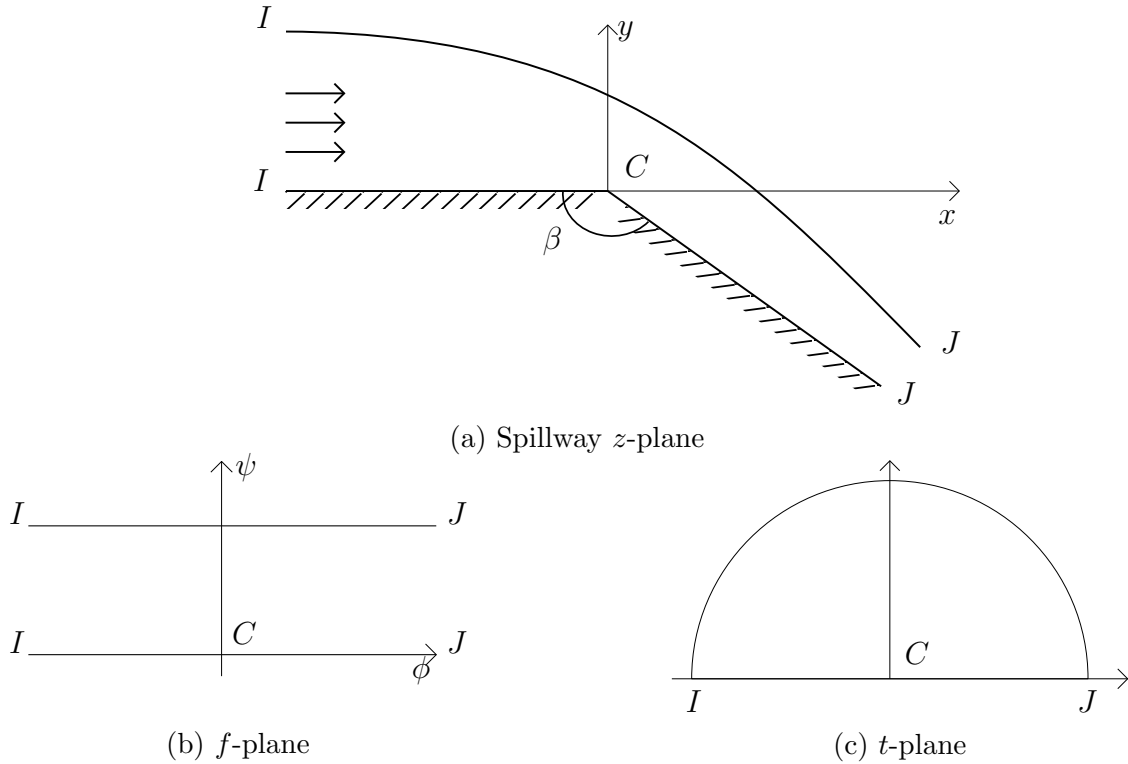


Figure 5: Complex planes for spillway flow.

The final complex variable to be introduced here is the complex velocity,  $\zeta$ , which is defined by  $\zeta = df/dz = u - iv = qe^{-i\theta}$ . Note that  $u$  and  $v$  are the horizontal and vertical components of velocity, respectively; and  $q$  and  $\theta$  are the magnitude and angle of the velocity, respectively. Finding  $\zeta$  as an analytic function of the complex potential is the aim. To achieve this, we first consider the behaviour and conditions at various points in the flow. Far upstream, as  $x \rightarrow -\infty$ , the flow approaches a uniform horizontal stream of constant unit velocity. Proceeding similarly to Vanden-Broeck [2010] in analysis of the flow approaching a uniform stream, we let  $y = 1 + \eta(x)$  be

the equation of the free surface  $IJ$ . Then, the governing equations for the flow far upstream are:

$$\phi_{xx} + \phi_{yy} = 0 \text{ for } 0 < y < 1 + \eta \quad (\text{Laplace's equation}) \quad (1.5)$$

$$\phi_y = \phi_x \eta_x \text{ on } y = 1 + \eta \quad (\text{Kinematic boundary condition on free surface}) \quad (1.6)$$

$$\frac{1}{2}(\phi_x^2 + \phi_y^2) + \frac{y}{F^2} = \frac{1}{2} + \frac{1}{F^2} \text{ on } y = 1 + \eta \quad (\text{Bernoulli equation}) \quad (1.7)$$

$$\phi_y = 0 \text{ on } y = 0 \quad (\text{Kinematic boundary condition along wall}). \quad (1.8)$$

Taking small perturbations about the equations for uniform horizontal flow of constant unit velocity, we write  $\zeta = 1 + \tilde{\zeta} + \dots$ ,  $\phi = x + \tilde{\phi} + \dots$  and  $\eta = \tilde{\eta} + \dots$ , where  $\tilde{\zeta}$ ,  $\tilde{\phi}$  and  $\tilde{\eta}$  are small. Then the linearised equations are

$$\tilde{\phi}_{xx} + \tilde{\phi}_{yy} = 0 \quad (1.9)$$

$$\tilde{\eta}_x = \tilde{\phi}_y \text{ on } y = 1 \quad (1.10)$$

$$\tilde{\phi}_x + F^{-2}\tilde{\eta} = 0 \text{ on } y = 1 \quad (1.11)$$

$$\tilde{\phi}_y = 0 \text{ on } y = 0. \quad (1.12)$$

Eliminating  $\tilde{\eta}$ , we arrive at

$$\tilde{\phi}_{xx} + F^{-2}\tilde{\phi}_y = 0 \text{ on } y = 1. \quad (1.13)$$

Using separation of variables to find a solution to (1.9) of the form  $\tilde{\phi}(x, y) = X(x)Y(y)$ , we have

$$\frac{X''(x)}{X(x)} = -\frac{Y''(y)}{Y(y)} = \pi^2 \lambda^2 \text{ and } Y'(0) = 0, \quad (1.14)$$

and we obtain the following solution:

$$X(x) = Be^{-\pi\lambda x} + Ce^{\pi\lambda x} \text{ and } Y(y) = D \cos \pi\lambda y, \quad (1.15)$$

where  $B$ ,  $C$ ,  $D$  are unknown constants. We require that  $\tilde{\phi}$  is bounded as  $x \rightarrow -\infty$  and so we set  $B = 0$ . Therefore, we have

$$\tilde{\phi} = \tilde{A}e^{\pi\lambda x} \cos \pi\lambda y, \quad (1.16)$$

where  $\tilde{A} = CD$  is an unknown constant. We can now utilise (1.13): substituting in for the partial derivatives of  $\tilde{\phi}$ , (1.13) becomes

$$\pi^2 \lambda^2 \tilde{A} e^{\pi \lambda x} \cos \pi \lambda y - F^{-2} \pi \lambda \tilde{A} e^{\pi \lambda x} \sin \pi \lambda y = 0, \quad (1.17)$$

on  $y = 1$ . Rearranging and simplifying leads us to

$$\pi \lambda = F^{-2} \tan \pi \lambda. \quad (1.18)$$

Since  $\phi = x + \tilde{\phi} + \dots$  and utilising (1.16), far upstream we have

$$\zeta = \frac{\partial \phi}{\partial x} - i \frac{\partial \phi}{\partial y} \sim 1 - \tilde{A} \pi \lambda e^{\pi \lambda x} \cos \pi \lambda y + i \pi \lambda \tilde{A} e^{\pi \lambda x} \sin \pi \lambda y = 1 - \tilde{A} \pi \lambda e^{\pi \lambda z}. \quad (1.19)$$

By noting that since  $df/dz = \zeta \rightarrow 1$  far upstream, we have  $z \sim f$  as  $\phi \rightarrow -\infty$ , and so

$$\zeta \sim (1 + A e^{\pi \lambda f}) \quad \text{as } \phi \rightarrow -\infty, \quad (1.20)$$

where  $A = \tilde{A} \pi \lambda$  is an unknown constant and  $\lambda$  is the smallest positive root of  $\pi \lambda - F^{-2} \tan \pi \lambda = 0$ . Here, we take the smallest positive root since we wish to remove the dominant singularity upstream, i.e. taking the value of  $\lambda$  that leads to the slowest decay in (1.20) as  $\phi \rightarrow -\infty$ . Note that if the Froude number is less than 1, then there is no real root for  $\lambda$  and from (1.20) we can see that we have subcritical flow with waves. However, we are investigating supercritical flow here, i.e. where  $F > 1$ .

Far downstream, the behaviour of the flow is

$$\zeta \sim f^{1/3} \quad \text{as } \phi \rightarrow +\infty, \quad (1.21)$$

since the flow approaches a thin wall jet [Keller and Weitz, 1957; Keller and Geer, 1973]. Keller and Geer [1973] present a method for computing asymptotic expansions for several types of flow that involve slender streams. In particular, their equation (4.8) allows for the calculation of the



first-order term of the outer expansion of a jet flow along a wall that is defined through some function  $y = \eta(x)$ . However, for the case of  $y = (\tan \beta)x$  for the wall that we have here, it is quick to show the origin of (1.21). Formally, we can write  $z(\phi + i\epsilon\psi; \epsilon)$  to be defined throughout the jet flow, where  $\epsilon$  is a measure of the slenderness of the jet. Hence, we look to expand  $z$  for small  $\epsilon$ . Since we are only looking for the first-order term, i.e. of order  $\epsilon^0$ , we simply look to find  $z(\phi) = x(\phi) + iy(\phi)$  to satisfy both the condition along the wall and the free surface (physically, due to the slenderness of the jet). Therefore, we solve

$$\begin{cases} \frac{1}{2}|x'(\phi) + iy'(\phi)|^{-2} + \frac{y}{F^2} = \frac{1}{2} + \frac{1}{F^2}, & \text{Bernoulli condition} \\ y = (\tan \beta)x, & \text{wall condition,} \end{cases} \quad (1.22)$$

which leads to

$$x'(\phi) = \cos \beta \left( 1 + \frac{2}{F^2} - \frac{2 \tan \beta}{F^2} x(\phi) \right)^{-1/2}. \quad (1.23)$$

Solving this ordinary differential equation by separation of variables and recalling that we wish to satisfy  $y = (\tan \beta)x$ , it follows that

$$z(\phi) = \frac{F^2}{2 \tan \beta} \left( 1 + \frac{2}{F^2} - (b_1 \phi + b_2)^{2/3} \right) + i \frac{F^2}{2} \left( 1 + \frac{2}{F^2} - (b_1 \phi + b_2)^{2/3} \right), \quad (1.24)$$

where  $b_1 = -3F^{-2} \sin \beta$  and  $b_2 = (1 + 2F^{-2})^{3/2}$ . Differentiating with respect to  $\phi$  and taking the leading order terms, we obtain that  $dz/d\phi \sim \phi^{-1/3}$ . We can then arrive at (1.21) for the behaviour of the complex velocity far downstream.

At the corner  $C$  of the spillway, we have flow around a corner where the angle between the walls is  $\beta$ . We know that the complex potential behaves like  $f(z) \sim z^{\frac{\pi}{2\pi-\beta}}$  near the corner  $C$  — a standard result of potential flow theory [Batchelor, 2010]. Since  $\zeta = f'(z) \sim z^{\frac{\beta-\pi}{2\pi-\beta}}$ , then

$$\zeta \sim f^{\beta/\pi-1} \quad \text{as } f \rightarrow 0. \quad (1.25)$$

Furthermore, due to the no normal flow condition along the spillway walls, we know that  $v = 0$  on  $\psi = 0$ ,  $\phi < 0$  (i.e. along the horizontal bed) and  $u \tan \beta - v = 0$  on  $\psi = 0$ ,  $\phi > 0$  (i.e. along the

sloped wall). Finally, the Bernoulli condition (1.3) should be satisfied along the free surface  $IJ$ .

It can be verified that

$$\zeta(t) = (-t)^{\beta/\pi-1}(-\log c(1-t))^{1/3}(-\log 2c)^{-1/3} \left( 1 + (1+t)^{2\lambda} \sum_{n=0}^{\infty} a_n t^n \right) \quad (1.26)$$

immediately satisfies all of the above conditions, apart from the Bernoulli equation. Note that  $c$  is a constant which we are free to choose such that  $0 < c < \frac{1}{2}$  and it has been introduced to ensure that the complex velocity is real for  $-1 < t < 0$ , i.e. no normal flow along the horizontal wall.

It now remains to find the unknown coefficients,  $a_n$ , for given values of the Froude number and angle between the spillway walls. As mentioned earlier, we will use a numerical approach, that is, series truncation and collocation. First, we truncate the infinite series in (1.26) after  $N$  terms, so we have

$$\zeta(t) = (-t)^{\beta/\pi-1}(-\log c(1-t))^{1/3}(-\log 2c)^{-1/3} \left( 1 + (1+t)^{2\lambda} \sum_{n=0}^{N-1} a_n t^n \right). \quad (1.27)$$

Since the image of the free surface  $IJ$  in the  $t$ -plane can be expressed by  $t = e^{i\sigma}$ , where  $0 < \sigma < \pi$ , we introduce  $N$  mesh points defined by

$$\sigma_I = \frac{\pi}{2N} + \frac{\pi}{N}(I-1), \quad \text{for } I = 1, \dots, N, \quad (1.28)$$

which gives  $N$  equally-spaced points along the image of the free surface. Recall that it still remains for  $\zeta$  to satisfy the Bernoulli condition (1.3) on the free surface. Therefore, for each of the  $N$  mesh points, we require the magnitude of the velocity and the corresponding  $y$ -value. We can obtain the speed at each mesh point by noting that  $q = |\zeta|$  and simply evaluating the expression (1.27) for  $\zeta$  at each point, in terms of the unknown coefficients  $a_n$ ,  $n = 0, \dots, N-1$ . We can also find the value of  $y$  at each of the mesh points by taking the imaginary part of the following integral for  $z_I$  (the value of  $z$  at the mesh point  $\sigma_I$ ):

$$z_I = z_0 + \int_{\pi/2}^{\sigma_I} \frac{dz}{df} \frac{df}{dt} \frac{dt}{d\sigma} d\sigma = z_0 + \int_{\pi/2}^{\sigma_I} \frac{1}{\zeta} \left( -\frac{4}{\pi} \frac{1}{t^2 - 1} \right) i e^{i\sigma} d\sigma, \quad (1.29)$$

using  $t = e^{i\sigma}$  and where  $z_0$  is

$$z_0 = \int_0^1 \frac{dz}{df} \frac{df}{d\psi} d\psi = i \int_0^1 \frac{1}{\zeta} d\psi, \quad (1.30)$$

using  $t = (e^{i\pi\psi/2} - 1)/(1 + e^{i\pi\psi/2})$  — found by inverting (1.4). Note that (1.29) arises from integrating from  $z = 0$  across the flow along the equipotential  $\phi = 0$  from  $\psi = 0$  to  $\psi = 1$  (i.e. the integral (1.30)), and then integrating from  $t = i$  (which corresponds to the point  $z_0$ ) along the arc of the unit semi-circle to each mesh point. By evaluating the Bernoulli condition at each of the  $N$  mesh points, we then have  $N$  algebraic equations in terms of  $N$  unknown coefficients  $a_n$ . To find the unknowns, we can solve the system numerically by iteration. Here, we use the `fsolve` function of MATLAB, starting with the initial guess of all the unknown coefficients being zero and the solution is obtained within 4 iterations for  $N = 100$ .

Once the coefficients have been found, we can then plot the results to find the shape of the free surface  $IJ$ . This is achieved by evaluating the integral in (1.29) for the  $z$ -values along the free surface. It should be noted that the resulting flow is for a given pair of parameters: the Froude number,  $F$ , and the angle between the spillway walls,  $\beta$ .

Figure 6 shows the resulting plot for the case where  $F = \sqrt{1.3}$  and  $\beta = 3\pi/4$ . In this case, 100 coefficients of the truncated series of the complex velocity expression were found. This free-surface plot matches well with that of Vanden-Broeck and Keller [1986]. Whilst the same method was utilised, there is a difference in the calculations: instead of working with the derivative of the Bernoulli equation (c.f. Vanden-Broeck and Keller [1986]), it is the Bernoulli equation itself that is imposed here for the condition to be satisfied along the free surface. However, the same results have been obtained. An advantage of using the differentiated form of the Bernoulli condition is that it is less computationally expensive. This is since, to find the  $y$ -values at the mesh points, many numerical integrations need to be performed; but when using the differentiated Bernoulli condition, the  $y$ -values are not required whilst solving for the unknown coefficients, hence it is then a less computationally-expensive system to solve. However, the undifferentiated form has been used in the calculations presented here since this will be the approach in subsequent problems where using the differentiated form is not possible (e.g. when there are two free surfaces).

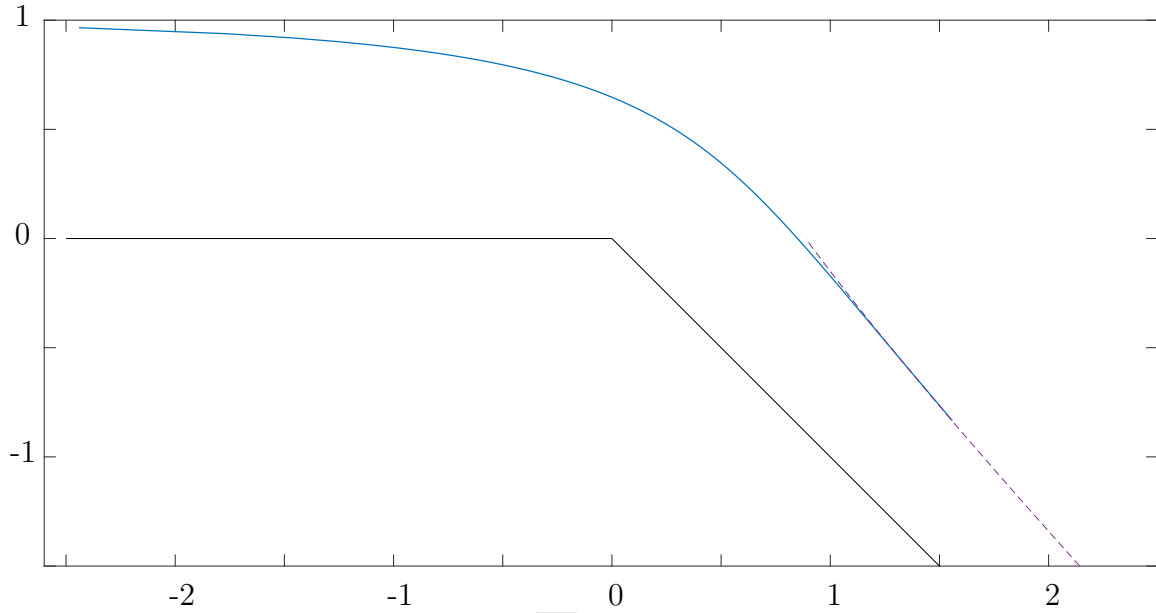


Figure 6: Spillway free-surface plot:  $F = \sqrt{1.3}$ ,  $\beta = 3\pi/4$ ,  $c = 0.2$ ,  $N = 100$ . The dashed line is the asymptotic solution (1.31), valid for  $y \ll -F^2$ .

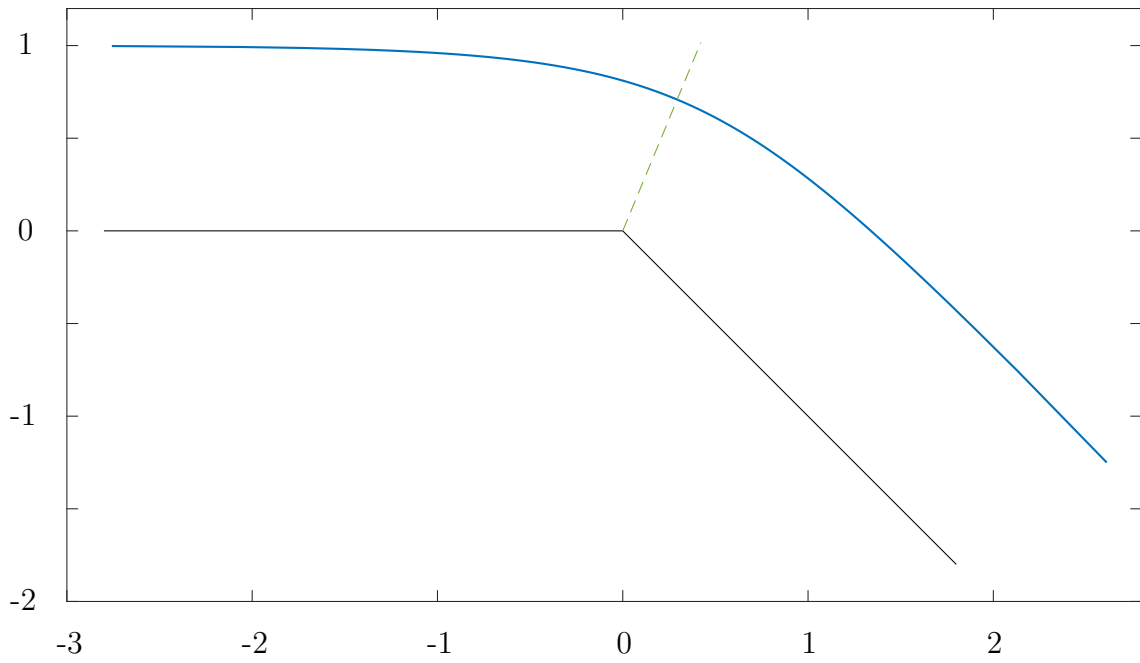


Figure 7: Spillway free-surface plot:  $F = 10$ ,  $\beta = 3\pi/4$ ,  $c = 0.2$ ,  $N = 100$ . The dashed line is the line of symmetry of the flow along  $\theta = 3\pi/8$ .

Coefficients, $a_n$	$N$			
	100	200	300	400
$a_0$	0.10658	0.10657	0.10656	0.10656
$a_1$	-0.08388	-0.08390	-0.08390	-0.08390
$a_2$	0.03037	0.03036	0.03036	0.03036
$a_3$	-0.01871	-0.01872	-0.01873	-0.01873
$a_4$	0.00950	0.00950	0.00949	0.00949

Table 1: Coefficients of the truncated series for  $F = \sqrt{1.3}$ ,  $\beta = 3\pi/4$ ,  $c = 0.2$ .

The asymptotic solution

$$x = y \cot \beta + \frac{F}{\sin \beta} \frac{1}{(F^2 + 2 - 2y)^{1/2}} \quad (1.31)$$

(as given by Vanden-Broeck and Keller [1986]) is also present in Figure 6 and shows that the numerical and asymptotic solutions fit well together, for  $y \ll -F^2$ . We can also validate the results by taking a large Froude number: the resulting flow profile should be symmetric about the corner,  $C$ , of the spillway walls due to the lack of dominance of gravity. This can be seen in figure 7 where the green dashed line is the line of symmetry and we have Froude number  $F = 10$ .

To further validate the numerical method involved here, there are some points to observe. We can take a number of the coefficients of the power series in  $t$  and check that their values do not vary greatly with the number of collocation points taken, and that the coefficients are each converging to some value. Table 1 shows that the coefficients do indeed behave as we would hope. We can also see that the coefficients decay rapidly, as shown by figure 8. Finally, various values within the interval  $(0, \frac{1}{2})$  have been tested for the constant  $c$  that is used in the complex velocity ansatz (1.27). Whilst the resulting coefficients do depend on the value chosen for  $c$ , the free-surface profiles are not affected.

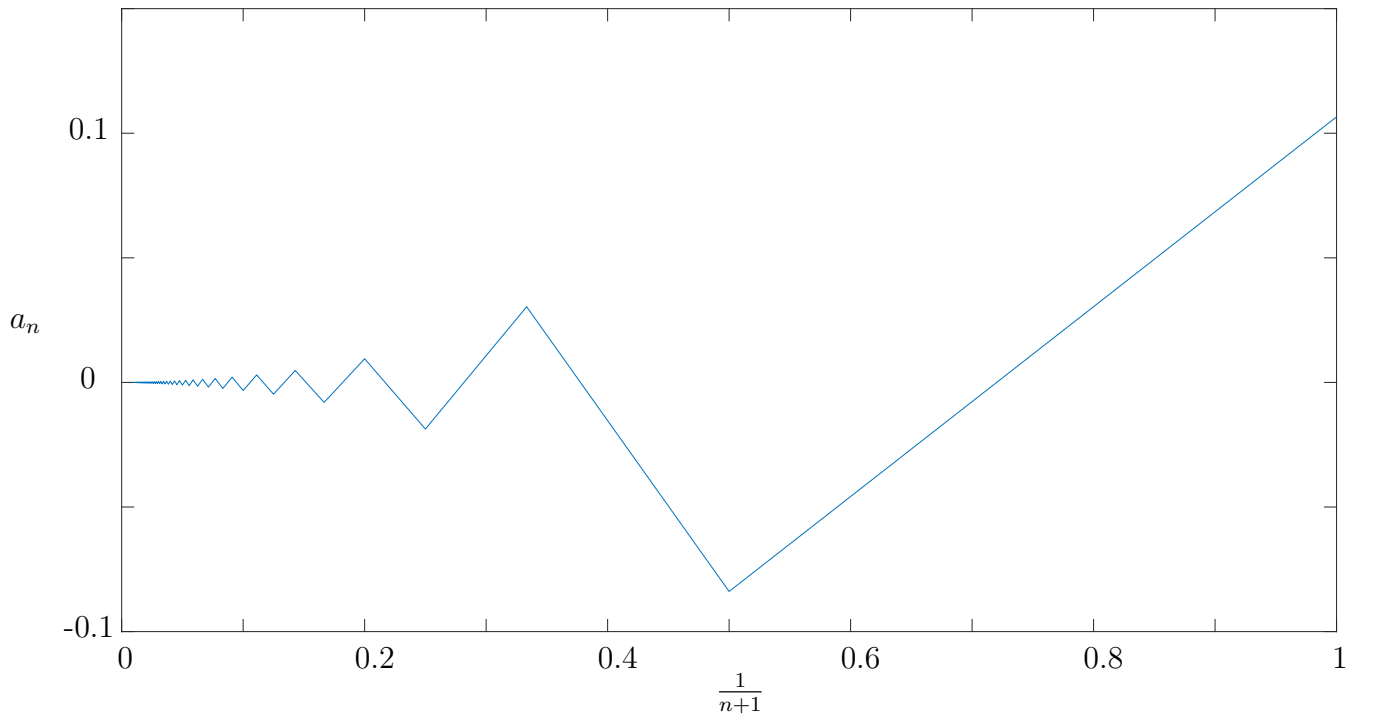


Figure 8: Coefficient decay for  $F = \sqrt{1.3}$ ,  $\beta = 3\pi/4$ ,  $c = 0.2$ ,  $N = 100$ .

### 1.1.2 Alternative mapping

We now adapt the numerical method presented in the previous section to enable us to consider spillway geometries where the walls are not straight. The first step will be to demonstrate, in this section, the validity of this new approach by reproducing the results of the previous section. The approach will remain largely the same as before, but different conformal mappings will be utilised. The initial set up is the same, as shown in figure 9a, and the variables have again been non-dimensionalised so we have unit velocity and depth far upstream. The pressure is, as before, assumed to be constant on the free surface and so the  $f$ -plane (for the complex potential) is as in figure 9b: an infinite strip of unit width.

We wish to map the flow region of the  $f$ -plane to the upper-half of a unit semi-circle centred at the origin of the  $t$ -plane, as before. Again, the interior of the infinite strip will map into the interior of the semi-circle. However, now we want the free surface  $IJ$  to map to the left-hand arc of the semi-circle, the sloped wall of the spillway to map to the right-hand arc of the semi-circle, and the horizontal wall of the spillway to map to the diameter of the semi-circle (c.f. figure 9c). It will be useful to have this mapping for later problems where the streamline along  $CJ$  is not just a straight, sloping wall. The mapping meeting the aforementioned specifications is stated in related works such as Vanden-Broeck and Keller [1987] and Dias and Tuck [1991]. However, it appears without derivation since the mapping can be verified if the reader so wishes. Here, we mention how the conformal mapping can be obtained. Using standard conformal mappings, we can map the unit half-disc to the upper half-plane (using the Möbius Transformation) and we can map the upper half-plane to the infinite unit-width strip of the  $f$ -plane (using the Schwarz-Christoffel mapping). Alternatively, loosely following Chaplygin's singular point method, we look to find and analyse the behaviour of the singularities in the flow region [Gurevich, 1965]. We have unit volume momentum flux, so at  $I$  we have a source of unit strength, i.e. there is a logarithmic singularity at  $t = -1$ . There must then be a sink of unit strength at  $J$ , so we have logarithmic singularity at  $t = i$ . We can analytically continue  $f(t)$  beyond the definition given for the upper-half unit semi-circle, extending the definition of the mapping over the real-axis of the  $t$ -plane, through use of the Riemann-Schwarz symmetry principle [Nehari, 1952; Lavrent'ev and Shabat, 1967]. It follows

that we have another sink of unit strength at  $t = -i$  and the source at  $t = -1$  is of double strength and so

$$f(t) = \frac{2}{\pi} \log(t+1) - \frac{1}{\pi} \log(t-i) - \frac{1}{\pi} \log(t+i) + f_0, \quad (1.32)$$

where  $f_0$  is an arbitrary constant. Setting the corner of the spillway to have zero complex potential leads to  $f_0 = -\frac{1}{\pi} \log 2$ . Therefore, the  $t$ -plane is defined by

$$f = \frac{1}{\pi} \log \frac{(t+1)^2}{2(t^2+1)}. \quad (1.33)$$

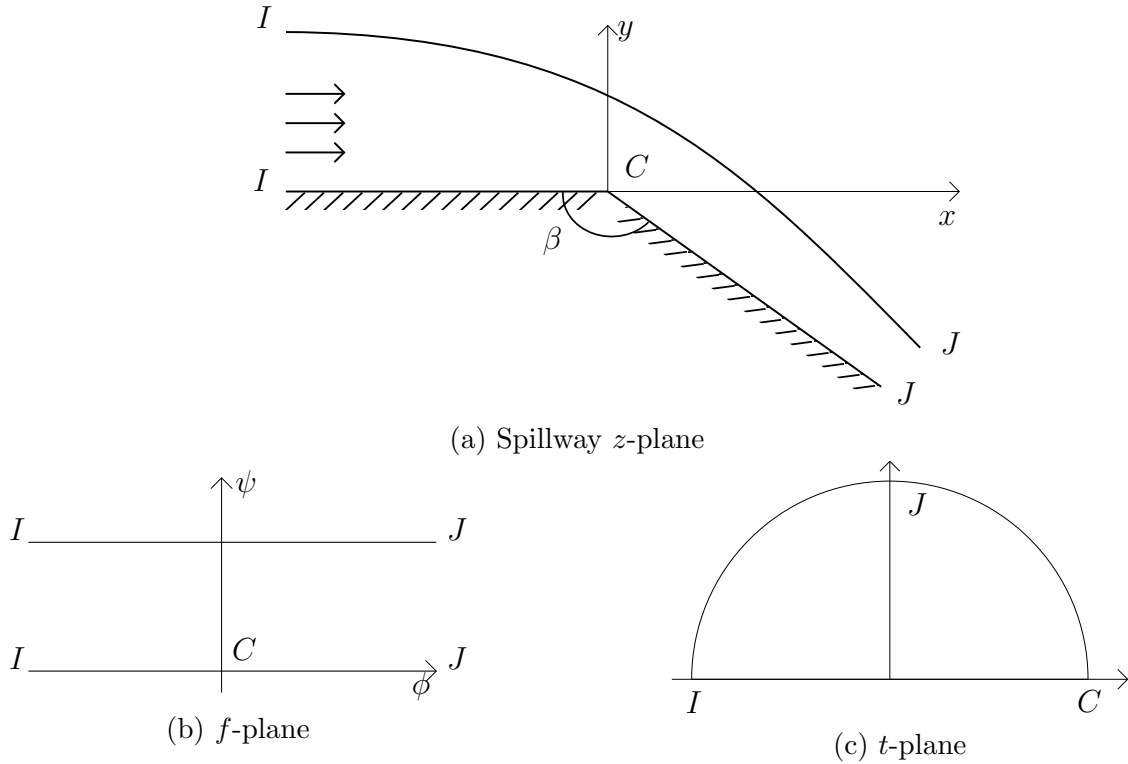


Figure 9: Complex planes for spillway flow.

The aim, as in the previous section, is to find  $\zeta$  as an analytic function of the complex potential,  $f$ . Our function for  $\zeta$  must satisfy the kinematic boundary conditions and the conditions far upstream and downstream, as discussed in the previous section. Due to a different relation between  $t$  and  $f$  utilised here, a new form for  $\zeta$  is required. Firstly, due to the uniform horizontal flow far upstream of unit velocity, we know that  $\zeta \sim (1 + Ae^{\pi\lambda f})$  as  $\phi \rightarrow -\infty$ , where  $A$  is an unknown constant and  $\lambda$  is the smallest positive root of  $\pi\lambda - F^{-2} \tan \pi\lambda = 0$ . Using the mapping (1.33), we have that  $f \sim (2/\pi) \log(t+1)$  as  $t \rightarrow -1$ . Therefore,  $\zeta \sim 1 + A(t+1)^{2\lambda}$  as  $t \rightarrow -1$ .



For the flow around the corner  $C$  as  $f \rightarrow 0$ , we consider the limit as  $t \rightarrow 1$ ; hence we set  $t = 1 + \epsilon$ , such that  $\epsilon \ll 1$ . Expanding (1.33) near  $t = 1$ , we have

$$\begin{aligned} f &= \frac{1}{\pi} \log \frac{(t+1)^2}{2(t^2+1)} \\ &= \frac{1}{\pi} \left( \log \left( 1 + \epsilon + \frac{\epsilon^2}{4} \right) - \log \left( 1 + \epsilon + \frac{\epsilon^2}{2} \right) \right) \\ &= -\frac{\epsilon^2}{4\pi} + O(\epsilon^3). \end{aligned} \tag{1.34}$$

Then  $f \sim -(t-1)^2/(4\pi)$  as  $t \rightarrow 1$ . It follows that, since  $\zeta \sim f^{\beta/\pi-1}$  as  $f \rightarrow 0$  (due to the flow around the corner), we have  $\zeta \sim [-(t-1)^2/(4\pi)]^{\beta/\pi-1}$  as  $t \rightarrow 1$ .

Finally, for the flow far downstream, we still have the jet along the spillway wall and so  $\zeta \sim f^{1/3}$ . Using (1.33), we have that  $f \sim -(1/\pi) \log(t^2+1)$  as  $t \rightarrow i$ . Therefore,  $\zeta \sim [-(1/\pi) \log(t^2+1)]^{1/3}$  as  $t \rightarrow i$ .

We try

$$\zeta(t) = (-\log 2c)^{-1/3} (-\log c(1+t^2))^{1/3} \left( \frac{1}{4}(t-1)^2 \right)^{\beta/\pi-1} \left( 1 + (1+t)^{2\lambda} \sum_{n=0}^{\infty} a_n t^n \right), \tag{1.35}$$

where  $\lambda$  is the smallest positive root of  $\pi\lambda - F^{-2} \tan \pi\lambda = 0$ , and  $c$  is a constant such that  $0 < c < 1/2$ . This is similar to the expression for the complex velocity that appears in the work of Dias and Tuck [1991] on weir flows and waterfalls where (1.33) is utilised. Note that the role of  $c$  is to ensure that the branch cut in the logarithm of  $c(1+t^2)$  lies outside the unit circle  $|t| = 1$ . In terms of verifying (1.35), it remains to show that the boundary conditions are satisfied.

For the kinematic boundary condition along the horizontal wall, it is clear that  $\zeta$  is real for  $-1 < t < 1$ , by considering each multiplicative term in turn, hence  $v = 0$  is satisfied along the horizontal spillway wall. Note that the constant  $c$  being restricted to the interval  $(0, \frac{1}{2})$  enables this result. Also, the coefficients  $a_n$  must be real in order for this condition to be satisfied. Another point to note is that we have  $\zeta(-1) = 1$  by carefully choosing the multiplicative constants so that the condition far upstream is met.

In this method of solution for the spillway, the boundary condition  $u \tan \beta - v = 0$  along the slope of the spillway is not automatically satisfied by our ansatz (1.35) for  $\zeta$ , with the unknown

coefficients,  $a_n$ . Instead, along with the Bernoulli equation, this will be a condition that will need to be satisfied through finding the coefficients of the power series in  $t$ .

As in the previous section, series truncation and collocation will be utilised: we truncate the series after  $N$  terms and introduce mesh points as defined in the previous section by (1.28) — equally-spaced along the arc of the unit semi-circle in the  $t$ -plane — for the collocation method. Only  $N/2$  of the mesh points correspond to the free surface, in particular the mesh points for which  $\pi/2 < \sigma < \pi$ . At these points, we impose the Bernoulli condition (1.3), so we then have  $N/2$  equations in terms of  $N$  unknown coefficients. Now, the other  $N/2$  algebraic equations arise from the kinematic boundary condition along the sloping wall by imposing  $\text{Im}(\zeta) + \text{Re}(\zeta) \tan \beta = 0$  at the  $N/2$  mesh points where  $0 < \sigma < \pi/2$ .

The two conditions to be satisfied numerically involve finding  $\zeta$  at each mesh point. This is easily achieved by simply using the ansatz (1.35) for the complex velocity, substituting in the values for the mesh points through use of  $t = e^{i\sigma}$ . In order to evaluate the Bernoulli condition at the necessary points, we need to find the value of  $y$  at each mesh point along the free surface, so we take the imaginary part of the following:

$$z_I = z_0 + \int_{\arccos(-\frac{1}{3})}^{\sigma_I} \frac{dz}{df} \frac{df}{dt} \frac{dt}{d\sigma} d\sigma = z_0 + \int_{\arccos(-\frac{1}{3})}^{\sigma_I} \frac{1}{\zeta} \left( \frac{2}{\pi} \frac{1-t}{(t+1)(t^2+1)} \right) i e^{i\sigma} d\sigma, \quad (1.36)$$

using  $t = e^{i\sigma}$  and where  $z_0$  is

$$z_0 = \int_0^1 \frac{dz}{df} \frac{df}{d\psi} d\psi = i \int_0^1 \frac{1}{\zeta} d\psi, \quad (1.37)$$

using  $t = (1 - \sqrt{1 - (2s - 1)^2}) / (2s - 1)$ ,  $s = e^{\pi i \psi}$ , from inverting (1.33). Figure 10 shows the image of the line  $\phi = 0$  where  $0 < \psi < 1$  in the  $t$ -plane, which we integrate along this curve to find  $z_0$ .

Overall, we have  $N$  equations in  $N$  unknowns and we can use a numerical iterative method to solve the system, as before. Once the coefficients have been found, we can then plot the free surface  $IJ$ , for a given Froude number,  $F$ , and angle between walls of the spillway,  $\beta$ .

Figure 11 shows a comparison of the free-surface profiles for  $F = \sqrt{1.3}$  and  $\beta = 3\pi/4$ , resulting from this calculation with (1.33) for  $N = 200$  (red line and markers), and from the mapping (1.4)

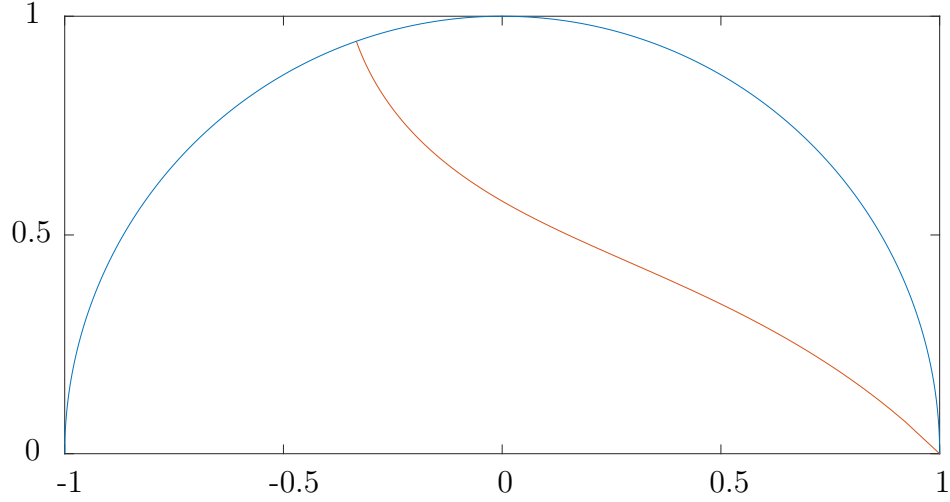


Figure 10: Here, we have the  $t$ -plane with the red line corresponding to  $\phi = 0$  and  $0 \leq \psi \leq 1$ , along which we integrate to find  $z_0$ .

of the previous section (blue line). The two free-surface profiles are very similar. The first point to note is that 200 collocation points are used for both plots but all of the mesh points are spread along the free surface in the previous section and only half of the points are along the free surface in the work presented here. This is due to the mapping used in each case and will be discussed later. Another point to note is that the profiles do not quite agree downstream. This is again down to the mappings used and the resulting spacing of the points in the physical plane: where only 100 points are used along the free surface (red line and markers), the accuracy is low for the final point compared with the blue line where 200 points are used and there is a great density of mesh points in the region. However, if 400 mesh points are instead taken with the calculation of this section using (1.33), the free-surface profiles are the same since both are calculated with 200 collocation points along the free surface.

The angle between the two spillway walls can be between 0 and  $\pi$ . So far, we have shown the results for the case where this angle is obtuse. As in the work of Vanden-Broeck and Keller [1986], the free-surface profile for pouring flows can be found, i.e. where  $\beta < \pi/2$ . Figures 12 and 13 show the free-surface profiles for the case  $\beta = \pi/4$  and with  $F = \sqrt{1.3}$  and  $F = 5$ , respectively. The sloping spillway wall has been plotted using the mesh points, instead of simply plotting  $y = (\tan \beta)x$ . This allows us to appreciate how short a distance can be reached downstream when 200 equally-spaced collocation points are used. This is due to the logarithmic behaviour of the

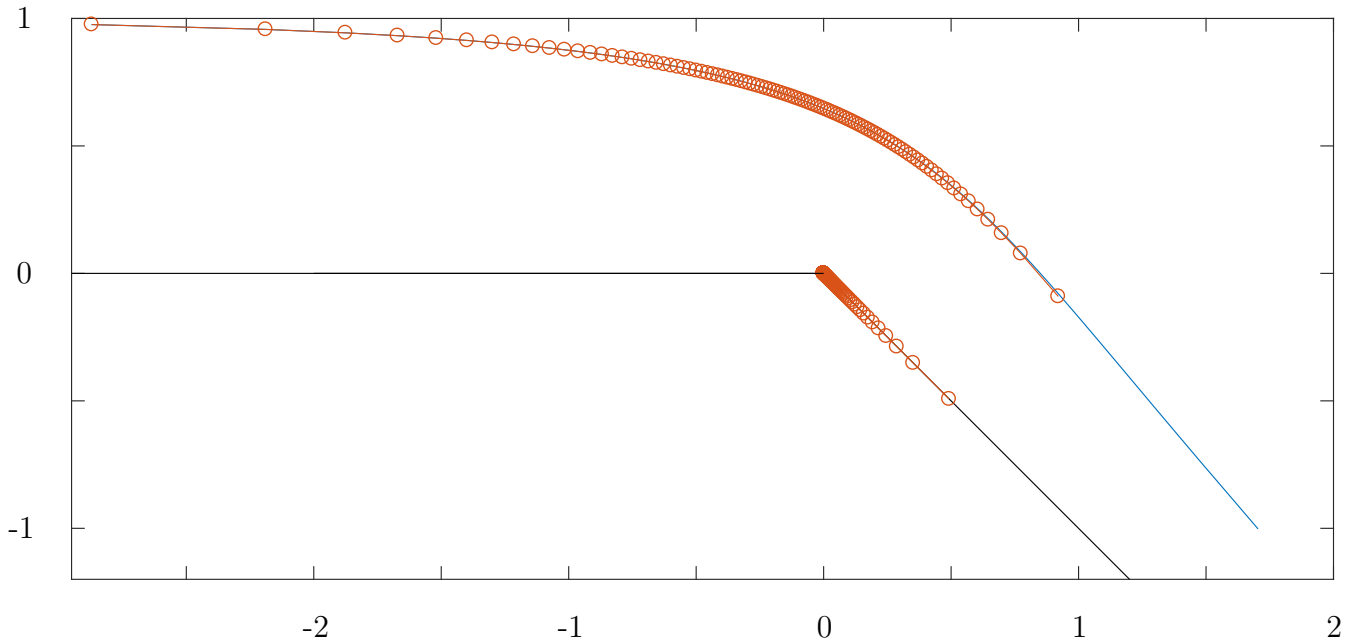


Figure 11: Spillway free-surface plot comparison with §1.1.1:  $F = \sqrt{1.3}$ ,  $\beta = 3\pi/4$ ,  $c = 0.2$ ,  $N = 200$ .

mapping (1.33): without either a very large value for  $N$  or using non-equally-spaced points, we cannot get sufficiently close to  $t = i$  such that we reach very far downstream. It seems logical to try mesh points that are not equally-spaced along the arc of the semi-circle in the  $t$ -plane, with a higher density of points close to  $t = i$ . However, this has not led to any better solutions. Either a solution which is similar in the  $z$ -plane is obtained but the coefficients do not decay well (in particular, instead of a nice decaying tail, the order of magnitude of the last few coefficients increases); or a converged solution cannot be obtained at all. Therefore, in the present study, interest in the flow downstream will be satiated either by taking a large value for  $N$  when solving, or by extrapolating the converged solution. One point to note is that the jet is made to stick to the sloped wall by requiring that there is no normal flow along the sloped spillway wall. Pouring flows with separation from the wall have been calculated by Vanden-Broeck and Keller [1989] where gravity has been neglected and, for a straight wall, the point of separation can be freely chosen.

One disadvantage of using the conformal mapping (1.33) of this section is that the efficiency of the numerical method decreases due to not only the free surface  $z$ -coordinates being unknown, but also the  $z$ -coordinates of the streamline along the sloping wall being unknown. Therefore,  $N$  in this section must be double value of the  $N$  chosen in the previous section for there to be the

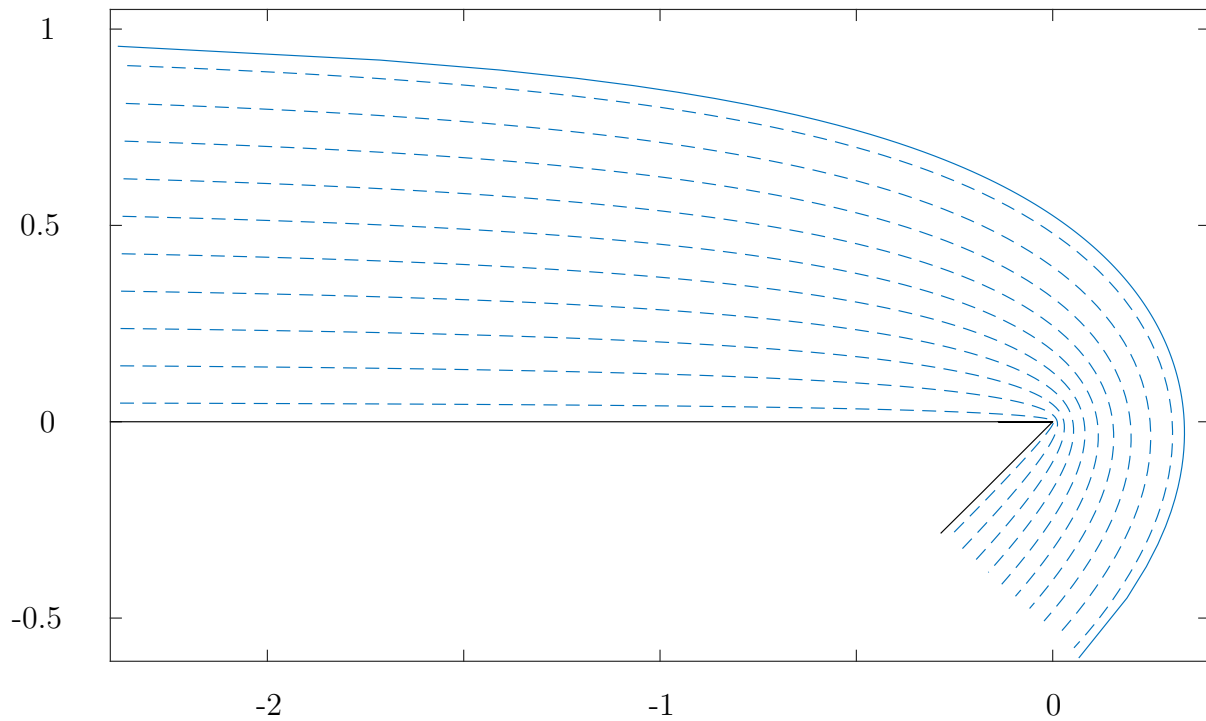


Figure 12: Spillway free-surface plot:  $F = \sqrt{1.3}$ ,  $\beta = \pi/4$ ,  $c = 0.2$ ,  $N = 200$ . Streamlines are for  $\psi = 0.05 + 0.1i$  for  $i = 0, 1, \dots, 9$ .

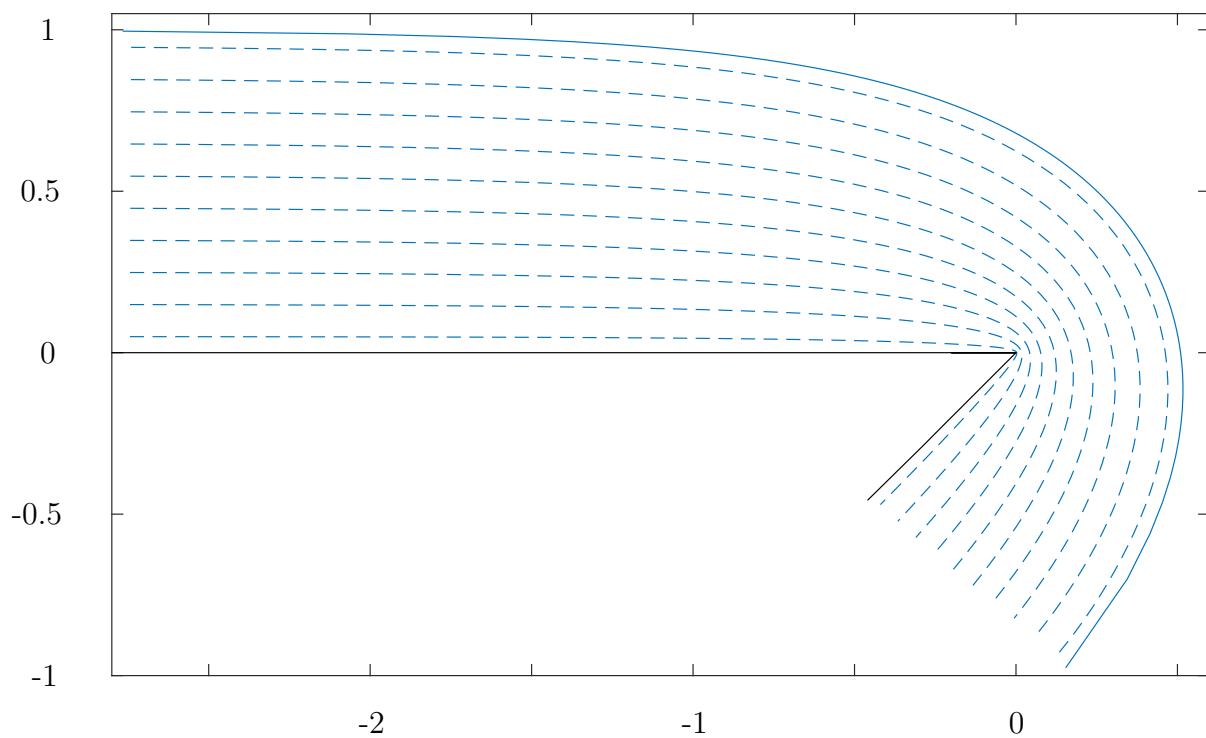


Figure 13: Spillway free-surface plot:  $F = 5$ ,  $\beta = \pi/4$ ,  $c = 0.2$ ,  $N = 200$ . Streamlines are for  $\psi = 0.05 + 0.1i$  for  $i = 0, 1, \dots, 9$ .

same number of collocation points along the free surface. On the other hand, the advantage of the conformal mapping introduced in this section is that the spillway shape can be more generalised. For example, the corner could instead be rounded; or the sloping wall of the spillway would not have to be just a straight wall. The following sections will show some examples of this.

## 1.2 Curved wall corner

Physical examples of spillways are very often not simply two straight walls at an angle to each other. Several of these structures, for example the Beaver Dam spillway (c.f. figure 14) in the United States of America, involve a curved corner (although, it should be noted here that the Beaver Dam spillway does not have uniform horizontal flow upstream along a flat horizontal wall — instead it has a deep basin of still water upstream). We will be able to study such spillways using the method presented in §1.1.2. To change the geometry of the corner of the spillway, there are two aspects of the method that we must alter. Firstly, the form of the no normal flow condition on the sloping wall will change. By expressing the sloping wall in parametric form, a normal vector can be found and then the no normal flow condition can be written in terms of a parametric variable (the distance along the wall from the origin) and the components of the velocity along the wall. Alternatively, the condition on the sloping wall can be specified by imposing that the streamline along the wall (i.e. when  $\psi = 0$ ) follows the spillway shape,  $y = p(x)$ . Then, the second alteration is to change the assumed form of the complex velocity,  $\zeta$ , if necessary, to capture any new singularities.

Let the constant  $\phi_D \in [0, \infty)$  be the value for the velocity potential at the point  $D$  along the spillway wall  $CDJ$ , as depicted in figure 15a. Then, we will consider a spillway composed of a horizontal wall for  $\phi < 0$ ; a curved wall for  $0 < \phi \leq \phi_D$ ; and a wall of constant negative gradient for  $\phi > \phi_D$ . It is important to note that the wall of constant negative gradient has the same gradient as that of the curved wall at the point corresponding to  $\phi_D$ . The curved portion of the wall will be defined by a function in  $x$ . Along the streamline  $\psi = 0$  for  $\phi > 0$ , we can impose the position of this streamline as a function of  $x$  in the  $z$ -plane by fixing it equal to the shape of the wall, i.e. the no normal flow condition. In terms of implementing the method, it is sensible to fix the value of  $\sigma_D$  instead of  $\phi_D$ , where  $\sigma_D$  is such that  $t_D = e^{i\sigma_D}$  maps to  $f_D = \phi_D$ . The value for  $\sigma_D$  should be chosen between zero and  $\pi/2$ . Note that the problem could instead be formulated for a particular physical geometry by prescribing the position of  $D$  in the  $z$ -plane. This is not shown here but the normalisation of solutions with respect to some specified geometry in the  $z$ -plane will be included in later problems.



Figure 14: Beaver Dam Spillway, by Seanfranklin. Adapted from Wikimedia Commons. Public Domain.

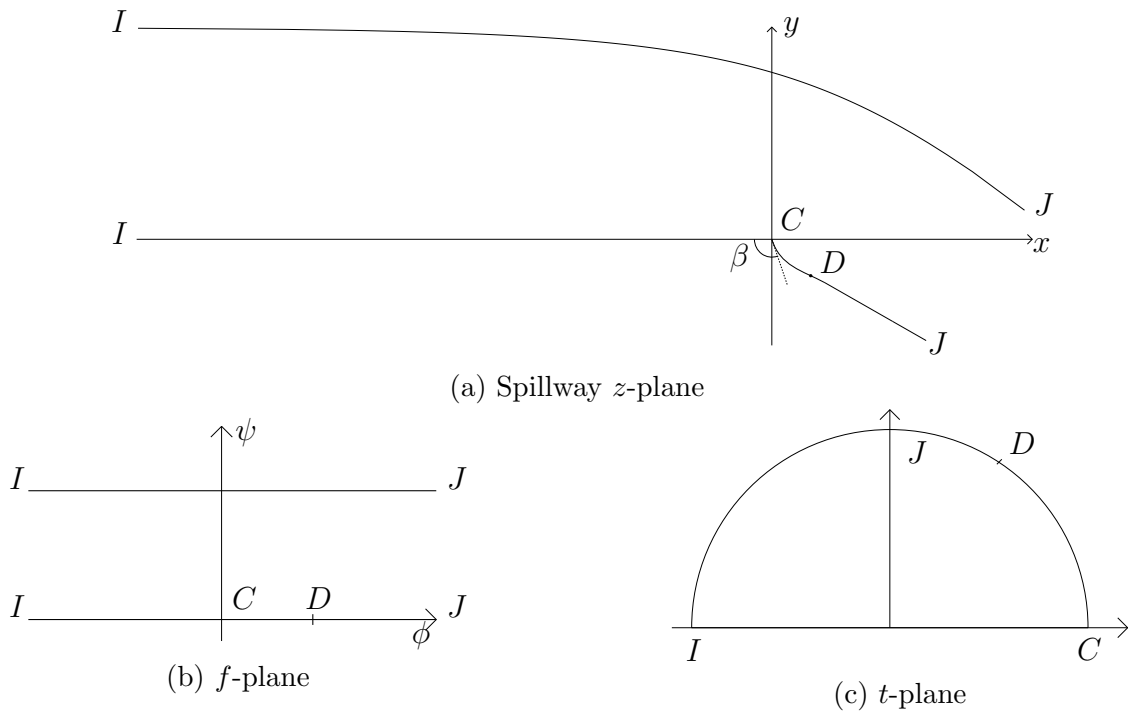


Figure 15: Complex planes for spillway with curved corner.



The rest of the flow will be as discussed in the previous section: uniform horizontal flow of unit speed and depth far upstream; and thin jet flow far downstream, running along the sloping spillway wall. Also,  $\beta$  will denote the angle between the horizontal wall and the tangent to the curved wall at  $z = 0$  (c.f. figure 15a). Hence, for some curved corner defined by  $y = y_{\text{corner}}(x)$ , the angle  $\beta$  satisfies  $\tan(\beta - \pi) = y'_{\text{corner}}(0)$ . Then, the previous mappings and complex planes of the previous section remain the same for this problem (c.f. figures 15b–15c); and the ansatz for the complex velocity will remain as before (c.f. (1.35)).

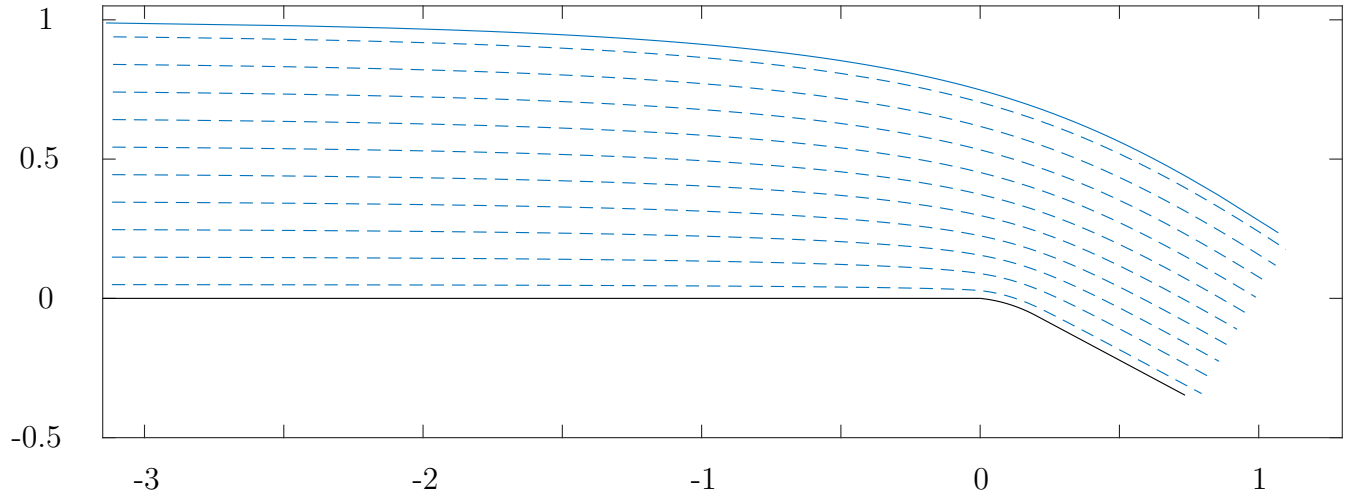
To summarise the formulation, there will be  $N$  equally-spaced mesh points (1.28) along the arc of the unit semi-circle in the  $t$ -plane and  $N$  unknown coefficients (after truncating the series in  $t$  after  $N$  terms) to be found. We have that the ansatz for the complex velocity,  $\zeta$ , is as stated in (1.35). The far-upstream, far-downstream and corner flow behaviours are satisfied by this form. It remains to satisfy the Bernoulli condition (1.3) along the free surface  $IJ$ , i.e. at mesh points where  $\pi/2 < \sigma < \pi$ ; and to satisfy the no normal flow condition along the wall  $CDJ$ . Along  $CD$  where  $0 < \sigma < \sigma_D$ , we have  $y(x) = y_{\text{corner}}(x)$ ; and along  $DJ$  where  $\sigma_D < \sigma < \pi/2$ , we have  $y(x) = m(x - x_D) + y_D$ . Here,  $m = y'_{\text{corner}}(x_D)$ ,  $x_D = \text{Re}(z_D)$  and  $y_D = \text{Im}(z_D)$  for

$$z_D = \int_0^{\sigma_D} \frac{dz}{df} \frac{df}{dt} \frac{dt}{d\sigma} d\sigma. \quad (1.38)$$

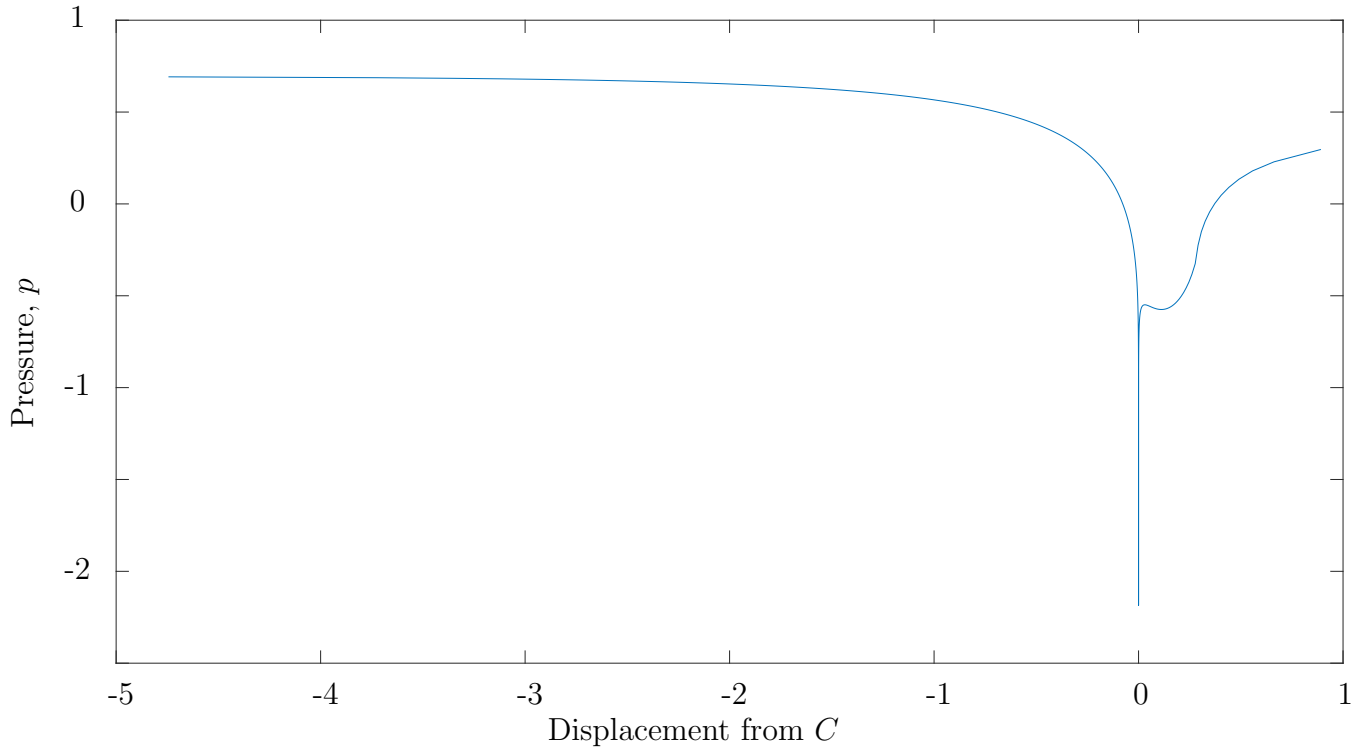
The known parameters to be specified are the Froude number  $F$  and the point  $\sigma_D$  marking the end of the curved part of the spillway wall. The shape of the wall  $CDJ$  is also to be given. We solve the system of  $N$  equations in the  $N$  unknowns numerically by iteration.

The first case we consider is where the curve is defined by a polynomial in  $x$ . Figure 16a shows the resulting free-surface profile (with other streamlines included) for  $F = 1.2$ ,  $\sigma_D = 1.4$  and  $y_{\text{corner}} = -x^4 - 0.1x^2 - x$ . Since the forces acting on the spillway walls are important to calculate from a practical point of view (to avoid constructing or to understand a defective spillway), we calculate the pressure along the walls. Using the Bernoulli equation (1.2), we have that

$$p = \frac{1}{2}(1 - |\zeta|^2) + \frac{1}{F^2}(1 - y). \quad (1.39)$$



(a) Free-surface profile: Streamlines are for  $\psi = 0.05 + 0.1i$  for  $i = 0, 1, \dots, 9$ .

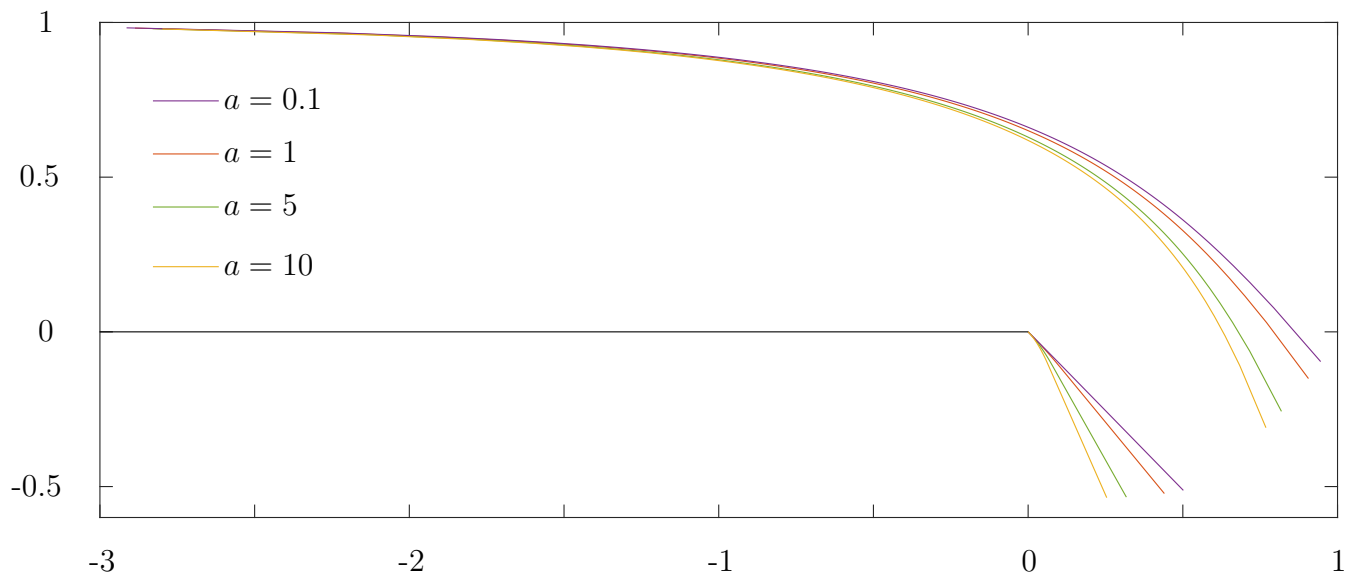


(b) Pressure against displacement from  $C$ .

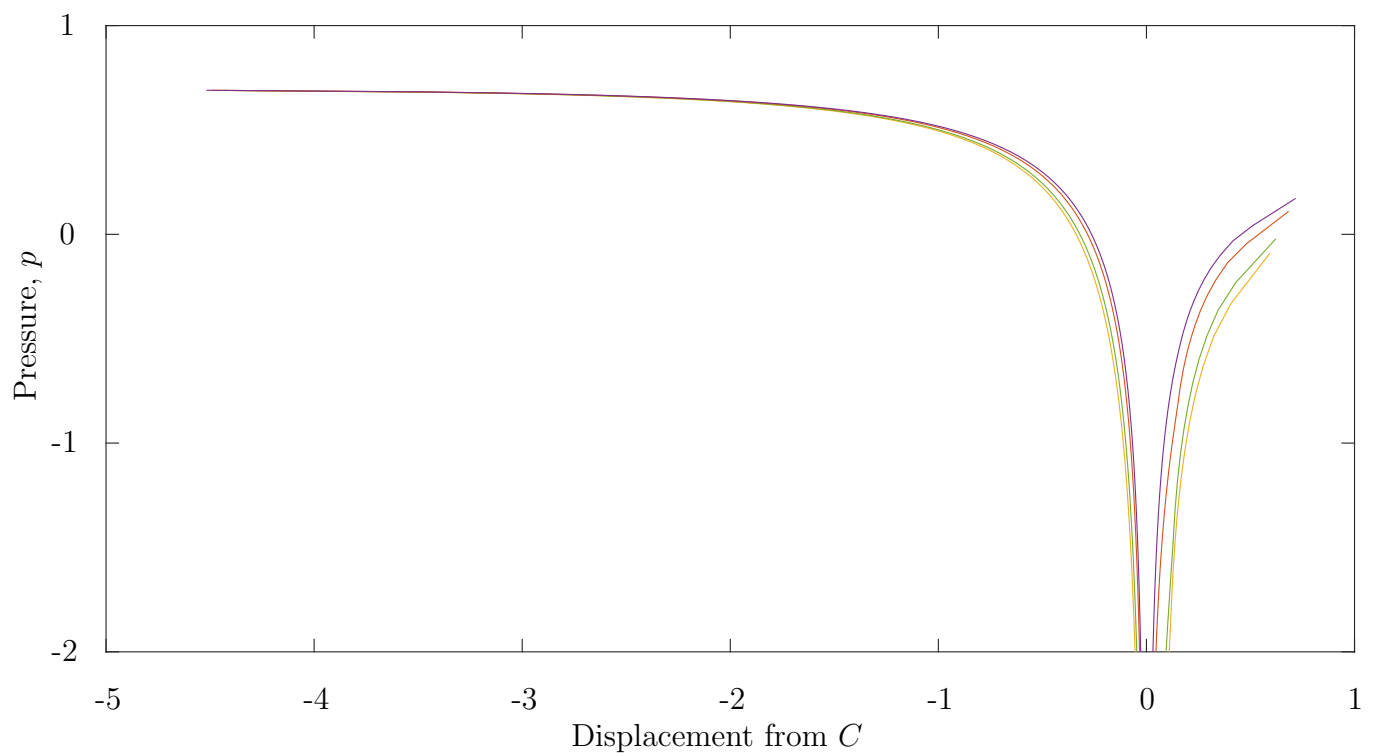
Figure 16:  $F = 1.2$ ,  $\sigma_D = 1.4$ ,  $N = 200$  and  $y_{\text{corner}} = -x^4 - 0.1x^2 - x$ .

Once the coefficients have been found, we can evaluate  $\zeta$  and  $y$  along the wall and so the pressure can be easily calculated. Figure 16b is a plot of the pressure along the walls against the displacement from the corner  $C$ . Clearly, there is a singularity in the pressure: from (1.39) the nature of the singularity is  $(t - 1)^{4(\beta/\pi - 1)}$  and since  $\beta \approx 3\pi/4$  here, we have  $(t - 1)^{-1}$ . Note that there is a ‘wobble’ in the pressure distribution just after the singularity at the corner  $C$ . This is due to the pressure gradient required to move the flow around the curved corner since the  $\psi = 0$  streamline flows along this wall, whilst maintaining the constant pressure along the  $\psi = 1$  free surface.

To investigate the effect of the curved corner of the spillway wall, we will define the corner by  $y_{\text{corner}} = -ax^2 - bx$ . Then, we know that  $\beta = \pi + \arctan(-b)$  and so, in keeping the value set for  $b$  fixed, we can vary  $a$  to vary the shape of the wall. We let  $F = 1.2$  and  $\sigma_D = 1.4$  and consider the case where  $b = 1$ , hence  $\beta = 3\pi/4$ . Figures 17a and 17b show the resulting free-surface profiles and pressure distributions along the spillway walls for  $a = 0.1, 1, 5$  and  $10$ . Note that, the greater the value of  $a$ , the greater the curvature of the wall near the corner  $C$ . Since the gradient of the straight portion of the wall is different for different values of  $a$ , the effect of the wall curvature alone cannot be discussed. The pressure distributions along the walls for the different values of  $a$  are similar: the overall shape of the distribution is similar; each has a singularity in the pressure at the corner  $C$  of nature  $(t - 1)^{-1}$ ; and far upstream, the value for the pressure is the same for each, i.e.  $p = F^{-2}$ . However, the greater the value of  $a$ , the slower the increase in pressure from the singularity. This initial slower recovery in the pressure around the corner for larger values of  $a$  is due to larger speed required for the  $\psi = 0$  streamline to flow along the curved wall around these corners of greater curvature. The pressure distribution lines appear to be on the way to a common asymptote downstream. However, note that there is a numerical accuracy issue to consider here: the last few points of the pressure distributions correspond to the last few mesh points along  $CJ$ , i.e. the mesh points closest to  $t = i$  whose arguments are less than  $\pi/2$ . Due to the logarithm involved in the mapping between the  $f$  and  $t$ -planes, the equally-spaced mesh points along the arc near to  $t = i$  map to points that are far apart in the physical plane. More points should be used throughout the calculation (both in solving for the unknowns and in any post-processing calculations) close to this singularity but, as discussed earlier, good converged solutions have not



(a) Free-surface profiles.



(b) Pressure against displacement from  $C$ .

Figure 17:  $F = 1.2$ ,  $\sigma_D = 1.4$ ,  $N = 200$  and  $y_{\text{corner}} = -ax^2 - x$ .

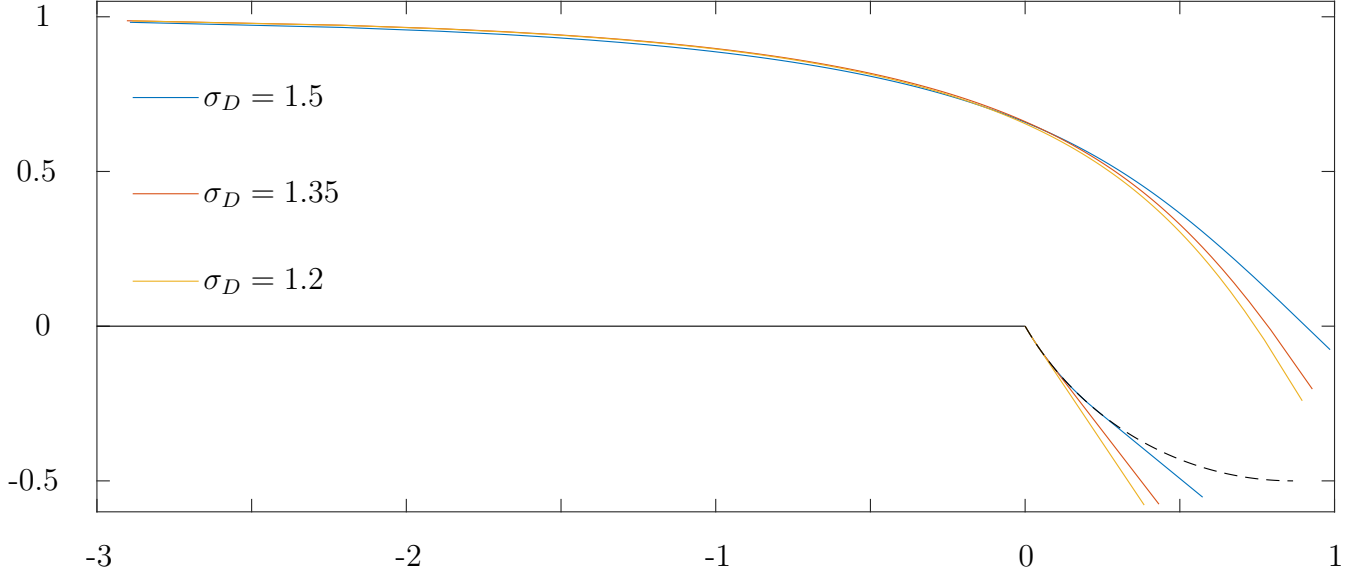
been obtained when this has been attempted. Overall, whilst the specific requirements of a spillway determine the interpretation of the results here, the pressure distributions suggest that it is most sensible to minimise  $a$  — in terms of designing a spillway that does not fail at any point along the sloping wall (and bearing in mind that a physical spillway would not involve a sloping wall of infinite length).

Now, we move to consider a concave corner for the spillway, for which we will use a circular arc. Let  $y_{\text{corner}} = y_a - \sqrt{R^2 - (x - x_a)^2}$ , where  $(x_a, y_a) = (\sqrt{R^2 - y_a^2}, y_a)$  is chosen to be the centre of the circular arc of constant radius  $R > 0$ . Note that, to choose the shape of this arc, we will specify the values of  $R$  and  $y_a$  such that  $0 < y_a < R$ . Then, the angle between the horizontal spillway wall and the tangent to the circular arc at  $z = 0$  is

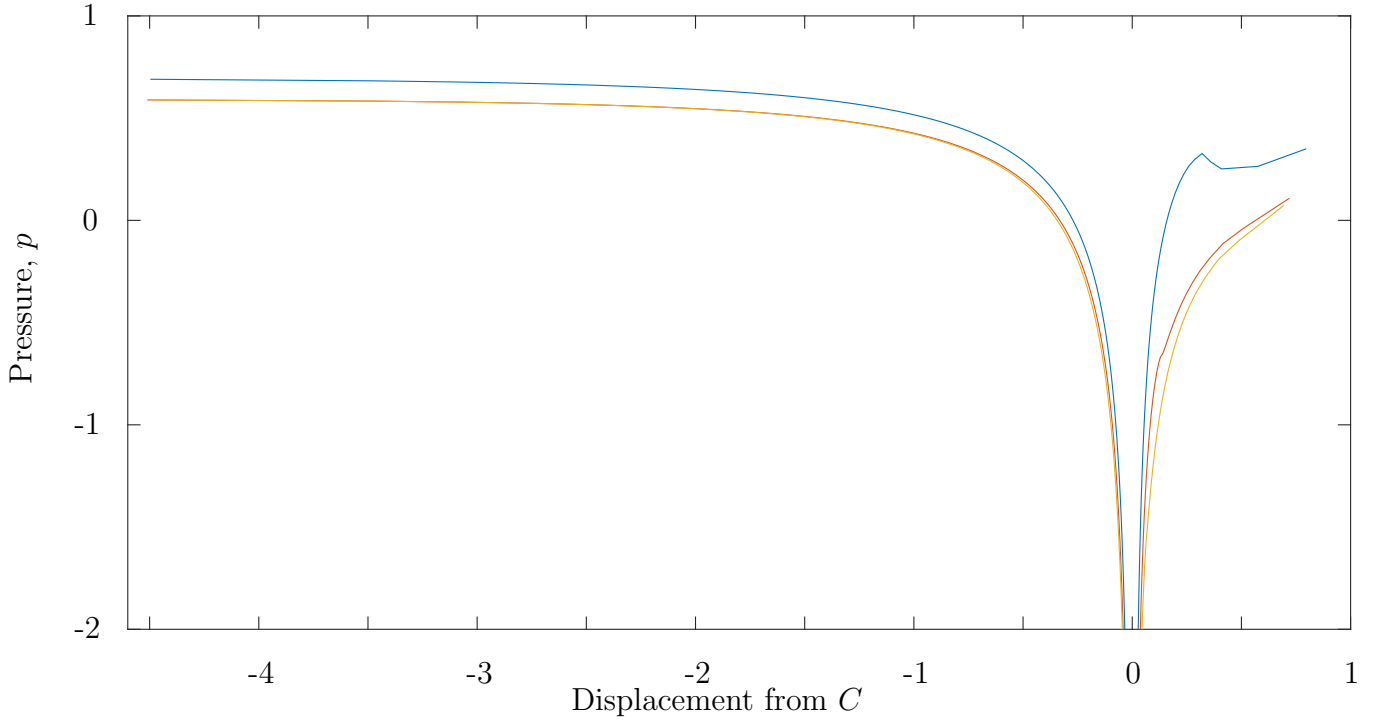
$$\beta = \pi + \arctan \left( \frac{(x_0 - x_a)}{\sqrt{R^2 - (x_0 - x_a)^2}} \right). \quad (1.40)$$

We can continue to use the same form for the complex velocity ansatz (1.35).

Figure 18a shows the resulting free surfaces for the case of  $F = 2$ , and the circular arc defined by  $R = 1$  and  $y_a = 0.5$ . We set various values for  $\sigma_D$  (the argument of the point in the  $t$ -plane marking the end of the curved corner): for larger  $\sigma_D$ , we have a longer arc for the spillway corner. The pressure distribution along the spillway wall is also presented in figure 18b. Obtaining these solutions is not problem-free. To find the solution for a large given value for  $N$ , we can start with an initial guess for the unknown coefficients that comprises of the solution coefficients from a smaller value for  $N$  and the remaining unknowns being zero. This usually works well in using the series truncation and collocation method but here, the number of iterations can still be large. This signifies a problem with the solution method, likely in the form taken for the complex velocity ansatz — in particular, a singularity in the flow may not have been correctly or sufficiently incorporated so that the power series in  $t$  can converge. There is a discontinuity in the curvature at  $D$  (the end of the corner wall section) and this has not been removed from the series representation for  $\zeta$ , although this singularity is likely to be relatively weak. Figure 19 shows this more clearly: we have a plot of the coefficient decay for  $N = 200$  and there is not a nice decaying tail for large  $n$  (i.e. the index of the coefficients) which supports the thought that the solution is problematic.



(a) Free-surface profiles for different values of  $\sigma_D$ . The dashed line is the curve of the corner if continued past the given  $\sigma_D$ .



(b) Pressure against displacement from  $C$ , for different values of  $\sigma_D$ .

Figure 18:  $F = 1.3$ ,  $N = 200$  and  $y_{\text{corner}} = y_a - \sqrt{R^2 - (x - x_a)^2}$  with  $y_a = 0.5$ ,  $R = 1$  and  $x_a = \sqrt{R^2 - y_a^2}$ .

Improving the complex velocity ansatz is left for future work, but these results serve as a useful example for showing the typical characteristics of a solution of this numerical approach where adjustments are required for a good solution.

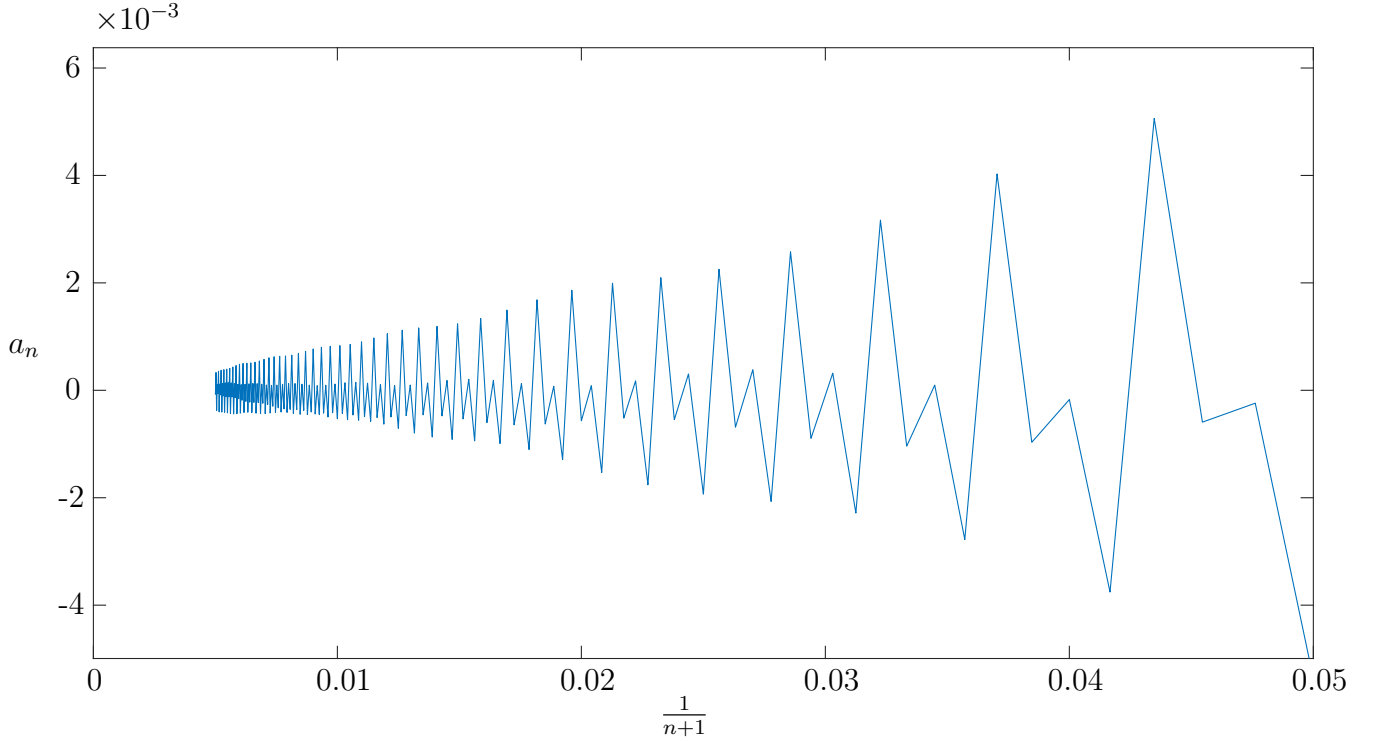


Figure 19: Coefficient decay for  $n = 19, 20, \dots, 199$  where  $F = 1.3$ ,  $N = 200$  and  $y_{\text{corner}} = y_a - \sqrt{R^2 - (x - x_a)^2}$  with  $y_a = 0.5$ ,  $R = 1$ ,  $x_a = \sqrt{R^2 - y_a^2}$  and  $\sigma_D = 1.35$ .

The method presented in this section can be applied to spillways with other shapes specified for the corner of the walls. The form of the complex velocity (1.35) can remain the same if the following conditions hold for the investigated flow:

1. uniform, horizontal flow far upstream of unit speed,
2. declining wall of constant gradient far downstream so that the thin wall jet behaviour is applicable with  $\zeta \sim f^{1/3}$  as  $\phi \rightarrow \infty$ ,
3. horizontal wall  $\psi = 0$ ,  $\phi < 0$ ,
4. corner at  $\psi = 0$ ,  $\phi = 0$  with angle of  $\beta$ ,
5. no singularities along the sloping spillway wall.

In the next section, we will consider a sloping wall consisting of steps. This will require the alteration of the complex velocity ansatz (1.35) that has been suitable for the spillways so far.



### 1.3 Stepped wall

We turn our attention to a spillway with a step built into the sloping wall. The (physical) importance of this modification to the spillways already considered in this work lies in the dissipation of energy of the fluid flow — although, with our assumptions on the fluid and flow, this cannot be investigated here. Figure 20 shows Leonardo da Vinci’s interest in water falling down over steps, and in his work he comments on the effect of deep and wide steps decreasing the destructive power of the flow [Richter, 1939]. Recently, interest in stepped spillways has increased due to the development of different building materials [Chanson, 1994].

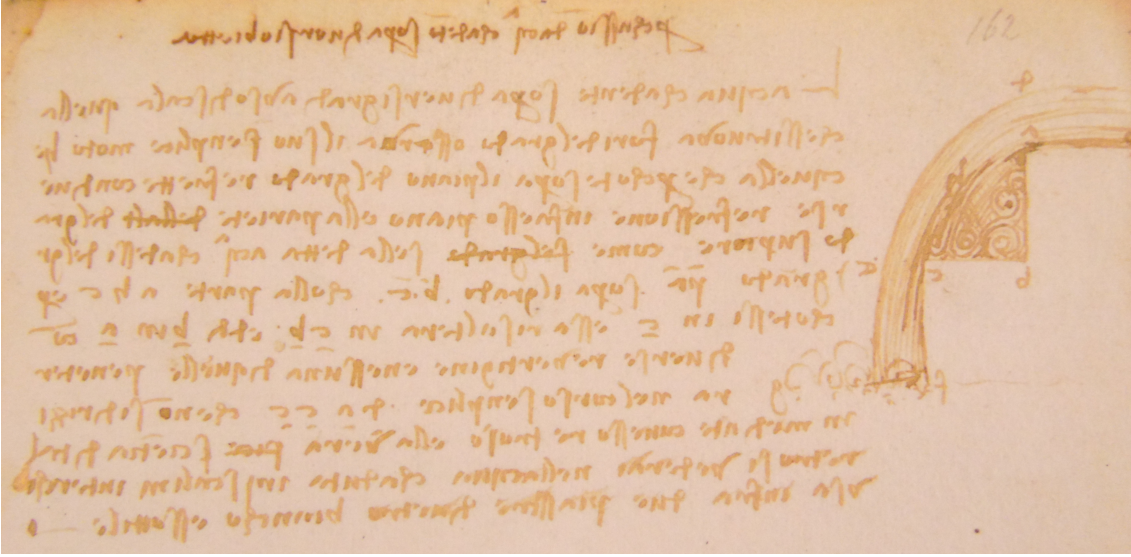


Figure 20: Leonardo da Vinci’s investigations into water cascading over steps [da Vinci, 1478-1518]. Courtesy of the British Library (Arundel MS 263, f.167v).

The schematic for the flow that we investigate here is as depicted in figure 21a. As before, we assume uniform, horizontal flow with unit depth and velocity far upstream. The walls  $IC$  and  $EF$  are horizontal, whilst walls  $CE$  and  $FJ$  are at an angle of depression of  $\pi - \beta$ . Finally, we have thin jet flow along the wall  $FJ$ . Note that the corner  $F$  is set at the origin of the  $z$ -plane. The method utilised in this section will closely follow that of the spillway problems covered so far. In particular, we set the complex potential to zero at  $F$  (i.e. the corner before the last sloping wall section) and the  $f$ -plane is still the infinite strip of unit width (c.f. figure 21b). Then, we use (1.33) to map the flow region of the  $f$ -plane to the unit semi-circle in the  $t$ -plane (c.f. figure 21c), as before. We denote by  $t_C$  and  $t_E$  the values of the image points of the corners  $C$  and  $E$ ,

respectively, in the  $t$ -plane. The positions of  $t_C$  and  $t_E$  can be chosen as any values between  $-1$  and  $1$ , such that  $t_C \leq t_E$ . The positions of the corners  $C$  and  $E$  in the  $z$ -plane will then be found as part of the solution (although, later we will instead fix the positions of  $C$  and  $E$  in the  $z$ -plane, leaving  $t_C$  and  $t_E$  unknown).

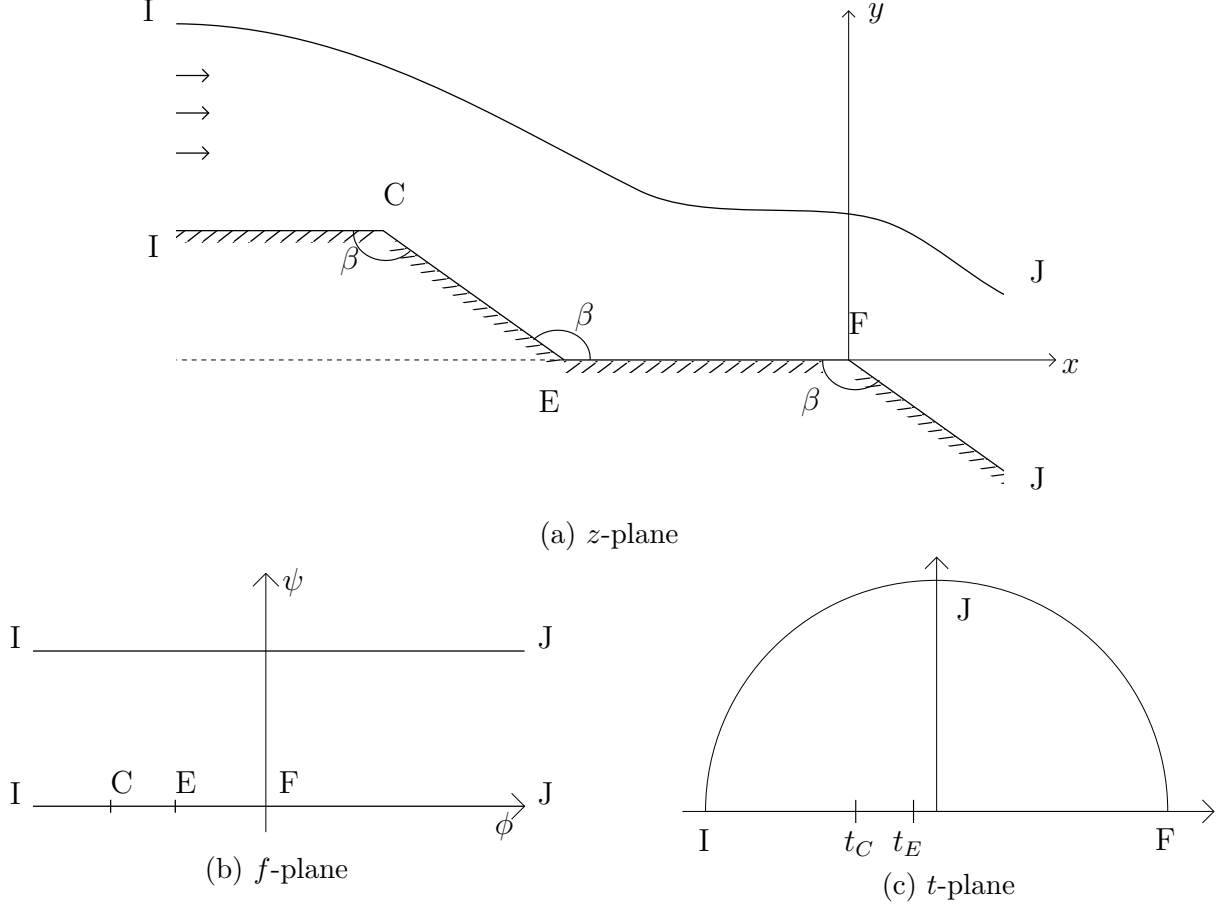


Figure 21: Complex planes for spillway step flow

Compared with the earlier spillways presented here, the conditions far upstream, far downstream and around the corner  $F$  remain as before. Therefore, the complex velocity  $\zeta$  must satisfy the following:  $\zeta \sim (1 + Ae^{\pi\lambda f})$  as  $\phi \rightarrow -\infty$ ;  $\zeta \sim f^{1/3}$  as  $\phi \rightarrow +\infty$ ; and  $\zeta \sim f^{\beta/\pi-1}$  as  $f \rightarrow 0$ . However, we have another two singularities to consider along the spillway wall: the flow around the corner of angle  $\beta$  at  $C$  and the flow inside the corner of angle  $\beta$  at  $E$ . Noting the standard results for flow inside and around a corner in potential flow theory, we have that  $\zeta \sim f^{\beta/\pi-1}$  near  $C$  and  $\zeta \sim f^{1-\beta/\pi}$  near  $E$ . Throughout the flow, the Bernoulli equation gives that

$$\frac{|\zeta|^2}{2} + \frac{y}{F^2} + p = \frac{1}{2} + \frac{1+h}{F^2}, \quad (1.41)$$

where  $h = |z_C - z_E| \sin(\pi - \beta)$  is the perpendicular height of the step, with  $z_C$  and  $z_E$  being the points in the  $z$ -plane corresponding to  $C$  and  $E$ , respectively. Further to this, we have the no normal flow condition to satisfy along the wall  $ICEFJ$  and the Bernoulli condition

$$\frac{|\zeta|^2}{2} + \frac{y}{F^2} = \frac{1}{2} + \frac{1+h}{F^2}, \quad (1.42)$$

to satisfy along the free surface  $IJ$ .

It follows that the assumed form for the complex velocity is

$$\begin{aligned} \zeta(t) = & (-\log 2c)^{-1/3} (-\log c(1+t^2))^{1/3} \left(\frac{1}{4}(t-1)^2\right)^{\beta/\pi-1} \left(1 + (1+t)^{2\lambda} \sum_{n=0}^{\infty} a_n t^n\right) \\ & \times \left(\frac{t_C - t}{1 - tt_C}\right)^{\beta/\pi-1} \left(\frac{t_E - t}{1 - tt_E}\right)^{1-\beta/\pi}, \end{aligned} \quad (1.43)$$

which is very similar to the form of  $\zeta$  in the earlier spillway cases — the difference here is the two extra multiplicative terms that encapsulate the singularities at corners  $C$  and  $E$ . It can be checked that the no normal flow boundary conditions along the walls  $IC$ ,  $CE$  and  $EF$  are satisfied by this complex velocity ansatz. Also,  $\zeta$  approaches 1 as  $t \rightarrow -1$ , i.e. far upstream. Downstream, we have the thin wall jet behaviour  $\zeta \sim f^{1/3}$  as  $t \rightarrow i$ . The conditions that remain to be imposed (since they are not automatically satisfied by the assumed form for  $\zeta$ ) are:

1. the Bernoulli equation along the free surface  $IJ$ ,
2. the no normal flow condition along the sloped wall  $FJ$ .

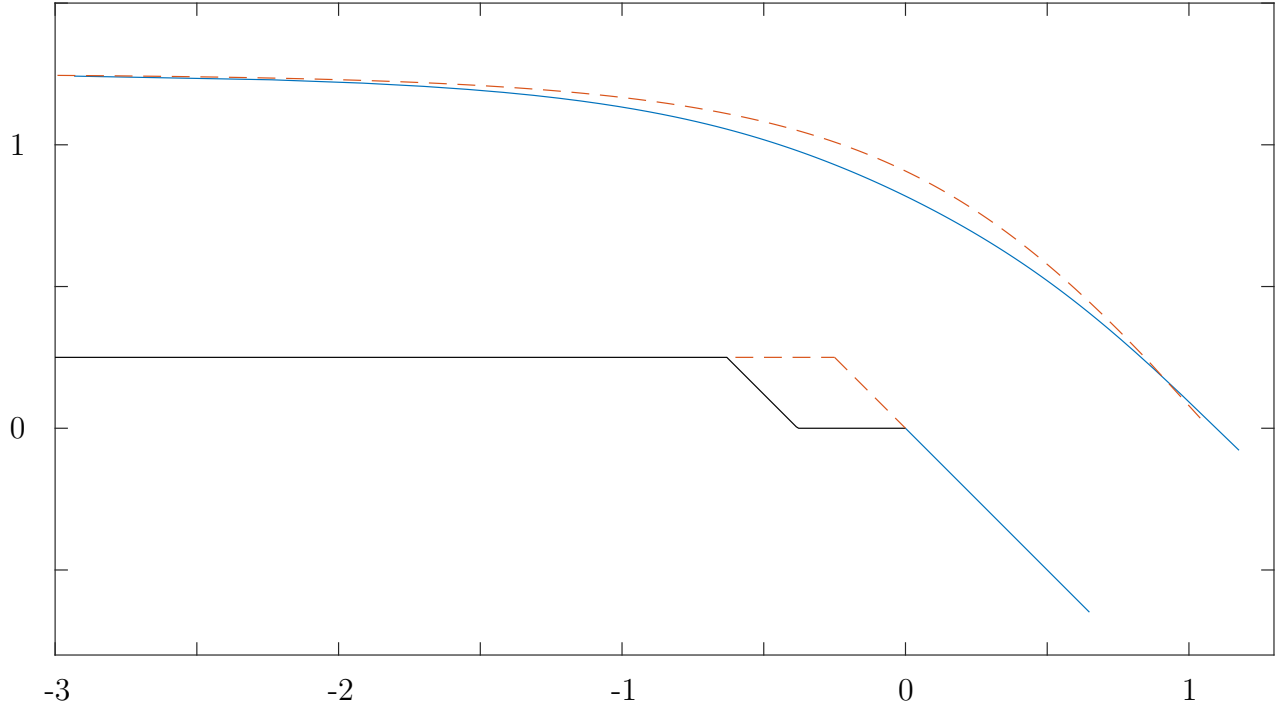
For the boundary along the wall  $FJ$ , the condition can either be specified by imposing that the  $\psi = 0$  streamline satisfies  $y = (\tan \beta)x$  or  $\mathbf{u} \cdot \mathbf{n} = 0$ , where  $\mathbf{u}$  and  $\mathbf{n}$  are the velocity and normal vectors, respectively. In the results presented here, the former option is taken.

We then proceed as usual: truncating the infinite series of (1.43) after  $N$  terms, so we have  $N$  unknowns; taking  $N$  collocation points, equally-spaced along the arc of the unit semi-circle in the  $t$ -plane; satisfying the Bernoulli condition at the mesh points along  $IJ$  and setting  $y = (\tan \beta)x$  at the mesh points along  $FJ$ ; and then solving the  $N$  equations in the  $N$  unknowns numerically, by iteration. Once the unknown coefficients are obtained, we can plot the free-surface profiles. Note

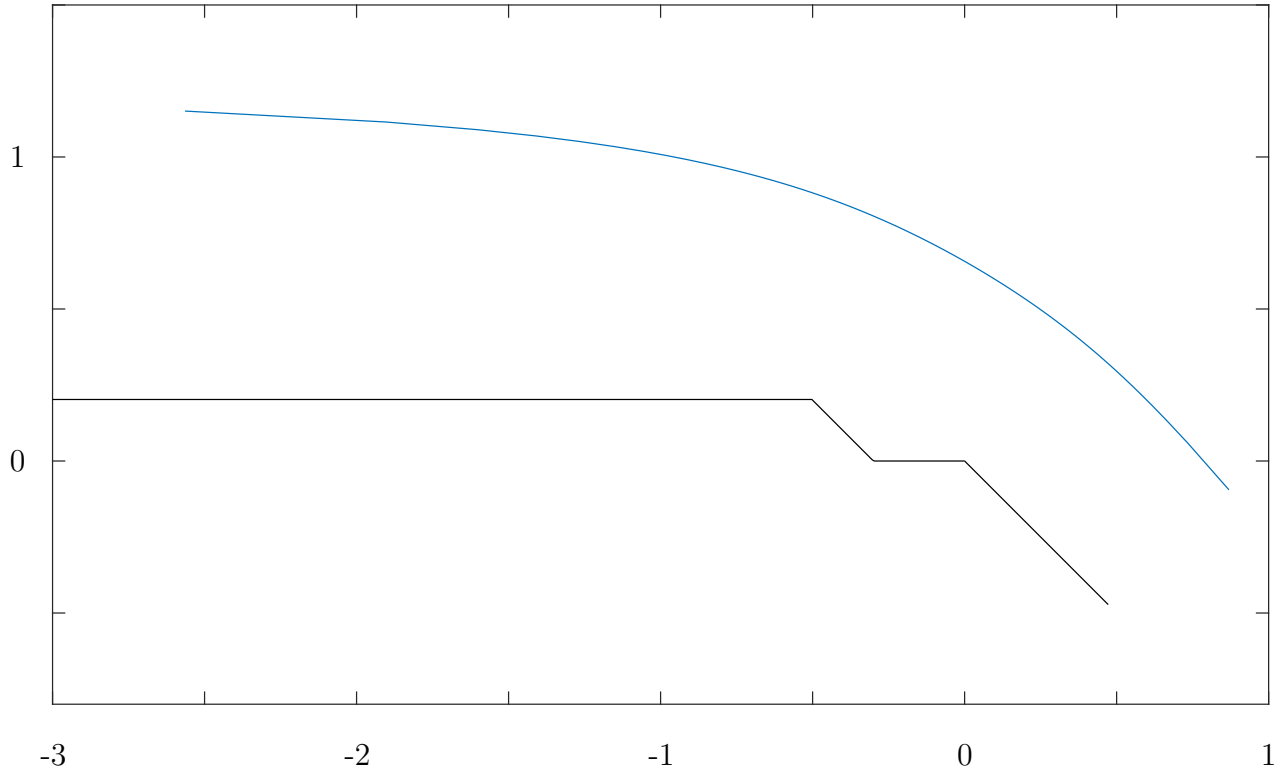
that the solution depends on the following set of parameters:  $F$ ,  $\beta$ ,  $t_C$  and  $t_E$ .

Some examples of resulting free-surface profiles are shown in figures 22–24. Figure 22a also shows a comparison with the free-surface profile of the spillway with one corner in the wall (i.e. that which was discussed in §1.1). Visually, the greatest difference in the free surfaces is as the flow falls around the corner/step, due to the maintenance of the pressure distribution across the stream. However, it is also of note that the free surfaces cross downstream and so the jet following the one corner thins more quickly than that following the stepped wall. This is to be expected due to the contribution of the pressure force along the sloped wall of the stepped spillway to the horizontal momentum flux. Overall, figures 22 and 23 show the variation of the free-surface profile with Froude number. It should be noted that, despite keeping  $t_C$  and  $t_E$  constant through the subfigures of figures 22 and 23, the variation in Froude number will affect the positions of  $C$  and  $E$  in the  $z$ -plane, i.e. the size of the step is not kept the same through these cases. Further to this, it is clear that the flow is horizontal far upstream and of unit depth for  $F = 2$  with  $t_C = -0.6$  and  $t_E = -0.3$  (c.f. figure 22a). However, for the other cases discussed so far, it is not so clear that this condition is met since, due to the size of the step and the Froude number, more mesh points are required to reach sufficiently far upstream to consider this point. Figure 24 shows the same flow as in figure 23b but with a larger value taken for  $N$  and the streamlines within the flow have been included. Here, we are more convinced that we do indeed head towards horizontal flow of unit depth far upstream, but more mesh points are still really required for this.

In terms of verifying the numerical method, the dependence on the constant  $c$  (c.f. the complex velocity ansatz of (1.43)) can be investigated. We find that the resulting coefficients ( $a_n$ ) do depend on the value of  $c$  chosen (between 0 and 0.5). However, the free-surface profiles do not depend on  $c$  (for values of  $c$  sufficiently far from 0 and 0.5, with  $N$  sufficiently large). The convergence of the coefficients can also be investigated. Figure 25 shows the coefficient  $a_4$  against  $1/N$ . The graph suggests that there is convergence to a particular value. Also, for  $N = 400$ , figure 26 is a plot of  $a_n$  against  $1/(n+1)$  which shows good convergence of the coefficients to zero as  $n \rightarrow \infty$ . To verify the efficacy of the method, we can consider limiting cases. For example, figure 27 is the case where  $\beta$  is chosen to be close to  $\pi$ . It appears to approach horizontal flow as  $\beta \rightarrow \pi$ , but there is still



(a)  $F = 2$ . For comparison with the one corner spillway discussed in §1.1, the dashed lines show the (translated) free surface and corner of the wall in that case with  $F = 2$ ,  $c = 0.2$  and  $N = 400$ .



(b)  $F = 1.1$

Figure 22: Spillway step free-surface plot:  $c = 0.2$ ,  $N = 200$ ,  $t_C = -0.6$ ,  $t_E = -0.3$ ,  $\beta = 3\pi/4$ .

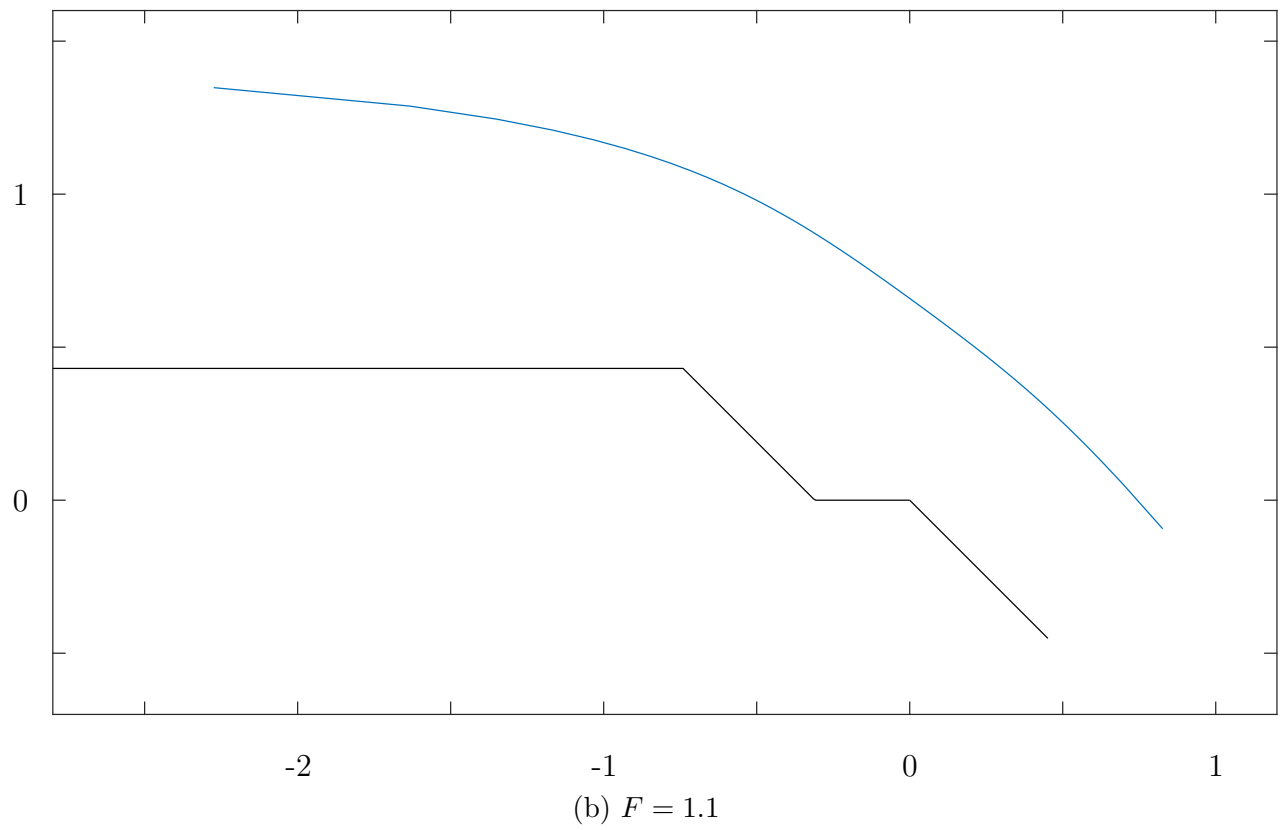
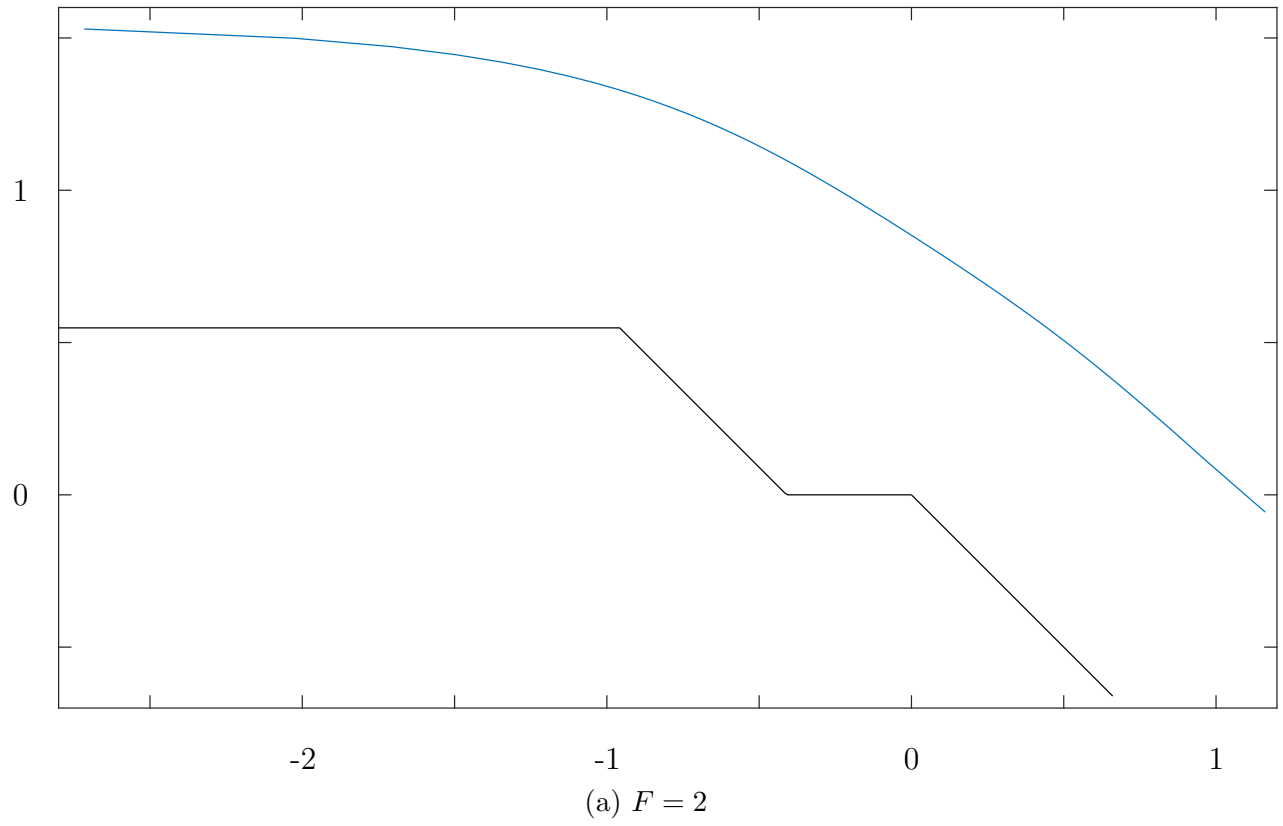


Figure 23: Spillway step free-surface plot:  $c = 0.2$ ,  $N = 150$ ,  $t_C = -0.8$ ,  $t_E = -0.3$ ,  $\beta = 3\pi/4$ .

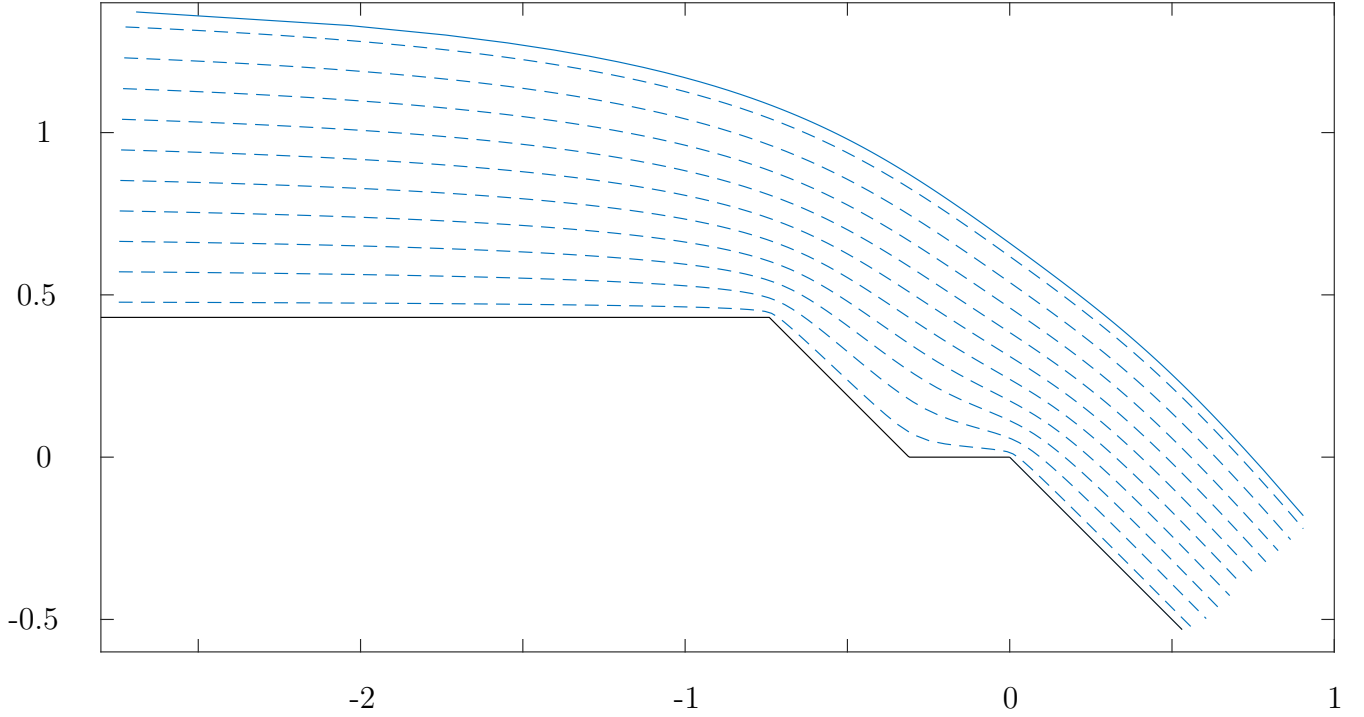


Figure 24: Free-surface profile for  $F = 1.1$ ,  $c = 0.2$ ,  $N = 400$ ,  $t_C = -0.8$ ,  $t_E = -0.3$ ,  $\beta = 3\pi/4$ . Streamlines are for  $\psi = 0.05 + 0.1i$  for  $i = 0, 1, \dots, 9$ .

evidence of jet flow downstream, particularly with a Froude number so close to 1. Note that, as  $\beta \rightarrow \pi$ , analysis of the spillway jet-flow far downstream (c.f. (1.22)) will result in the coefficient of the  $f^{1/3}$  term approaching zero, and leading to simply  $\zeta(f) \equiv 1$ . Another example to consider is a step of very small perpendicular height to check that, as the step diminishes, we retrieve the results of §1.1 where there is not a step. Figure 28 shows a comparison of the free surface obtained for a spillway with and without a small step. The profiles are very similar with the largest difference appearing far upstream in the height of the free surface. This is to be expected since we should have unit depth flow far upstream in both cases but, in the case including the step, the horizontal wall will not run along  $y = 0$ .

We can find the pressure distribution along the spillway wall, which, from a practical perspective, will be of use for understanding the potentially destructive nature of the flow. Utilising the Bernoulli equation (1.41), we have the following expression for the pressure,  $p$ , along the wall

$$p = \frac{1}{2}(1 - |\zeta|^2) + \frac{1}{F^2}(1 + h - y), \quad (1.44)$$

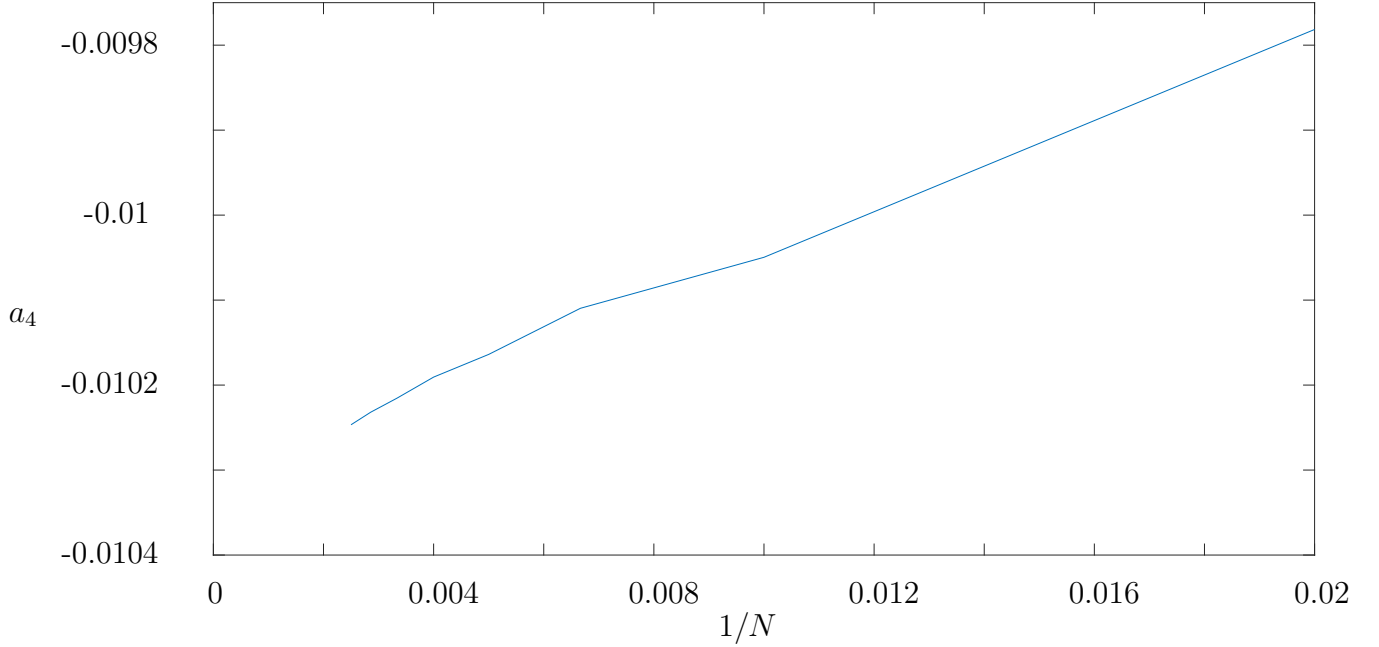


Figure 25: A plot of  $a_4$  against  $1/N$  to show convergence of this coefficient with  $F = 1.1$ ,  $c = 0.2$ ,  $t_C = -0.8$ ,  $t_E = -0.3$ ,  $\beta = 3\pi/4$ .

where  $h$  is the height of the step. Figure 29 shows the pressure distribution along the spillway wall *ICEFJ* for an earlier discussed set of given parameters. As expected, the pressure asymptotes towards a positive constant,  $F^{-2}$ , as we approach the point *I* far upstream; and there are singularities at the corners *C*, *E* and *F*. We know that the nature of these singularities in the pressure are  $(t_C - t)^{2(\beta/\pi-1)}$ ,  $(t_E - t)^{2(1-\beta/\pi)}$  and  $(t - 1)^{4(\beta/\pi-1)}$  at *C*, *E* and *F*, respectively.

A logical next step here is to rework the method to specify the positions of the corners *C* and *E* in the  $z$ -plane, instead of prescribing  $t_C$  and  $t_E$ . This will enable us to check that the method gives the same results. It will also mean that this work can be applied more easily to a physical spillway geometry. For this, we simply add two extra unknowns to the system (i.e.  $t_C$  and  $t_E$ ), along with two conditions to impose which fix the positions corresponding to points *C* and *E* in the  $z$ -plane (i.e.  $z_C$  and  $z_E$ , respectively). These conditions take the following form:

$$z_{C,E} = \int_{t_{C,E}}^1 \frac{1}{\zeta} \left( \frac{2}{\pi} \frac{1-t}{(t+1)(t^2+1)} \right) dt. \quad (1.45)$$

This can be simplified by considering the direction of the velocity along the wall sections *CE* and *EF*. First, we notice that  $\zeta(t)$  is real along the wall *EF* and so for  $z_E$  we can adjust the condition



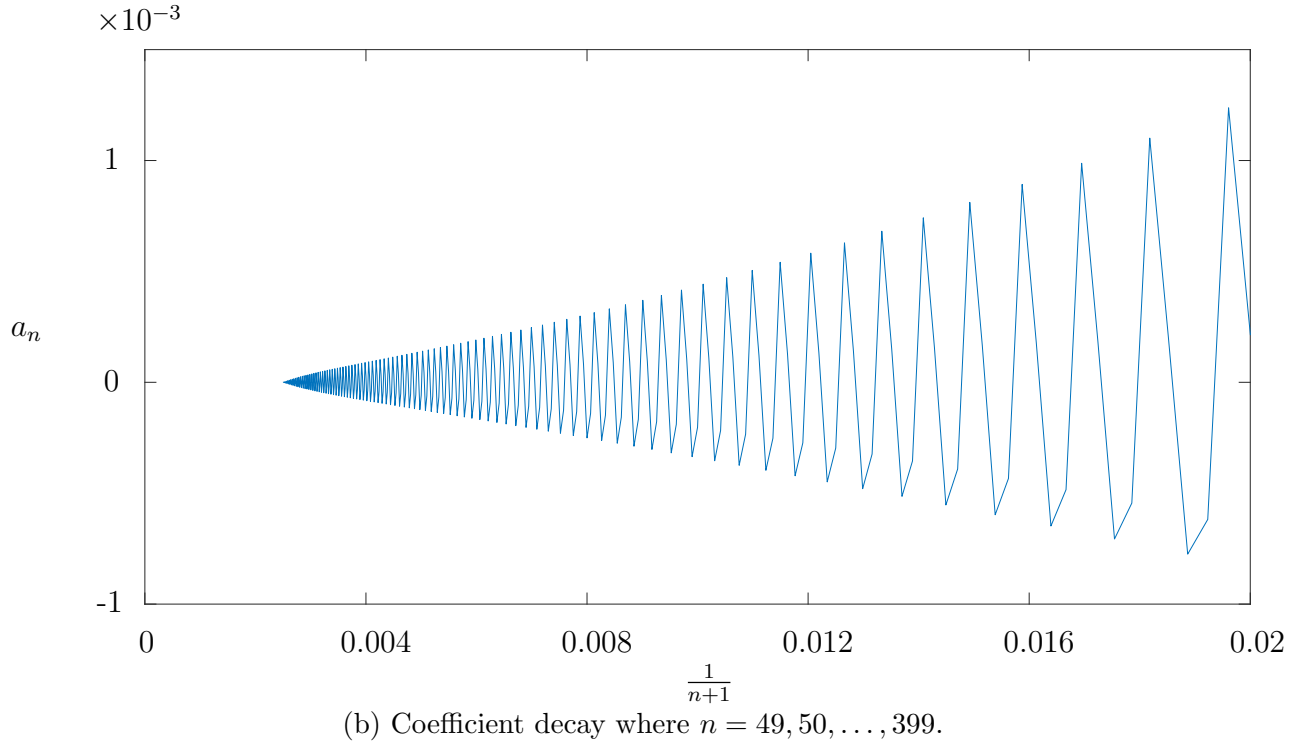
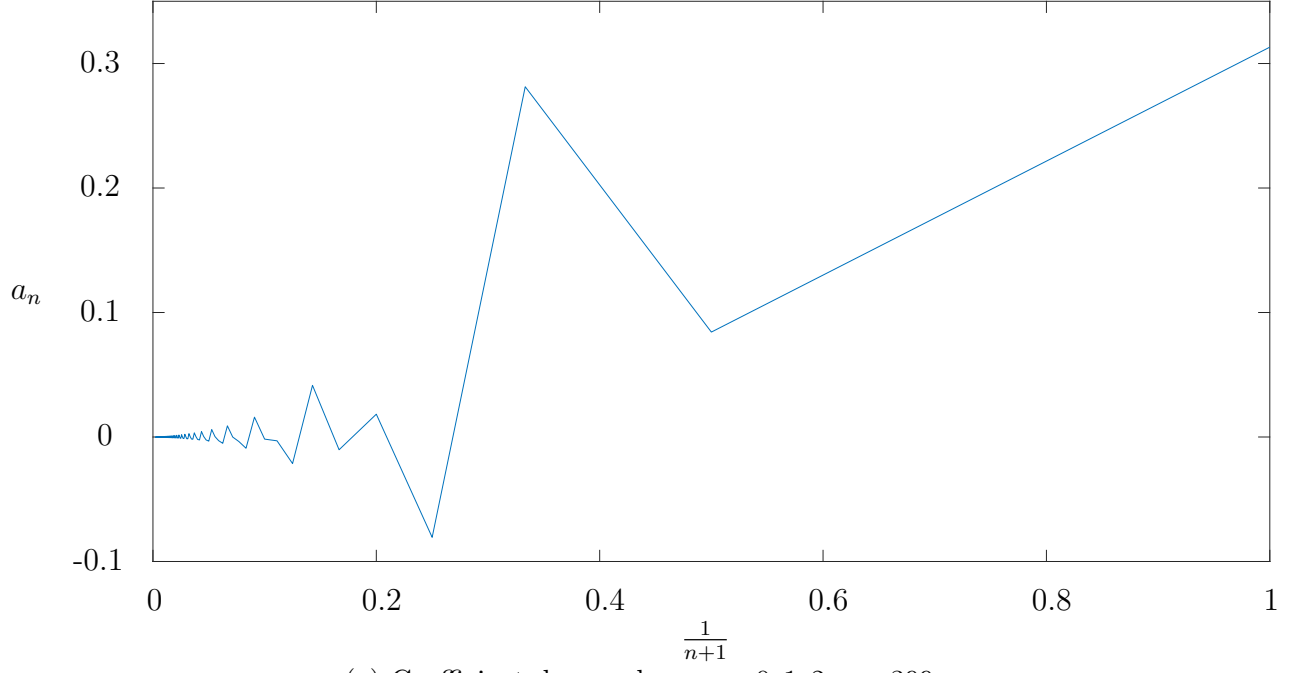


Figure 26: Coefficient decay plot of  $a_n$  against  $1/(n+1)$  for  $c = 0.2$ ,  $N = 400$ ,  $F = 1.1$ ,  $t_C = -0.8$ ,  $t_E = -0.3$ ,  $\beta = 3\pi/4$ .

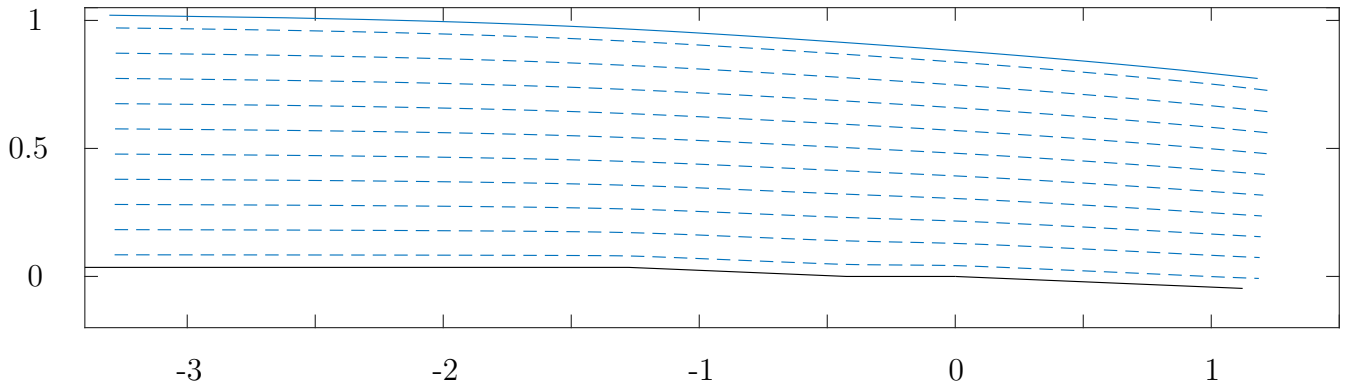


Figure 27: Free-surface profile for  $F = 1.1$ ,  $c = 0.2$ ,  $t_C = -0.8$ ,  $t_E = -0.3$ ,  $\beta = 3.1$ . Streamlines are for  $\psi = 0.05 + 0.1i$  for  $i = 0, 1, \dots, 9$ .

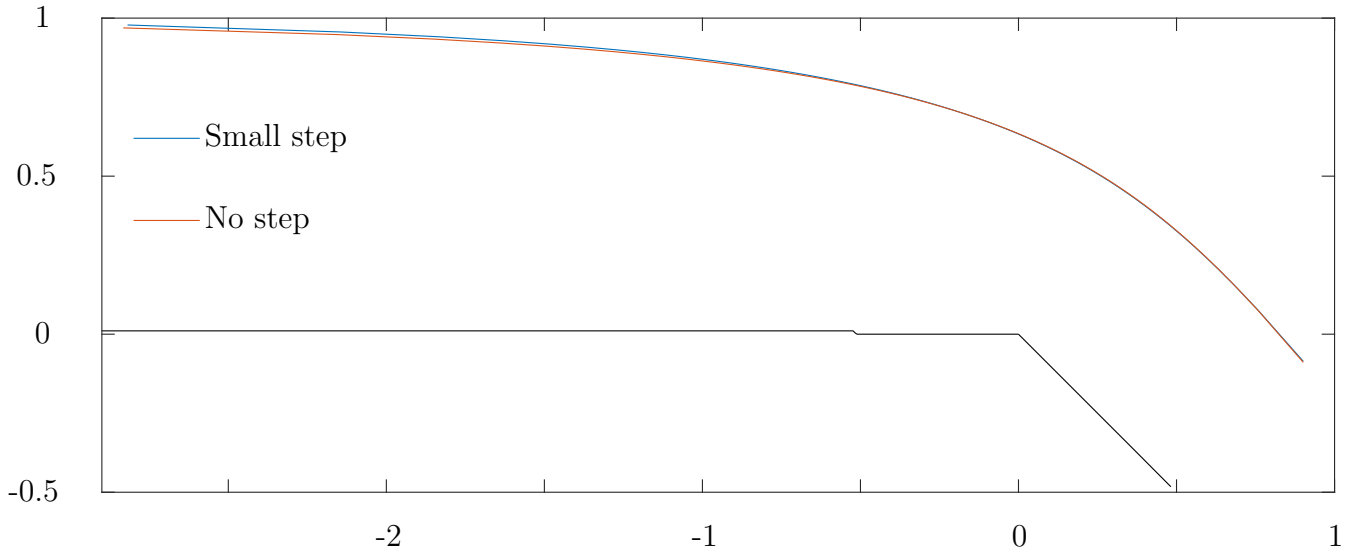


Figure 28: Comparison of free-surface profiles with and without step for  $F = 1.1$ ,  $c = 0.2$ ,  $N = 200$  and  $\beta = 3\pi/4$ . In the case of the step  $t_C = -0.8$  and  $t_E = -0.3$ .

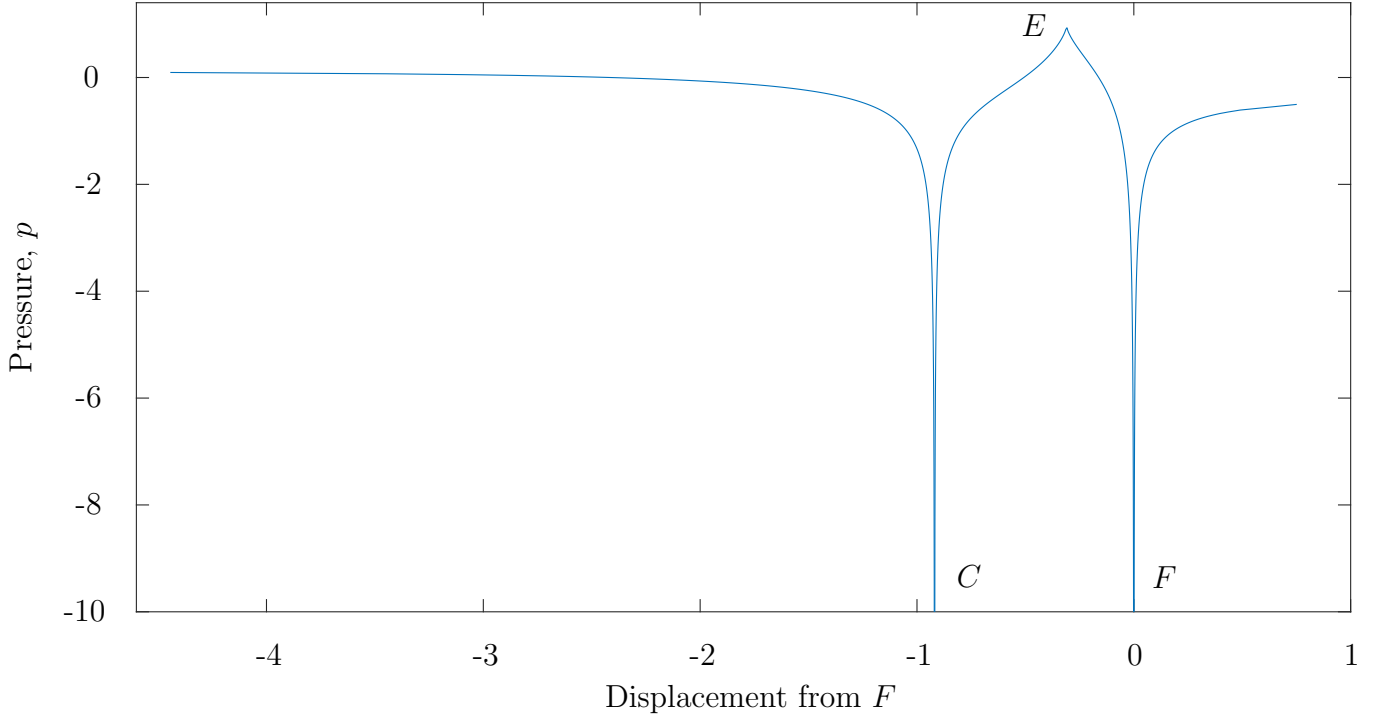


Figure 29: Pressure against displacement from  $F$  for  $F = 1.1$ ,  $c = 0.2$ ,  $N = 400$ ,  $t_C = -0.8$ ,  $t_E = -0.3$ ,  $\beta = 3\pi/4$ .

to involve only a real integral, i.e.

$$z_E = \int_{t_E}^1 \frac{1}{|\zeta|} \left( \frac{2}{\pi} \frac{1-t}{(t+1)(t^2+1)} \right) dt. \quad (1.46)$$

Now, along the wall  $CE$ , the velocity has direction  $\exp i(\beta - \pi)$ . Also, we can express  $z_C$  as  $z_E + \delta \exp(i\beta)$ , where  $\delta > 0$  is a real constant. Then we can write

$$z_E + \delta e^{i\beta} = z_E + \int_{t_E}^{t_C} \frac{1}{|\zeta| e^{i(\pi-\beta)}} \left( \frac{2}{\pi} \frac{1-t}{(t+1)(t^2+1)} \right) dt \quad (1.47)$$

and this can be simplified to

$$\delta = - \int_{t_E}^{t_C} \frac{1}{|\zeta|} \left( \frac{2}{\pi} \frac{1-t}{(t+1)(t^2+1)} \right) dt. \quad (1.48)$$

As before, truncating the infinite series of (1.43) after  $N$  terms, we have  $N$  unknowns, along with two extra unknowns  $t_C$  and  $t_E$ . Choosing  $N$  collocation points, we obtain  $N$  equations in the unknowns, along with the two extra conditions, (1.46) and (1.48). Now, we can use a numerical,

iterative method to solve this system of  $N + 2$  equations in  $N + 2$  unknowns. It should be noted that since  $z_E$  and  $\delta$  are used in the extra conditions, the spillway dimensions are specified by the lengths of the walls  $CE$  and  $EF$ . Several examples have been worked through to check that the two methods, i.e. starting with the values of  $t_C$  and  $t_E$  known or unknown, give the same results.

Finally, we can generalise the work presented here on the spillway with a step upstream to instead have multiple steps upstream. Only the formulation is given here and examples are left for future work. Let us consider  $M$  steps where each declining wall (apart from the last wall section) is followed by a horizontal section as depicted in figure 30a. The corners before and after the sloping walls are labelled as  $C_i$  and  $E_i$ , respectively, for  $i = 1, 2, \dots, M$ . The angles at these corners are  $\alpha_i$  at both  $C_i$  and  $E_i$ . At  $F$ , the angle between the walls is  $\beta$ . The  $f$ - and  $t$ -planes remain as before, but with the extra points corresponding to the additional corners also labelled (c.f. figures 30b and 30c). Note that  $t_{C_i}$  and  $t_{E_i}$  are the points in the  $t$ -plane corresponding to the corners  $C_i$  and  $E_i$ , respectively, for  $i = 1, 2, \dots, M$ . The overall method is as for the one-step case already discussed. We take the following ansatz for the complex velocity

$$\begin{aligned} \zeta(t) = & (-\log 2c)^{-1/3} (-\log c(1+t^2))^{1/3} \left(\frac{1}{4}(t-1)^2\right)^{\beta/\pi-1} \left(1 + (1+t)^{2\lambda} \sum_{n=0}^{\infty} a_n t^n\right) \\ & \times \left(\frac{t_{C_1}-t}{1-tt_{C_1}}\right)^{\alpha_1/\pi-1} \left(\frac{t_{E_1}-t}{1-tt_{E_1}}\right)^{1-\alpha_1/\pi} \left(\frac{t_{C_2}-t}{1-tt_{C_2}}\right)^{\alpha_2/\pi-1} \left(\frac{t_{E_2}-t}{1-tt_{E_2}}\right)^{1-\alpha_2/\pi} \\ & \times \dots \times \left(\frac{t_{C_M}-t}{1-tt_{C_M}}\right)^{\alpha_M/\pi-1} \left(\frac{t_{E_M}-t}{1-tt_{E_M}}\right)^{1-\alpha_M/\pi} \end{aligned} \quad (1.49)$$

and truncate the infinite series after  $N$  terms. We still use the equally-spaced collocation points along the arc of the unit semi-circle of the  $t$ -plane; and so we satisfy the no normal flow condition at the points along the wall  $FJ$  (i.e.  $y = (\tan \beta)x$ ) and we satisfy the Bernoulli condition at the points along the free surface. More specifically, for the condition along the free surface  $IJ$ , we satisfy

$$\frac{|\zeta|^2}{2} + \frac{y}{F^2} = \frac{1}{2} + \frac{1+h}{F^2}, \quad (1.50)$$

where

$$h = |z_{C_1} - z_{E_1}| \sin(\pi - \alpha_1) + |z_{C_2} - z_{E_2}| \sin(\pi - \alpha_2) + \dots + |z_{C_M} - z_{E_M}| \sin(\pi - \alpha_M). \quad (1.51)$$

If we wish to set the physical lengths of the wall sections, then we can leave the values of  $t_{C_i}$  and  $t_{E_i}$  for  $i = 1, 2, \dots, M$  to be found; and we then impose the lengths of the walls similarly to (1.46) and (1.48). Overall, there are then  $N + 2M$  unknowns to be found: the unknown coefficients  $a_n$  for  $n = 0, 1, \dots, N - 1$  and the values of  $t$  corresponding to the first  $2M$  corners. There are  $N + 2M$  equations from satisfying the Bernoulli condition or no normal flow condition at the relevant  $N$  mesh points; and from imposing the lengths of the  $2M$  finite length wall sections.

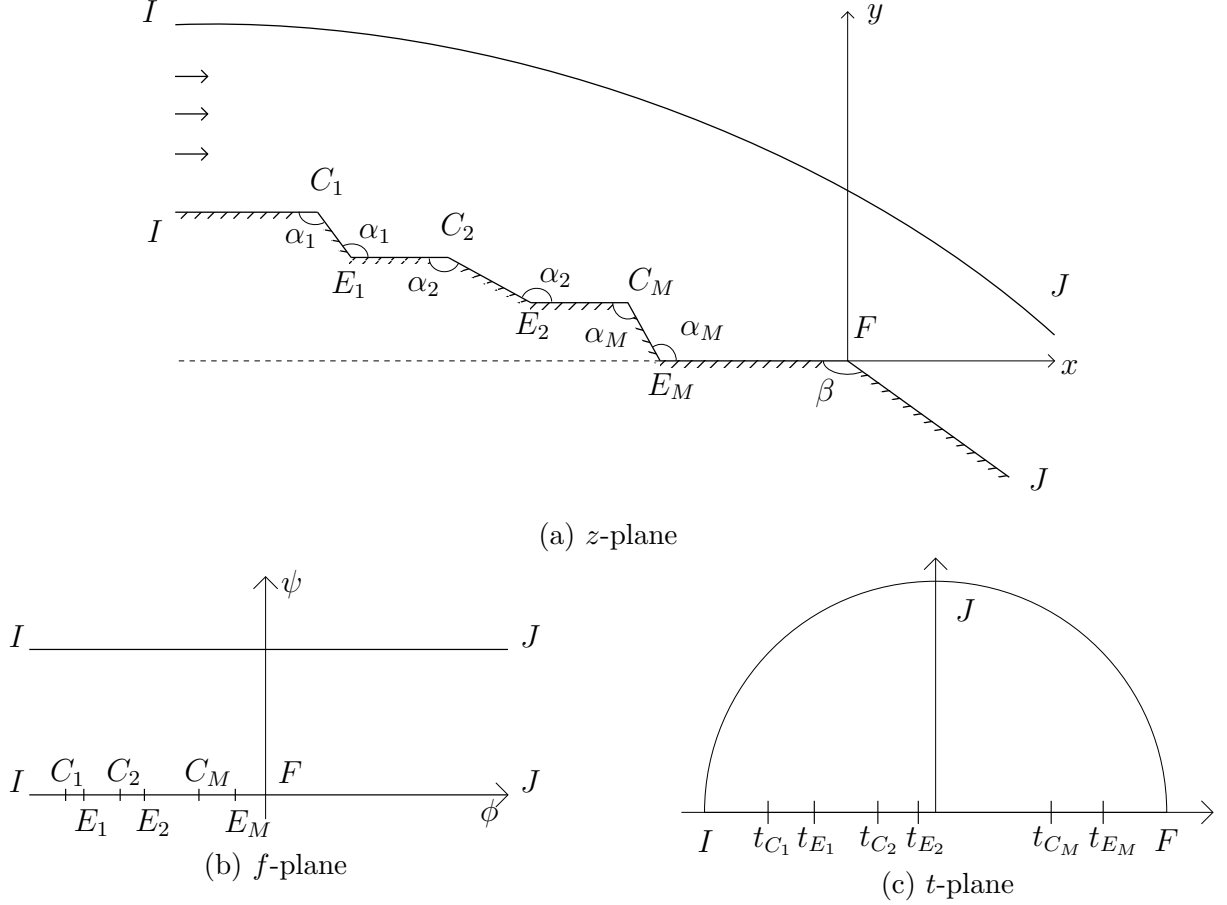


Figure 30: Complex planes for spillway step flow.

So far, all the spillway cases presented here involve a straight sloping wall far downstream. This allowed us to take  $\zeta \sim f^{1/3}$  as  $\phi \rightarrow +\infty$  for the behaviour of the jet singularity downstream, in order to form the complex velocity ansatz similarly each time. In the following section, we will consider cases where this is not so.

## 1.4 Parabolic wall

We consider a spillway where the sloping wall is described by  $y = -ax^2 - bx$ , where  $a$  and  $b$  are real, positive constants. It should be pointed out that this differs from the curved corner spillway discussed in §1.2 since there we had a wall of constant slope following the corner. The fluid and flow assumptions are as in the previous cases and the  $f$ - and  $t$ -planes remain as in figures 9b and 9c. For the flow around the corner of the horizontal and sloping walls, we note that the angle between the horizontal wall and the tangent to the sloping wall at the origin is  $\pi + \arctan(-b)$ . Hence,  $\zeta \sim f^{\arctan(-b)/\pi}$  as  $f \rightarrow 0$ . We can analyse the flow far downstream similarly to the linear spillway wall case that has been discussed earlier. Most simply, for the dominant term of the expansion for  $\zeta(f)$ , we can make use of the work of Keller and Geer [1973]. In particular, solving their first-order differential equation (4.8) with  $\eta(x) = -x^2 - x$  for the boundary condition along the wall will lead to finding the first term of the expansion for the complex velocity to be of order  $f^{1/3}$ . If we take the behaviour of the jet flow far downstream to be  $\zeta \sim f^{1/3}$  as  $\phi \rightarrow +\infty$ , then we can take the complex velocity ansatz to be

$$\zeta(t) = (-\log 2c)^{-1/3} (-\log c(1+t^2))^{1/3} \left( \frac{1}{4}(t-1)^2 \right)^{\arctan(-b)/\pi} \left( 1 + (1+t)^{2\lambda} \sum_{n=0}^{\infty} a_n t^n \right). \quad (1.52)$$

Note that at the end of this section and in later chapters, we will look at subsequent terms in the expansion of  $\zeta$  for the jet far downstream and (in the case of waterfall flow) we will include these extra terms in the complex velocity ansatz. However, for now we proceed as usual: from truncating the infinite series above after  $N$  terms and introducing  $N$  mesh points along the arc of the unit semi-circle in the  $t$ -plane, we have  $N$  unknown coefficients and we have  $N$  equations in these unknowns. The  $N$  equations are formed by evaluating  $y = -ax^2 - bx$  at the mesh points with argument (in the  $t$ -plane) less than  $\pi/2$  (i.e. points corresponding to the streamline  $\psi = 0$  for  $\phi > 0$ ) and evaluating the Bernoulli condition (1.3) at the remaining mesh points.

Figure 31 shows the resulting free-surface profiles for the case where  $a, b = 1$  (note  $\beta = 3\pi/4$  in this case) and different Froude numbers are considered. The condition on the wall of the spillway is imposed by specifying  $y = -x^2 - x$  on  $\psi = 0$ , for  $\phi > 0$ , and this is adhered to in each of the

profiles. The width of the flow downstream increases as the Froude number increases. This is to be expected since the larger the Froude number, the more diminished the effect of gravitational forces.

We can investigate the effect of increased curvature on the pressure along the spillway wall. In terms of our parabolic form taken for the wall, we set  $b = 1$  and vary  $a$ . Therefore, the angle at the origin remains constant, i.e.  $\beta = 3\pi/4$ . The expression for calculating the pressure is obtained using the Bernoulli condition (1.2) and is given by

$$p = \frac{1}{2}(1 - |\zeta|^2) + \frac{1}{F^2}(1 - y). \quad (1.53)$$

Figure 32b shows the pressure along the wall, plotted against the displacement from the origin, for a number of different values of  $a$ . Since the angle between the horizontal wall and the tangent to the curved wall at the origin is the same for all the cases in figure 32, the nature of the singularity in the pressure at this corner is also the same for each case and is  $(t - 1)^{4(\arctan(-1)/\pi)}$ , i.e.  $(t - 1)^{-1}$ . This results in the similarity that can be observed, near to  $x = 0$ , between the pressure distribution plots for the different values of  $a$ . There is also similarity and a clear trend between the upstream pressure distributions. The greater the value of  $a$ , the quicker the pressure descends towards the singularity. Furthermore, the starting value for the pressure far upstream is the same for all values taken for  $a$ . More of a difference can be seen downstream in both the free-surface profiles and the pressure distributions. Here, we can see that along the sloping wall, the greater the value of  $a$ , the slower the increase in pressure from the singularity. The pressure distribution lines appear to cross further down the wall than calculated here. As discussed earlier, this may be as a result of the limited number of mesh points close to  $t = i$  along the wall.

A limitation of this calculation is that only the range of the mesh points used in the collocation method can be used in the free-surface profiles, i.e. we cannot then use additional points to extrapolate the free surfaces to see further both up- and downstream. This is since these additional points will not satisfy the boundary condition on the spillway's parabolic wall (since it is only imposed at the specified mesh points) and the only requirement for the downstream flow is that  $\zeta \sim f^{1/3}$  as  $\phi \rightarrow +\infty$  (so only imposing a jet flow along a linear, declining wall). Earlier, the work

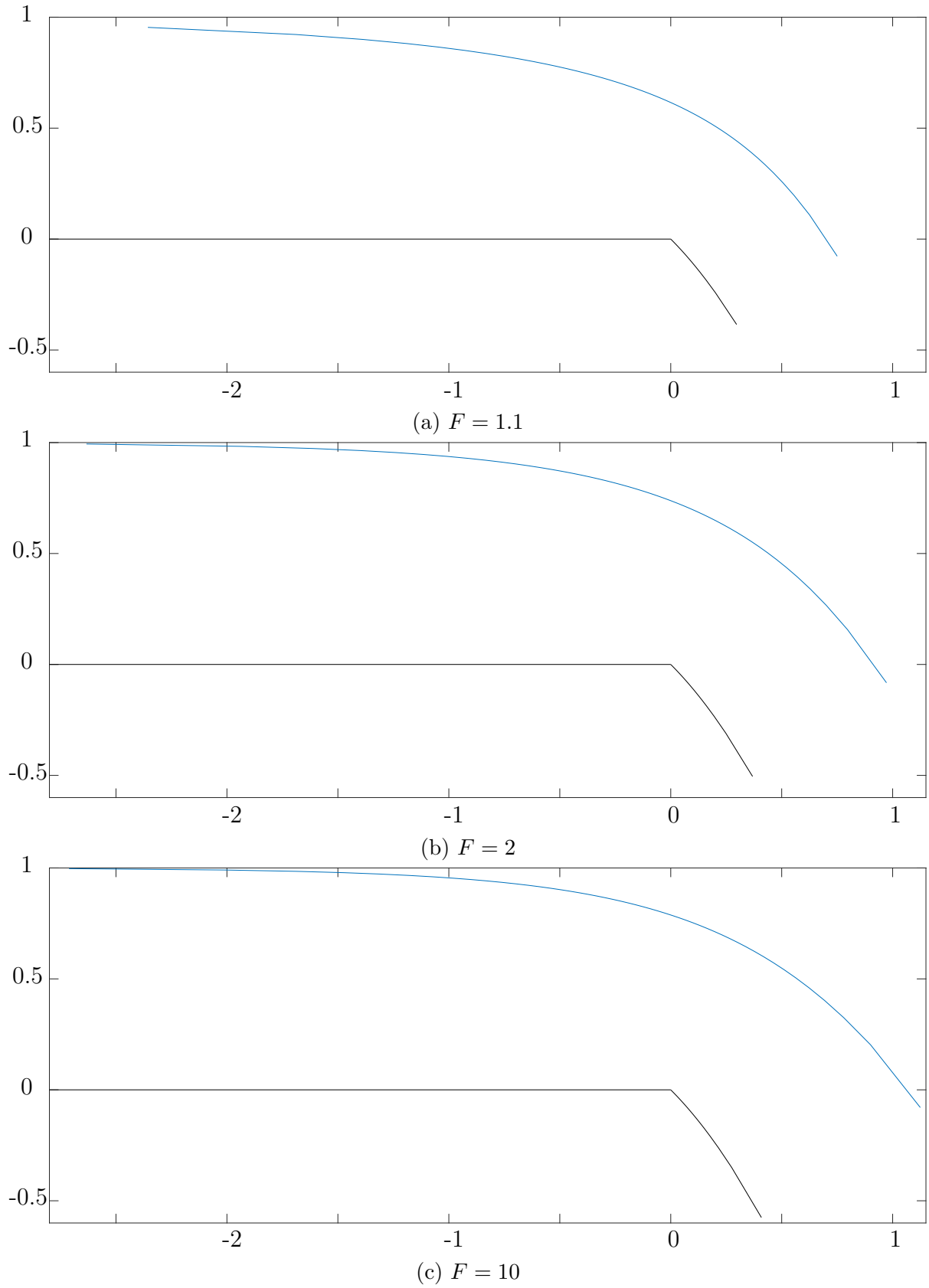
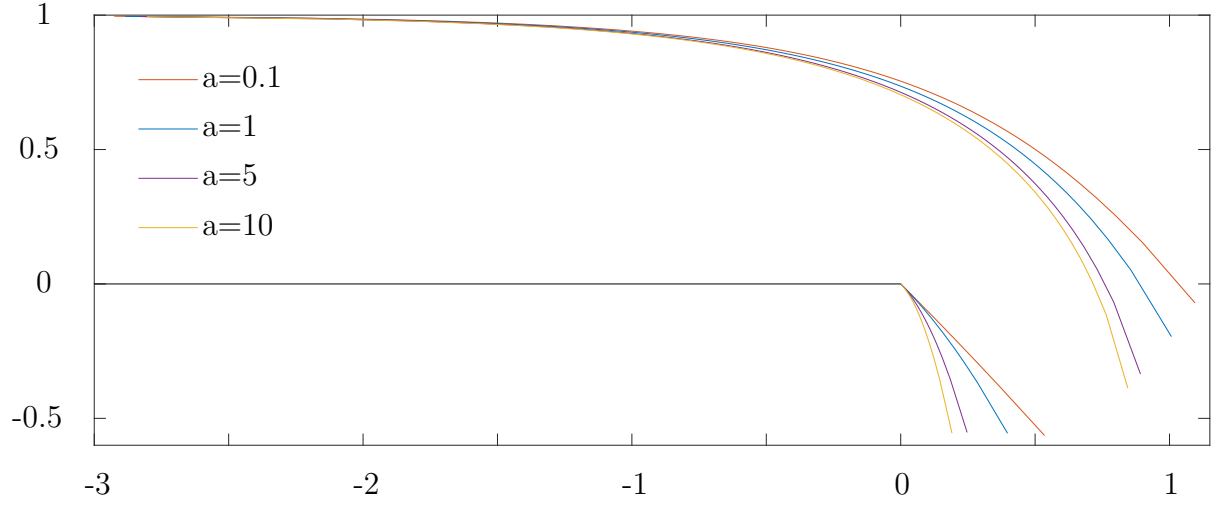
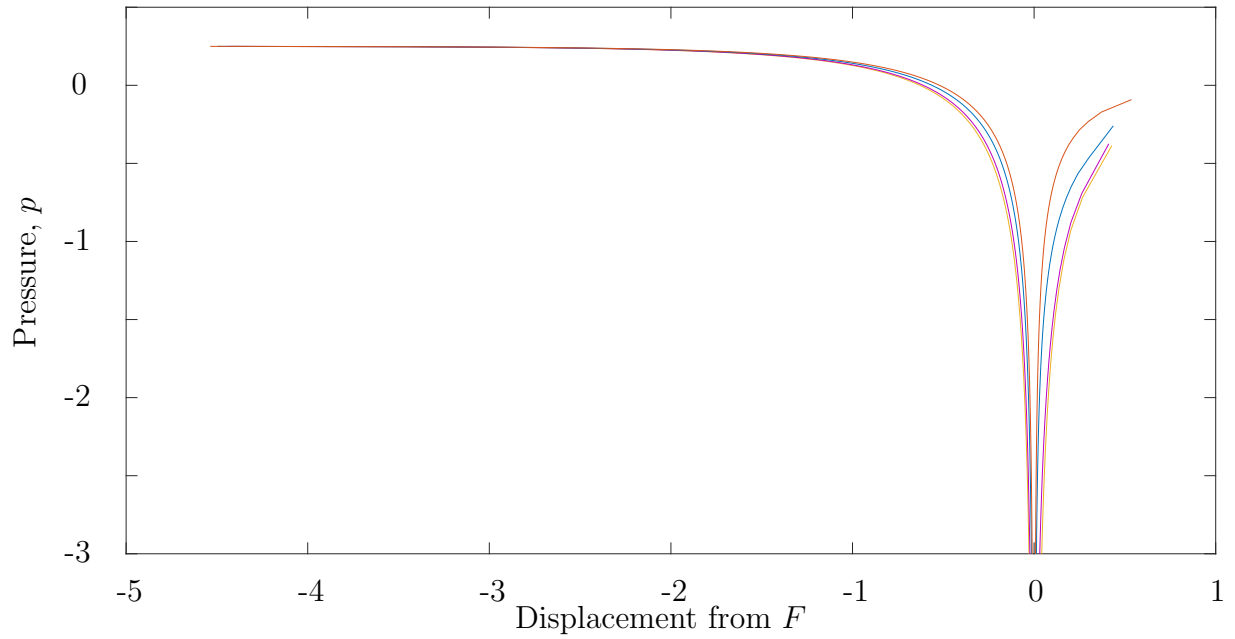


Figure 31: Free-surface profile for spillway with parabolic wall  $y = -x^2 - x$  and  $c = 0.2$ ,  $N = 100$ .





(a) Free-surface profiles.



(b) Pressure along the spillway wall.

Figure 32: Free-surface profiles and pressure distribution plots for spillways with parabolic walls defined by  $y = -ax^2 - x$  for various values of  $a$ . Here, we take  $F = 2$ ,  $c = 0.2$ ,  $N = 150$ .

of Keller and Geer [1973] was discussed in relation to finding the suitable form for the downstream singularity. Calculating the next term of the asymptotic expansion in this way leads to finding that

$$\zeta \sim Af^{1/3} + B + \dots \quad \text{as} \quad \phi \rightarrow +\infty \quad (1.54)$$

where  $A$  and  $B$  are constants. Therefore, better results could be obtained by including both of these terms for a more appropriate form for the singularity in the complex velocity ansatz. This is left for future work. However, this idea for improvement will be employed in chapter 2 where the focus is on waterfall flow, i.e. including a jet bounded by two free surfaces.

## 1.5 Stepped wall to horizontal channel

Before moving on to waterfall flow in the next chapter, the final case that we consider here is a spillway with a horizontal wall downstream (c.f. figure 33). It is a physically relevant problem to consider since often the purpose of a spillway is to provide a controlled escape route for water from a full reservoir to another basin of water below. However, depending on the ratio of the depth of the flow far upstream to the height of the sloping wall, these calculations can also be interpreted for open channel flow navigating a small change in the horizontal bed.

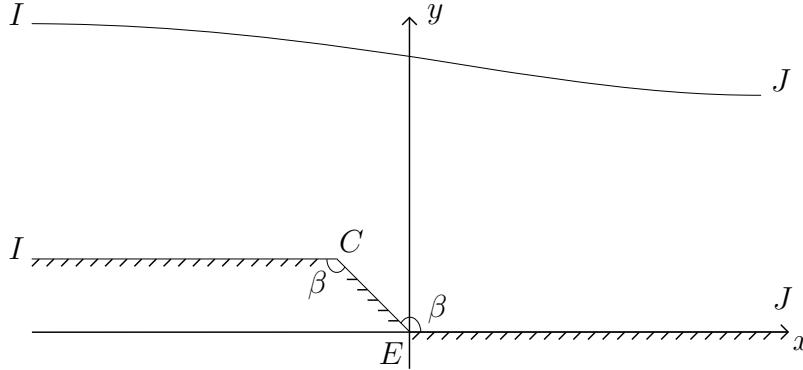


Figure 33: The  $z$ -plane for the spillway with a horizontal wall downstream.

We start by considering the zero-gravity case, leading to an exact solution. Surprisingly, such a free-streamline solution has not been found in existing searched literature. We reintroduce

$$f = \frac{2}{\pi} \log \frac{1+t}{1-t} \quad (1.55)$$

for mapping the complex potential  $f$  (c.f. figure 34a) to the unit semi-circle in the  $t$ -plane (c.f. figure 34b). This mapping was utilised in the first spillway problem (see §1.1.1). As with the previously considered cases, we assume uniform horizontal flow of unit velocity upstream. Then, due to neglecting the effects of gravity, we have unit speed along the free streamline  $IJ$ . This allows for the complex velocity  $\zeta$  to be written simply as

$$\zeta(t) = t^{1-\beta/\pi} \left( \frac{t-t_C}{1-t t_C} \right)^{\beta/\pi-1}. \quad (1.56)$$

This form for  $\zeta$  satisfies the no normal flow condition along the spillway wall; and the flow conditions

around and inside corners  $C$  and  $E$ , respectively. It also satisfies the condition that the flow has unit speed along the free streamline  $IJ$  since for  $\sigma \in [0, \pi]$  we have

$$\begin{aligned}
|\zeta(e^{i\sigma})| &= |e^{i\sigma}|^{1-\beta/\pi} \left| \frac{e^{i\sigma} - t_C}{1 - e^{i\sigma} t_C} \right|^{\beta/\pi-1} \\
&= \left| \frac{(\cos \theta - t_C) + i \sin \theta}{(1 - t_C \cos \theta) - i t_C \sin \theta} \right|^{\beta/\pi-1} \\
&= \left( \frac{t_C^2 - 2t_C \cos \theta + \cos^2 \theta + \sin^2 \theta}{t_C^2 (\cos^2 \theta + \sin^2 \theta) - 2t_C \cos \theta + 1} \right)^{(\beta/\pi-1)/2} \\
&= 1.
\end{aligned} \tag{1.57}$$

This expression for  $\zeta$  adopts a similar form to that used by Dias and Vanden-Broeck [1989] when considering flow past submerged objects, and its particularly useful quality is that it naturally satisfies  $|\zeta| = 1$  for  $t = e^{i\sigma}$ .

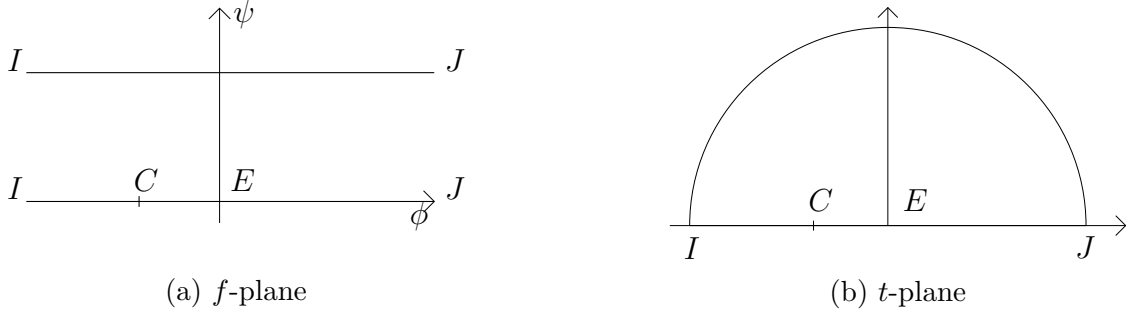


Figure 34: Complex planes for the spillway with a horizontal wall downstream.

We eliminate  $t$  from (1.55) and (1.56) and arrive at a closed-form solution for the complex velocity in terms of the complex potential:

$$\zeta(f) = \left( \tanh \left( \frac{\pi f}{4} \right) \right)^{1-\beta/\pi} \left( \frac{\tanh \left( \frac{\pi f}{4} \right) - t_C}{1 - t_C \tanh \left( \frac{\pi f}{4} \right)} \right)^{\beta/\pi-1}. \tag{1.58}$$

Recalling that the complex velocity can also be written by  $df/dz$ , we can integrate the reciprocal of  $\zeta$  with respect to  $f$  to obtain the position of the free streamlines in terms of the complex velocity and the constant  $t_C$ . We can then plot the profiles where, for  $\phi \in \mathbb{R}$ , points along the wall  $ICEJ$

can be found via

$$z(\phi) = \int_0^\phi \left( \tanh \left( \frac{\pi\phi'}{4} \right) \right)^{\beta/\pi-1} \left( \frac{\tanh \left( \frac{\pi\phi'}{4} \right) - t_C}{1 - t_C \tanh \left( \frac{\pi\phi'}{4} \right)} \right)^{1-\beta/\pi} d\phi', \quad (1.59)$$

and points along the free streamline  $IJ$  are found by evaluating

$$z(\phi) = z_0 + \int_0^\phi \left( \tanh \left( \frac{\pi(\phi' + i)}{4} \right) \right)^{\beta/\pi-1} \left( \frac{\tanh \left( \frac{\pi(\phi' + i)}{4} \right) - t_C}{1 - t_C \tanh \left( \frac{\pi(\phi' + i)}{4} \right)} \right)^{1-\beta/\pi} d\phi', \quad (1.60)$$

with

$$z_0 = i \int_0^1 \left( \tanh \left( \frac{\pi i\psi}{4} \right) \right)^{\beta/\pi-1} \left( \frac{\tanh \left( \frac{\pi i\psi}{4} \right) - t_C}{1 - t_C \tanh \left( \frac{\pi i\psi}{4} \right)} \right)^{1-\beta/\pi} d\psi. \quad (1.61)$$

Figure 35 shows the free-streamline plots with  $\beta = 3\pi/4$  for a number of different values of  $t_C \in (-1, 0]$ . Note that as  $t_C$  increases towards zero, the size of the step decreases. As  $t_C \rightarrow 0$ , the flow approaches the limiting behaviour: uniform horizontal flow of unit speed. On the other hand, the limiting configuration at  $t_C = -1$  is the flow along an infinite slope before the final horizontal wall, i.e. the flow without the wall  $IC$ . In this case,  $\zeta$  does not satisfy the condition far upstream of uniform horizontal flow as  $t \rightarrow -1$ .

Now we look to include the effects of gravity. In particular, we are searching for solutions that are supercritical downstream. Therefore, assuming no waves, we have  $u^2 + v^2 \sim \text{constant}$  as  $x \rightarrow +\infty$  and so the flow approaches a uniform stream of constant velocity, say  $U_D$ , and constant depth, say  $H_D$ . Recall that, throughout this study so far, we have non-dimensionalised with respect to the upstream parameters. Here,  $U_D$  and  $H_D$  denote the non-dimensionalised speed and depth of the downstream flow. We let  $y = H_D + \eta(x)$  be the equation of the free surface  $IJ$ . The governing equations for the flow far downstream, in terms of the velocity potential, are:

$$\phi_{xx} + \phi_{yy} = 0 \text{ for } 0 < y < H_D + \eta \quad (\text{Laplace's equation}) \quad (1.62)$$

$$\phi_y = \phi_x \eta_x \text{ on } y = H_D + \eta \quad (\text{Kinematic boundary condition on free surface}) \quad (1.63)$$

$$\frac{1}{2}(\phi_x^2 + \phi_y^2) + \frac{y}{F^2} = \frac{1}{2}U_D^2 + \frac{H_D}{F^2} \text{ on } y = H_D + \eta \quad (\text{Bernoulli equation}) \quad (1.64)$$

$$\phi_y = 0 \text{ on } y = 0 \quad (\text{Kinematic boundary condition along wall}). \quad (1.65)$$

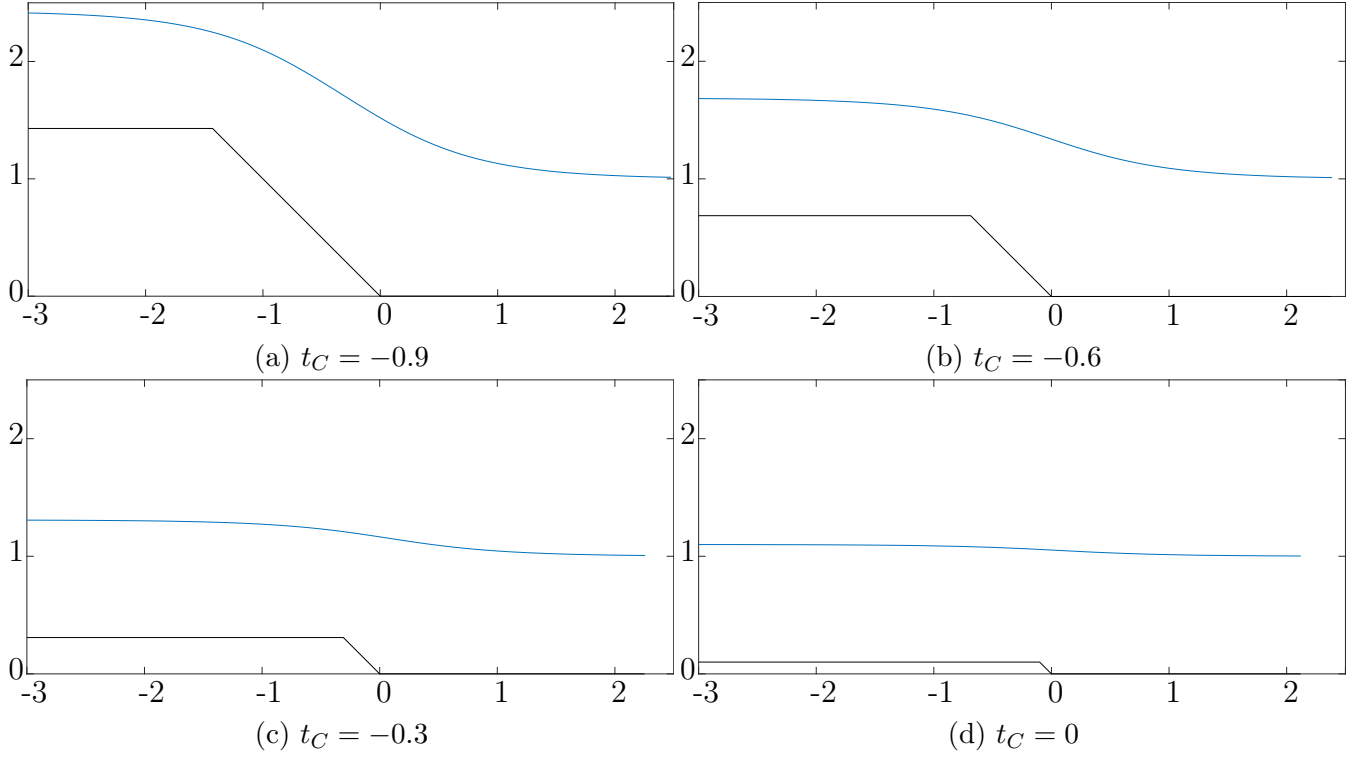


Figure 35: Profiles for the spillway with a horizontal step downstream with  $g = 0$ , i.e. the exact solution. Here, we take  $\beta = 3\pi/4$ .

Note that the Froude number  $F$  is based on the upstream speed and depth of the flow. Similarly to the calculations presented in §1.1.1, we take small perturbations about the equations for uniform horizontal flow of constant velocity  $U_D$ . Using the linearised equations, far downstream we have

$$\zeta \sim U_D + B e^{-\tilde{\mu} z} \quad (1.66)$$

where  $B \in \mathbb{R}$  is a constant and

$$\tilde{\mu} = \frac{1}{F^2 U_D^2} \tan(\tilde{\mu} H_D). \quad (1.67)$$

We define the downstream Froude number  $F_D = \tilde{U}_D / \sqrt{g \tilde{H}_D}$  and hence the relation becomes

$$\tilde{\mu} H_D = \frac{1}{F_D^2} \tan(\tilde{\mu} H_D). \quad (1.68)$$

Note that  $\tilde{U}_D$  and  $\tilde{H}_D$  denote the dimensional speed and depth of the flow downstream.

Utilising (1.33) for the complex potential in terms of  $t$ , it follows that far downstream, we

have  $f \sim -(2/\pi) \log(1-t)$ . Then, since  $df/dz = \zeta \rightarrow U_D$  as  $t \rightarrow 1$ , we have  $z \sim f/U_D$  far downstream. It follows that

$$\zeta \sim U_D + B(1-t)^{2\mu} \quad \text{as } t \rightarrow 1, \quad (1.69)$$

where  $\mu = \tilde{\mu}/(U_D\pi)$ . Similarity can be seen between this expression and that taken for the exponential decay of the flow far upstream from uniform horizontal flow of unit velocity (c.f.  $\zeta \sim (1 + Ae^{\pi\lambda f})$  as  $\phi \rightarrow -\infty$ ).

Proceeding as we have in the previous problems, we look to find a suitable form for the complex velocity that removes the singularities of the flow. Aside from (1.69) for the downstream singularity, we also need to incorporate  $\zeta \sim (1 + Ae^{\pi\lambda f})$  as  $\phi \rightarrow -\infty$  for the upstream flow; and the flows around and inside the corners of the spillway wall which were already included in the zero-gravity case (c.f. (1.56)). Difficulty arises here in attempting to combine the flow behaviours far up- and downstream into one expression. Dias and Vanden-Broeck [1989] consider a similar problem with flow past a submerged obstacle with supercritical flow both up- and downstream. However, due to the symmetry involved (since the obstacle is an isocles triangle) a suitable complex velocity ansatz is obtainable where the same exponential decay expression for  $\zeta$  is taken at either end of the flow. A similar approach cannot be taken here. Using the Bernoulli condition along with conservation of mass, we can find the downstream constant horizontal velocity,  $U_D$ . We have

$$\frac{1}{2} + \frac{1}{F^2}(1+h) = \frac{1}{2}U_D^2 + \frac{1}{F^2}U_D^{-1}, \quad (1.70)$$

where  $h$  is the non-dimensional perpendicular height of the step. Then, neglecting to remove the downstream singularity, we can form a complex velocity ansatz and compare the resulting downstream values with those expected (as calculated from (1.70)). We take

$$\zeta(t) = t^{1-\beta/\pi} \left( \frac{t-t_C}{1-t t_C} \right)^{\beta/\pi-1} \left( 1 + (1+t)^{2\lambda} \sum_{n=0}^{\infty} a_n t^n \right), \quad (1.71)$$

which satisfies the flow conditions upstream, at the corners  $C$  and  $E$ , and along the walls. As

usual, we truncate the series after  $N$  terms. The unknowns will be the  $N$  coefficients of the truncated series and  $t_C$ . We will have the usual equally-spaced mesh points along the arc in the  $t$ -plane (corresponding to the free surface  $IJ$ ), leading to  $N$  equations by evaluating the Bernoulli condition

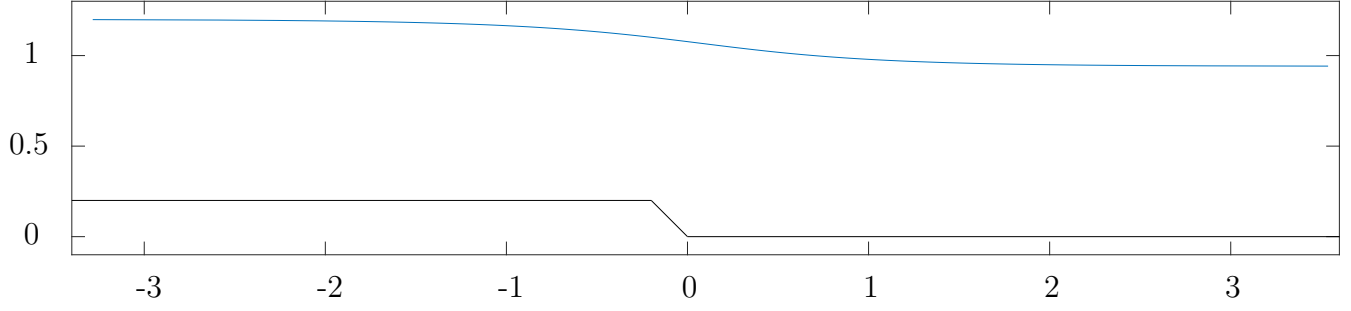
$$\frac{1}{2}q^2 + \frac{y}{F^2} = \frac{1}{2} + \frac{1}{F^2}(1 + h) \quad (1.72)$$

at these points. Note that the specified parameters will be  $\beta$ ,  $F$  and  $h$ . Therefore, the final equation is formed by imposing that the calculated perpendicular height of the step is indeed the given value for  $h$ . Then, we solve the  $N + 1$  equations for the  $N + 1$  unknowns numerically by iteration.

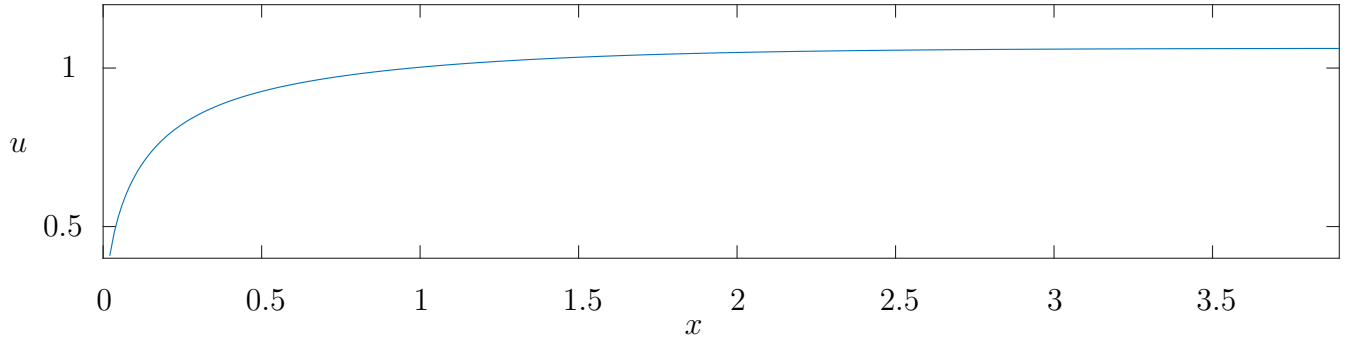
Figure 36a shows the resulting free-surface profile for  $F = 2$ ,  $\beta = 3\pi/4$  and  $h = 0.2$  with 200 collocation points. Waves are not apparent downstream and so, despite not incorporating the exponential decay of the flow far downstream, it seems that a supercritical solution has been obtained. The horizontal component  $u$  of the velocity along the wall is plotted against  $x$  in figure 36b where it seems that the flow develops constant speed far downstream. The same is plotted in figure 36c, but for  $u$  along the free surface instead. The values of  $u$  downstream are  $U_D \approx 1.0618$  and  $U_D \approx 1.0626$  along the wall and free surface, respectively. This compares well with one of the expected possible values from (1.70), i.e.  $U_D = 1.0628$ , which can also be seen from figure 36d. For this value of  $U_D$ , it follows that  $H_D = 0.9409$  and  $F_D = FU_D/\sqrt{H_D} = 2.1913$ .

Recalling that we have not removed the downstream singularity in the complex velocity ansatz (1.71), it is of interest to consider the quality of the solution. Figure 37 shows the decay of the coefficients  $a_n$ . Whilst the coefficients are of order  $10^{-5}$  for large  $n$ , there is not a nice decaying tail of the coefficients as seen in previous problems (e.g. figure 26). Since we want the infinite series of the ansatz (1.71) to be convergent inside the unit disc  $|t| < 1$ , there is a problem with the solution. A development to likely improve this would be to find a more suitable form for  $\zeta$  where the behaviour of the flow far downstream is included.

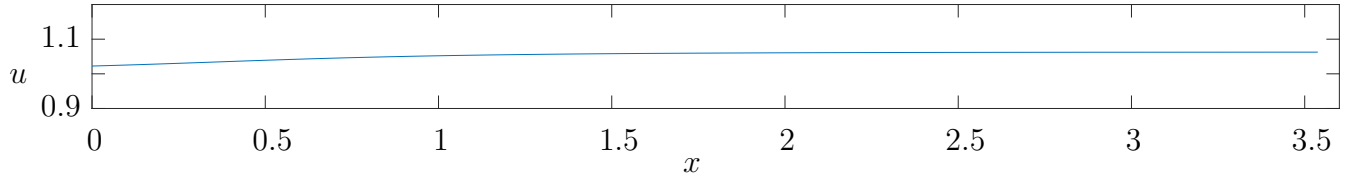




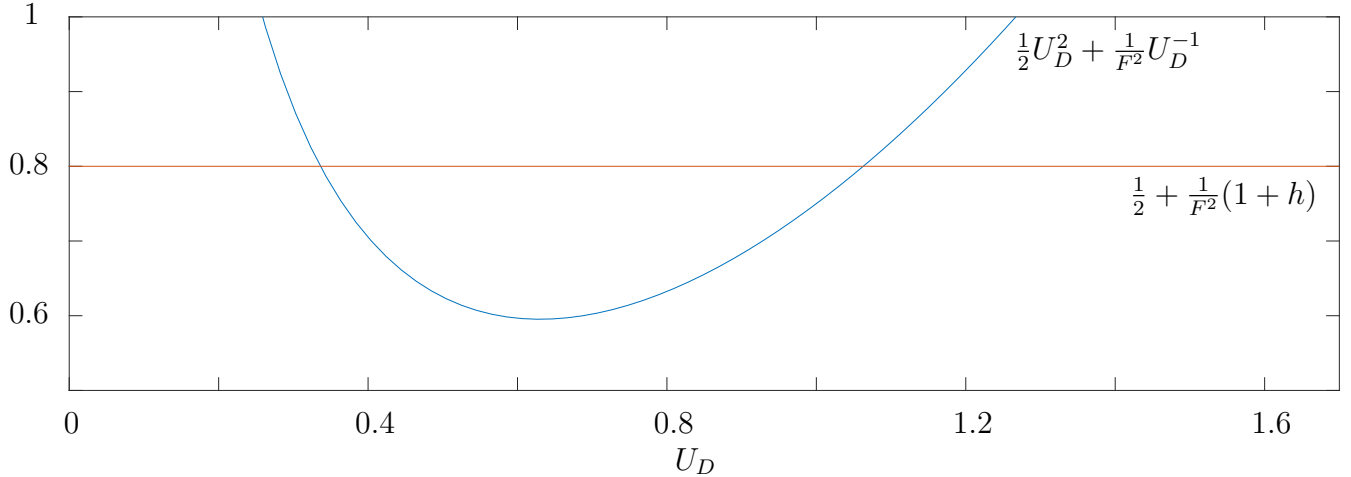
(a)  $z$ -plane for spillway with horizontal wall downstream



(b) Horizontal component  $u$  of velocity against  $x$ , along the wall



(c) Horizontal component  $u$  of velocity against  $x$ , along the free surface



(d) Finding the possible values for  $U_D$ , c.f. (1.70).  $U_D = 0.3363$  or  $1.0628$

Figure 36: Results for the  $g \neq 0$  case of the spillway with a horizontal step downstream. Here, we have used (1.71) for the complex velocity ansatz and we have set  $F = 2$ ,  $\beta = 3\pi/4$  and  $h = 0.2$  where  $N = 200$ .

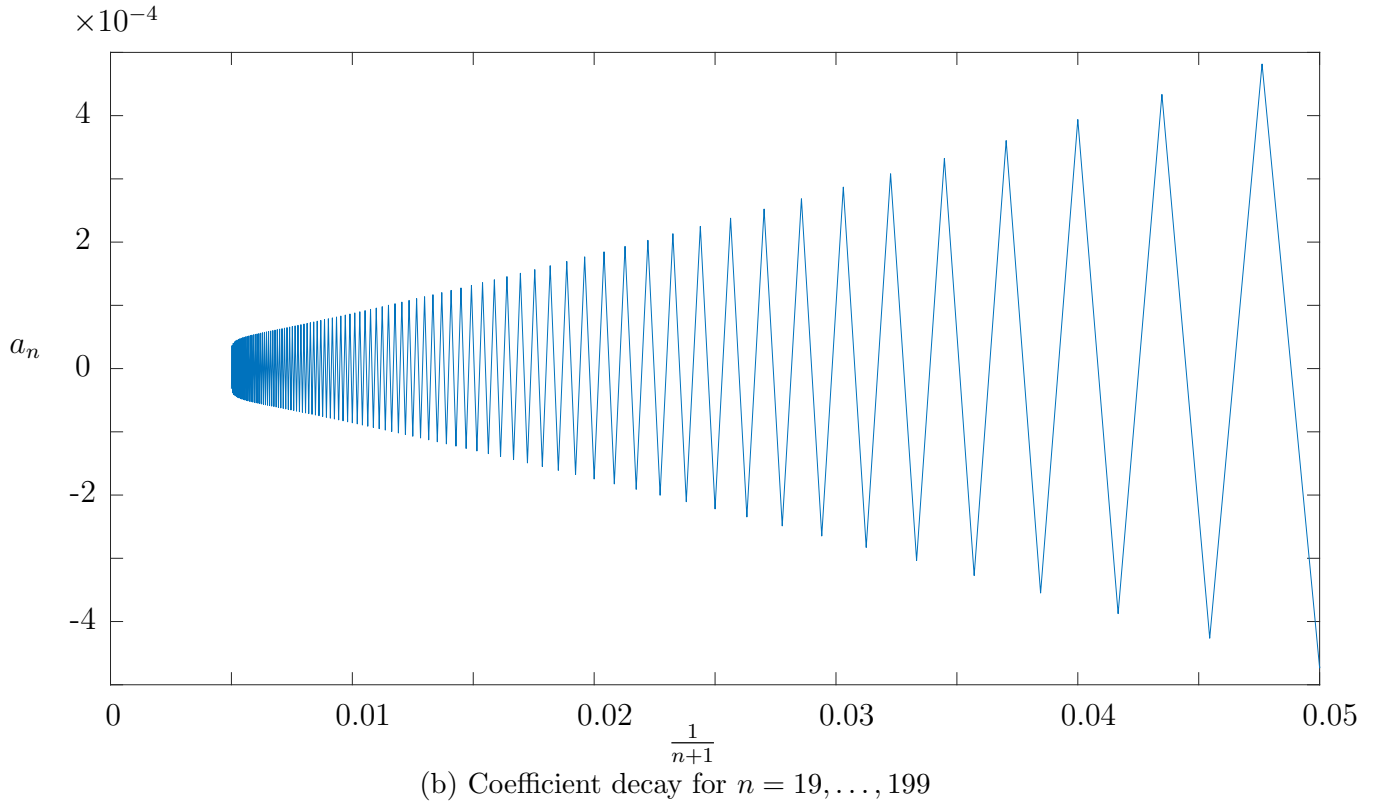
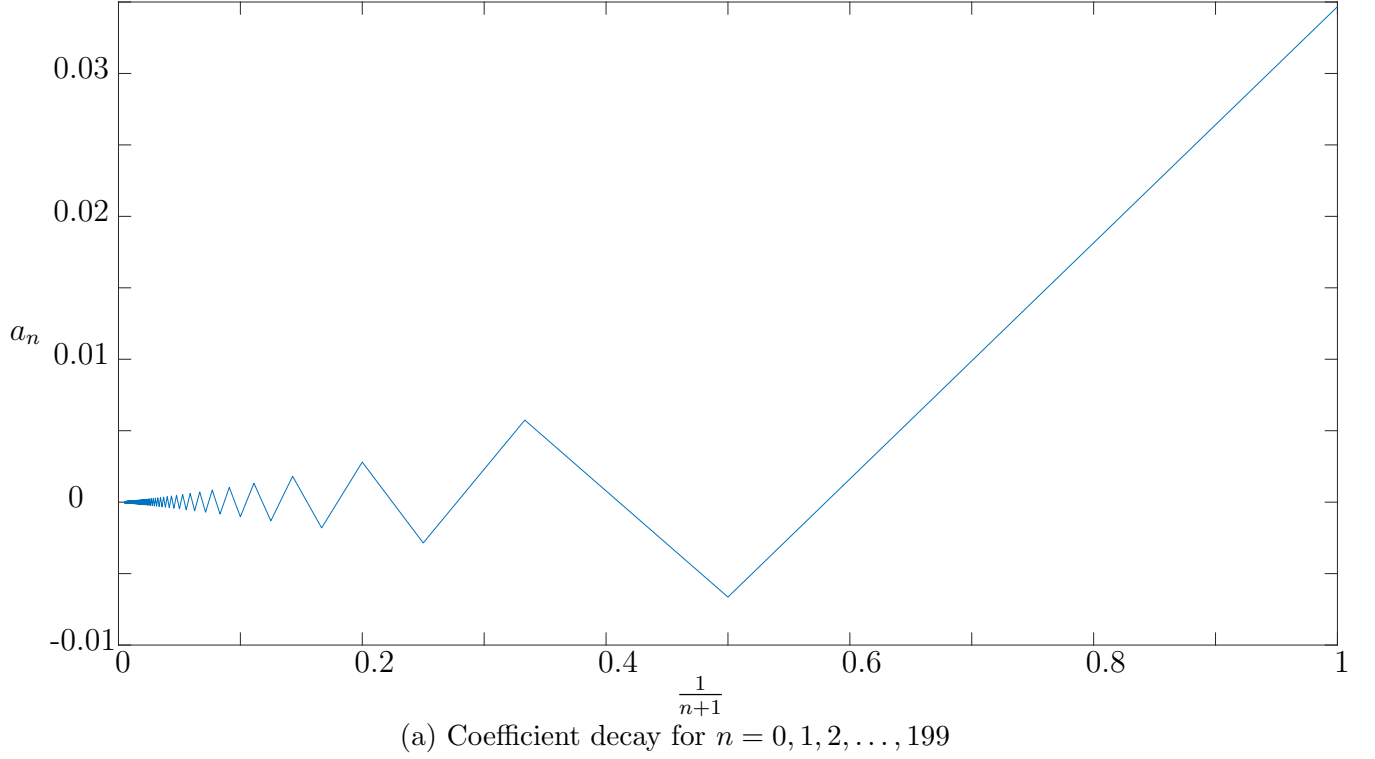


Figure 37: Further results for the  $g \neq 0$  case of the spillway with a horizontal step downstream where we have used (1.71) for the complex velocity ansatz (i.e. not including the downstream singularity) and we have set  $F = 2$ ,  $\beta = 3\pi/4$  and  $h = 0.2$  where  $N = 200$ .

We can include the downstream behaviour by taking

$$\zeta(t) = t^{1-\beta/\pi} \left( \frac{t-t_C}{1-tt_C} \right)^{\beta/\pi-1} \times \left( \frac{1-t}{2} \left( 1 + (1+t)^{2\lambda} \sum_{n=0}^{\infty} a_n t^n \right) + \frac{1+t}{2} \left( U_D + (1-t)^{2\mu} \sum_{n=0}^{\infty} b_n t^n \right) \right). \quad (1.73)$$

This form for the complex velocity ansatz involves two power series in  $t$ . We can still proceed as usual by truncating the series after  $N$  terms, leading to  $2N$  unknown coefficients. We also leave  $t_C$  unknown. The values for the Froude number  $F$ , angle  $\beta$  between the walls and perpendicular height  $h$  of the step in the spillway wall will be specified. Furthermore, we know the value of  $U_D$  *a priori* through use of (1.70); and the values of  $H_D$ ,  $F_D$  and  $\mu$  follow directly from conservation of mass,  $F_D = FU_D^{3/2}$  and (1.68), respectively. Note that the value taken, of the (maximum) two possible values, for  $U_D$  is that which corresponds to supercritical flow downstream. We introduce  $2N$  mesh points along the arc of the semi-circle in the  $t$ -plane and we satisfy the Bernoulli condition (1.72) at each point, leading to  $2N$  equations. The last equation, as before, is from setting the value for  $h$ . Therefore, we have  $2N + 1$  equations in  $2N + 1$  unknowns that can be solved numerically by iteration.

Here, we discuss the results where the parameters are set as  $F = 2$ ,  $\beta = 3\pi/4$  and  $h = 0.2$ . Note that we utilise the value  $U_D = 1.0628$ , obtained from (1.70), in the complex velocity ansatz. At first glance, this solution is ideal, since we have been able to incorporate both the up- and downstream behaviours in the form for  $\zeta$ . The free-surface profile is not presented here since it is the same (to order  $10^{-5}$ ) as that of figure 36a where the downstream singularity was not removed from the series representation for the complex velocity. A comparison of free-surface profiles that are extrapolated up- and downstream also agree to order  $10^{-4}$ . There does not appear to be any marked improvement in the profiles by incorporating the downstream behaviour. Further to this, neither of the power series in  $t$  of (1.73) appear to have coefficients that decrease to zero with  $n$ . Additionally, there is not clear convergence of individual coefficients as  $N$  increases. On the other hand, the value of  $t_C$  is consistent and appears to converge to some value as  $N$  increases. Also, the value of the power series with coefficients  $a_n$  at  $t = -1$  and the value of the power series with

coefficients  $b_n$  at  $t = 1$  seem to converge with  $N$ . However, these positives do little to distract from the lack of a distinct improvement with the inclusion of the downstream behaviour and the lack of convergence of the power series' coefficients.

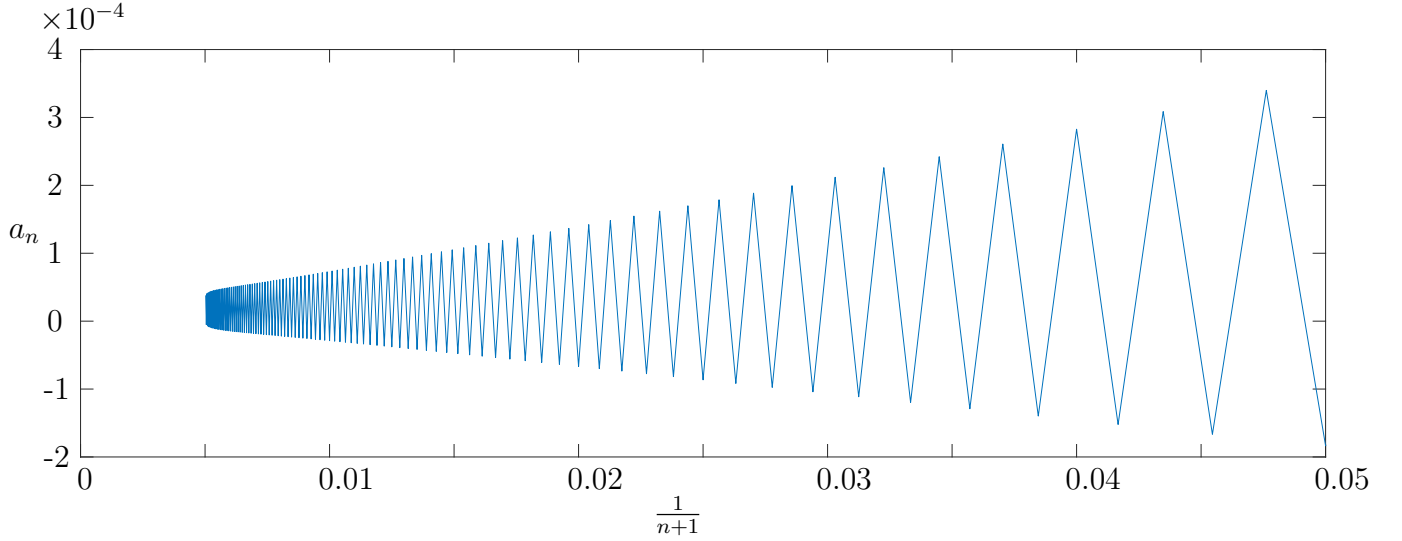
The issues of the previous attempt are likely due to the two power series in  $t$  involved in the complex velocity ansatz as a result of too many degrees of freedom. Instead, we reattempt removing the downstream singularity from the series representation for the complex velocity by retaining the power series in  $t$  associated with the upstream behaviour and simply introducing an unknown coefficient of the downstream exponential decay. More specifically, we take

$$\zeta(t) = t^{1-\beta/\pi} \left( \frac{t - t_C}{1 - t t_C} \right)^{\beta/\pi-1} \left( \frac{1-t}{2} \left( 1 + (1+t)^{2\lambda} \sum_{n=0}^{\infty} a_n t^n \right) + \frac{1+t}{2} \left( U_D + B(1-t)^{2\mu} \right) \right), \quad (1.74)$$

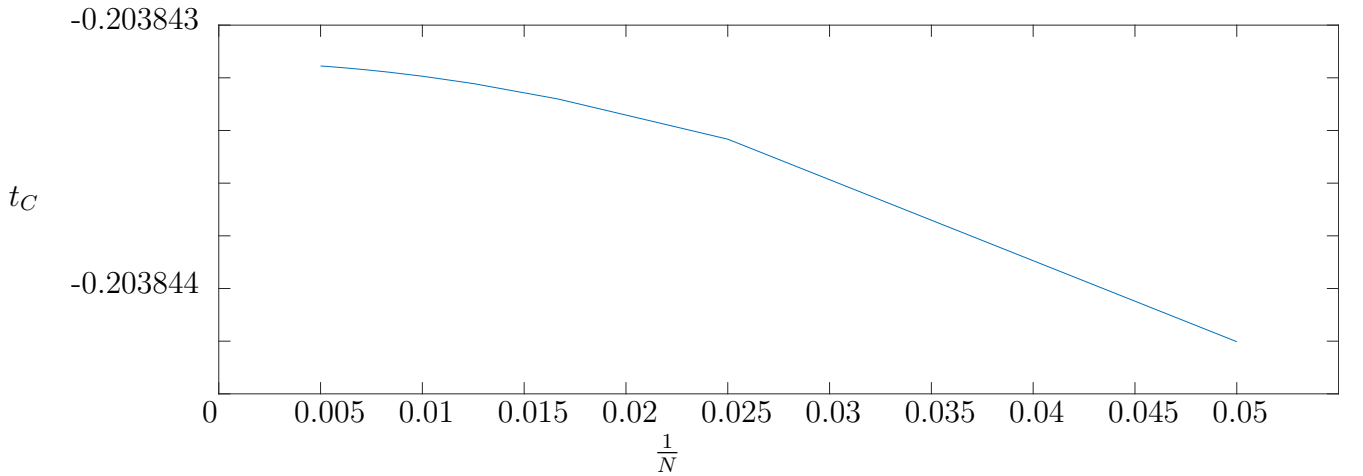
where  $B$  is an unknown constant to be found. We truncate the series after  $N - 1$  terms and we have  $t_C$  and  $B$  also as unknowns. We utilise  $N$  mesh points that are equally-spaced along the arc of the unit semi-circle in the  $t$ -plane. Satisfying the Bernoulli condition (1.72) at these points gives rise to  $N$  equations. As before, we impose the perpendicular height  $h$  of the step. Overall, we have  $N + 1$  equations in  $N + 1$  unknowns. We keep the same the other details of the previous attempt: the parameters are  $F$ ,  $\beta$  and  $h$ ; and we can know the value of  $U_D$  by (1.70) prior to solving the  $(N + 1) \times (N + 1)$  system.

Again, we discuss the results for  $F = 2$ ,  $\beta = 3\pi/4$  and  $h = 0.2$ . The free-surface profile is not presented here since it is the same as previously obtained (c.f. figure 36a) to order  $10^{-5}$ . We obtain  $t_C = -0.2038$  and  $B = -0.0895$  (recall that  $B$  is the coefficient of the exponential decay downstream). The quality of the numerical solution appears to be much better than the previous attempt where two power series were included in the complex velocity ansatz since we have now recovered the usual coefficient decay for large  $n$  (c.f. figure 38a). The coefficient decay is also slightly improved compared with an earlier attempt (c.f. figure 37) where the downstream singularity is not taken into account at all in the form adopted for  $\zeta$ . We still do not have a particularly nice decaying tail in the coefficients for large  $n$ , but the amplitude of the oscillation of the coefficients is smaller. Another test of the efficacy of the method is looking for convergence of

the value obtained for  $t_C$  (the position in the  $t$ -plane corresponding to the corner  $C$ ) as  $N \rightarrow +\infty$ . Figure 38b shows the values of  $t_C$  obtained against  $1/N$  for  $N = 20, 40, 60, \dots, 200$  and it seems that we do indeed have convergence as  $N \rightarrow +\infty$ . Finally, a further example free-surface profile is included in figure 39 where we set the perpendicular height of the step to be  $h = 1$ . This serves to demonstrate the capability of the numerical method for larger steps rather than just the smaller value of  $h = 0.2$  that has been discussed through the analysis of the results.



(a) Coefficient decay plot for  $N = 200$ .



(b) Convergence of  $t_C$  as  $N \rightarrow +\infty$ .

Figure 38: Results for the  $g \neq 0$  case of the spillway with a horizontal step downstream. Here, we have used (1.74) for the complex velocity ansatz to include the downstream singularity. We set  $F = 2$ ,  $\beta = 3\pi/4$  and  $h = 0.2$ .

Overall, it appears that the downstream singularity does not need to be incorporated into the complex velocity ansatz in order to obtain the numerical solution, particularly if interest is mainly

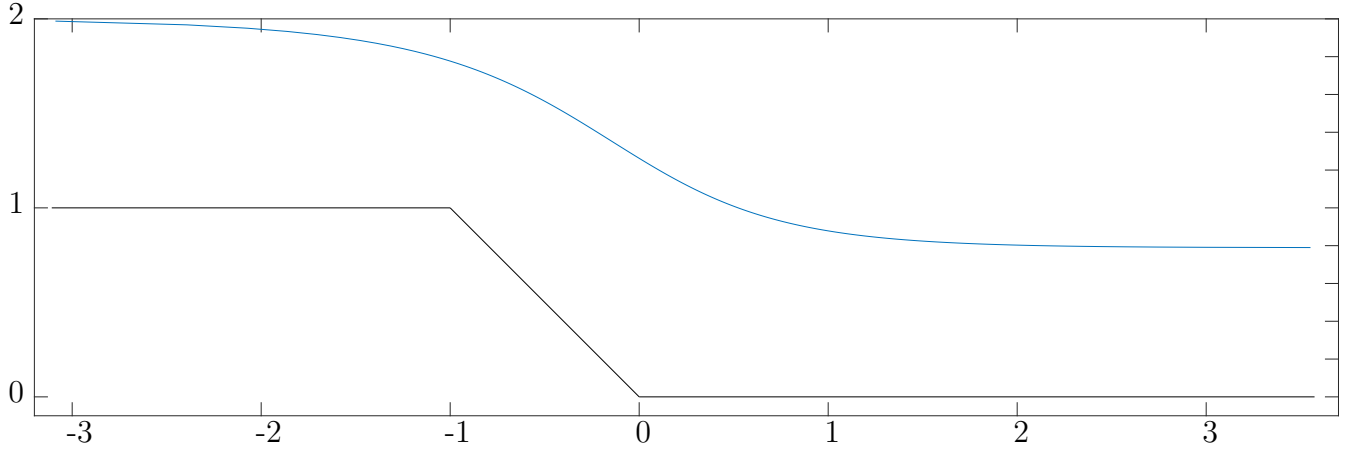


Figure 39: Free-surface profile for  $F = 2$ ,  $\beta = 3\pi/4$  and  $h = 1$  for  $N = 400$ . This has been obtained through use of (1.74) for the complex velocity ansatz which includes the downstream singularity.

in the free-surface profile. However, when forming the ansatz for  $\zeta$ , the upstream exponential decay is included by replacing the unknown coefficient of this decay by an unknown function in  $t$ . This function is analytic for  $|t| < 1$  and continuous for  $|t| \leq 1$  and so we replace it by a power series in  $t$ , with unknown coefficients to be found. Due to the properties of the unknown function, to have obtained a good numerical solution means to obtain coefficients such that the series is convergent inside the unit disk and coefficients that decay sufficiently quickly so that we do not have a sizeable error due to the truncation of the series. Therefore, whilst we have not obtained a good decaying tail to the coefficients for large  $n$  by removing the downstream singularity from the power series in  $t$ , we have decreased the amplitude of the oscillations of the coefficients for large  $n$ .

---

In this chapter, we have demonstrated the use of the mapping (1.33) in solving for the flow in the most basic spillway case (i.e. consisting of two straight walls, as in §1.1.2) when utilising the numerical approach of series truncation and collocation. We have then shown the application of this mapping and numerical approach when the walls of the spillway are defined piecewise or are curvilinear. Whilst using a different mapping in the case of the stepped wall in the horizontal channel (of §1.5), we still utilise the same approach to obtain a numerical solution. The decay of the coefficients of the power series involved in the complex velocity ansatz has been used to analyse the quality of the solutions in these different examples. It is clear that, for good coefficient decay (and therefore a numerical solution of good quality) it is required that we suitably capture the

singularities of the flows. In particular, with reference to the case of the spillway with a parabolic sloping wall (of §1.4), we have discussed the potential need for more terms in the expansion for the complex velocity  $\zeta$  for the jet singularity downstream, as opposed to taking  $\zeta \sim f^{1/3}$  far downstream. This will be discussed and explored further in the following chapter where we turn our concern to waterfall flow.

## 2 Waterfall flows

As discussed in the introduction, we now move on to look at waterfall flows. The difference here (compared with the spillway flows) is that we now have two free surfaces downstream, bounding the jet. The fluid and flow assumptions remain as before, meaning that we can still utilise potential flow theory. The overall method of solving is the same as already employed, i.e. we use conformal mappings, form an ansatz for the complex velocity and then use series truncation and collocation to numerically find the unknown coefficients of the series involved in the ansatz. As usual, to achieve this we must analyse the flow to identify the behaviour of any flow singularities. The focus will be on the jet flow far downstream. Existing literature uses the form  $\zeta \sim f^{1/3}$  for the jet (as seen and frequently used in the previous chapter for the spillways) but we will show that a more suitable expression can be applied for the waterfall. Following this, the numerical solutions will be further investigated and improvements to the solution method will be introduced. These lead to enhanced coefficient decay of the power series that appears in the complex velocity ansatz. This work on improvements to the waterfall problem has been previously published [McLean et al., 2022].

### 2.1 Reproduction

Here, we formulate the problem and present the numerical method and solutions, as obtained by Dias and Tuck [1991], which will later be used for comparison. We consider two-dimensional, free-surface flow past the trailing edge of a horizontal plate, where the flow is uniform and horizontal far upstream and two free surfaces form a free jet far downstream. The physical  $z$ -plane is as depicted in figure 40a and note that the origin is set to be at the edge of the plate at point  $C$ . The flow is assumed to be steady and irrotational, whilst the fluid is assumed to be inviscid and incompressible, and gravity is taken into account. As in the spillway chapter, we non-dimensionalise with respect to the upstream flow velocity and depth; and so we have unit depth and velocity far upstream. This non-dimensionalisation gives rise to the Froude number, as defined earlier. However, for later ease of notation, we further define  $G = F^{-2}$ . In the calculations here, we focus on supercritical flow, i.e.  $G < 1$ .



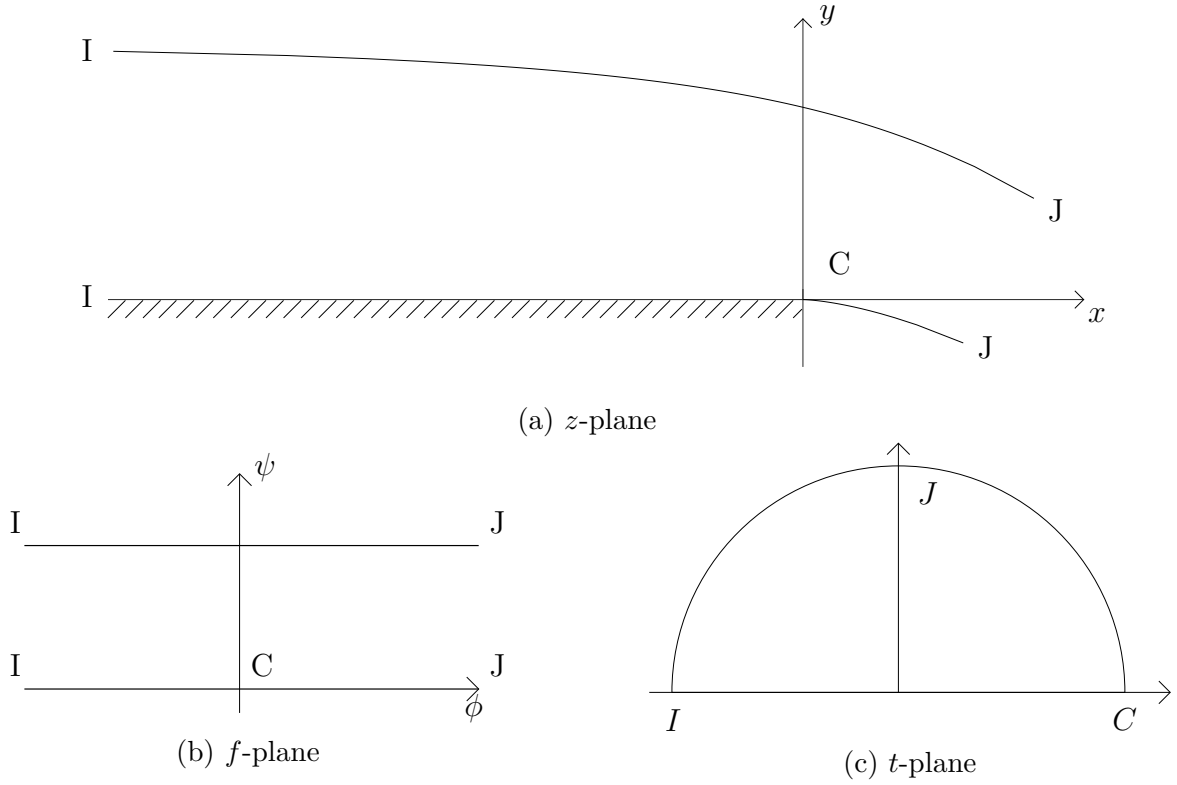


Figure 40: Complex planes for waterfall flows.

Throughout the flow, the Bernoulli condition yields

$$\frac{1}{2}q^2 + Gy + p = \frac{1}{2} + G, \quad (2.1)$$

where  $q$  is the magnitude of velocity and  $p$  is the pressure. Atmospheric pressure is assumed along both the upper ( $IJ$ ) and lower ( $CJ$ ) free surfaces. Since the pressure is equal and constant along these free surfaces, we set this pressure to be zero. Then, we arrive at  $\frac{1}{2}q^2 + Gy = \frac{1}{2} + G$  along both free surfaces. The complex potential is still denoted by  $f$  with  $\phi$  and  $\psi$  denoting the velocity potential and the streamfunction, respectively. We set  $\phi = 0$  at  $C$ . We also set  $\psi = 0$  and  $\psi = 1$  along the lower and upper free surfaces, respectively. Then, the  $f$ -plane is as shown in figure 40b: an infinite strip of width 1.

We now introduce the intermediate  $t$ -plane which is defined by

$$f = \frac{1}{\pi} \log \frac{(t+1)^2}{2(t^2+1)}. \quad (2.2)$$

This maps the  $f$ -plane to the upper-half of a unit semi-circle centred at the origin of the  $t$ -plane. The interior of the infinite strip maps into the interior of the semi-circle, whilst the upper free surface  $IJ$  maps to the left-hand arc of the semi-circle and the lower free surface  $CJ$  maps to the right-hand arc of the semi-circle (c.f. figure 40c). This mapping was utilised in the spillway chapter in cases where we required collocation points along the sloping spillway wall.

The complex velocity is defined as before and is still denoted by  $\zeta$ . The aim now is to find  $\zeta$  as an analytic function of the complex potential,  $f$ . Dias and Tuck [1991] use the following conditions:

1.  $\zeta \sim (1 + ae^{\lambda f})$  as  $\phi \rightarrow -\infty$ , where  $a$  is an unknown constant and  $\lambda$  is the smallest positive root of  $\lambda - G \tan \lambda = 0$ ,
2.  $v = 0$  on  $\psi = 0$ ,  $\phi < 0$ ,
3.  $\zeta \sim f^{1/3}$  as  $\phi \rightarrow +\infty$ .

The first condition above describes the upstream flow such that as  $\phi \rightarrow -\infty$ , the flow approaches a uniform horizontal stream of constant unit velocity. The second condition simply ensures no normal flow along the horizontal wall. The third condition describes the downstream behaviour of the free-falling jet — this condition will later be reconsidered. This is because the current form is appropriate for the jet of spillway-flow (as seen earlier, c.f. Vanden-Broeck and Keller [1986]), but instead we expect parabolic flow for the free-falling jet.

The Dias and Tuck [1991] form for the complex velocity is

$$\zeta(t) = (-\log 2c)^{-1/3} (-\log c(1+t^2))^{1/3} \left( 1 + (1+t)^{2\lambda} \sum_{n=0}^{\infty} a_n t^n \right), \quad (2.3)$$

where  $\lambda$  is the smallest positive root of  $\pi\lambda - F^{-2} \tan \pi\lambda = 0$ , and  $c$  is a constant such that  $0 < c < 1/2$ . Recall that different choices of  $c$  will affect the value of the coefficients  $a_n$  but will not affect the function  $\zeta(t)$  represented by (2.3) and so the solution will also not be impacted. It can be checked that this analytic function (2.3) for  $\zeta(t)$  satisfies the necessary flow conditions far upstream, downstream and along the horizontal bed.

It remains to satisfy the Bernoulli condition (2.1) on both free surfaces which will, for a given Froude number, enable us to find the unknown coefficients  $a_n$ . We truncate the series (convergent inside the unit disc) of (2.3) after  $N$  terms and it remains to find the unknown coefficients  $a_n$ ,  $n = 0, 1, 2, \dots, N - 1$ . Recall that, for the image of the free surfaces in the  $t$ -plane, we can use  $t = e^{i\sigma}$  where  $0 < \sigma < \pi$ . We introduce  $N$  mesh points  $\sigma_I = \pi/2N + (\pi/N)(I - 1)$ , for  $I = 1, \dots, N$  for the collocation method, as before. We evaluate the Bernoulli equation at each collocation point and so we have  $N$  equations in  $N$  unknowns which can be solved numerically by iteration, for example using Newton's method. As mentioned earlier, we have used the `fsolve` function of MATLAB to obtain our numerical solutions. Once the coefficients have been found for a given Froude number,  $F$ , we can plot the free surfaces for the waterfall.

Figure 41 shows the resulting free-surface profiles for the cases where the Froude number is 1.2, 1.6 and 2. As expected, the downfall curvature is greater for smaller Froude numbers since, for such Froude numbers, the flow is dominated by gravitational forces. The plotting points (which correspond to the mesh points in the  $t$ -plane) are shown in figure 41a. It shows that it is difficult to plot the free-surface profiles far downstream if only plotting using the mesh points. This is since an abundance of points are required to see a very small distance further downstream due to the logarithm involved in the conformal mappings; and the last few (equally-spaced) mesh points close to  $t = i$  map to the last few points downstream that are spaced quite far apart in physical space. If we extrapolate the profiles further downstream, a concern is that the flow may not be parabolic but instead follow a more spillway-like path. In comparisons made later, following analysis of the jet singularity far downstream, we will see that this is indeed the case (c.f. figure 43).

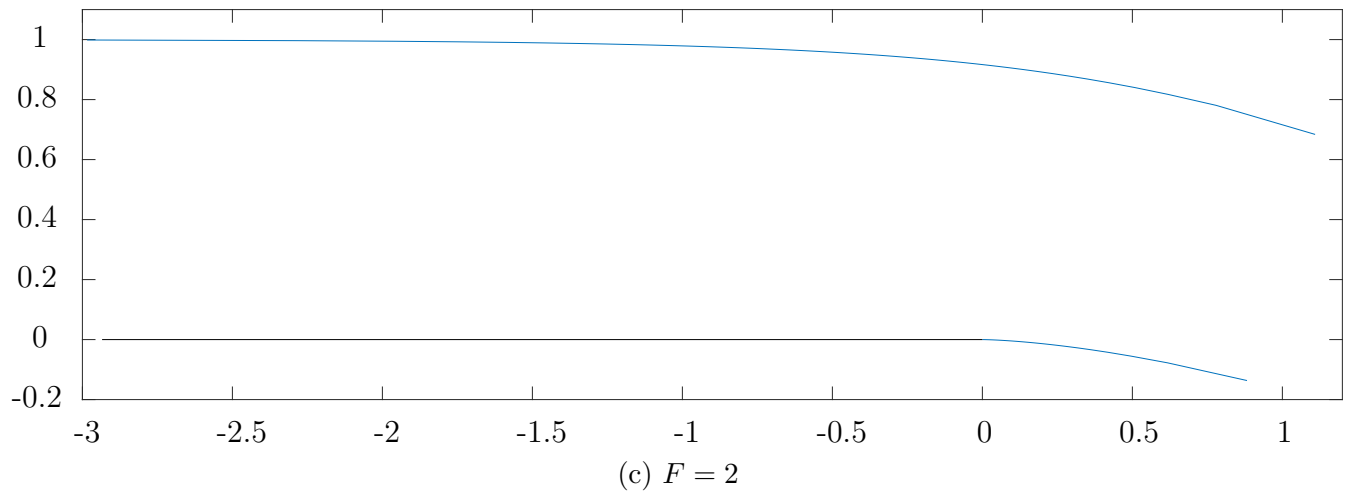
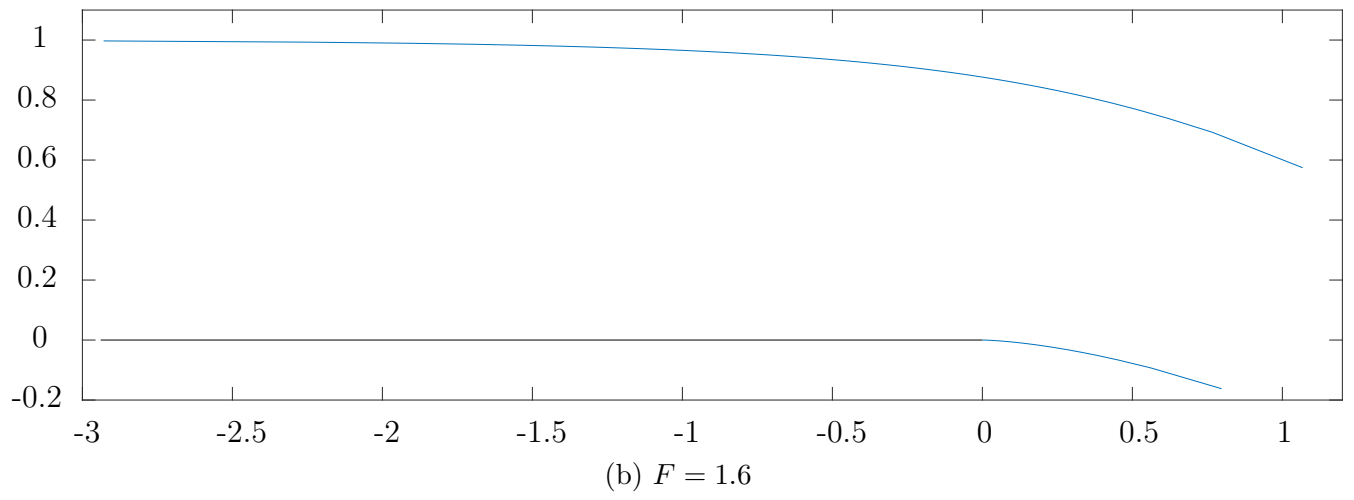
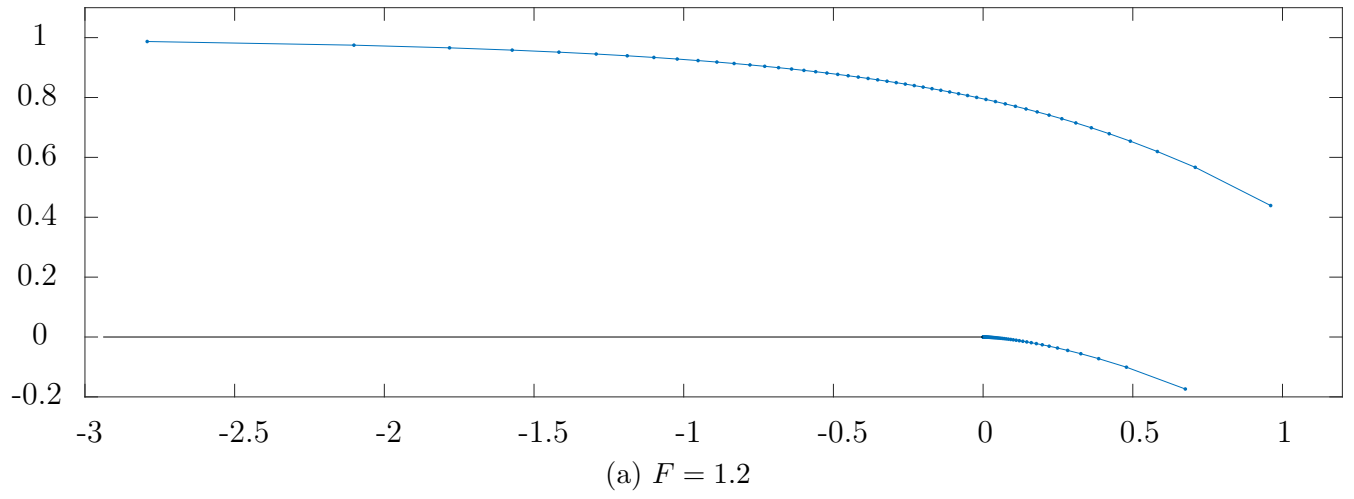


Figure 41: Free-surface profiles for the waterfall flow with  $c = 0.2$  and  $N = 100$ . Here, we have utilised the complex velocity ansatz (2.3).

## 2.2 Large- $\phi$ analysis: flow far downstream

We wish to analyse the waterfall flow far downstream in order to obtain a multiple-term expansion for the behaviour of  $\zeta$  as  $\phi \rightarrow +\infty$ . To obtain a form of Torricelli's law — which, generally with reference to gravitational flow out of an orifice of a tank, states that the speed  $q$  of a jet out of the hole is proportional to the depth  $h$  below the surface at which the jet starts, specifically  $q = \sqrt{2gh}$  where  $g$  denotes the gravitational acceleration — we introduce the following shift:

$$x_s = x - x_0, \quad y_s = y - 1 - \frac{1}{2G} \quad \text{and} \quad \phi_s = \phi - \phi_0. \quad (2.4)$$

It follows that  $z_s = x_s + iy_s$  and  $f_s = f - \phi_0 = \phi_s + i\psi$ , where  $x_0$  and  $\phi_0$  are real constants. We rewrite the Bernoulli condition (2.1) on the free surfaces in terms of the new variables, so we have

$$\left| \frac{df_s}{dz_s} \right|^2 = -2Gy_s. \quad (2.5)$$

Therefore, we have obtained Torricelli's law. We have a conserved horizontal momentum flux since there are no external forces acting in this direction, and so there is some finite value, say  $u_\infty$ , for the horizontal component of velocity far downstream. Also, we have  $|\zeta| \sim -v$  as  $y \rightarrow -\infty$ . It follows that

$$\frac{dy}{dx} = \frac{dy}{dt} \frac{dt}{dx} \sim -\frac{|\zeta|}{u_\infty} \quad (2.6)$$

along streamlines, far downstream. Then,

$$\left( \frac{dy_s}{dx_s} \right)^2 \sim -\frac{2Gy_s}{u_\infty^2} \quad (2.7)$$

far downstream through use of (2.5). It still remains to find the value of  $u_\infty$ .

We define  $y_\infty$  to be the vertical width of the jet far downstream and note that, by conservation of mass, we know  $y_\infty = 1/u_\infty$ . The angle approaches  $-\pi/2$  far downstream and the jet thins such that the pressure becomes ambient. Then, due to the conserved horizontal net momentum flux,

we have that

$$\int_{\psi=0}^{\psi=1} (u^2 + p) \, dy \quad (2.8)$$

at some  $x$ -position takes the same value far downstream as it does far upstream. We can utilise (2.1) and (2.5) to evaluate this integral far up- and downstream and this leads to the constraint

$$u_\infty = 1 + \frac{G}{2}. \quad (2.9)$$

Therefore, we can now rewrite (2.7) as

$$\left(\frac{dy_s}{dx_s}\right)^2 \sim -\frac{2Gy_s}{(1 + G/2)^2}, \quad (2.10)$$

far downstream. It should be noted that the integrated form of this is already found as a result of the integral horizontal momentum balance as equation (6-29) of Henderson [1966]. From (2.10), we infer

$$y_s \sim -\frac{G}{2} \frac{1}{(1 + G/2)^2} x_s^2, \quad (2.11)$$

also far downstream. This highlights that the shape of the free-falling jet far downstream should be parabolic (as found by Clarke [1965]), not following a linear path like a spillway flow (i.e.  $\zeta \sim f^{1/3}$ , c.f. Keller and Weitz [1957] and Vanden-Broeck and Keller [1986]).

Using (2.5), we have that the vertical component of velocity behaves like  $-(-2Gy_s)^{1/2}$  as  $y_s \rightarrow -\infty$  and so we can deduce that, far downstream,

$$f_s \sim (-2G)^{1/2} \left( -\frac{2}{3} y_s^{3/2} + i x_s y_s^{1/2} \right). \quad (2.12)$$

Also, by expanding

$$z_s^{3/2} = i^{3/2} y_s^{3/2} \left( 1 - i \frac{x_s}{y_s} \right)^{3/2} \quad (2.13)$$

as  $y_s \rightarrow -\infty$ , we can then show that

$$z_s^{3/2} \sim \frac{3}{2i^{1/2}} \left( -\frac{2}{3} y_s^{3/2} + i x_s y_s^{1/2} \right) \text{ as } y_s \rightarrow -\infty. \quad (2.14)$$

It follows that we arrive at

$$z_s \sim \tilde{A}f_s^{2/3} + \tilde{B}f_s^\alpha + \dots \text{ as } \phi_s \rightarrow +\infty, \quad (2.15)$$

where  $\alpha < 2/3$ ,  $\tilde{A}$  and  $\tilde{B}$  are unknown constants to be found. Focusing attention on the streamline corresponding to  $\psi = 0$ , we can then write

$$z_s \sim (A_1 + iA_2)\phi_s^{2/3} + (B_1 + iB_2)\phi_s^\alpha + \dots \text{ as } \phi_s \rightarrow +\infty, \quad (2.16)$$

where  $A_1, A_2, B_1$  and  $B_2$  are unknown, real constants. Utilising this with (2.11), we find  $A_1 = 0$ . Now, we obtain the following expression:

$$\frac{dz_s}{d\phi_s} \sim i\frac{2}{3}A_2\phi_s^{-1/3} + \alpha(B_1 + iB_2)\phi_s^{\alpha-1} + \dots \text{ as } \phi_s \rightarrow +\infty. \quad (2.17)$$

We can utilise the form of Torricelli's law obtained earlier (c.f. (2.5)) to find the value of the constant  $A_2$ : far downstream, we have

$$\frac{4}{9}A_2^2\phi_s^{-2/3} + \frac{4}{3}A_2\alpha B_2\phi_s^{\alpha-4/3} + \alpha^2(B_1^2 + B_2^2)\phi_s^{2(\alpha-1)} + \dots \sim -\frac{1}{2G}\left(\frac{\phi_s^{-2/3}}{A_2} - \frac{B_2}{A_2^2}\phi_s^{\alpha-4/3} + \dots\right). \quad (2.18)$$

The leading order terms give

$$A_2 = -\left(\frac{9}{8G}\right)^{1/3}. \quad (2.19)$$

It remains to calculate the value of  $B_1$ ,  $B_2$  and  $\alpha$ . For this, we look to the next order and find that

$$\frac{4}{3}A_2\alpha B_2 = \frac{1}{2G}\frac{B_2}{A_2^2} \Rightarrow B_2 = 0 \text{ or } \alpha = -\frac{1}{3}. \quad (2.20)$$

To choose the correct solution here, we recall that earlier we found that the finite constant for the horizontal velocity far downstream is  $u_\infty = 1 + G/2$ . Utilising (2.17) and recalling that  $df/dz = u - iv$ , we can write

$$1 + \frac{G}{2} \sim \frac{9\alpha}{4A_2^2}B_1\phi_s^{\alpha-1/3} + \dots \text{ as } \phi_s \rightarrow +\infty. \quad (2.21)$$

It follows that  $\alpha = 1/3$ , and so we can then find that

$$B_1 = \frac{2}{3}(2 + G)A_2^2. \quad (2.22)$$

We can also conclude that  $B_2 = 0$ .

Now, we look to find the next term, i.e. finding the constants  $C_1$ ,  $C_2$  and  $\beta$  of

$$z_s \sim iA_2 f_s^{2/3} + B_1 f_s^{1/3} + (C_1 + iC_2)f_s^\beta + \dots \quad \text{as } \phi_s \rightarrow +\infty, \quad (2.23)$$

noting that  $\beta < 1/3$ . Again, utilising Torricelli's law, we find that far downstream

$$\frac{4}{9}A_2^2\phi_s^{-2/3} + \frac{1}{9}B_1^2\phi_s^{-4/3} + \frac{4}{3}A_2\beta C_2\phi_s^{\beta-4/3} + \frac{2}{3}B_1\beta C_1\phi_s^{\beta-5/3} + \quad (2.24)$$

$$+ \beta^2(C_1^2 + C_2^2)\phi_s^{2(\beta-1)} + \dots \sim -\frac{1}{2G}\left(\frac{\phi_s^{-2/3}}{A_2} - \frac{C_2}{A_2^2}\phi_s^{\beta-4/3} + \dots\right). \quad (2.25)$$

To leading order, we recover the already known value for  $A_2$ . Since we know  $B_1 \neq 0$  and  $\beta < 1/3$ , then to the next leading order (i.e.  $O(\phi_s^{-4/3})$ ) we find that  $\beta = 0$ . Therefore, we have

$$z_s \sim iA_2 f_s^{2/3} + B_1 f_s^{1/3} + (C_1 + iC_2) + \dots \quad \text{as } \phi_s \rightarrow +\infty. \quad (2.26)$$

Since this next term is just a constant, and noting that we introduced a shift for the  $z$ -variable earlier in the derivation for the behaviour near the downstream singularity, we leave  $C_1$  and  $C_2$  as unknown constants.

Finally, we can deduce that

$$\zeta \sim i(3G)^{1/3}f^{1/3} + \left(1 + \frac{G}{2}\right) + Cf^{-1/3} \quad \text{as } \phi \rightarrow +\infty, \quad (2.27)$$

where  $C$  is an unknown constant. This captures the parabolic nature of the free-falling jet and this expansion will be used to alter the complex velocity ansatz (2.3) when using the series truncation and collocation numerical approach.

It should be noted that only the first term of (2.27) is included in the form for  $\zeta$  taken by Dias



and Tuck [1991]. Before moving on to make use of the new form for  $\zeta$  far downstream, we can investigate the downstream jet of the numerical solutions obtained using the Dias and Tuck [1991] complex velocity ansatz. We can compare the expected value of  $\zeta/f^{1/3}$  far downstream with the value obtained through the numerical solution. We take the example where the Froude number is 1.2. Table 2 contains the complex velocity on the free surfaces far downstream (i.e. as  $\sigma \rightarrow \pi/2$ ), acquired using 400 collocation points but 40 000 plotting points along the free surfaces. In other words, we have extrapolated the numerical results to get closer to the downstream singularity. The coefficient of the  $f^{1/3}$  term of complex velocity expansion (2.27) should be purely imaginary. However, the values calculated here do not find this coefficient to be purely imaginary. A possible reason may be that the values taken are not from sufficiently far downstream. Alternatively, it may be due to the current complex velocity ansatz (2.3) not sufficiently encapsulating the behaviour of the flow far downstream, at least when extrapolating the numerical results further downstream. In the next section, a new form for  $\zeta$  is considered where more terms of the expansion of (2.27) are incorporated.

$\sigma$	$f$	$\zeta$	$\zeta/f^{1/3}$
1.57068	$2.6590 + 0i$	$1.5330 + 0.8934i$	$1.1065 + 0.6449i$
1.57076	$3.0086 + 0i$	$1.5787 + 0.9304i$	$1.0935 + 0.6445i$
1.57084	$3.0086 + 1i$	$1.4818 + 1.0721i$	$1.0808 + 0.6179i$
1.57091	$2.6589 + 1i$	$1.4244 + 1.0411i$	$1.0865 + 0.6095i$

Table 2: Complex velocity as  $\sigma \rightarrow \pi/2$ , for  $F = 2$  and  $c = 0.2$  using the Dias and Tuck [1991] ansatz (2.3).

### 2.3 Improved calculation

The aim here is to find the complex velocity as an analytic function of  $f$  such that it now satisfies:

1.  $\zeta \sim i(3G)^{1/3}f^{1/3} + (1 + G/2) + Cf^{-1/3}$  as  $\phi \rightarrow +\infty$ , where  $C$  is a constant to be found,
2.  $\zeta \sim (1 + ae^{\lambda f})$  as  $\phi \rightarrow -\infty$ , where  $a$  is an unknown constant and  $\lambda$  is the smallest positive root of  $\lambda - G \tan \lambda = 0$ ,
3.  $v = 0$  on  $\psi = 0$ ,  $\phi < 0$ .

It is the first condition above that differs from that utilised in the work of Dias and Tuck [1991] for the behaviour of the flow far downstream: here, the three-term expansion (2.27) of  $\zeta(f)$  for the free-falling jet is adopted.

It can be checked that the following form for  $\zeta$  satisfies those conditions:

$$\zeta(t) = 1 + (1 + t)^{2\lambda/\pi} B(t), \quad (2.28)$$

where

$$B(t) = \left(\frac{3G}{\pi}\right)^{1/3} \left(-\log\left(c(1+t^2)\right)\right)^{1/3} l_1(t) + \frac{G}{2} l_2(t) + \sum_{n=0}^{\infty} a_n t^n \left(-\log\left(c(1+t^2)\right)\right)^{-1/3}, \quad (2.29)$$

and  $l_1$  and  $l_2$  are the following linear functions:

$$l_1(t) = 2^{-\lambda/\pi} \left( \sin\left(\frac{\lambda}{2}\right) + t \cos\left(\frac{\lambda}{2}\right) \right), \quad l_2(t) = 2^{-\lambda/\pi} \left( \cos\left(\frac{\lambda}{2}\right) - t \sin\left(\frac{\lambda}{2}\right) \right). \quad (2.30)$$

The constants  $a_n$ ,  $n = 0, 1, 2, \dots$  are to be found; and  $c$  is a real constant such that  $0 < c < 1/2$ . This constant  $c$  is needed to ensure the complex velocity is real along the horizontal wall, where  $-1 < t < 1$ . The form of (2.28) allows for the upstream condition to be satisfied as  $t \rightarrow -1$ , whilst (2.29) is necessary to incorporate the form of the revised three-term expansion (2.27) for the behaviour of the jet far downstream as  $t \rightarrow i$ . Note that the power series in  $t$  that appears in (2.29) replaces an unknown analytic function of  $t$  that is analytic for  $|t| < 1$  and continuous for

$|t| \leq 1$ . The linear functions  $l_1$  and  $l_2$  of  $t$  are required to enforce the correct coefficients of the three-term expansion as  $t \rightarrow i$ , given the form adopted for  $\zeta$  in (2.28).

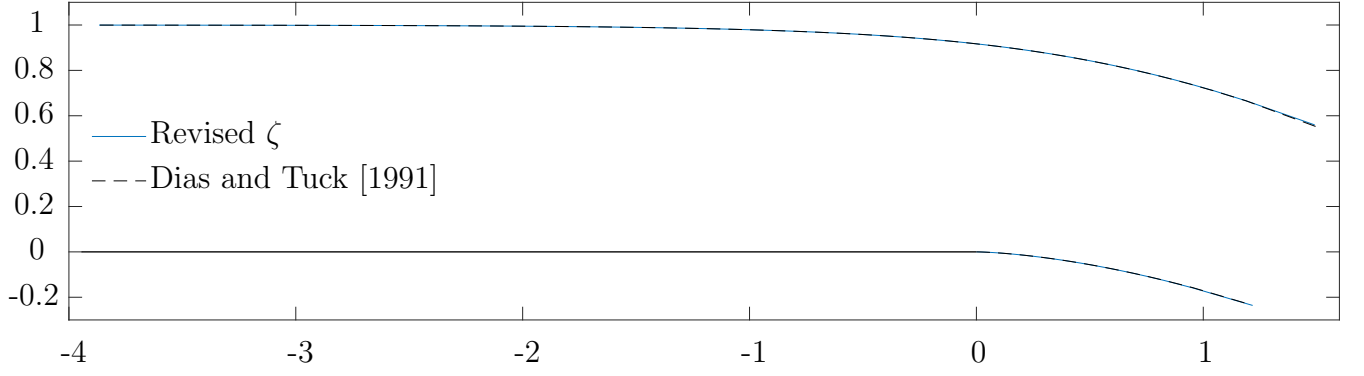
It remains to satisfy Bernoulli's equation on both free surfaces which will, for a given Froude number, enable us to find the unknown coefficients  $a_n$ . We truncate the infinite series in (2.29) after  $N$  terms. For the image of the free surfaces in the  $t$ -plane, we can use  $t = e^{i\sigma}$ , for  $0 < \sigma < \pi$ . We introduce  $N$  mesh points

$$\sigma_I = \frac{\pi}{2N} + \frac{\pi}{N}(I - 1), \quad (2.31)$$

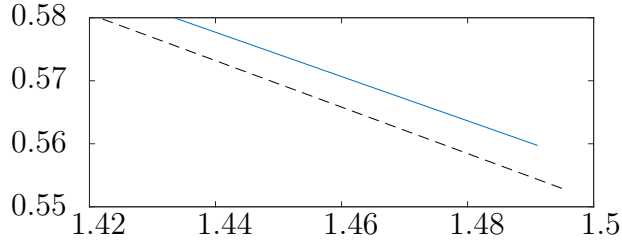
for  $I = 1, \dots, N$  for the collocation method. For the  $N$  mesh points, we obtain  $N$  equations in  $N$  unknowns (the  $N$  unknown coefficients) to be solved numerically by iteration.

The results presented here have been obtained through use of the `fsolve` function of MATLAB in order to solve the system of  $N$  equations. For the numerical integration (with respect to  $\sigma$ ) to each mesh point along the free surfaces to find the  $z$ -coordinates, the `integral` function of MATLAB has been utilised. Figure 42 shows a comparison of the free-surface profiles obtained using the Dias and Tuck [1991] complex velocity and the revised form. The profiles are the same to order  $10^{-3}$  and so are very similar. There is a small difference that can be observed between the two profiles downstream, depicted in figures 42b and 42c.

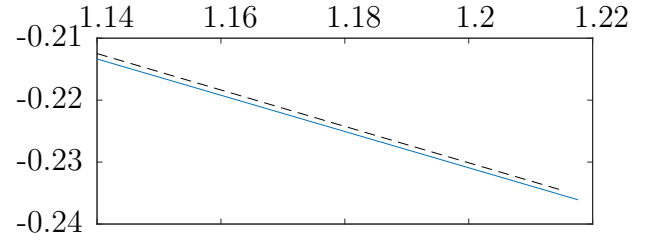
The effect of the altered complex velocity ansatz can better be seen in figure 43. Here, the system has been solved with 400 equations in 400 unknowns, as before, but 40 000 mesh points have been used to plot the free surfaces — hence, the profiles have been extrapolated and we can now see further downstream. In the work of Dias and Tuck [1991], the assumed form for the complex velocity far downstream (i.e.  $\zeta \sim f^{1/3}$ ) means that the flow will approach a jet of constant slope. The new waterfall appears to approach a more parabolic shape, as hoped for. Figure 43 also includes the asymptotic outer solution of Clarke [1965] which agrees well with the free-surface profile obtained via the revised complex velocity form. It is computationally expensive to plot free surfaces far downstream if plotting using the same number of mesh points as used for solving the system. This is due to the logarithmic singularity of the  $t$ -plane mapping (2.2). An increase in the number of equally-spaced mesh points means that we have collocation points closer to the singularity at  $t = i$ , but this leads to only a very small advancement in distance



(a) Free-surface profile.



(b) Upper free surface.



(c) Lower free surface.

Figure 42: Comparison of waterfall free-surface profiles for  $G = 0.25$ ,  $c = 0.2$  and  $N = 400$ .

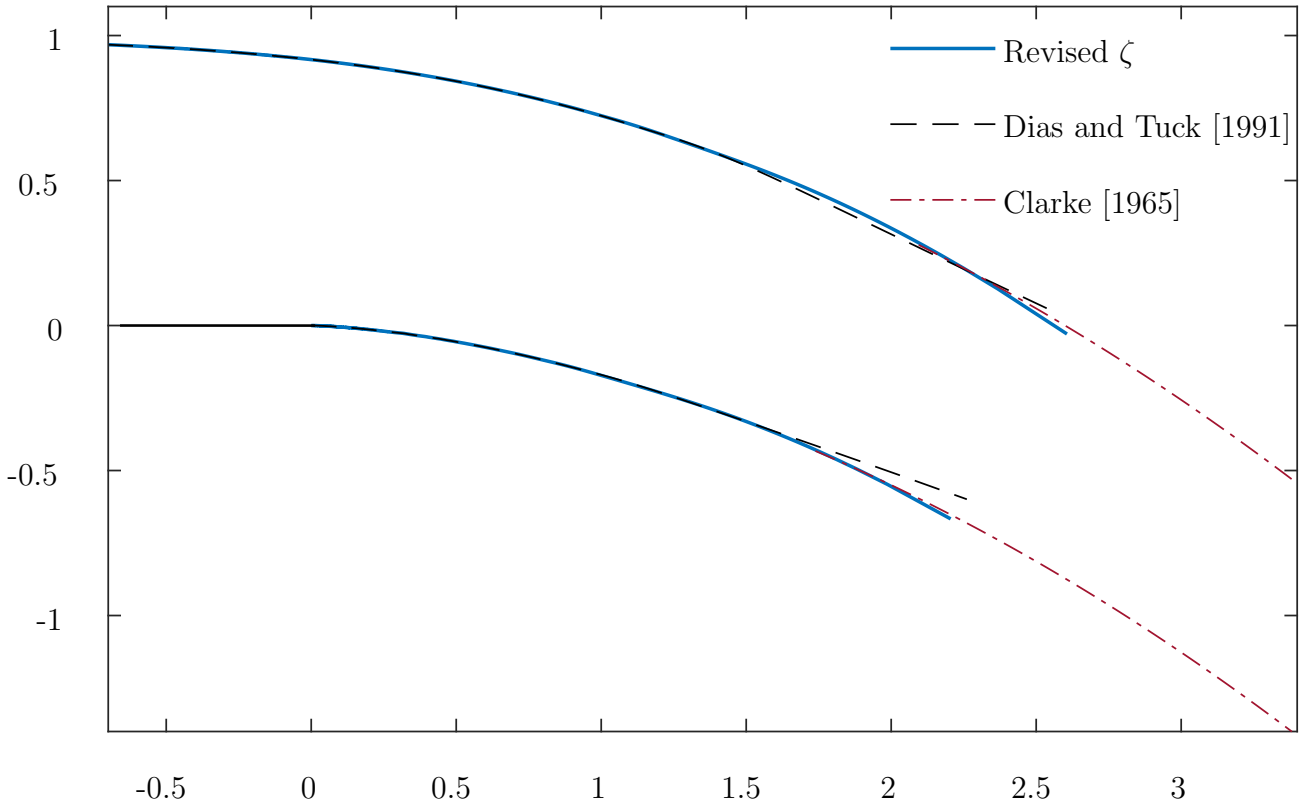


Figure 43: Comparison of extrapolated waterfall free-surface profiles for  $G = 0.25$ ,  $c = 0.2$  and  $N = 400$ . The asymptotic solution of Clarke [1965] has also been included.

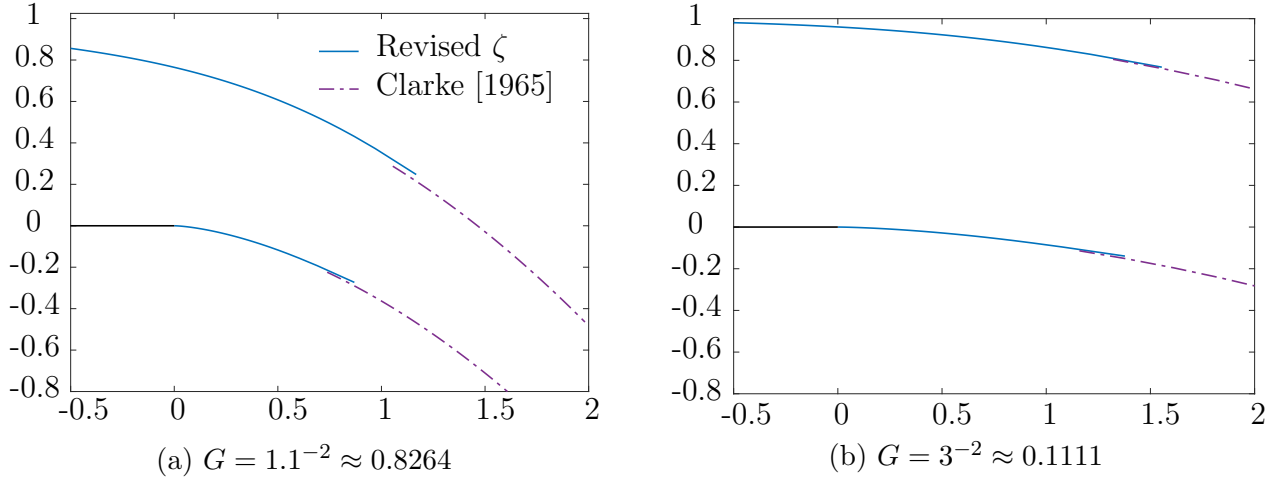


Figure 44: Free-surface profiles with  $N = 400$  and  $c = 0.2$  for revised  $\zeta$  form compared with the outer solution of Clarke [1965].

downstream. This is particularly evident from figure 43 where 40 000 mesh points have been used to plot the free surfaces and yet we only reach  $x \approx 2.6$ , i.e. an extra 39 600 mesh points results in an extra horizontal distance downstream of only around 1.1. Therefore, the improvement in the extrapolated profiles far downstream points to the revised complex velocity ansatz being computationally beneficial.

Figure 44 shows further examples of comparisons with the outer solution of Clarke [1965] for different values of  $G$ . The agreement improves as  $G$  decreases (or as the Froude number increases). This is to be expected since the asymptotic solution works from a perturbation of flow under weak gravity. Therefore, it is more appropriate to utilise the numerical method described here with the revised complex velocity — rather than to utilise the asymptotic solution of Clarke [1965] — for larger values of  $G$  (or smaller Froude numbers) where the gravitational effects are more dominant.

The effect of the value of the constant,  $c$ , can also be investigated. For all values of  $c$  between 0 and 0.5 that have been tested, whilst the value affects the coefficients of the finite series, the free-surface profiles do not depend on  $c$  (up to order  $10^{-4}$ ) and so we obtain equivalent solutions.

We have seen that the inclusion of the extra terms of the expansion for  $\zeta$  in terms of the complex potential  $f$  leads to extrapolated solutions which are more parabolic in nature far downstream (as hoped for) and agree (with some dependence on the Froude number) with the asymptotic solution of Clarke [1965]. Additional numerical investigations can lead to further improvements in the numerical solutions for this waterfall problem, as will be discussed in the following section.

## 2.4 Further numerical investigations

The decay of coefficients from the truncated series can be improved upon. Closer inspection of the resulting velocity (here we take just the horizontal component) highlights an area of concern far downstream. Figures 45 and 46 are plots of the horizontal component  $u$  of the velocity against  $\sigma$  (the argument of a point along the free surface in the  $t$ -plane). Interpolation accentuates the spurious oscillations in the velocity: in figures 45 and 46, the interpolation plot for  $u$  is obtained by evaluating the solution  $\zeta$  at intermediate mesh points. We see that the amplitude of these oscillations increases far downstream along both free surfaces as  $\sigma \rightarrow \pi/2$ . The line of  $u = 1 + G/2$  is also indicated on the plot since this is the value expected (c.f. (2.9)) for  $u_\infty$ . It is apparent that the values of  $u$  along the free surfaces do not reach  $u_\infty$ , but it must be noted that we do not reach very far downstream, even with  $N = 400$ , due to the logarithm involved in the mapping (2.2). Previously, it was discussed that we are able to arrive further downstream by extrapolating the solution (see §2.3), however, here we focus only on the actual solution (i.e. without extrapolation). Overall, the jump discontinuity in  $u$  as  $\sigma \rightarrow \pi/2$  may explain the appearance of the spurious oscillations as the solution attempts to correct for the discontinuity between  $u$  on the two free surfaces far downstream, analogous to the Gibbs phenomenon.

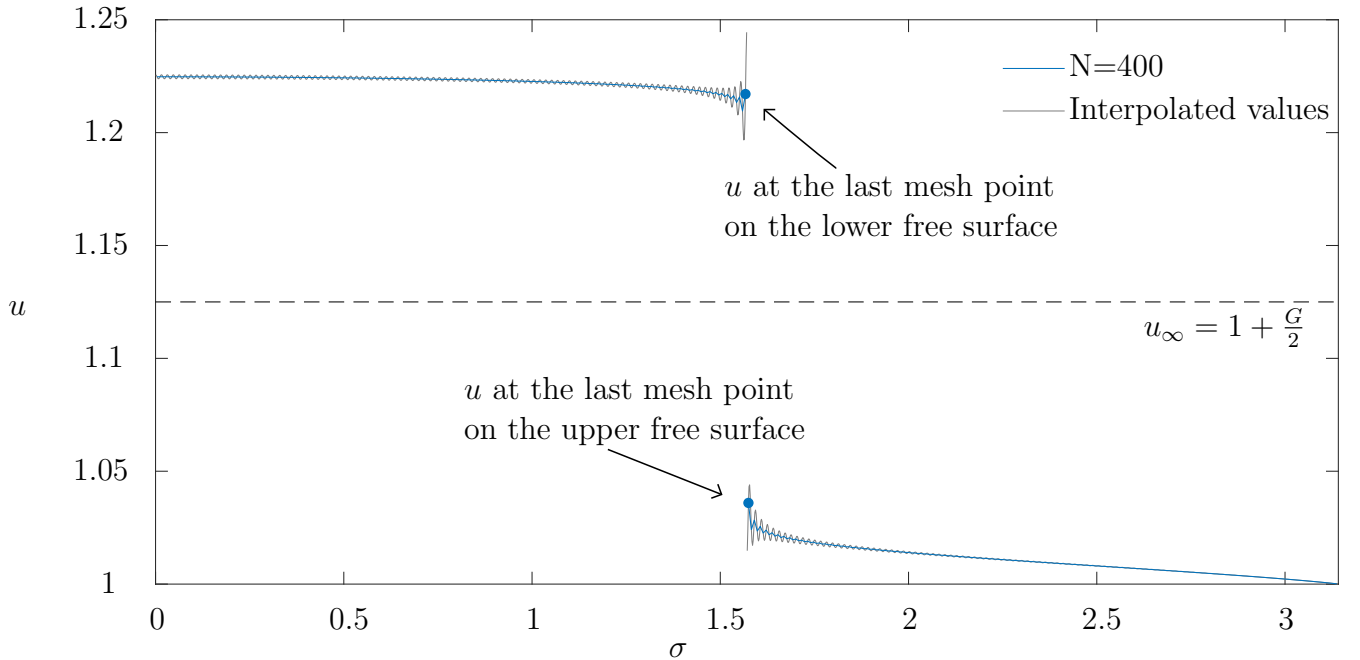


Figure 45: Horizontal component  $u$  of the velocity against  $\sigma$ , for  $G = 0.25$ ,  $N = 400$ . Figure 46 shows the oscillations more clearly.

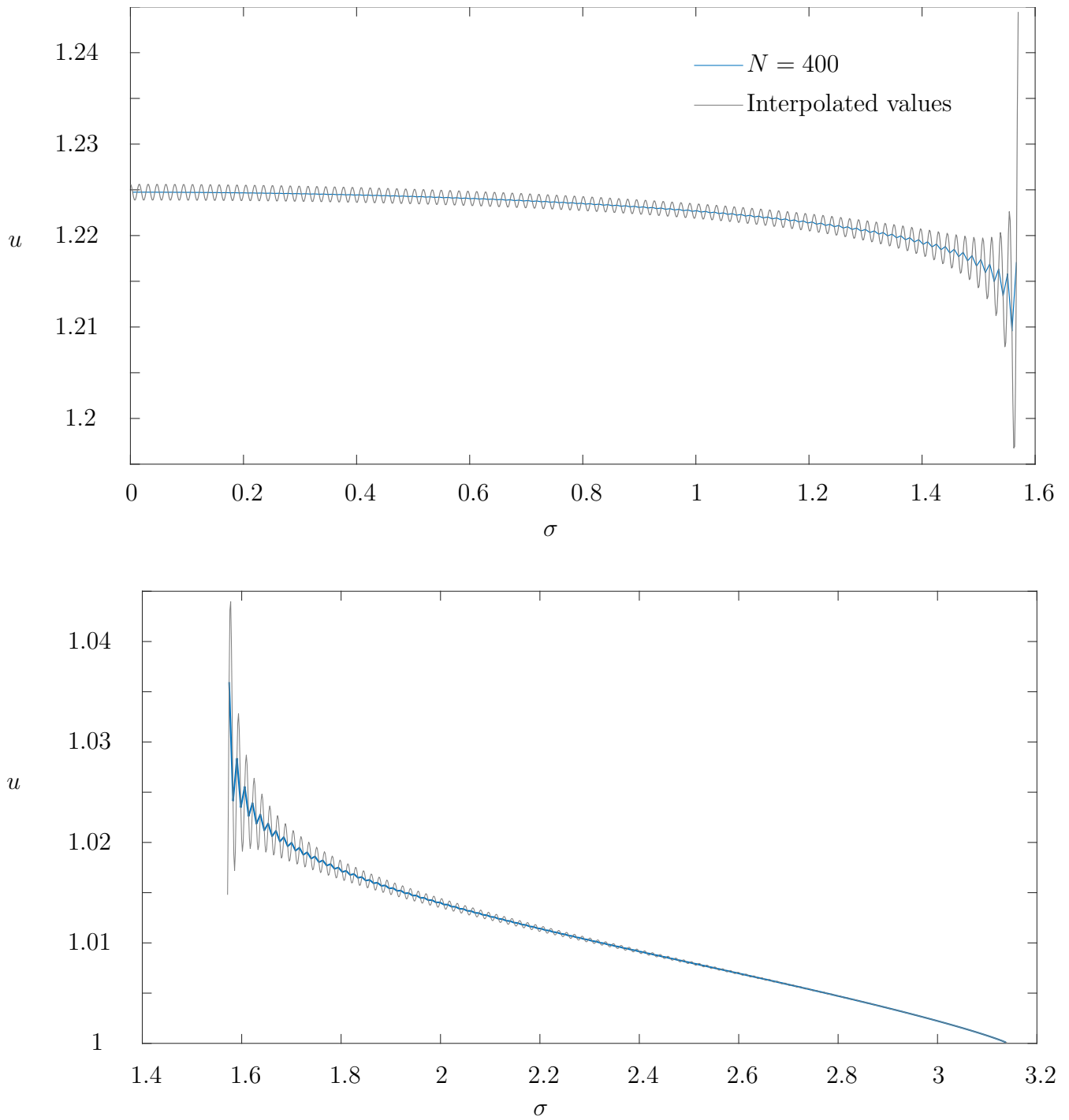


Figure 46: Horizontal component  $u$  of the velocity against  $\sigma$ , for  $G = 0.25$ ,  $N = 400$ . These figures are magnifications of figure 45, allowing for closer examination of the oscillations that arise from evaluating the velocity at intermediate mesh points.

One resolution to this problem is to modify our approach in finding  $y$  at the collocation points (these values are utilised in satisfying the Bernoulli equation). In the results presented so far, the MATLAB `integral` function (performed to an accuracy of order  $10^{-6}$ ) has been used to evaluate

the integral

$$z_I = \int_0^{\sigma_I} \frac{dz}{df} \frac{df}{dt} \frac{dt}{d\sigma} d\sigma, \quad (2.32)$$

where  $\sigma_I$  is a collocation point, in order to obtain the values of  $z$  (and hence  $y$ ) along the free surfaces at the collocation points. Instead, we can utilise the MATLAB `integral` function to find  $y$  at two points either side of a collocation point and then take the average of these values to be the  $y$  value at the collocation point. This leads to a smoothing effect — visible in the plot of figure 47 where we interpolate the newly obtained values for the horizontal velocity  $u$ , for comparison with figure 46 — and it results in improved decay of the coefficients: the first ten coefficients are the same as previously obtained, to order  $10^{-4}$ ; and the last few coefficients have improved from being of order  $10^{-4}$  to being of order  $10^{-6}$ . Note that the correct value for  $u$ , approached (ideally, continuously) from both sides at  $\sigma = \pi/2$ , is given by  $u_\infty$  (c.f. (2.9)).

Further altering the form of the complex velocity  $\zeta$  grants additional improvement to coefficient decay. If, for the  $y$ -values along the upper free surface, we integrate from  $t = -1$  (i.e.  $\sigma = \pi$ ) and set  $y = 1$  at this point, then we force unit depth and velocity of the flow as  $x \rightarrow -\infty$  through several conditions:

1.  $y = 1$  (Limit of integration),
2.  $\zeta(-1) = 1$  (c.f. (2.28)),
3.  $\frac{1}{2}|\zeta(-1)|^2 + G = \frac{1}{2} + G$  (Bernoulli constant).

The first and second points above imply that the volume flux has been normalised to unity, which is implicit in the third point. However, the explicit imposition of all three has an impact on the decay rate of the coefficients  $a_n$  in the numerical method we utilise. We can instead use the following form for the complex velocity:

$$\zeta = A + (1 + t)^{2\lambda/\pi} B(t), \quad (2.33)$$

with the function  $B(t)$  defined as before (c.f. (2.29)-(2.30)) and where  $A$  is an additional unknown for which to solve, but which we expect to converge to unity as more collocation points are used. We



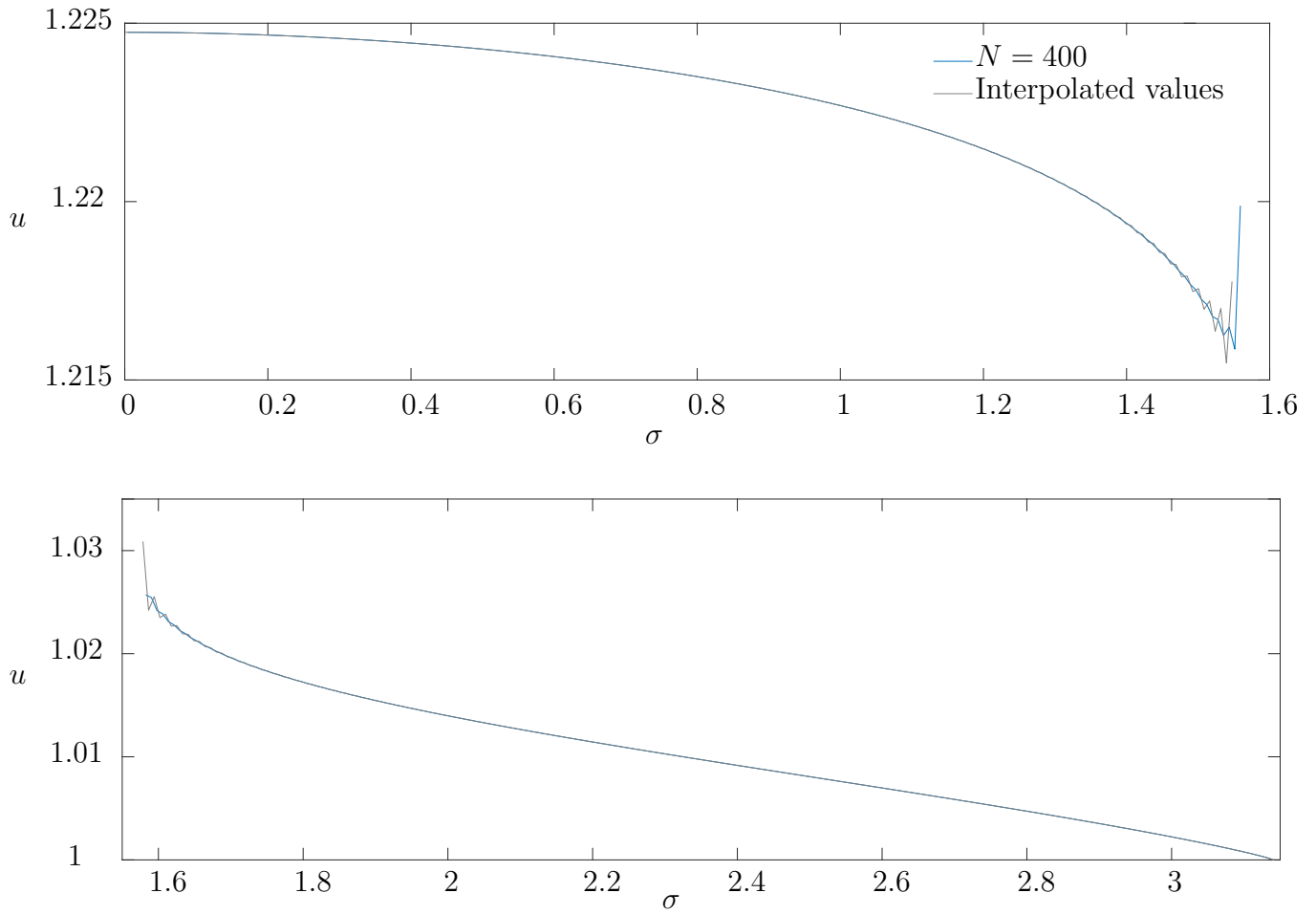


Figure 47: Horizontal component  $u$  of the velocity against  $\sigma$ , for  $G = 0.25$ ,  $N = 400$ . This plot is obtained using the solution obtained via smoothing, i.e. averaging for the  $y$ -values at the mesh points.

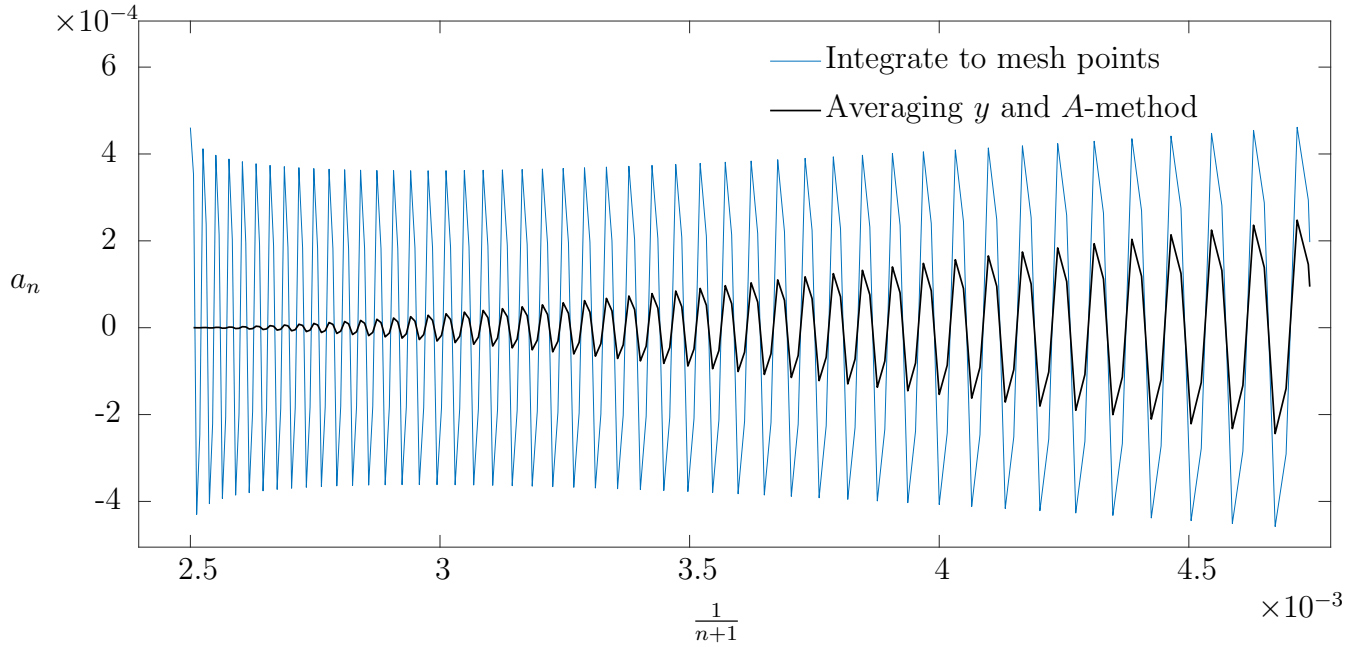


Figure 48: Coefficient decay resulting from integrating to each collocation point directly ( $N = 400$ ) compared with coefficient decay from finding  $y$  by averaging values either side of the collocation point and using  $A$ -method ( $N = 399$ ), for  $G = 0.25$ ,  $c = 0.2$ .

will refer to the employment of this additional unknown in the form for  $\zeta$  as the ‘ $A$ -method’. Figure 48 shows the improved coefficient decay when both averaging  $y$ -values either side of collocation points and employing the  $A$ -method, compared with simply integrating directly to each collocation point. The first few coefficients agree very well, to order  $10^{-4}$ ; the last few coefficients have decayed to be of order  $10^{-7}$ ; and a clearly improved decaying tail is apparent in figure 48. As for the value found for  $A$  as part of the solution, for  $N = 400$  and  $G = 0.25$  we have  $A = 0.999991$ , i.e. very close to 1 as expected.

The  $A$ -method can also be utilised for spillway flows. Here, the form for the complex velocity (as discussed earlier, c.f. (1.35)) is altered to become

$$\zeta(t) = \left( A + (1+t)^{2\lambda} \sum_{n=0}^N a_n t^n \right) (-\log(c(1+t^2)))^{1/3} (-\log(2c))^{-1/3} \left( \frac{1}{4}(t-1)^2 \right)^{\beta/\pi-1}, \quad (2.34)$$

in order to use the  $t$ -plane defined through (2.2). This complex velocity form has the extra unknown constant  $A$  to be found as part of the solution and it results in similar improvement in the decay of the coefficients as can be seen in the case of the waterfall. Note that, unless stated otherwise, the smoothing of the  $y$ -values and the  $A$ -method will be utilised in subsequent supercritical waterfall

and weir problems with unit horizontal velocity far upstream.

Before moving on to study the applications of the numerical method improvements presented in this section, it is worth noting some other relevant numerical investigations. In what has been presented so far on this improved calculation of the waterfall flow, the coefficients of (2.29) are fixed to be the known values as determined from the expansion (2.27) for the complex velocity in terms of  $f$  for the jet far downstream. Now, we may consider leaving these coefficients unknown to be found as part of the solution. This means taking the revised complex velocity ansatz (2.28)-(2.30) but instead writing (2.29) as

$$B(t) = a \left( -\log \left( c(1+t^2) \right) \right)^{1/3} l_1(t) + b l_2(t) + \sum_{n=0}^{\infty} a_n t^n \left( -\log \left( c(1+t^2) \right) \right)^{-1/3}, \quad (2.35)$$

leaving  $a$  and  $b$  to be found. In order to leave these unknown, we can keep the number of unknown coefficients of the truncated power series in  $t$  the same, but increase the number of mesh points by two. Therefore, we are still able to solve a square system of equations, numerically by iteration.

When we set  $a$  and  $b$  fixed to be the predetermined values, we obtain the expected parabolic shape of the jet (including when extrapolating the solution) since we then impose the downstream asymptote as in (2.27). Taking the case of a Froude number of 2, if we concern ourselves with just one coefficient of the power series in  $t$ , we can see from figure 49 that the value of  $a_3$  appears converge to some value at  $N \rightarrow +\infty$ . We also have good coefficient decay, as discussed earlier (c.f. figure 48).

If, instead, we leave  $a$  and  $b$  to be found as part of the solution, then we obtain improved coefficient decay as shown in figure 50: in particular, the last few coefficients are of order  $10^{-9}$  and this plot can be compared with the black line of figure 48 where  $a$  and  $b$  are fixed. However, the convergence of individual coefficients appears to be inferior compared to when the values of  $a$  and  $b$  are fixed — figure 51a is a plot of the coefficient  $a_3$  against  $1/N$  to support this. Furthermore, figures 51b and 51c show the plots of the values obtained for  $a$  and  $b$  against  $1/N$ . Here, we see that the values found for these constants do not appear to approach the expected values, i.e.  $a = (3G/\pi)^{1/3}$  and  $b = G/2$ . Whilst the coefficient decay is better when  $a$  and  $b$  are unknown, the convergence of  $a$ ,  $b$  and the individual coefficients of the truncated series is not so good. Note that

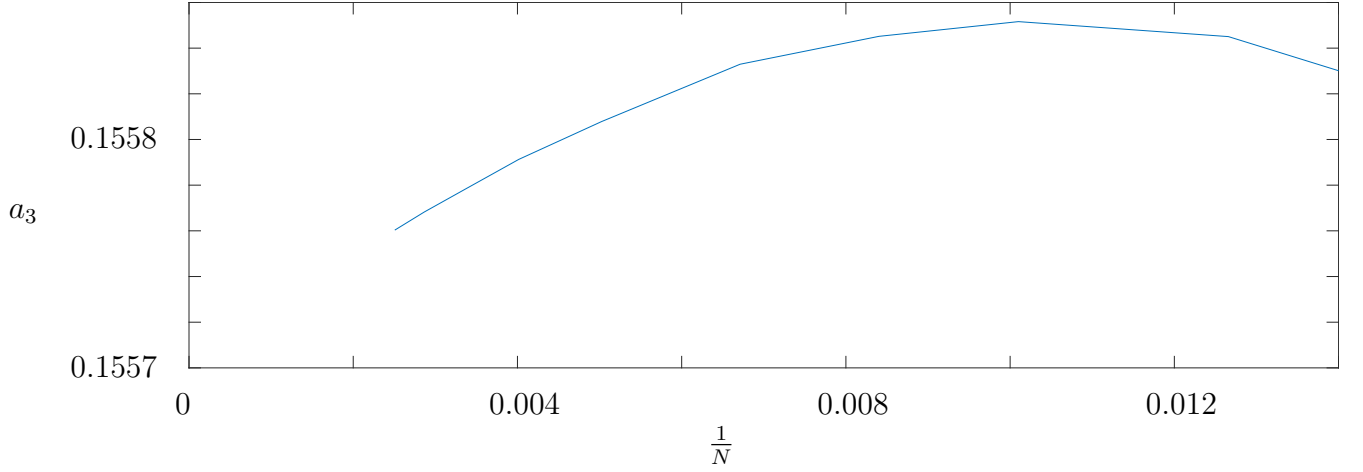


Figure 49: Plot of the coefficient  $a_3$  against  $1/N$  when  $a$  and  $b$  are fixed. Note that  $F = 2$  and  $c = 0.2$ .

part of the judgment of the efficacy of the method is based on the independence of the coefficients from  $N$ , i.e. the independence of the numerical solution from the truncation of the power series. These results support the method of fixing the values of  $a$  and  $b$  to their predetermined values. Note also that our discussion has frequently concerned the extrapolated solutions further downstream: if we leave  $a$  and  $b$  unknown and their values obtained are not as in the expansion (2.27) for  $\zeta(f)$ , then we cannot expect the jet of the extrapolated profiles to be correct. It should also be noted that, as  $N$  increases (with  $a$  and  $b$  unknown), obtaining a converged solution becomes more difficult: the initial guess has to be chosen carefully, e.g. from a converged solution for a smaller (but close) value of  $N$ .

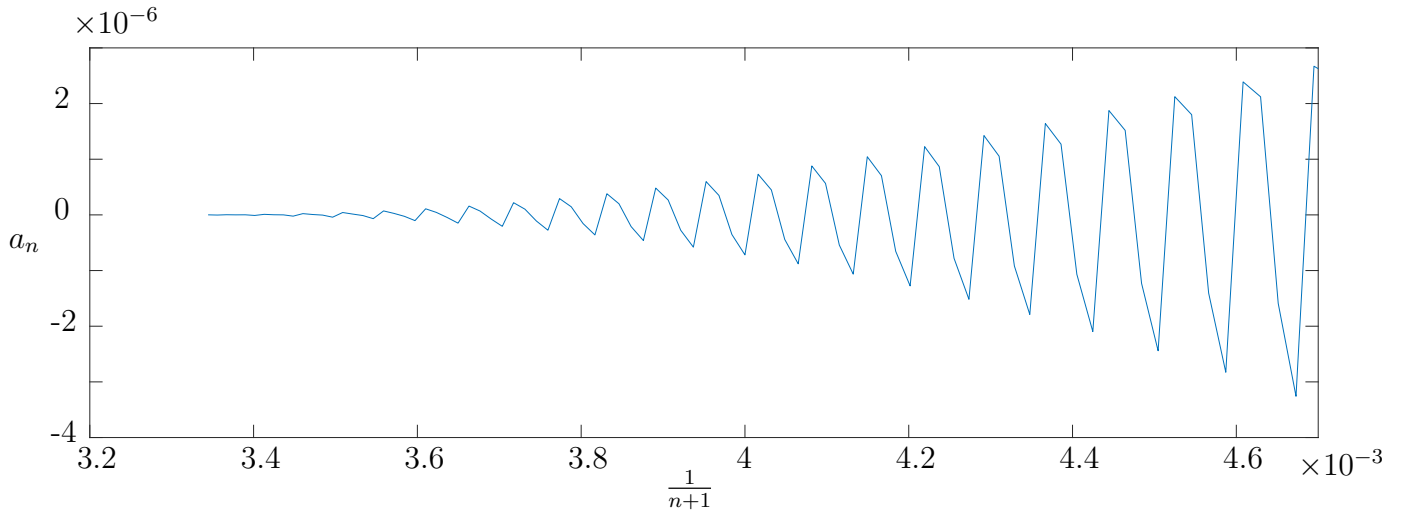
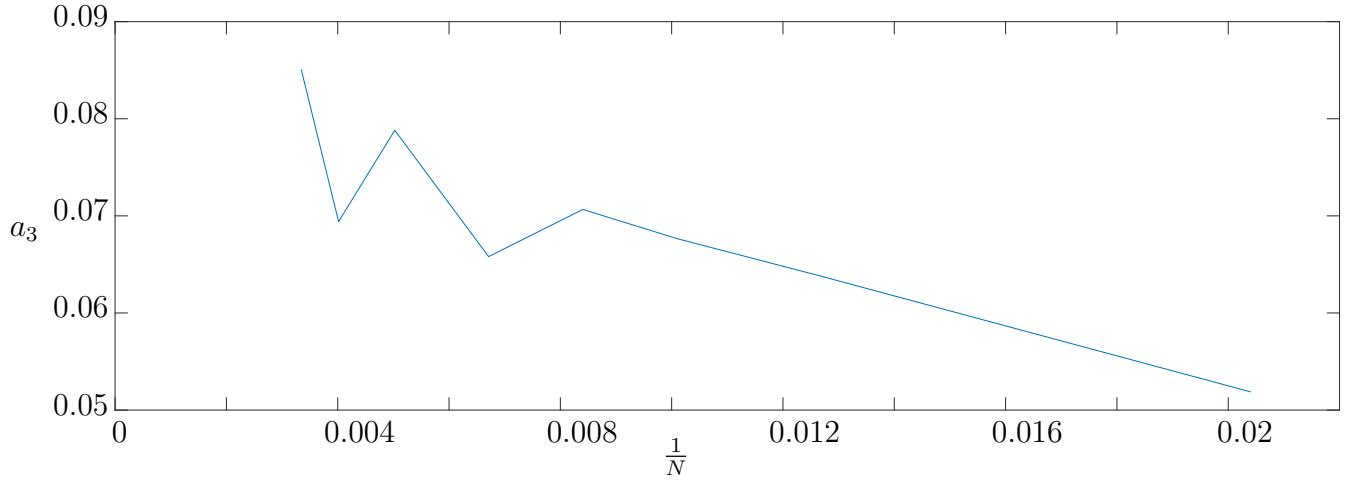
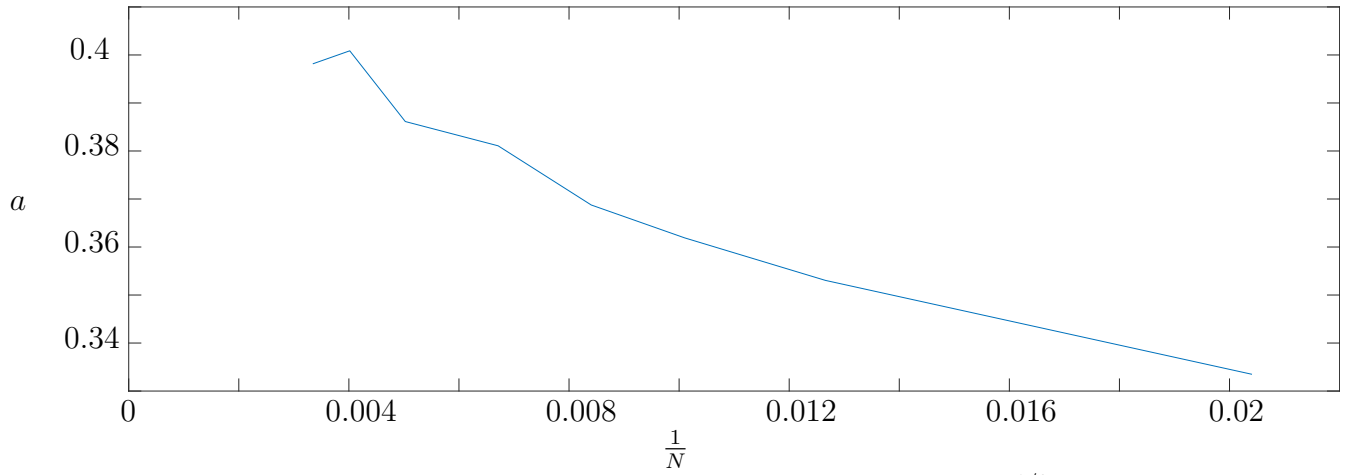


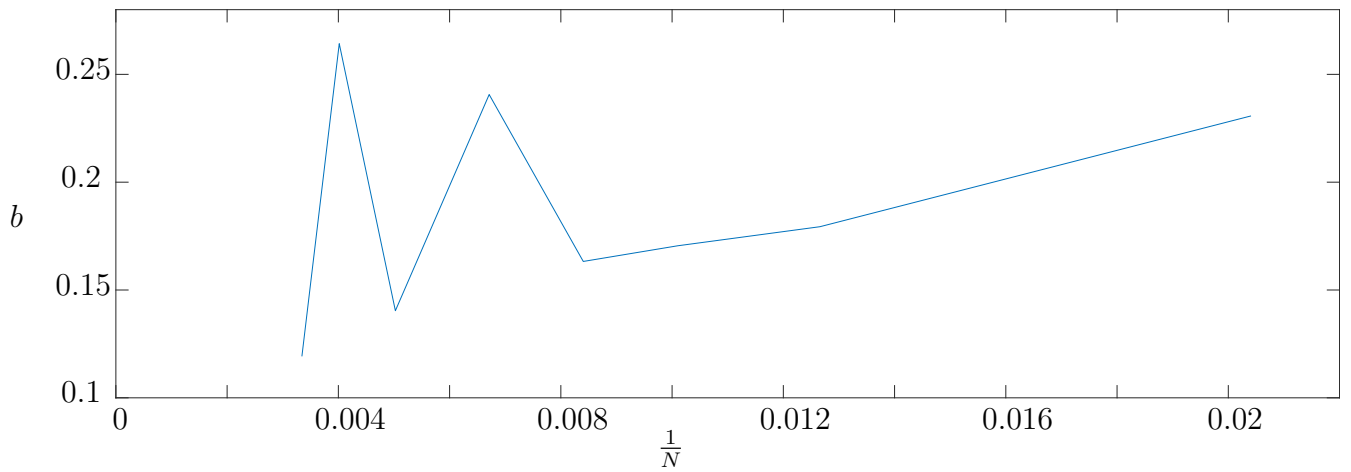
Figure 50: Coefficient decay for  $n = 212 \dots, 299$ , where  $F = 2$  and  $c = 0.2$ . Here,  $a$  and  $b$  have been left unknown to be found as part of the solution.



(a) Convergence of coefficient  $a_3$



(b) Convergence of  $a$ . Note that the expected value is  $a = (3G/\pi)^{1/3} = 0.6204$ .



(c) Convergence of  $b$ . Note that the expected value is  $b = G/2 = 0.1250$ .

Figure 51: Plots relating to the numerical investigations when  $a$  and  $b$  are left unknown. Note that  $F = 2$  and  $c = 0.2$ .

A similar story can be observed if we instead fix one and leave the other to be found. In particular, in the case of fixing  $a$  and leaving  $b$  to found, the coefficient decay is not even so good and the (pre-extrapolated) free-surface profiles are problematic downstream. Overall, given that we can (in the case of the waterfall) determine the values of  $a$  and  $b$ , these known values should be utilised in the complex velocity ansatz.

---

In this chapter, we have focused on the behaviour of the jet singularity far downstream in the case of waterfall flow. We have retained the use of the numerical approach of series truncation and collocation, as utilised by Dias and Tuck [1991] to solve this potential flow problem. Improvements to the method have been presented: a three-term expansion for  $\zeta(f)$  of the jet singularity has been derived and this has been incorporated into a revised form for the complex velocity ansatz; smoothing the  $y$ -values at the collocation points has been utilised; and the ‘ $A$ -method’ has been introduced which involves adding an extra unknown to the system by replacing the known upstream unit velocity in the complex velocity ansatz with the unknown constant  $A$ . The adjustment to the form of the ansatz due to the three-term expansion around the jet singularity leads to improved extrapolated free-surface profiles that capture the parabolic nature of the free-falling jet and the profiles agree well with asymptotic solutions. Smoothing the  $y$ -values and utilising the  $A$ -method results in improved numerical solutions which is apparent due to the superior coefficient decay. We now move on to apply the numerical method improvements (i.e. the three-term expansion for the jet singularity; smoothing the  $y$ -values at the collocation points; and the  $A$ -method) to other flows that involve a free-falling jet downstream.

### 3 Application of three-term jet singularity

The numerical improvements presented in the previous chapter on waterfall flow can be applied to other similar cases. We will first consider supercritical and subcritical weir flows. The formulation is very similar to that of the waterfall, but weir flow includes a vertical wall that must be navigated before the free-falling jet downstream. This leads to there being an unknown contribution to the conserved horizontal momentum flux due to the pressure force along the vertical wall and this must be calculated in order to apply the revised form for the behaviour of the jet singularity downstream. Following this, flows will be considered where there is a disturbance upstream, such as a triangular obstacle or a stepped wall, before falling over the edge of a horizontal plate as a waterfall.

#### 3.1 Finite-depth, supercritical weir flows

For weir flows, as depicted in figure 52a, we can employ the revision to the complex velocity  $\zeta$  that incorporates the improved form for the behaviour of the jet far downstream. This work on applying the improvements to supercritical weir flow has been previously published [McLean et al., 2022]. The variables are non-dimensionalised, resulting in unit depth and velocity far upstream as earlier in the waterfall case. We retain (2.2) to relate  $f$  and  $t$ ; and the complex planes (c.f. figure 52b and 52c) are very similar to those used for the waterfall.

Dias and Tuck [1991] present supercritical solutions for this weir problem, utilising the same expansion for the assumed behaviour of the jet far downstream as in their waterfall calculations (i.e.  $\zeta \sim f^{1/3}$  as  $\phi \rightarrow +\infty$ ). As seen earlier, for the jet we take

$$\zeta \sim i(3G)^{1/3}f^{1/3} + u_\infty + Cf^{-1/3} \text{ as } \phi \rightarrow +\infty, \quad (3.1)$$

where  $u_\infty$  and  $C$  are unknown constants. It is important to note that the constant term  $u_\infty$  in this expression is unknown here (in contrast to the waterfall case, where it is known to be  $1 + G/2$ ). This is due to the unknown contribution (or rather, reduction) to the horizontal momentum flux provided by the vertical weir wall. It can be checked that the following form for  $\zeta$  satisfies the





Also,  $t_O$  denotes the point in the  $t$ -plane corresponding to the origin in the  $z$ -plane. Of (3.3) and (3.5), the constants  $u_\infty$  and  $a_n$ ,  $n = 0, 1, 2, \dots$  are to be found. The solution (3.2)–(3.5) is formed similarly to the solution for the waterfall of the previous chapter. Here, the difference for the weir is the need to satisfy the condition of flow inside the corner at the origin of the  $z$ -plane.

The constant  $u_\infty$  can be found by adding an extra equation to the system. This constraint is derived similarly to (2.9), taking care to include the pressure force due to the vertical portion of the wall in the horizontal momentum balance. Then, the extra equation to be satisfied is

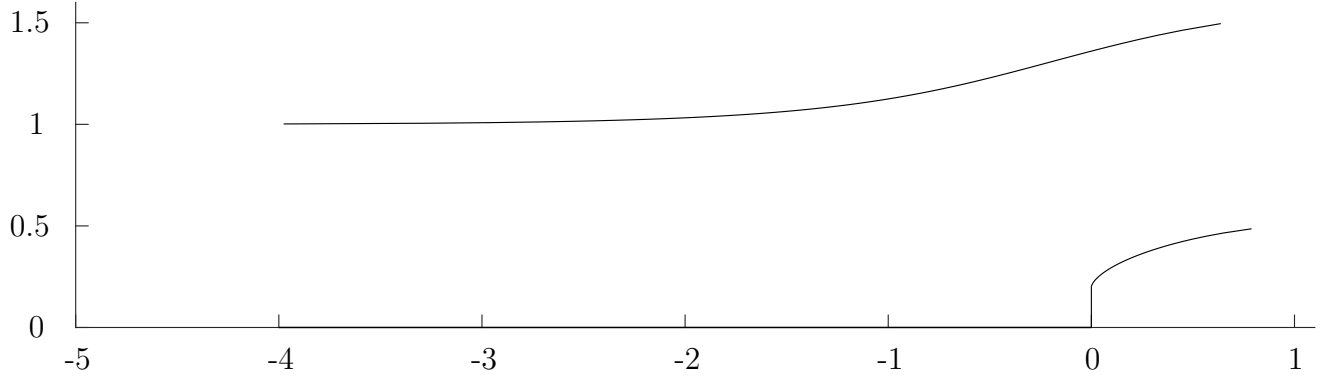
$$u_\infty = 1 + \frac{G}{2} - \int_0^w p \Big|_{\psi=0} ds, \quad (3.6)$$

with  $s$  being the displacement from the origin along the vertical wall and  $w$  denoting the length of the vertical weir wall. The pressure  $p$  along this wall can be found via

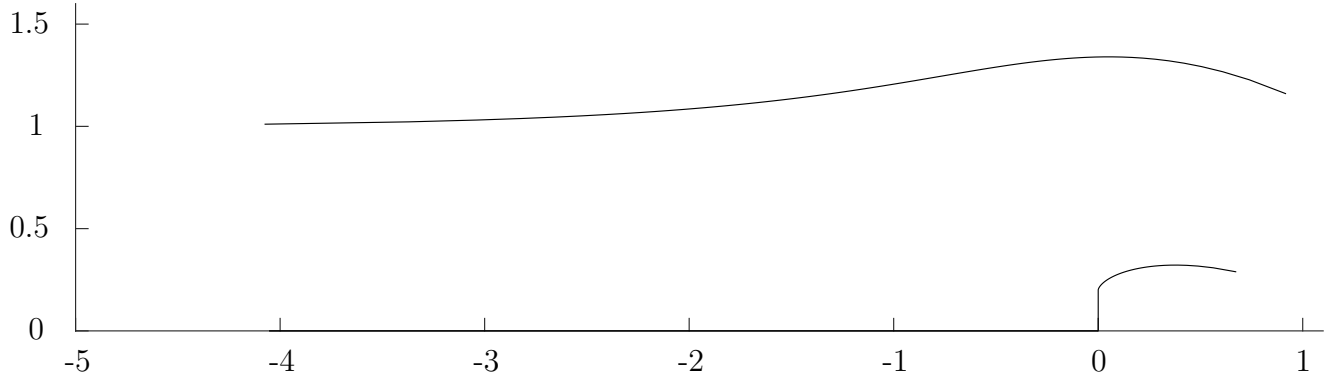
$$p = \frac{1}{2}(1 - |\zeta|^2) + G(1 - y). \quad (3.7)$$

As before, we truncate the series in the complex velocity  $\zeta$  after  $N$  terms. We impose the height,  $w$ , of the vertical weir wall and so leave  $t_O$  as an unknown to be found as part of the solution. We also wish to find  $u_\infty$  — overall we have  $N + 2$  unknowns to find. Satisfying the Bernoulli condition along the free surfaces at  $N$  collocation points, along with imposing the height of the vertical weir and the condition (3.6) on  $u_\infty$ , results in  $N + 2$  equations in  $N + 2$  unknowns. The  $A$ -method (introduced in the previous chapter) can also be employed here to improve coefficient decay.

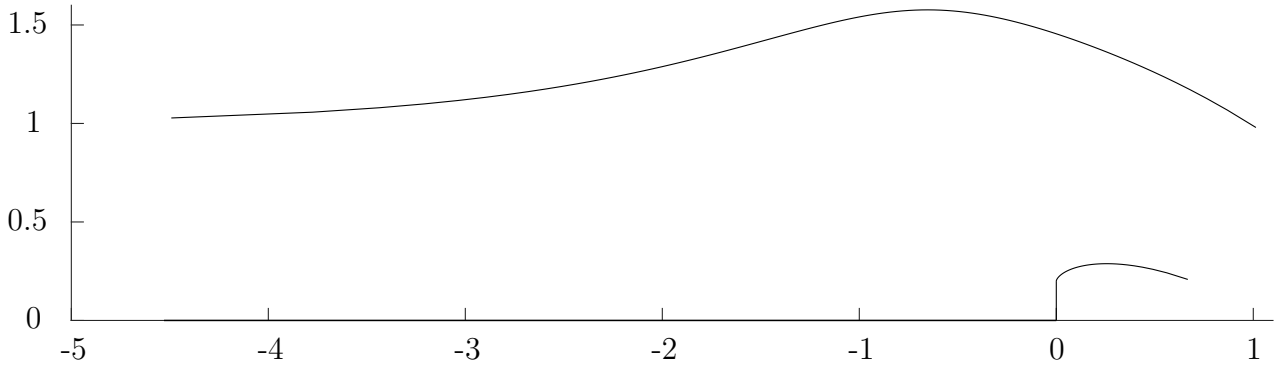
Application of the revised form for the complex velocity leads to free-surface profiles that are very similar to those obtained by Dias and Tuck [1991] for supercritical weir flows. Figure 53 shows profiles obtained for a weir wall height of  $w = 0.2$  with various values taken for  $G$ . Note here that for  $G = 0.64$  we have two supercritical solutions. This agrees with the findings of Dias and Tuck [1991]: for sufficiently large values of  $w$  and for Froude numbers sufficiently close to 1, we obtain two solutions — a waterfall-type solution (c.f. figures 53a and 53b) and a solitary-wave-type solution (c.f. figure 53c). The difference between these two solution types is characterised by the ‘bump’ in the free surface for the solitary-wave-type. In particular, the latter solution type heads



(a)  $G = 0.25$ ,  $y^* = 1.25$ . An example of a waterfall-type solution.



(b)  $G = 0.64$  (or  $F = 1.25$ ),  $y^* = 1.32$ . An example of a waterfall-type solution.



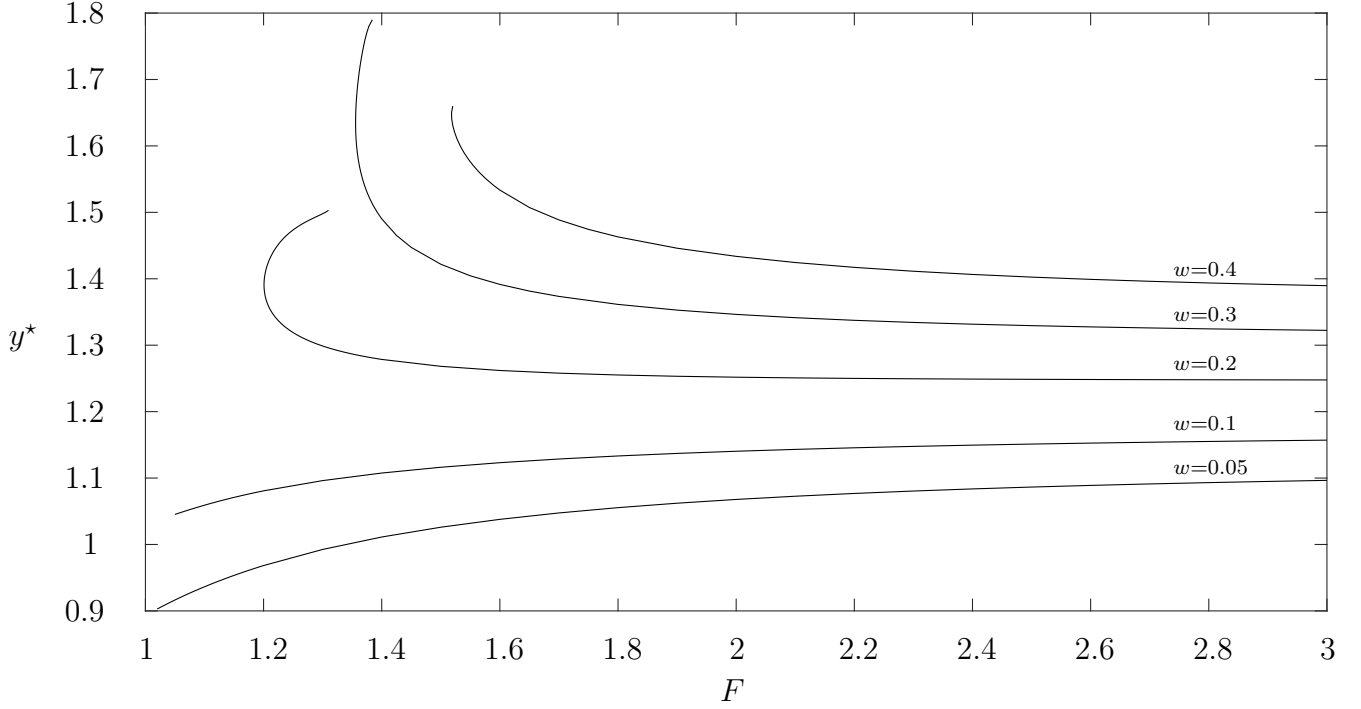
(c)  $G = 0.64$  (or  $F = 1.25$ ),  $y^* = 1.47$ . An example of a solitary-wave-type solution.

Figure 53: Free-surface profiles for  $w = 0.2$ ,  $N = 200$ ,  $c = 0.2$ .

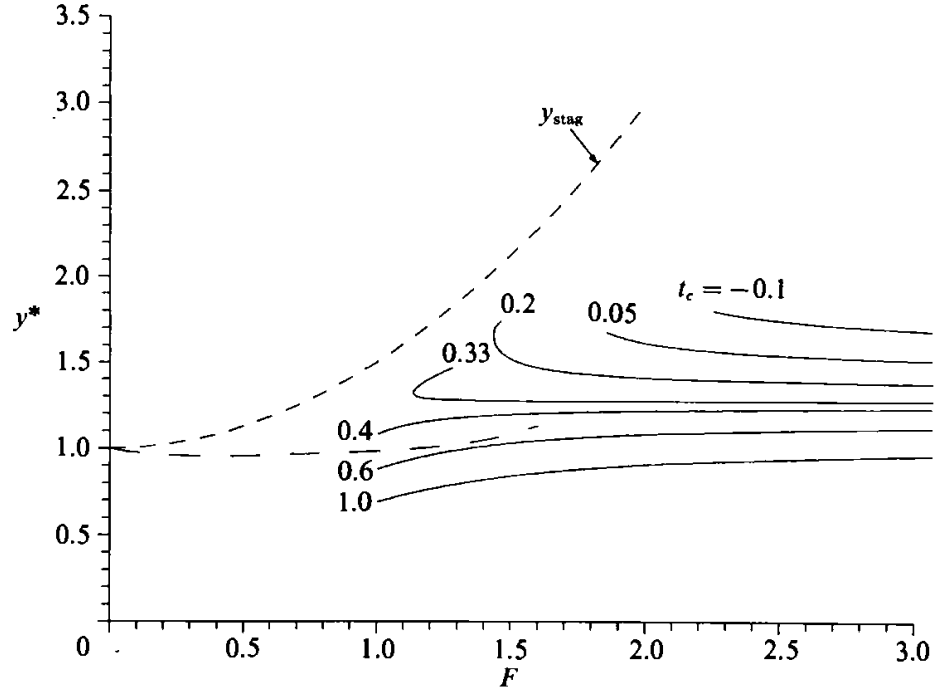
toward a limiting configuration where there is a stagnation point (with difficulty in obtaining such solutions due to the unknown location of the stagnation point), which is conjectured and discussed by Dias and Tuck [1991]. Figure 54a shows many solutions by focusing on the values obtained for  $y^*$  (value of  $y$  corresponding to the point  $\psi = 1$  and  $\phi = 0$ ) plotted against the Froude number, for different choices of the physical weir wall height  $w$ . This may be compared with figure 9 of Dias and Tuck [1991] (shown here in figure 54b) which shows similar curves but instead for different choices of  $t_O$ , marking the position of the corner of the weir in the  $t$ -plane. As  $t_O$  increases towards 1, the weir height decreases to zero. A qualitative comparison of the curves shows similar features.

From figure 54a it can also be observed that, for sufficiently tall weir walls (e.g.  $w = 0.2$ ), there is a maximum value for  $G$  above which (or a minimum value for  $F$  below which) a solution cannot be obtained. These maximum values of  $G$  correspond to maximum values of the unknown constant  $u_\infty$  for the same wall height (c.f. figure 55). It is interesting to note that, for a particular value of  $G$  for which there exist two supercritical solutions (e.g. figures 53b and 53c), the values obtained for the unknown constant  $u_\infty$  are very similar despite resulting in very different free-surface profiles: one of waterfall-type and the other of solitary-wave-type. This is due to the global nature of the constant  $u_\infty$  for the flow. The value of  $u_\infty$  is dominated by  $1 + G/2$  and the contribution from the pressure force along the vertical weir wall is comparatively small.

More generally, figure 55 shows the increase in  $u_\infty$  as the wall height  $w$  decreases, whilst  $u_\infty$  always remains less than  $1 + G/2$  (the value of  $u_\infty$  for the waterfall), as expected. It should be noted that the value of  $u_\infty$  appears to converge as  $N$  increases — see table 3 for the case where  $G = 0.25$ ,  $w = 0.2$  and  $c = 0.2$ . For each wall height, the value of  $u_\infty$  also increases as  $G$  increases, until a maximum value of  $u_\infty$  (as mentioned above) is reached. In the absence of gravity, an exact solution can be found (c.f. equations 17 and 18 of Dias and Tuck [1991]) and then we can integrate the pressure  $p = \frac{1}{2}(1 - |\zeta|^2)$  along the vertical weir wall in order to obtain  $u_\infty$ , the (finite) value of the horizontal velocity far downstream. Whilst the constant  $u_\infty$  is not involved in the complex velocity form in the case of zero-gravity, this physical quantity is still relevant and allows us to compare the results obtained through the exact and numerical solutions as  $G \rightarrow 0$ . The lines on figure 55 have been extrapolated to  $G = 0$  to facilitate this comparison and table 4 gives the values



(a)  $N = 99$  ( $A$ -method has been applied) and  $c = 0.2$ . Plots of curves for various values of wall height  $w$ .



(b) Figure 9 of Dias and Tuck [1991], where instead curves are for fixed values of  $t_O$  (denoted by  $t_c$  in their study). Additional lines on this plot are: maximum elevation that the free surface can reach (short dashes); and the family of subcritical solutions (long dashes). Note the subcritical case will be discussed in §3.2. Reproduced with permission, © 1991 Cambridge University Press.

Figure 54:  $y^*$  (value of  $y$  at point corresponding to  $\psi = 1$  and  $\phi = 0$ ) against  $F$ . Here, we plot trends with the Froude number  $F$  for comparison with figure 9 of Dias and Tuck [1991].

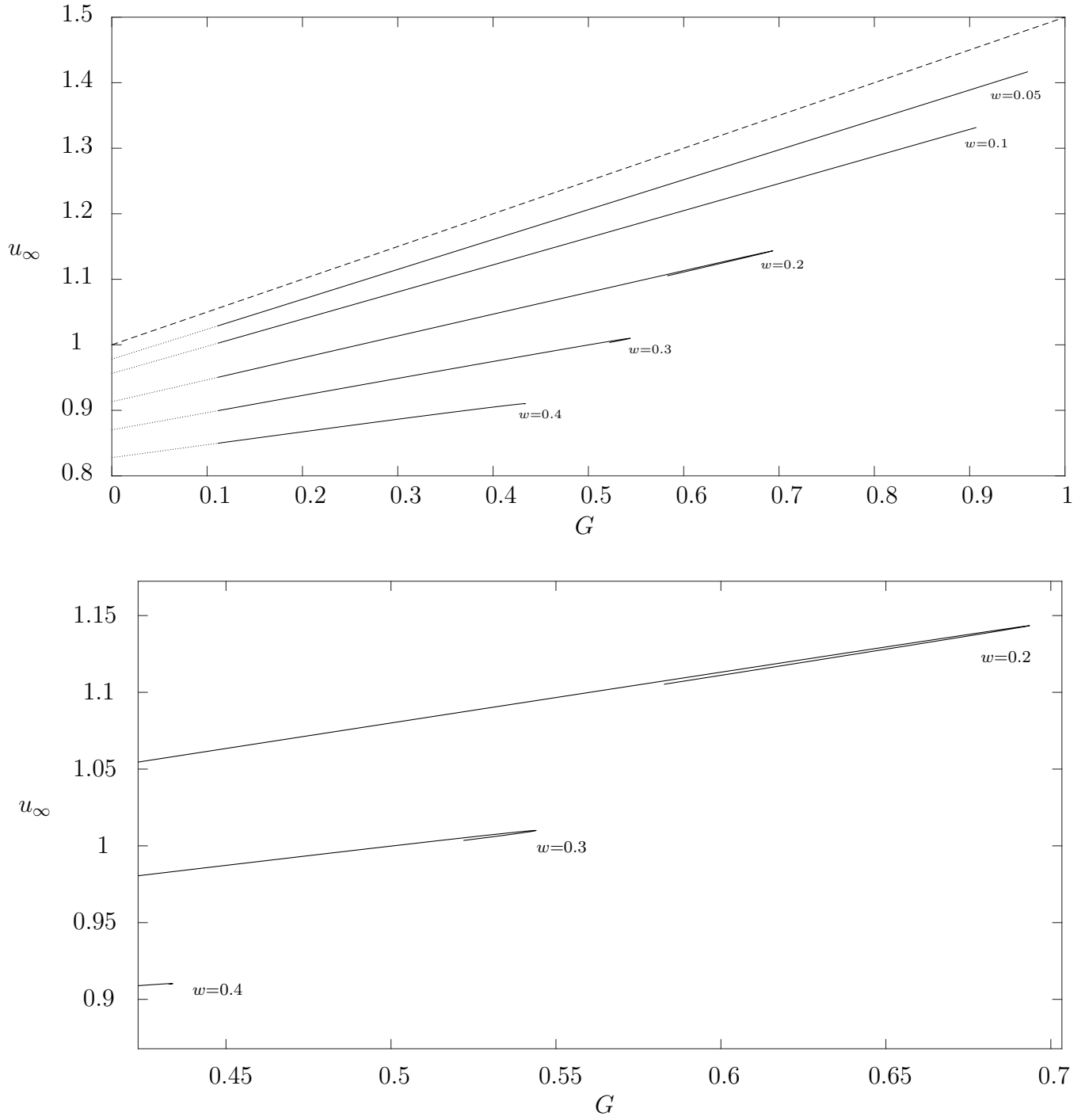


Figure 55: A plot of  $u_\infty$  against  $G$  with  $N = 99$  ( $A$ -method has been applied) and  $c = 0.2$  for various wall heights. The dashed line is  $1 + G/2$  (the value of  $u_\infty$  for the waterfall, i.e. when  $w = 0$ ).

$N$	$u_\infty$
50	0.996750
100	0.996764
200	0.996768
300	0.996769
400	0.996770

Table 3: Values obtained for  $u_\infty$  for various values of  $N$  where  $G = 0.25$ ,  $w = 0.2$  and  $c = 0.2$ .

$w$	$u_\infty$ (exact)	$u_\infty$ (numerical)
0.4	0.827747	0.827845
0.3	0.870165	0.870228
0.2	0.913041	0.913076
0.1	0.956336	0.956350
0.05	0.978129	0.978134

Table 4: Comparison of values obtained for  $u_\infty$  when  $G = 0$  via the exact solution and numerical solution.

of  $u_\infty$  obtained through the exact solution — the values agree to order  $10^{-3}$ . Also, note that as  $G \rightarrow 0$ , then  $u_\infty \rightarrow 1 - \int_0^w p \Big|_{\psi=0} ds$ . Hence, it is as expected that the values of  $u_\infty$  presented in table 4 approach 1 as the weir wall height  $w$  decreases to zero.

The effect of the revised form for the complex velocity  $\zeta$  can be seen in the free-surface profiles of figure 56. This figure compares the profiles obtained through the Dias and Tuck [1991] form for  $\zeta$  with the profiles obtained through use of the revised  $\zeta$  form (along with use of the  $A$ -method). Also, note that both are extrapolated free-surface profiles and the revised form leads to a jet that appears to approach a more parabolic shape. It is surely expected for the free-surface profiles to differ more considerably after the points on the free surfaces that correspond to the last two collocation points downstream (these points are marked on figure 56). This is since the Bernoulli condition is not imposed on the mesh points used in extrapolating the profiles and so the form taken for  $\zeta$  will have greater influence. However, it may not be so expected for the free-surface profiles to be so very similar up to the last collocation points downstream, as can be seen in figure 56. This can be explained since the Bernoulli condition is explicitly imposed up to these last points downstream which is a local condition, whereas the difference in the assumed form for  $\zeta$  due to the inclusion of more terms in the downstream singularity expansion has a more global effect (but

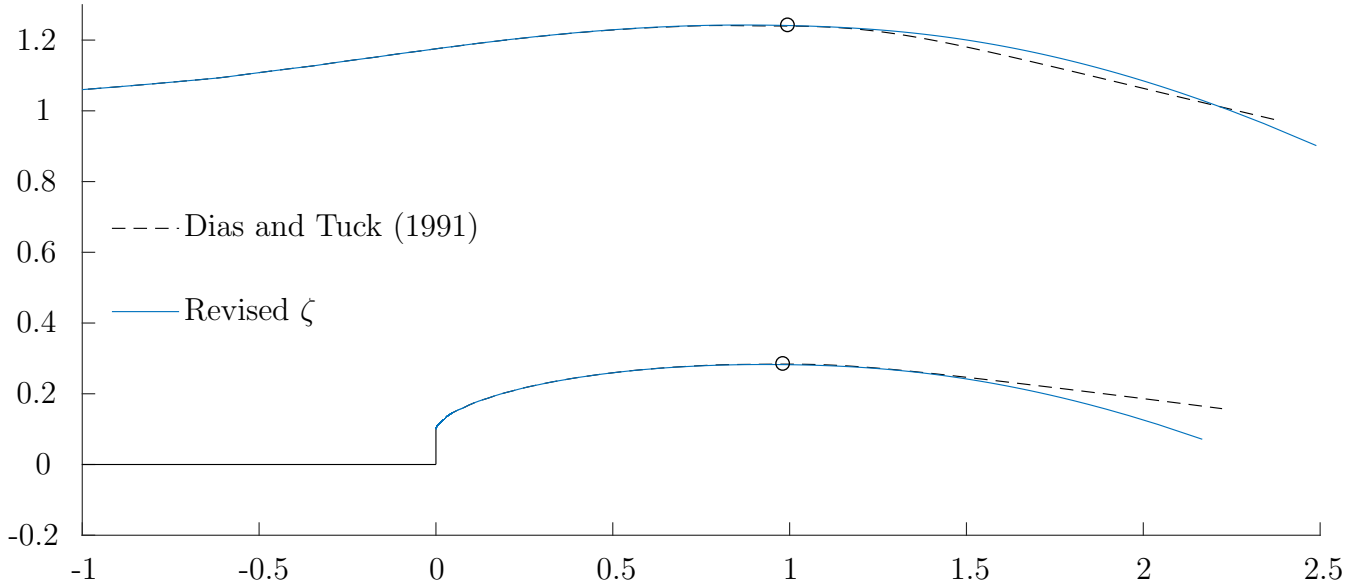
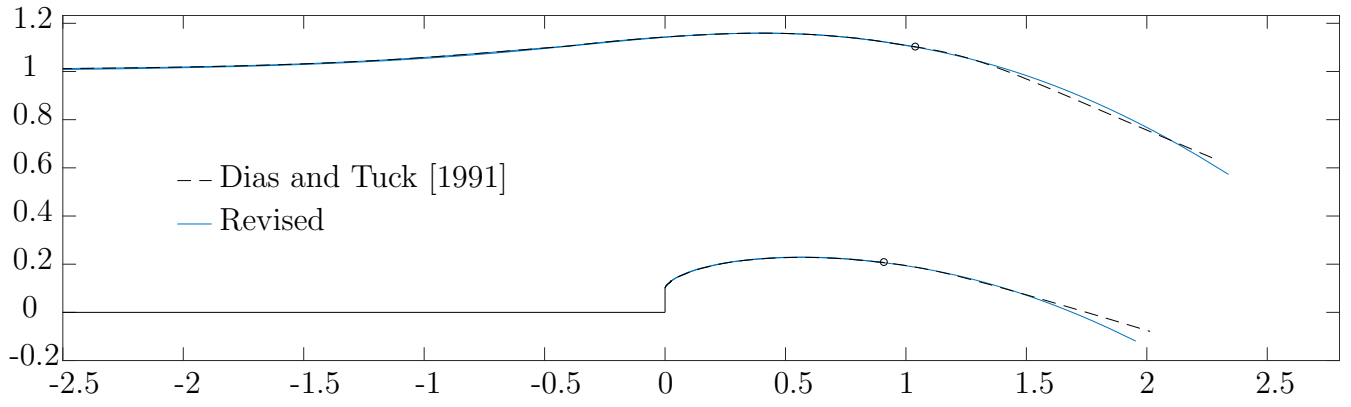


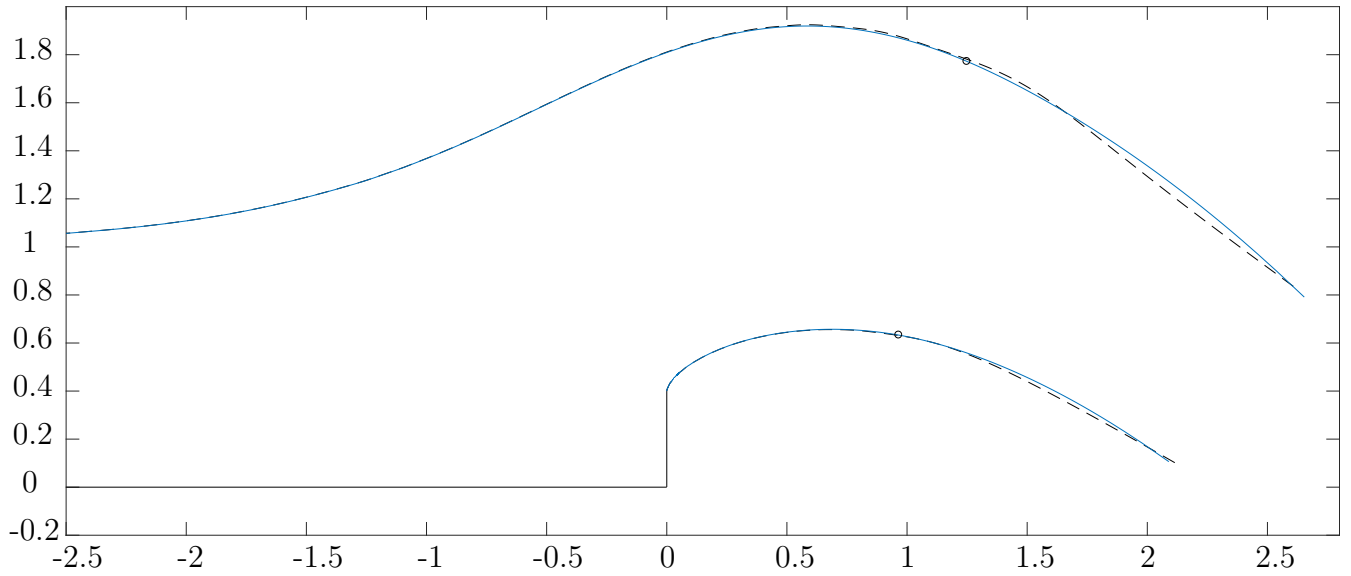
Figure 56: Comparison of extrapolated weir free-surface profiles for  $G = 0.25$ ,  $c = 0.2$  and  $w = 0.1$ . The  $A$ -method has been utilised here for the revised  $\zeta$  free surfaces only, i.e.  $N = 399$  for the revised  $\zeta$  case and  $N = 400$  for the Dias and Tuck [1991] free surfaces. The two circles are the last two points of the non-extrapolated profiles.

less dominant locally). As in the case of the waterfall, whilst the revised complex velocity ansatz leads to very similar profiles when the number of mesh points used for plotting is the same as used in finding the unknown coefficients, the improvements observed when extrapolating the profiles downstream point towards great computational benefit from the revised  $\zeta$  form.

Further extrapolated free-surface profiles are shown in figure 57. They serve to demonstrate the difference in the shape of the parabolic downfall for a fixed value of  $G$  but different vertical weir wall heights. In particular, recall that the revised form (3.2)–(3.5) for  $\zeta$  involves the unknown horizontal component  $u_\infty$  of the velocity far downstream. Here, we find that for  $w = 0.1$  we have  $u_\infty = 1.1181$ ; and for  $w = 0.4$  we obtain  $u_\infty = 0.9032$ . The effect of the wall height on the value obtained for  $u_\infty$  is relatively small. However, the effect of the value of  $u_\infty$  on the extrapolated profiles is evident when compared with those obtained via the approach of Dias and Tuck [1991]. In both cases shown in figure 57, the shape is clearly adjusted from a linear, spillway-like jet flow to a parabolic flow. It is also apparent (and expected) that the smaller value of  $u_\infty$  (i.e. corresponding to the larger vertical weir wall) corresponds to a more steeply declining parabolic jet. In §2.3, we discuss the increased suitability of the revised form for  $\zeta$  in the case of the waterfall, particularly for larger values of  $G$  where the effect of gravity is more significant, by comparison to the work



(a)  $w = 0.1$ , where we find  $u_\infty = 1.1181$ .



(b)  $w = 0.4$ , where we find  $u_\infty = 0.9032$ .

Figure 57: Comparison of extrapolated weir free-surface profiles for  $G = 0.3906$  (since we set  $F = 1.6$  here) and  $c = 0.2$ . The  $A$ -method has been utilised here for the revised  $\zeta$  free surfaces only, i.e.  $N = 399$  for the revised  $\zeta$  case and  $N = 400$  for the Dias and Tuck [1991] free surfaces.

The two circles are the last two points of the non-extrapolated profiles.

of Clarke [1965] and Dias and Tuck [1991]. On top of this, here we also have increased suitability across the range of possible values for the parameter  $w$ , compared with Dias and Tuck [1991].



### 3.2 Finite-depth, subcritical weir flows

Finite-depth weirs with subcritical flow can also be studied in much the same way as the supercritical case in the previous section. Recall that the Froude number  $F$  is based on the upstream conditions and that subcritical flow refers to the case of  $F < 1$  (or  $G > 1$ ). The complex planes of figure 52 can be used here since the geometry has not been altered and we are still seeking wave-free solutions. Vanden-Broeck and Keller [1987] and Dias and Tuck [1991] present such solutions to this problem, taking  $\zeta \sim f^{1/3}$  for the downstream singularity. To form the complex velocity ansatz, we note that inside the corner at  $O$ , the flow behaves like  $\zeta \sim (t - t_O)^{1/2}$  as  $t \rightarrow t_O$ ; and we have the aforementioned  $\zeta \sim f^{1/3}$  as  $\phi \rightarrow +\infty$ , for the jet downstream. We also have the following conditions:

1.  $v = 0$  on  $\psi = 0$ ,  $\phi < \phi(t_O)$  (no normal flow along wall section  $IO$ ),
2.  $u = 0$  on  $\psi = 0$ ,  $\phi(t_O) < \phi < 0$  (no normal flow along wall section  $OC$ ),
3.  $\zeta(t = -1) = 1$  (unit horizontal flow far upstream),
4. Bernoulli condition (2.1) along the free surfaces  $IJ$  and  $CJ$ , with  $p = 0$  as before.

In this case, the form for the complex velocity is

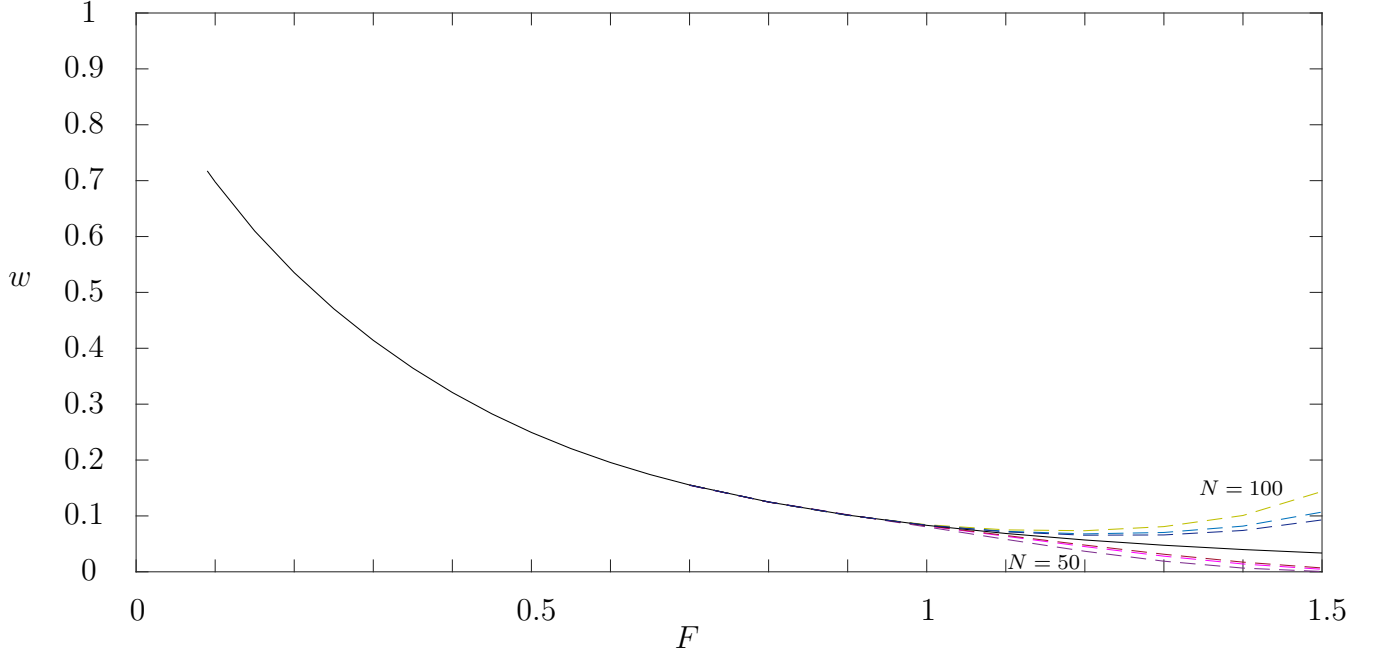
$$\zeta(t) = -i(t - t_O)^{1/2}(-\log c(1 + t^2))^{1/3} \exp \left( \sum_{n=0}^{\infty} a_n t^n \right), \quad (3.8)$$

where  $0 < c < 1/2$ . Note that the last two conditions are not automatically satisfied by the ansatz, so they will be additionally imposed. As usual, we truncate the series in  $t$  after  $N$  terms, leaving  $N$  unknown coefficients to be found. Either, we can set the value for the Froude number and leave  $w$  (the length of the vertical weir wall) to be found in post-processing, or we can set  $w$  as in the supercritical case and leave  $F$  to be found. Regardless, we will have  $N + 1$  unknowns. We temporarily refer mostly to the Froude number  $F$  rather than  $G$  — this is to facilitate more convenient comparisons with previous works. The remainder of the method details remain the same: we introduce  $N$  mesh points which are equally-spaced along the arc of the semi-circle in the  $t$ -plane, and recall that we require  $\zeta(-1) = 1$ . Then, we solve numerically by iteration. Note

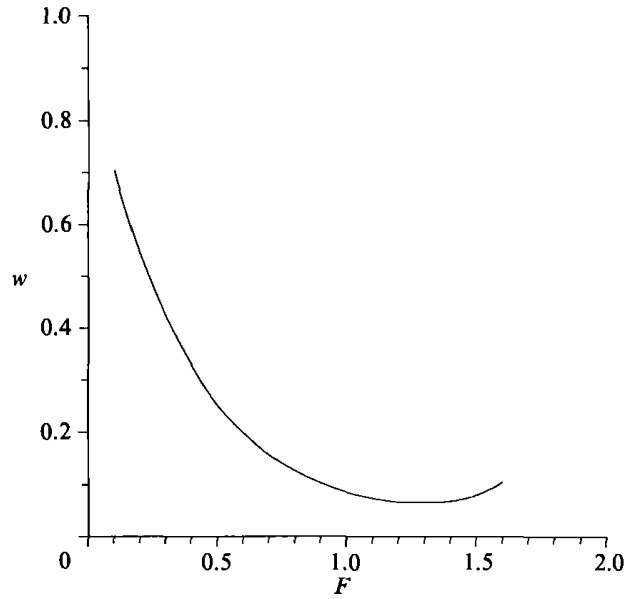
that the  $A$ -method is not utilised here since the upstream conditions are only specified through the Bernoulli condition and through  $\zeta(-1) = 1$ , and not through the complex velocity ansatz.

Of particular note is that a one-parameter family of solutions is obtained by Vanden-Broeck and Keller [1987] and Dias and Tuck [1991], i.e. for a given Froude number, there is a particular vertical weir wall height for which a wave-free solution exists. Vanden-Broeck and Keller [1987] concentrate on very small Froude numbers in order to make comparisons with experimental data, while Dias and Tuck [1991] demonstrate that wave-free solutions without exponential decay upstream — recall that exponential decay upstream is associated with the supercritical flow — can be obtained for Froude numbers  $0 < F \leq 1.6$ . However, here (c.f. figure 58a) we show that such solutions exist for a greater range of Froude numbers. First, we comment that for  $F < 1$ , the plot of figure 58a is very similar to figure 5 of Dias and Tuck [1991] (shown here in figure 58b). As the Froude number decreases from 1, the weir wall height increases. Taking  $N = 250$ , we are able to obtain a converged solution for  $F = 0.09$  but no smaller. Note that, as  $N$  increases, the smallest value of  $F$  for which a converged solution is obtainable decreases, hence increasing  $N$  leads closer to the limiting case of  $F \rightarrow 0$ . At the other end of the Froude number range, instead of there being a minimum weir wall height corresponding to  $F \approx 1.3$  (beyond which the weir wall height increases with the Froude number, c.f. figure 5 of Dias and Tuck [1991]), we have a monotonic relationship between the Froude number and weir wall height. This result is most readily obtained by ‘smoothing’ the  $y$ -values obtained through integration (as discussed in §2.4), which works to diminish any spurious oscillations that can appear in the solutions (particularly apparent if one interpolates the resulting components of velocity). Figure 58a also shows the relation between the Froude number and wall height when smoothing the  $y$ -values is not employed. The lines obtained where  $N$  is a multiple of 100 most closely resemble the result presented by Dias and Tuck [1991]. However, as  $N$  increases, the monotonic branches (when  $N = 50, 150, 250$ ) and non-monotonic branches (when  $N = 100, 200, 300$ ) appear to be converging towards the line obtained through smoothing. Therefore, whilst for smaller values of  $N$  (say  $N = 100$ ) three solution branches appear in figure 58a, for sufficiently large  $N$  it seems that there will be only one solution (i.e. one value for the weir wall height for each Froude number) — and this one solution can be obtained when taking

smaller values for  $N$  if ‘smoothing’ is employed.



(a) The solid black line is obtained when smoothing the  $y$ -values for  $N = 250$ . The dashed lines result from only integrating directly to each mesh point to find the  $y$ -values. The lines curving upwards are for  $N = 100, 200, 300$  (from top to bottom); and the lines appearing to asymptote to the  $x$ -axis are for  $N = 50, 150, 250$  (from bottom to top).



(b) Figure 5 of Dias and Tuck [1991]. Reproduced with permission, © 1991 Cambridge University Press.

Figure 58: Vertical weir wall length  $w$  against  $F$ .

The justification for this investigation of the results is that, at first glance, the results of Dias and Tuck [1991] were not initially reproduced; but the numerical integration options appear to account for the differences. However, it should be noted that the wave-free solutions obtained

here where  $F > 1$  are just special cases of results obtained from the supercritical formulation (c.f. equation (16) of Dias and Tuck [1991]) but with the coefficient of the exponential decay term for the velocity far upstream being  $\sum_{m=0}^{\infty} a_m (-1)^m = 0$ .

Now, we turn our attention to develop the complex velocity ansatz in order to better encapsulate the parabolic nature of the free-falling jet far downstream. Employing the three-term expansion for  $\zeta$  far-downstream, the complex velocity must now instead satisfy (3.1), i.e. as  $\phi \rightarrow +\infty$ , we have that  $\zeta \sim i(3G)^{1/3} f^{1/3} + u_{\infty} + C f^{-1/3}$ , where  $u_{\infty}$  and  $C$  are unknown constants. Then, we can take

$$\zeta(t) = -i \left( \frac{t - t_O}{1 - t t_O} \right)^{1/2} B(t), \quad (3.9)$$

where

$$B(t) = \left( \frac{1}{\pi} \right)^{1/3} \left( -\log \left( c(1 + t^2) \right) \right)^{1/3} l_1(t) + l_2(t) + \sum_{n=0}^{\infty} a_n t^n \left( -\log \left( c(1 + t^2) \right) \right)^{-1/3}, \quad (3.10)$$

and  $l_1$  and  $l_2$  are the linear functions:

$$l_1(t) = \text{Re}(m_1) + t \text{Im}(m_1), \quad l_2(t) = \text{Re}(m_2) + t \text{Im}(m_2), \quad (3.11)$$

with

$$m_1 = -(3G)^{1/3} \left( \frac{1 - i t_O}{i - t_O} \right)^{1/2}, \quad m_2 = i u_{\infty} \left( \frac{1 - i t_O}{i - t_O} \right)^{1/2}. \quad (3.12)$$

As with the supercritical case,  $u_{\infty}$  satisfies (3.6).

We truncate the series in the complex velocity  $\zeta$  after  $N$  terms. The point  $t_O$  and  $u_{\infty}$  are also unknowns to be found. By evaluating the Bernoulli condition at  $N$  mesh points along the free surfaces, we have  $N$  equations. We also impose  $\zeta(-1) = 1$  and the condition (3.6) on  $u_{\infty}$ , resulting in  $N + 2$  equations in  $N + 2$  unknowns. It should be noted that we still only specify the Froude number.

Figure 59a shows the resulting free-surface profile for  $F = 0.3$ . For this Froude number, we obtain  $w = 0.4142$ . We also find  $u_{\infty} = 2.8988$  which is, as expected, smaller than  $1 + G/2$  (the value of the constant term for the behaviour of the downstream singularity for the waterfall with no

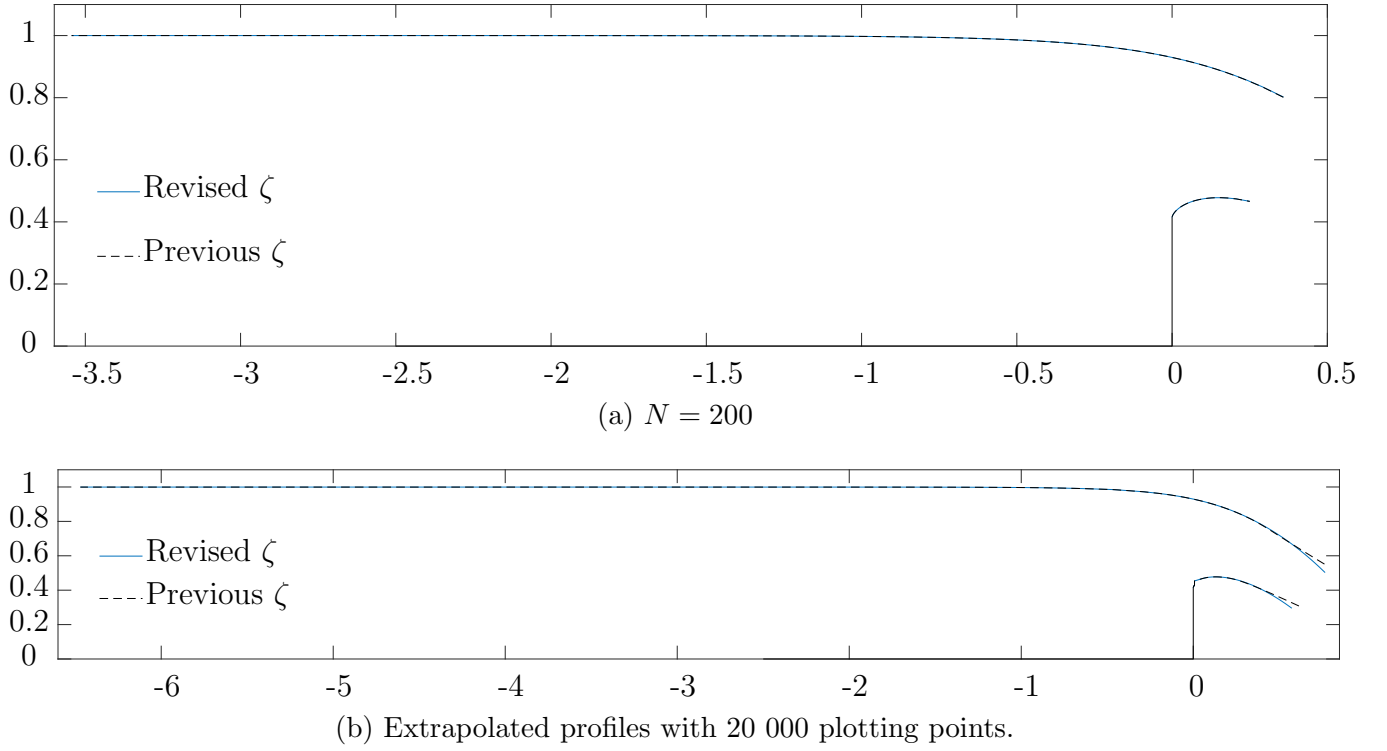
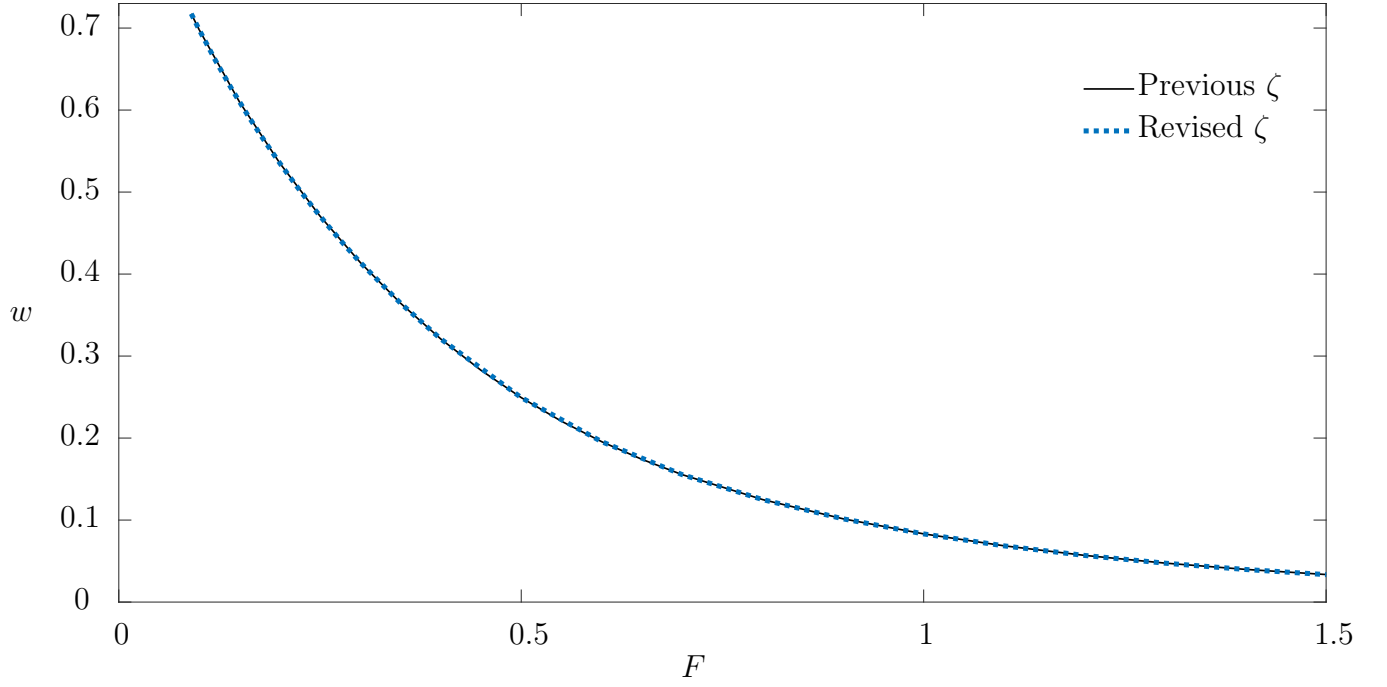


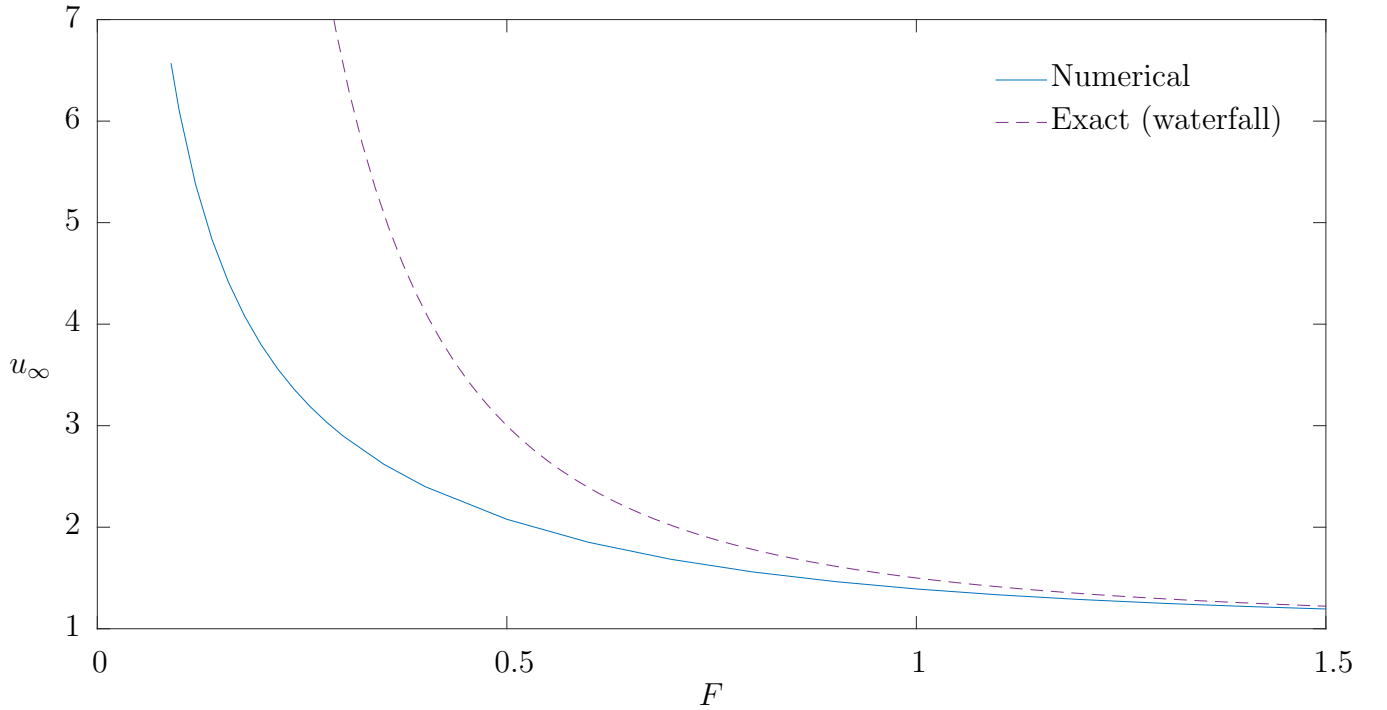
Figure 59: Comparison of free-surface profiles for  $F = 0.3$  and  $c = 0.2$ .

vertical weir wall). Despite the change in form for the complex velocity ansatz, for a given Froude number we obtain the same value for  $t_C$  and  $w$  to order  $10^{-4}$ . Hence, we are able to compare the free-surface profiles from the original [Vanden-Broeck and Keller, 1987; Dias and Tuck, 1991] and the revised ansatz for  $\zeta$ . Figure 59a shows this comparison. The profiles agree well with each other with some difference appearing in the last few points downstream of order  $10^{-4}$ . The extrapolated free-surface profiles are shown in figure 59b. As expected, the revised form for  $\zeta$  leads to a more parabolic jet downstream instead of the spillway-like linear jet flow. Figure 60a is a plot of  $w$  against  $F$  and it is very similar to that obtained before revising complex velocity ansatz. However, it should be noted that there is improvement to the numerical efficiency of the method. The plot shown in figure 60a compares the results from the form of  $\zeta$  employed by Vanden-Broeck and Keller [1987] and Dias and Tuck [1991] taking  $N = 250$  with the results obtained from the revised form (3.9)–(3.12) taking  $N = 200$ . Both reach the lower limit of  $F = 0.09$  for which a converged solution is found, but the revised form requires fewer points to do so.

Now, we look at the quality of the numerical solutions obtained. As in the supercritical case, the value for  $u_\infty$  approaches  $1 + G/2$  as the vertical weir wall height decreases to zero (note that



(a) A comparison plot of the vertical weir wall length  $w$  against Froude number  $F$ . The solid line corresponds to the revised form for  $\zeta$  with  $N = 200$ ; and the dotted line results from the original form for the  $\zeta$  with  $N = 250$ .



(b) A plot of  $u_\infty$  against  $F$ . The solid line is the numerically obtained value and the dashed line is the expected value for  $u_\infty$  in the case of the waterfall.

Figure 60: Subcritical weir results when employing (3.9)–(3.12) for the complex velocity  $\zeta$ .

increasing the Froude number results in decreasing  $w$ ). This is evident in figure 60b and is to be expected since  $u_\infty = 1 + G/2$  in the case of the waterfall. Moreover, the numerical method results in good convergence as  $N$  increases. This is apparent in figure 61 which is a plot of  $t_C$  against  $1/N$  where  $t_C$  is constant to order  $10^{-3}$  for  $N \in [100, 400]$ .

Overall, the inclusion of the extra terms of the expansion for the jet singularity downstream has been shown to improve the shape of the jet downstream, the computational efficiency and the quality of the numerical solutions in terms of convergence. Now, we will look at further examples of applying the revised expression for the downstream singularity.

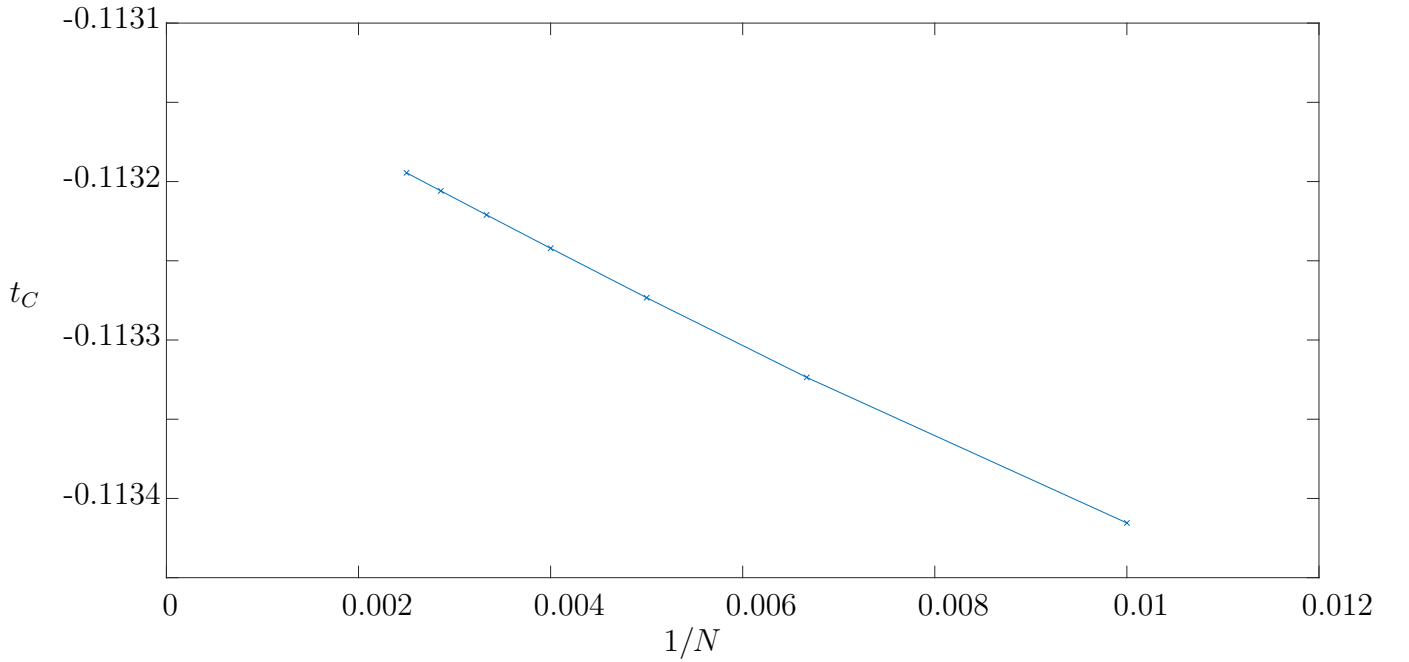


Figure 61: A plot of  $t_C$  against  $1/N$  to show the convergence of this value as  $N \rightarrow \infty$ . Here,  $F = 0.3$  and  $c = 0.2$ .

### 3.3 Steps upstream of waterfall

We return to investigating supercritical overfall problems, now with steps in the wall upstream (c.f. figure 62a). After non-dimensionalising with respect to the upstream depth and velocity, we have uniform horizontal flow far upstream, of unit velocity. Recall that we define  $G = F^{-2}$ , where the  $F$  is the Froude number. The step is of perpendicular height  $h$  and the angles between the walls are both denoted by  $\beta$ . The Bernoulli condition throughout the flow is

$$\frac{1}{2}q^2 + Gy + p = \frac{1}{2} + G(1 + h), \quad (3.13)$$

where  $q$  is the magnitude of the velocity. Once again, the complex potential plane is the infinite strip of unit width (c.f. figure 62b) and we retain (2.2) that relates  $f$  and  $t$ . The flow region is, therefore, mapped to the unit semi-circle of the  $t$ -plane as depicted in figure 62c.

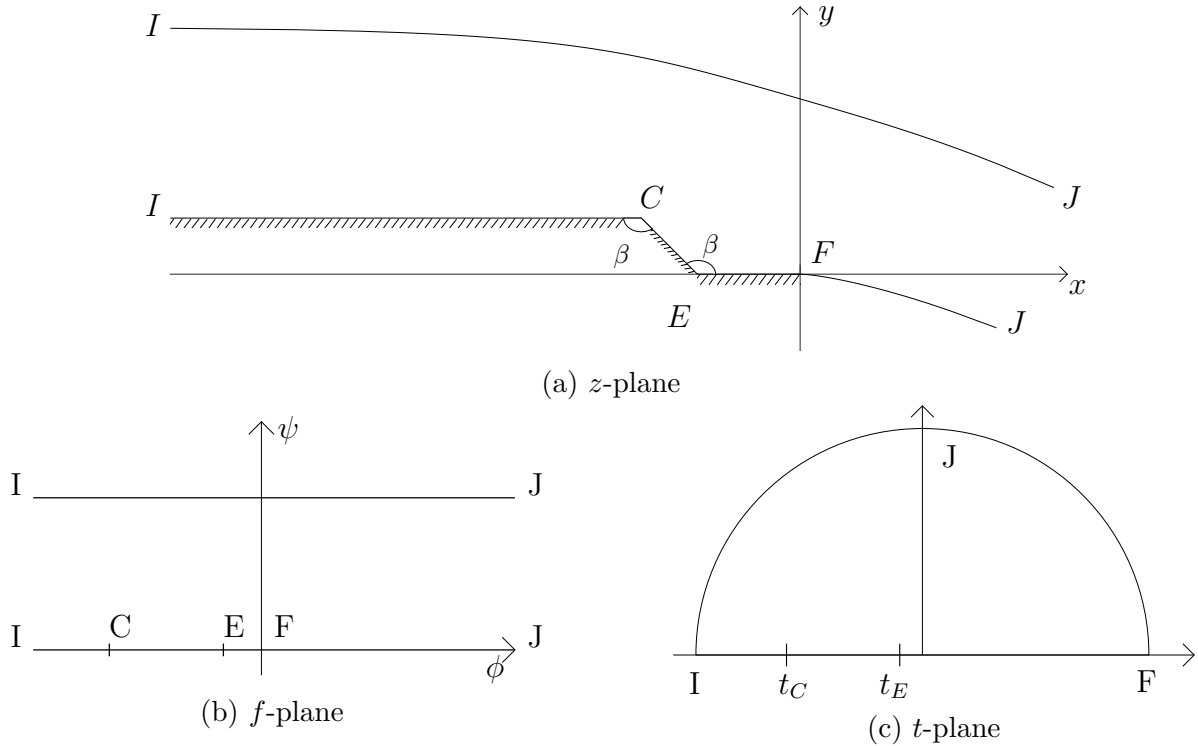


Figure 62: Complex planes for the waterfall flow with a step upstream.

We will proceed as usual, considering the various flow behaviours involved and constructing an ansatz for the complex velocity  $\zeta$ . We have

1.  $\zeta \sim (1 + ae^{\lambda f})$  as  $\phi \rightarrow -\infty$ , where  $a$  is an unknown constant and  $\lambda$  is the smallest positive



root of  $\lambda - G \tan \lambda = 0$ ,

2.  $\zeta \sim i(3G)^{1/3} f^{1/3} + u_\infty + C f^{-1/3}$  as  $\phi \rightarrow +\infty$ , where  $C$  is a constant to be found,

3.  $\zeta \sim (t - t_C)^{\beta/\pi-1}$  as  $t \rightarrow t_C$ ,

4.  $\zeta \sim (t - t_E)^{1-\beta/\pi}$  as  $t \rightarrow t_E$ ,

5.  $v = 0$  on  $\psi = 0$ :  $\phi < \phi_C$  and  $\phi_E < \phi < 0$ ,

6.  $v + u \tan \beta = 0$  on  $\psi = 0$ ,  $\phi_C < \phi < \phi_E$ .

Note that  $\phi_C$  and  $\phi_E$  denote the points in the  $f$ -plane corresponding to corners  $C$  and  $E$ , respectively; and similarly,  $t_C$  and  $t_E$  are the points in the  $t$ -plane corresponding to corners  $C$  and  $E$ . The first condition describes the upstream behaviour: as  $\phi \rightarrow -\infty$ , the flow approaches a uniform horizontal stream of constant unit velocity. The second condition listed here describes the downstream behaviour of the free-falling jet. The use of this three-term expansion is as discussed in the earlier overfall cases. The third and fourth conditions describe the flow around the corners  $C$  and  $E$ . The final two conditions simply ensure no through-flow along the walls.

It can be checked that the conditions listed above are satisfied by

$$\zeta(t) = \left( \frac{t_C - t}{1 - t t_C} \right)^{\beta/\pi-1} \left( \frac{t_E - t}{1 - t t_E} \right)^{1-\beta/\pi} (1 + (1+t)^{2\lambda/\pi} B(t)), \quad (3.14)$$

where

$$B(t) = \left( \frac{1}{\pi} \right)^{1/3} \left( -\log \left( c(1+t^2) \right) \right)^{1/3} l_1(t) + l_2(t) + \sum_{n=0}^{\infty} a_n t^n \left( -\log \left( c(1+t^2) \right) \right)^{-1/3}, \quad (3.15)$$

and  $l_1$  and  $l_2$  are the following linear functions:

$$l_1(t) = \operatorname{Re}(m_1) + t \operatorname{Im}(m_1), \quad l_2(t) = \operatorname{Re}(m_2) + t \operatorname{Im}(m_2), \quad (3.16)$$

with

$$m_1 = i(3G)^{1/3} (1+i)^{-2\lambda/\pi} \left( \frac{t_C - i}{1 - i t_C} \right)^{1-\beta/\pi} \left( \frac{t_E - i}{1 - i t_E} \right)^{\beta/\pi-1} \quad (3.17)$$

and

$$m_2 = (1 + i)^{-2\lambda/\pi} \left( u_\infty \left( \frac{t_C - i}{1 - it_C} \right)^{1-\beta/\pi} \left( \frac{t_E - i}{1 - it_E} \right)^{\beta/\pi-1} - 1 \right). \quad (3.18)$$

Recall that  $c$  is a constant such that  $0 < c < 1/2$ , and  $u_\infty$  is an unknown constant to be found.

Note that

$$u_\infty = 1 + \frac{G}{2} - Gh + \int_{s_C}^{s_E} p \Big|_{\psi=0} \sin \beta \, ds, \quad (3.19)$$

with  $s_C$  and  $s_E$  being the displacement along the wall from the origin to corners  $C$  and  $E$ , respectively. This expression for  $u_\infty$  is derived similarly to (3.6), where we integrate the  $x$ -momentum Euler equation over the flow region.

The power series that appears in the complex velocity ansatz (3.15) is truncated after  $N$  terms, leaving the coefficients  $a_n$ ,  $n = 0, 1, 2, \dots, N-1$  as unknown constants. We also leave  $u_\infty$ ,  $t_C$  and  $t_E$  as unknowns to be found as part of the solution — the latter two allowing us to set the positions of corners  $C$  and  $E$  in the  $z$ -plane. Overall, we have  $N+3$  unknowns. Now, we introduce  $N$  equally-spaced collocation points along the arc of the semi-circle in the  $t$ -plane. We evaluate the Bernoulli condition (3.13) (noting that  $p = 0$  along the free surfaces) at each collocation point and so we have  $N$  equations. Another two equations arise from setting the positions of corners  $C$  and  $E$ . More specifically, we set the values of  $z_E$  (position of  $C$  in the  $z$ -plane) and  $\delta$  (the length of the wall  $CE$ ) by imposing

$$z_E = \int_{t_E}^1 \frac{1}{|\zeta|} \left( \frac{2}{\pi} \frac{1-t}{(t+1)(t^2+1)} \right) dt, \quad (3.20)$$

and

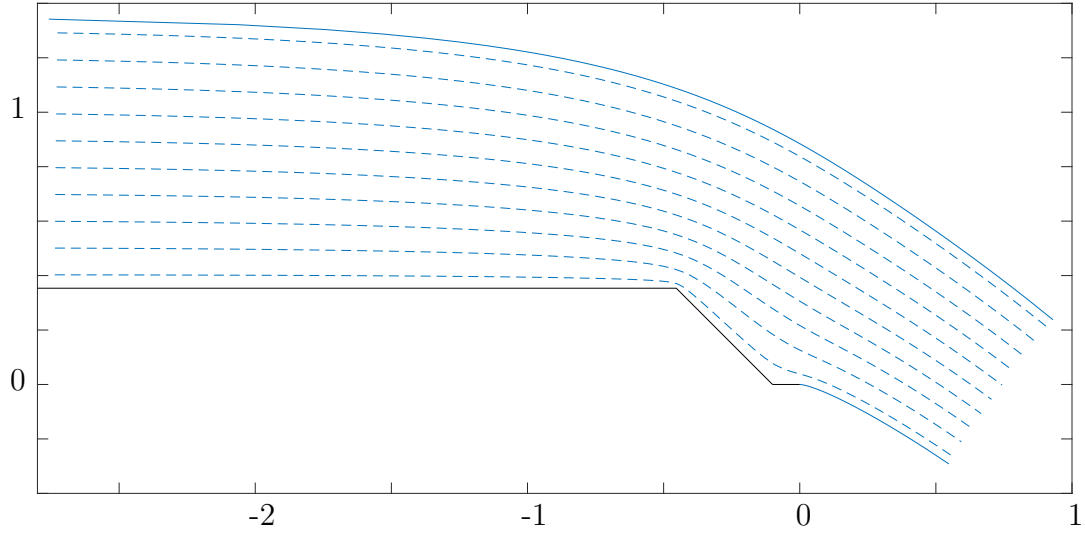
$$\delta = - \int_{t_E}^{t_C} \frac{1}{|\zeta|} \left( \frac{2}{\pi} \frac{1-t}{(t+1)(t^2+1)} \right) dt. \quad (3.21)$$

These expressions are obtained as discussed earlier for the spillway case with a stepped wall (c.f. (1.45)–(1.48)). Finally, we have  $N+3$  equations in the  $N+3$  unknowns by also imposing the condition (3.19) on the value for  $u_\infty$ . This system can be solved numerically by iteration. It should be noted that  $G$ ,  $\beta$ ,  $z_E$  and  $\delta$  are the parameters for the problem. In theory, numerical solutions can be obtained for any (suitable) values taken for  $F$ ,  $\beta$ ,  $z_E$  and  $\delta$ . However, due to the limitation

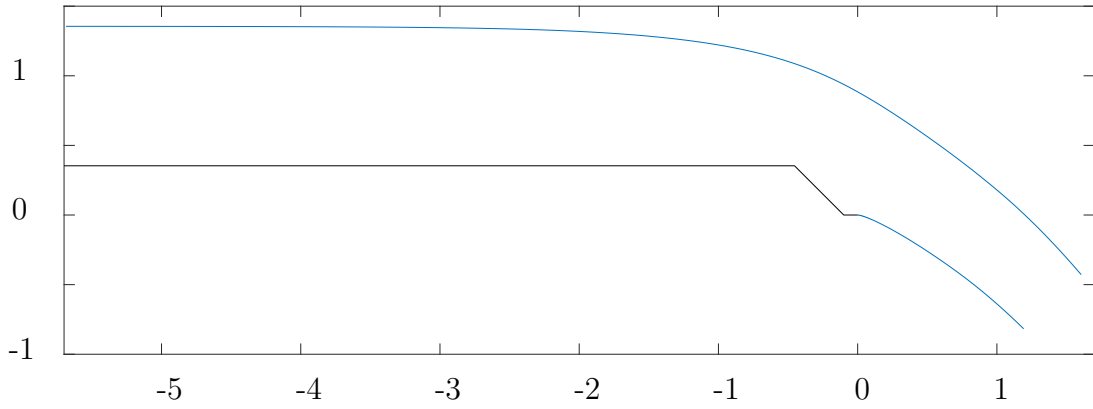
of the method in needing many collocation points to reach far up- and downstream, the number  $N$  of mesh points chosen will limit the size of the step that can be taken.

In the results presented, interpolation of the  $y$ -values and the  $A$ -method are utilised, as presented in §2.4. A few example free-surface profiles are presented here. Figure 63a depicts the case of  $G = 0.5$  where  $\beta = 3\pi/4$ ,  $z_E = -0.1$  and  $\delta = 0.5$ . As usual, the larger the value of  $G$ , the faster the flow around the corner and over the step, and the greater the curvature of the parabolic downfall. In the interest of avoiding repeating analysis of the numerical results as presented for the previous cases, they are summarised as follows: the values of  $u_\infty$ ,  $t_C$  and  $t_E$  appear to converge as  $N \rightarrow \infty$  (c.f. figure 64); the value of  $u_\infty$  converges to  $1 + G/2$  as the size of the step diminishes (c.f. figure 65); and there is good coefficient decay (c.f. figure 66).

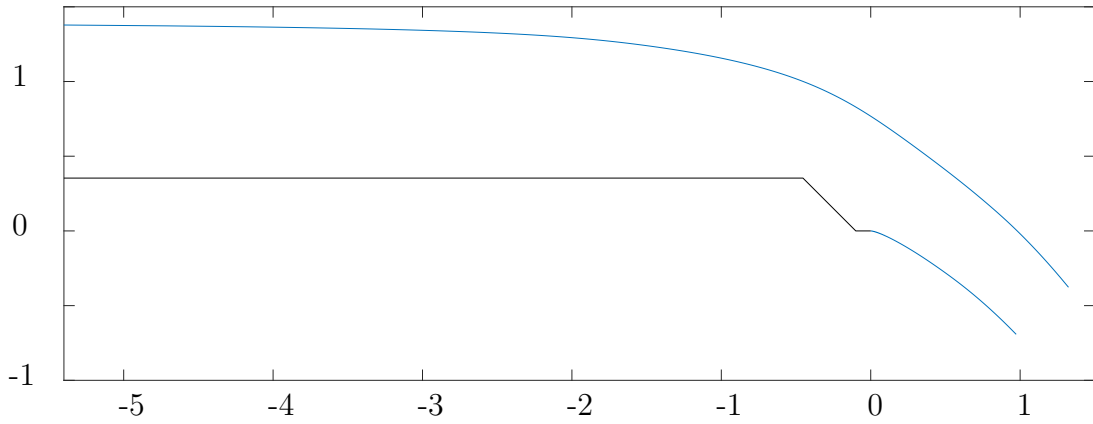
Overall, these new solutions are obtained using a numerical method that has earlier been rigorously justified in the case of the standard waterfall (see chapter 2); and results presented here, specifically relating to the problem of the waterfall with a step upstream, support the conclusion that we obtain good, converged solutions. Recalling that a physical justification for investigating or constructing stepped spillway or waterfall is for energy dissipation of the flow, a useful modification would be to incorporate a dissipation factor in order to retain the potential flow approach presented here. This is left for future work.



(a) Here, we calculate with 199 unknown coefficients for  $G = 0.5$ . Streamlines are for  $\psi = 0.05 + 0.1i$  for  $i = 0, 1, \dots, 9$ .

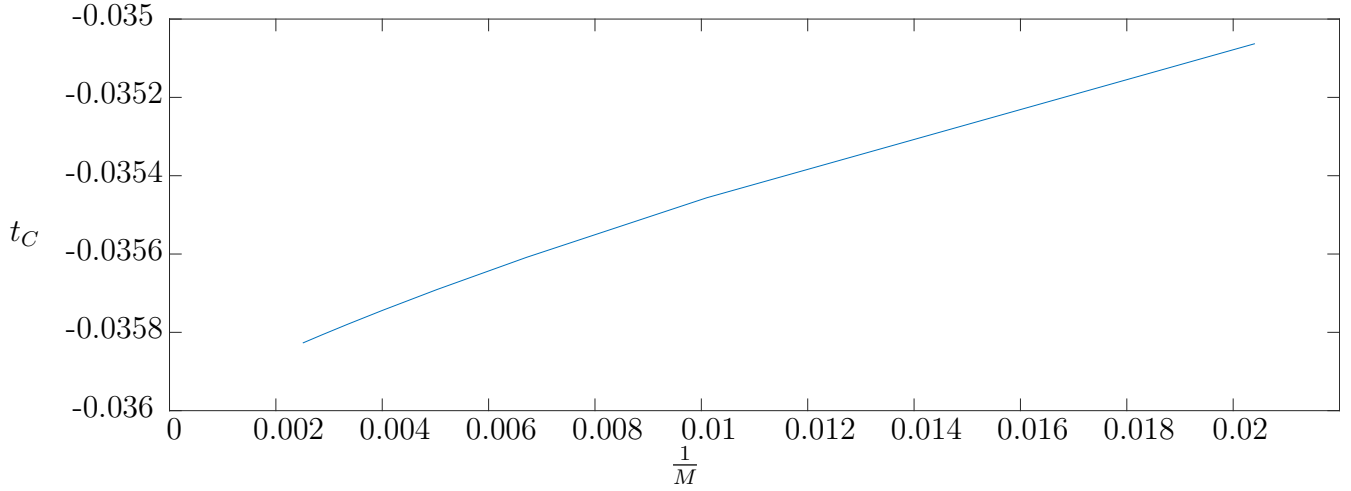


(b) Extrapolated free-surface profile for  $G = 0.5$ .

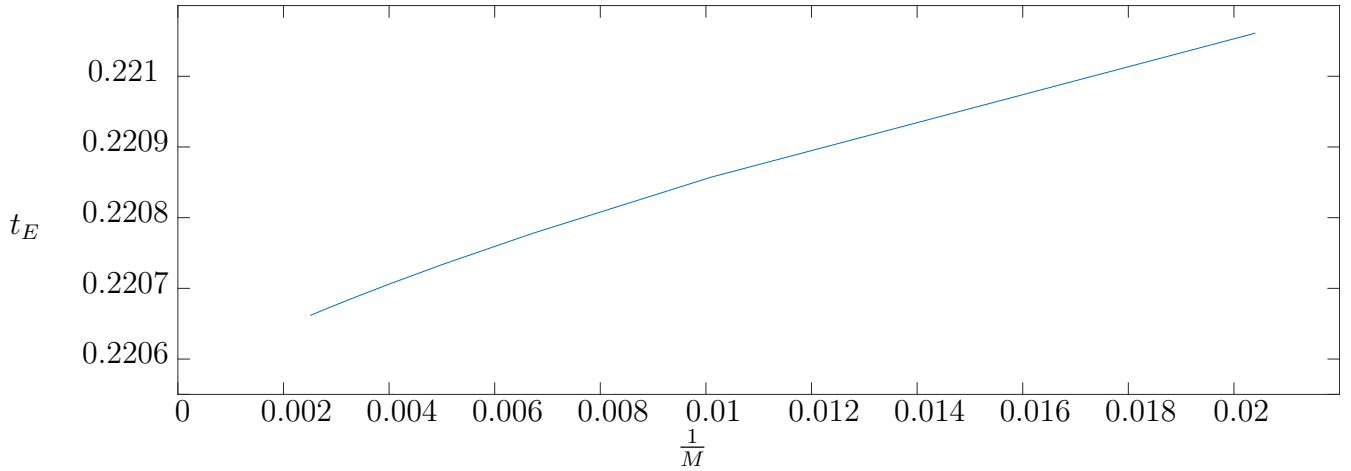


(c) Extrapolated free-surface profile for  $G = 0.9$ .

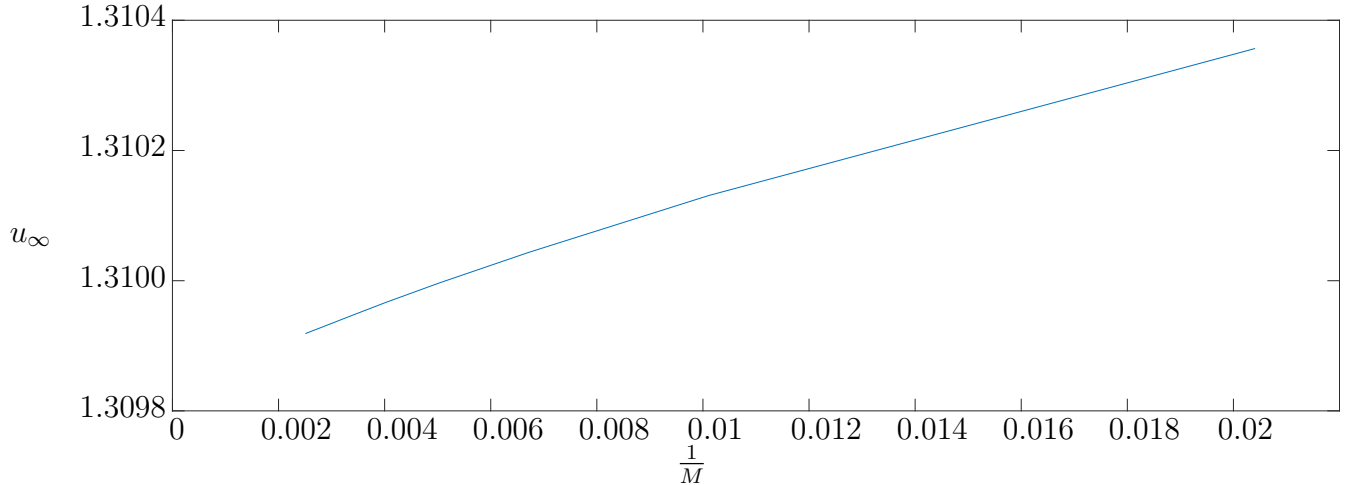
Figure 63: Free-surface profiles for  $\beta = 3\pi/4$ ,  $\delta = 0.5$  and  $z_E = -0.1$  with  $c = 0.2$ .



(a) Values of  $t_C$  obtained, plotted against the reciprocal of the number of unknown coefficients.



(b) Values of  $t_E$  obtained, plotted against the reciprocal of the number of unknown coefficients.



(c) Values of  $u_\infty$  obtained, plotted against the reciprocal of the number of unknown coefficients.

Figure 64: These plots show the convergence of  $t_C$ ,  $t_E$  and  $u_\infty$  as  $N \rightarrow +\infty$ . Here, we take  $G = 0.7$ ,  $\beta = 3\pi/4$ ,  $\delta = 0.1$  and  $z_E = -0.1$  with  $c = 0.2$ . Due to the use of the  $A$ -method and averaging of the  $y$ -values to improve the numerical method,  $N$  does not actually denote the number of unknown coefficients. Therefore, for clarity and ease of reproducibility, in this figure we denote by  $M$  the number of unknown coefficients.

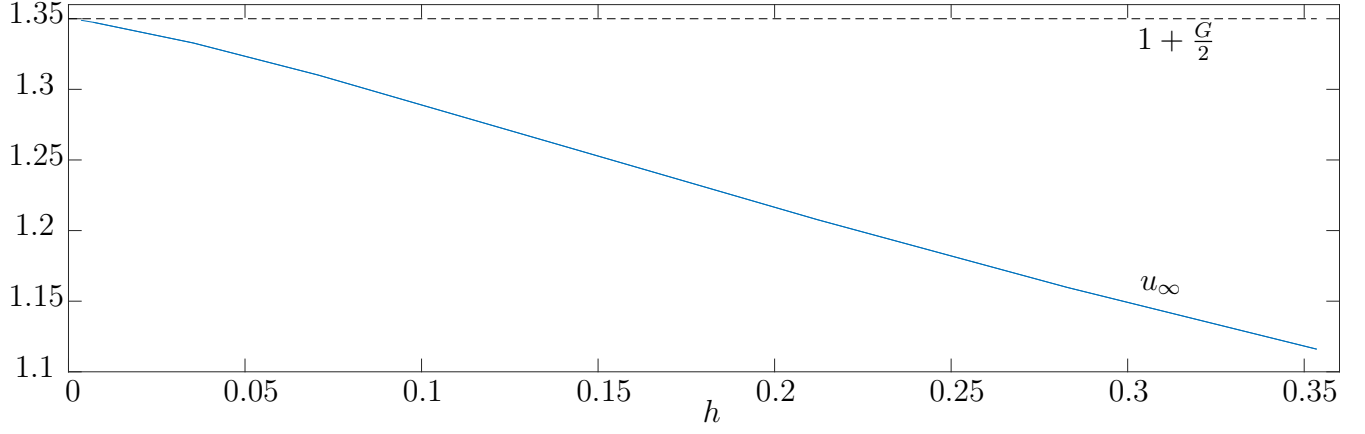


Figure 65: A plot of the values obtained for  $u_\infty$  against the perpendicular step height  $h$ . These results are from setting  $G = 0.7$ ,  $\beta = 3\pi/4$  and  $z_E = -0.1$  with  $c = 0.2$  for 99 unknown coefficients.

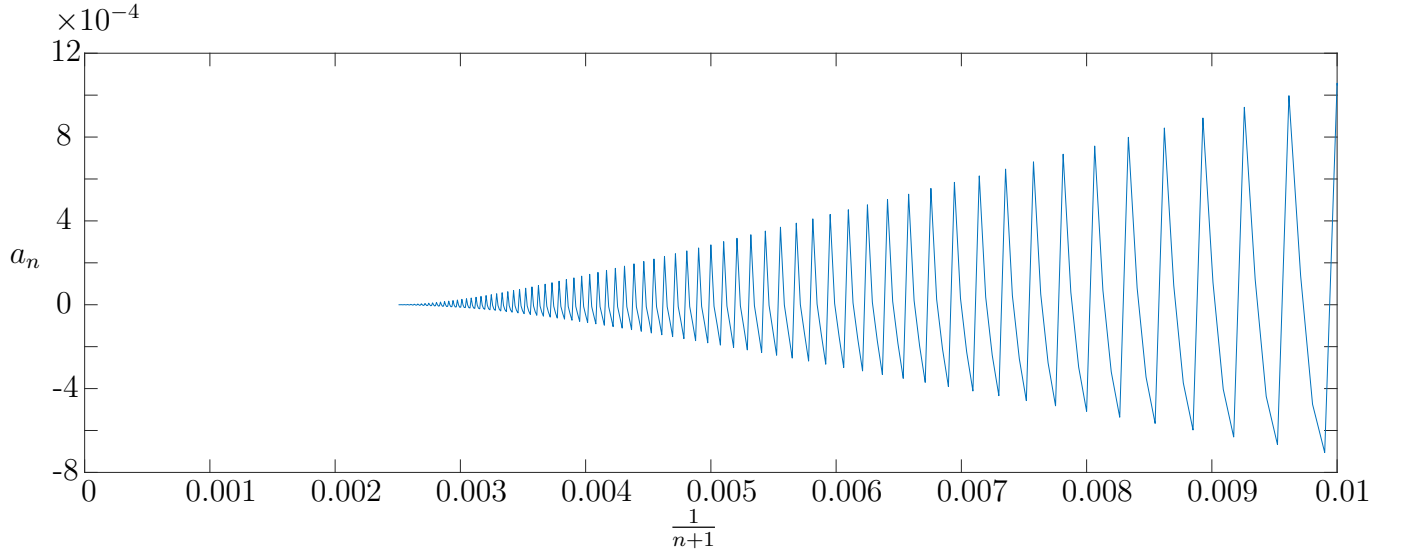


Figure 66: Coefficient decay: a plot of coefficients  $a_n$  against  $1/(n+1)$ . Here, we take  $G = 0.7$ ,  $\beta = 3\pi/4$ ,  $\delta = 0.1$  and  $z_E = -0.1$  with  $c = 0.2$  and  $N = 399$ .

### 3.4 Obstacle upstream of waterfall

Another example is explored here, to which we can apply the revised form for the downstream jet singularity. We can calculate the waterfall flow with an upstream disturbance, which here we take to be an isosceles triangular obstruction on the horizontal bed (c.f. figure 67a). The sides of the triangle that are of equal length are the walls  $CD$  and  $DE$ , with the angle between them denoted by  $\alpha$  and these walls make the angle  $\beta$  with the horizontal walls on either side. We proceed in much the same manner as the previous example. Recall that we assume the dimensional pressure along the free surfaces is set to atmospheric pressure (i.e. a constant). After non-dimensionalising as usual, with respect to the far-upstream depth and speed of the flow, we have uniform horizontal flow far upstream of unit speed and depth. Note that the edge of the horizontal bed at  $F$  is set at the origin on the  $z$ -plane. The Bernoulli condition throughout the flow is

$$\frac{1}{2}q^2 + Gy + p = \frac{1}{2} + G \quad (3.22)$$

and along the free surfaces  $IJ$  and  $FJ$  we have

$$\frac{1}{2}q^2 + Gy = \frac{1}{2} + G, \quad (3.23)$$

where  $G = F^{-2}$ . It follows that the  $f$ -plane remains as an infinite strip of unit width (c.f. figure 67b) and, retaining (2.2) for the relation between  $f$  and  $t$ , we have the unit semi-circle in the  $t$ -plane (c.f. figure 67c).

Similarly to the previous cases considered, we must form an ansatz for the complex velocity  $\zeta$ . The flow behaviours to be incorporated are

1.  $\zeta \sim (1 + ae^{\lambda f})$  as  $\phi \rightarrow -\infty$ , where  $a$  is an unknown constant and  $\lambda$  is the smallest positive root of  $\lambda - G \tan \lambda = 0$ ,
2.  $\zeta \sim i(3G)^{1/3}f^{1/3} + u_\infty + Cf^{-1/3}$  as  $\phi \rightarrow +\infty$ , where  $C$  is a constant to be found and  $u_\infty$  denotes the horizontal component of the velocity far downstream,
3.  $\zeta \sim (t - t_C)^{1-\beta/\pi}$  as  $t \rightarrow t_C$ ,

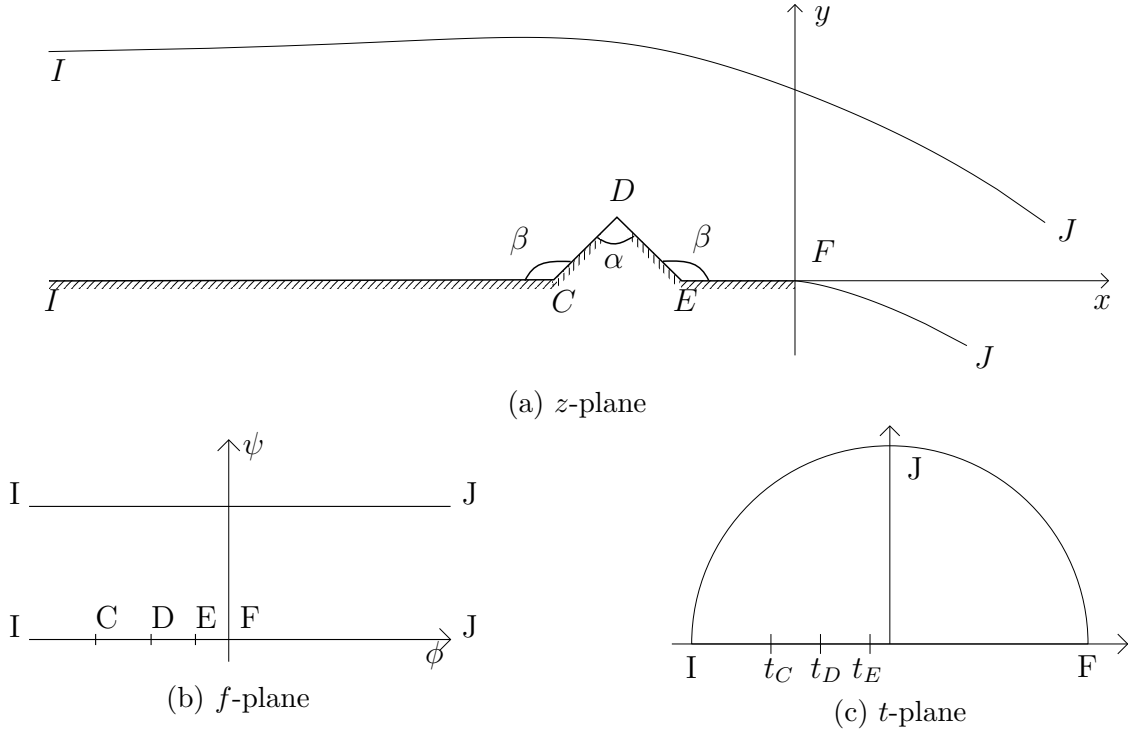


Figure 67: Complex planes for waterfall flow with a triangular obstacle upstream.

4.  $\zeta \sim (t - t_D)^{\alpha/\pi-1}$  as  $t \rightarrow t_D$ ,
5.  $\zeta \sim (t - t_E)^{1-\beta/\pi}$  as  $t \rightarrow t_E$ ,
6.  $v = 0$  on  $\psi = 0$ :  $\phi < \phi_C$  and  $\phi_E < \phi < 0$ ,
7.  $\text{Arg}(\zeta) = \beta - \pi$  on  $\psi = 0$ ,  $\phi_C < \phi < \phi_D$ ,
8.  $\text{Arg}(\zeta) = \pi - \beta$  on  $\psi = 0$ ,  $\phi_D < \phi < \phi_E$ .

Note that  $\phi_C$ ,  $\phi_D$  and  $\phi_E$  denote the points in the  $f$ -plane corresponding to corners  $C$ ,  $D$  and  $E$ , respectively; and similarly,  $t_C$ ,  $t_D$  and  $t_E$  are the points in the  $t$ -plane corresponding to corners  $C$ ,  $D$  and  $E$ . The first condition listed above describes how the flow approaches a uniform horizontal stream of constant unit velocity as  $\phi \rightarrow -\infty$ , i.e. far upstream. The second condition describes the downstream behaviour of the free-falling jet, as derived in §2.2. The third, fourth and fifth conditions describe the flow inside the corners  $C$  and  $E$ , and the flow around corner  $D$ . The final three conditions impose no normal flow along the walls.



For the complex velocity ansatz, we take

$$\zeta(t) = \left(\frac{t-t_C}{1-tt_C}\right)^{1-\beta/\pi} \left(\frac{t-t_D}{1-tt_D}\right)^{\alpha/\pi-1} \left(\frac{t-t_E}{1-tt_E}\right)^{1-\beta/\pi} (1 + (1+t)^{2\lambda/\pi} B(t)), \quad (3.24)$$

where

$$B(t) = \left(\frac{1}{\pi}\right)^{1/3} \left(-\log\left(c(1+t^2)\right)\right)^{1/3} l_1(t) + l_2(t) + \sum_{n=0}^{\infty} a_n t^n \left(-\log\left(c(1+t^2)\right)\right)^{-1/3}, \quad (3.25)$$

and  $l_1$  and  $l_2$  are the following linear functions:

$$l_1(t) = \operatorname{Re}(m_1) + t \operatorname{Im}(m_1), \quad l_2(t) = \operatorname{Re}(m_2) + t \operatorname{Im}(m_2), \quad (3.26)$$

with

$$m_1 = i(3G)^{1/3} (1+i)^{-2\lambda/\pi} \left(\frac{i-t_C}{1-it_C}\right)^{\beta/\pi-1} \left(\frac{i-t_D}{1-it_D}\right)^{1-\alpha/\pi} \left(\frac{i-t_E}{1-it_E}\right)^{\beta/\pi-1} \quad (3.27)$$

and

$$m_2 = (1+i)^{-2\lambda/\pi} \left(u_{\infty} \left(\frac{i-t_C}{1-it_C}\right)^{\beta/\pi-1} \left(\frac{i-t_D}{1-it_D}\right)^{1-\alpha/\pi} \left(\frac{i-t_E}{1-it_E}\right)^{\beta/\pi-1} - 1\right). \quad (3.28)$$

The flow conditions discussed above are satisfied by (3.24)–(3.28).

Unsurprisingly, we truncate the series of (3.25) after  $N$  terms, leading to  $N$  unknown coefficients. We also solve for  $t_C$ ,  $t_D$ ,  $t_E$  and  $u_{\infty}$ . Hence, we have  $N+4$  unknowns. We will impose conditions on the physical geometry of the obstacle by setting the positions of the corners in the  $z$ -plane. By  $z_C$ ,  $z_D$  and  $z_E$  we denote the corners of  $C$ ,  $D$  and  $E$  in the  $z$ -plane. In particular, we impose

$$\int_1^{t_E} \frac{1}{|\zeta|} \left(\frac{2}{\pi} \frac{1-t}{(t+1)(t^2+1)}\right) dt = z_E, \quad (3.29)$$

$$\int_{t_E}^{t_D} \frac{1}{|\zeta|} \left(\frac{2}{\pi} \frac{1-t}{(t+1)(t^2+1)}\right) dt = \delta, \quad (3.30)$$

and

$$\int_{t_D}^{t_C} \frac{1}{|\zeta|} \left(\frac{2}{\pi} \frac{1-t}{(t+1)(t^2+1)}\right) dt = \delta, \quad (3.31)$$

where we specify the values of  $z_E$  and  $\delta$ . Therefore, we are setting the position of the corner  $E$  in

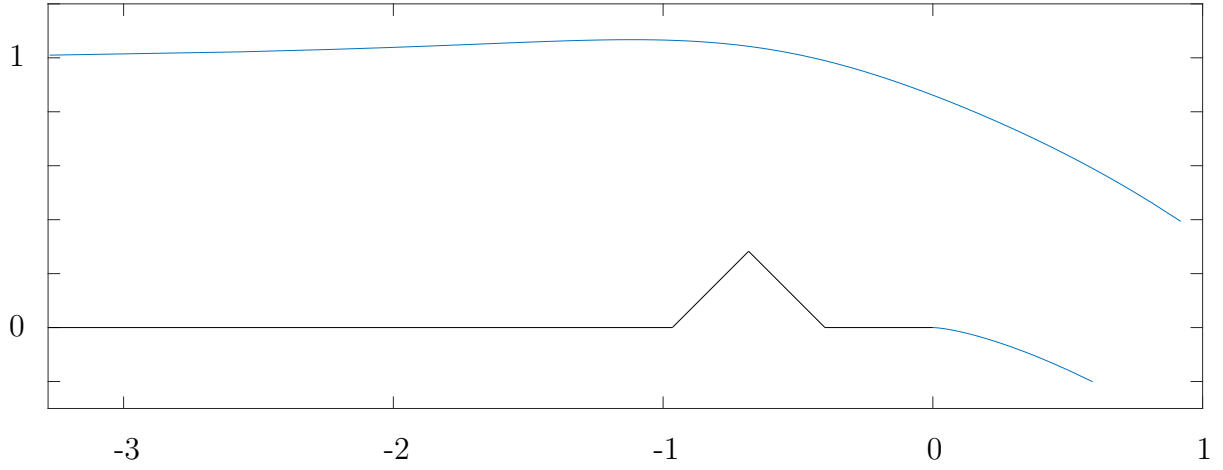
the  $z$ -plane and the lengths of the sides  $CD$  and  $DE$  of the triangular obstacle. Note that we also have the condition on the horizontal component  $u_\infty$  of the velocity far downstream. This is

$$u_\infty = 1 + \frac{G}{2} - \int_{s_C}^{s_D} p \Big|_{\psi=0} \sin \beta \, ds + \int_{s_D}^{s_E} p \Big|_{\psi=0} \sin \beta \, ds \quad (3.32)$$

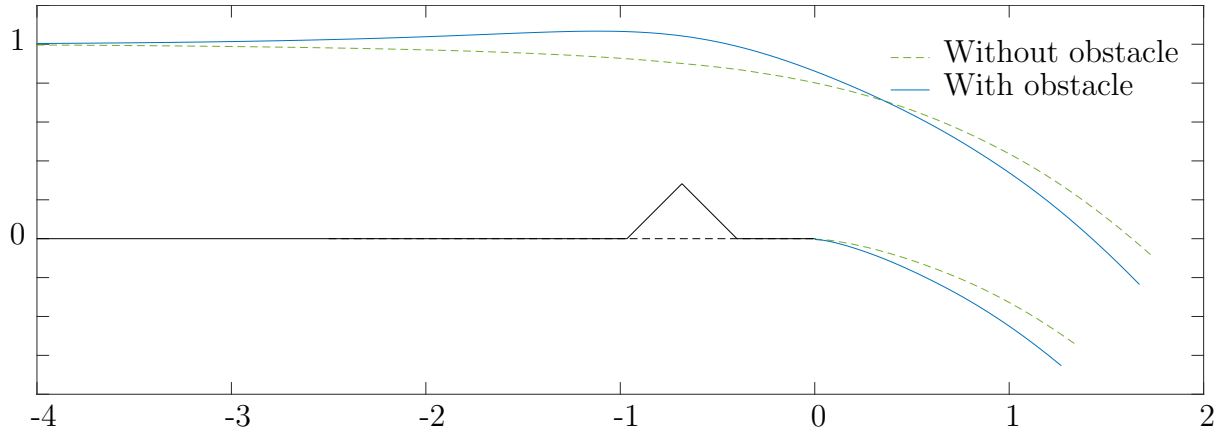
and it is derived in much the same way as in the previous cases, integrating the  $x$ -momentum Euler equation over the flow region, just as (3.6) is obtained. Then, introducing  $N$  equally-spaced mesh points along the arc of the semi-circle in the  $t$ -plane and satisfying the Bernoulli condition (3.23) at each of these points leads to another  $N$  equations. Overall, we have  $N + 4$  equations in  $N + 4$  unknowns and the parameters to be fixed are  $G$ , the position  $z_E$  of  $E$  in the  $z$ -plane and the length  $\delta$  of the walls  $CD$  and  $DE$ . As usual, this can be solved numerically by iteration.

The motivation for investigating this problem is not a particular physical scenario, but instead this further example serves to demonstrate the applicability of the revised approach in solving for potential flows that involve jets and obstacles. Hence, the presentation and discussion of the results will be brief. Note that the  $A$ -method (introduced in §2.4) is utilised in obtaining the following results. Figure 68a shows an example free-surface profile where  $G = 2/3$  and we set  $\beta = 3\pi/4$ ,  $z_E = -0.4$  and  $\delta = 0.4$ . The following plot shown in figure 68b shows a comparison of extrapolated free-surface profiles obtained for a channel with and without the triangular obstacle. In the case where the obstacle is present compared with the case where it is absent, we can observe (as expected) upwards displacement of the upper free surface locally to the obstacle. With the triangular obstacle, the resulting value of the horizontal component of velocity in this case (presented in figure 68) is  $u_\infty = 1.343$ . This is greater than the theoretical value for the simple waterfall case, i.e.  $u_\infty = 1 + G/2$ . However, the difference between the values for  $u_\infty$  with and without the obstacle is very small, of order  $10^{-3}$  in the particular case discussed here, and so the effect of the obstacle on the value obtained for  $u_\infty$  is relatively small because the pressure forces along the walls of the obstacle are small. This observation is as noted in earlier cases, such as the finite-depth supercritical weir flows of §3.1, where we comment that the value of  $u_\infty$  is dominated by the  $1 + G/2$  contribution.

We also find that, as  $\delta$  increases (resulting in an increase in the perpendicular height of the

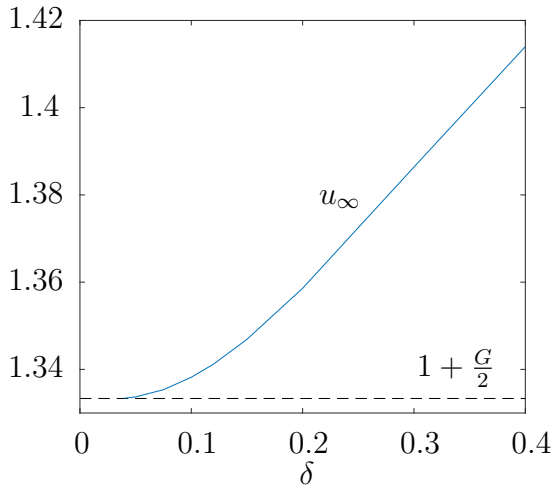


(a) Profile obtained by plotting the mesh points.

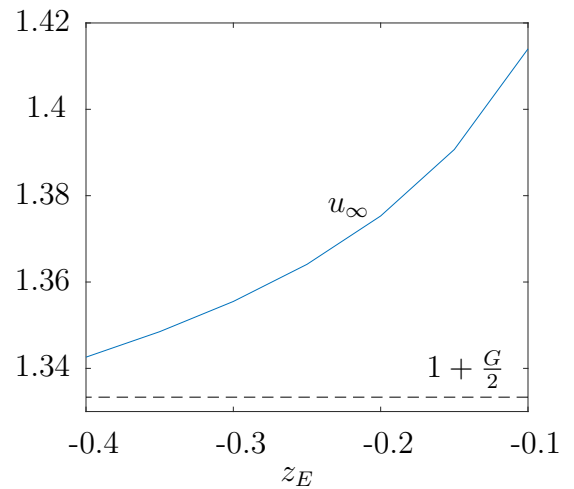


(b) Extrapolated profile.

Figure 68: Free-surface profiles for flow past the triangular obstacle where we set  $G = 2/3$  (i.e.  $F = \sqrt{1.5}$ ),  $\beta = 3\pi/4$ ,  $z_E = -0.4$  and  $\delta = 0.4$  with 200 collocation points used in solving.



(a)  $u_\infty$  against  $\delta$  where we set  $z_E = -0.1$



(b)  $u_\infty$  against  $z_E$  where we set  $\delta = 0.4$

Figure 69: Values of  $u_\infty$  obtained for varying positions and sizes of triangular obstacle where we set  $G = 2/3$  and  $\beta = 3\pi/4$  with 200 collocation points.

triangle), the horizontal component  $u_\infty$  of the velocity far downstream increases too. The value of  $u_\infty$  also increases as the triangle approaches the edge of the horizontal plate. These observations are supported by the plots of figure 69. As to be expected, we conclude that the larger the obstacle, the greater the effect on the flow; and the further upstream the obstacle, the lesser the effect of the obstacle on the flow. Note that, when the obstacle has a lesser effect, the value of  $u_\infty$  approaches the theoretical value for the simple waterfall case, i.e.  $u_\infty = 1 + G/2$ . Whilst the following point has not been investigated in detail, there is a further observation that can be made, with greater analysis left for future work. There appears to be a maximum length  $\delta$  that can be chosen for a given set of values for  $G$ ,  $\beta$  and  $z_E$  in order to obtain a converged solution. For a given configuration where  $\beta$  and  $z_E$  are fixed, the maximum height of the triangular obstacle is dependent on  $G$ . For example, given  $\beta = 3\pi/4$  and  $z_E = -0.4$ , if  $G = 2/3$  then a converged solution has not been obtained for  $\delta > 0.64$ , whereas for  $G = 5/6$  a converged solution has not been obtained for  $\delta > 0.46$ . Therefore, for a larger value of  $G$ , the maximum height of the obstacle is smaller. This is as seen earlier in the supercritical finite-depth weir case discussed in §3.1: for sufficiently tall weir walls, there is a maximum value for  $G$  above which a solution cannot be obtained.

Overall, the results presented here for the waterfall flow past a triangular obstacle upstream are qualitatively similar to those discussed for the supercritical finite-depth weir. It should be noted that the flow studied in the present section could be viewed as a particular case of a broad-crested weir flow when the triangular obstacle is near to the edge of the horizontal plate (i.e. near to the point labelled by  $F$ ). It has been demonstrated that the three-term expansion for the downstream jet singularity can be incorporated into the complex velocity ansatz in a case where there is an obstacle lying on the horizontal bed of the channel upstream.

---

Chapter 3 has included several examples of free-surface flow problems that include a free-falling jet and where it is suitable to apply the improvements to the numerical approach that were introduced in chapter 2. This includes the adoption of the three-term expansion for the behaviour of the gravity-driven jet and the use of the  $A$ -method to advance the decay of the coefficients of

the truncated power series involved in the complex velocity ansatz. The various cases to which we have applied these improvements are weir flows and waterfalls that follow on from steps or obstacles upstream. The efficacy of the method in several cases has been investigated, with a focus on the decay of the coefficients and the convergence (with  $N$ , i.e. the number of coefficients of the truncated series) of various unknowns of the problems. The good decay and convergence that was seen in the simple waterfall case of chapter 2 has also been achieved in the applications explored in the current chapter. It is clear that the revised approach can be applied to many physical problems with free-falling jets, including those with complex geometry upstream.

## 4 Zero-gravity cavity and wake flows

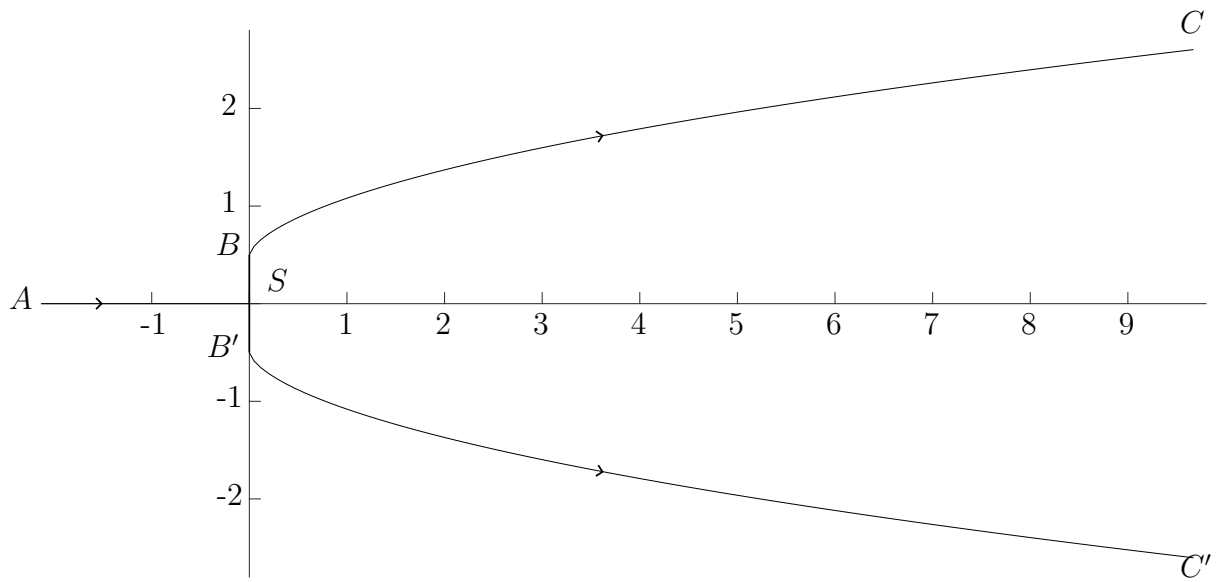
We now consider another problem involving free surfaces — in particular, building towards a gravity model for flow past a submerged bluff body. The calculations here will demonstrate how numerical methods other than series truncation and collocation can be used to solve free-surface flow problems. Here, we investigate the flow past a finite-length plate that is normal to a uniform horizontal stream, with a wake or cavity forming behind the plate. As discussed in the introduction, in this chapter we predominately make reference to a cavity forming behind the plate, but the calculations are also applicable to a wake forming instead.

We first discuss the problem where a cavity of ambient pressure and of infinite extent forms. Utilising conformal mappings leads to an exact solution for the position of the free streamlines in terms of the complex potential  $f$ . Then, we move to discuss the case of a cavity that forms behind the plate but using a horizontal wall closure model (also known as the open-wake model). Again, conformal mappings lead to an exact solution. This problem is then reconsidered with an alternative approach: an integral equation is obtained for the unknown flow angle of the free streamlines. This can then be solved by inverting a finite Hilbert transform that is involved, or we discretise to form a system of equations and unknowns to be solved by matrix inversion. It should be noted that the problems and results presented here have previously been obtained, as discussed in the introduction. However, they are included here for completeness of the discussion and to build towards the overarching wake-flow problem that is of interest. Further to this, the demonstration of the additional two methods of inverting the finite Hilbert transform or inverting the matrix is useful in highlighting their potential use for other problems. They each have their own flexibilities compared with solving by exclusively using conformal mappings to relate the physical plane to the complex potential — the latter requires much more careful consideration when not dealing with simple geometries, i.e. if the finite-length plate is not simply flat. Following the presentation of these methods in §4.2.2 and §4.2.3, it will become clear where their benefits lie in simplifying the calculations for solution in more complex cases.

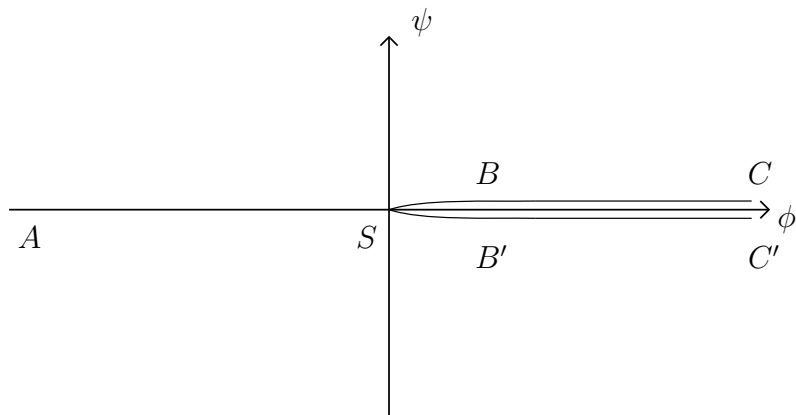
## 4.1 Cavity of infinite extent

We have a finite plate of length  $l$  that is perpendicular to uniform horizontal flow of speed  $U$ . A cavity forms behind this obstacle with a dividing streamline splitting to form two free streamlines that bound the cavitation bubble. This is as depicted in figure 70a. The assumptions on the fluid and flow remain as in the previous chapters, i.e. such that we have potential flow. We neglect the effects of gravity here. The pressure within the cavity is taken to be equal to that of the far-field. Batchelor [2010] mentions that potential flow theory allows for the pressure within a cavity to be chosen freely. However, the method utilised here does require that the cavitation bubble is at ambient pressure. As discussed earlier in the introduction, the solution of this problem is commonly accredited to Kirchhoff [1869], whilst the method of approach (using free streamline theory) is credited to Helmholtz [1868]. Batchelor [2010] also presents the method of solution for this problem in detail. Therefore, it will not be rederived here, but the salient points will be summarised.

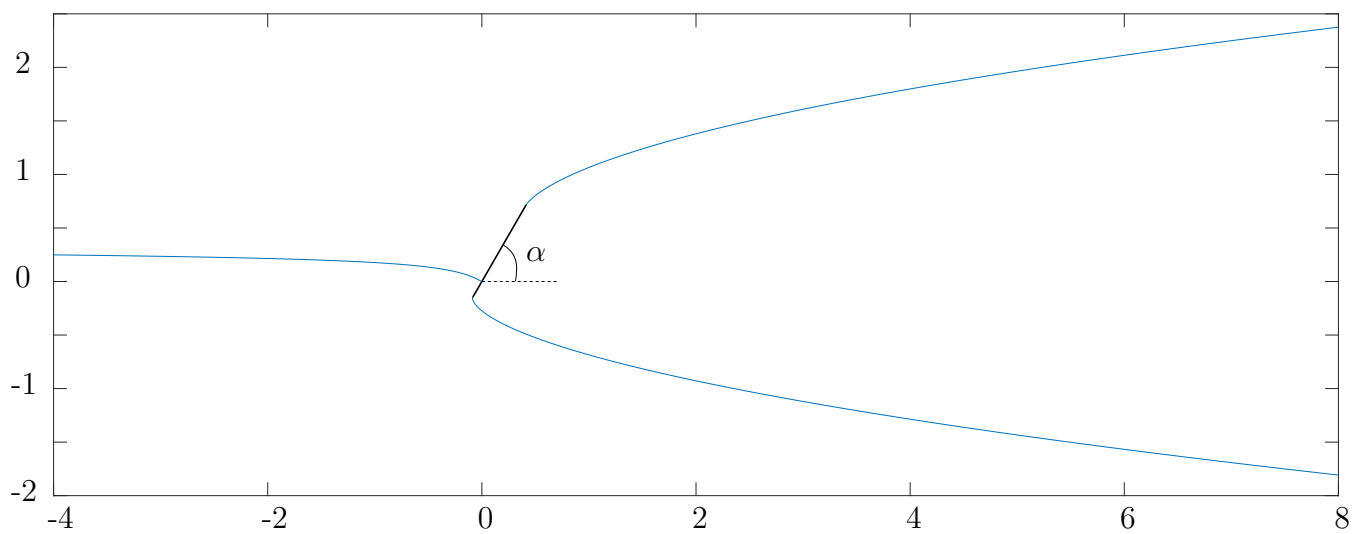
We non-dimensionalise with respect to the upstream flow velocity and blade length so that we have unit velocity far upstream and unit blade length. We set  $z = 0$  at the midpoint of the blade and note that, due to the symmetry of the problem and the absence of gravity, the dividing streamline runs along  $y = 0$ . Note that the stagnation point occurs at  $z = 0$ . As usual, we use  $f$  to denote the complex potential of the flow. We set  $\psi = 0$  along the dividing streamline and along the free streamlines bounding the cavity. The complex potential plane is then, as depicted in figure 70b, the whole plane with a branch cut along the positive real-axis. We look to find an expression for  $z$  in terms of  $f$ . Several conformal mappings are utilised to map between these planes: we define  $\omega = \log(dz/df)$  which maps the flow region to a semi-infinite strip of width  $\pi$  that is symmetric in the positive real-axis of the  $\omega$ -plane; the flow region in the  $f$ -plane can be opened up to the upper-half of an intermediate complex plane (say  $\lambda$ -plane) by  $\lambda = (k/f)^{1/2}$  with  $k$  a constant to be determined; and then the Schwarz-Christoffel theorem can be utilised to map the (polygonal) flow region of the  $\omega$ -plane to the upper-half of the  $\lambda$ -plane. Note that these mappings are discussed here due to their relevance to problems in later sections. It follows that a closed-form solution is obtained for  $z(f)$ . From this, parametric equations can be written down for



(a) Free streamlines bounding the cavity of infinite extent.



(b)  $f$ -plane for the cavity of infinite extent.



(c) Free streamlines for cavity of infinite extent behind a plate at angle  $\alpha = \pi/3$  of attack.

Figure 70: Various planes for the cavity of infinite extent.



the free streamlines that bound the cavity. Then, we find that the boundaries asymptote to  $x \sim s$  and  $y \sim \pm(sk)^{1/2}$  as  $s \rightarrow +\infty$ , hence the free streamlines asymptote to the parabola  $y^2 = 4kx$  where  $k = 1/(\pi + 4)$ .

To obtain the drag force on the finite plate, we integrate the pressure difference along the plate. An expression for the pressure along the plate is obtainable through use of the Bernoulli condition, also requiring knowledge of the velocity along the plate which is obtainable from the expression for the solution  $z(f)$ . The magnitude of the drag is  $D = \pi/(\pi + 4)$  on the unit length plate and it follows that the coefficient of drag is  $c_D = 2\pi/(\pi + 4)$ .

Note that the concise nature of the method of solution and the solution itself is due to the symmetry of the problem (since gravity is neglected and the finite-length plate is normal to the uniform horizontal stream) and the fact that we have ambient pressure within the cavity with no closure model. A very similar approach can be taken if the current problem is modified to now be a plate at an arbitrary angle of attack to the stream. As mentioned earlier, the solution to this is given by Rayleigh [1876], but the details provided for the calculation are brief. A thorough presentation of the calculation is not included here since this was included in work submitted for assessment towards the author's undergraduate degree [McLean, 2018]. We still define the  $\omega$  and  $\lambda$ -planes as in the case of the plate normal to the flow and the constant  $k$  is again to be determined. During calculation, it is also convenient to rotate the  $z$ -plane so that the flat plate lies along the  $y$ -axis with the stagnation point on the plate fixed at  $z = 0$ . However, the results written here are orientated in the  $z$ -plane so that the uniform horizontal stream is indeed horizontal and so the plate is at the arbitrary angle,  $\alpha$ , of attack (c.f. figure 70c). Again, a closed-form solution is obtainable and then parametric equations for the free streamlines lead to the fact that the cavity boundaries asymptote to the parabola  $y^2 = 4kx/\sin^2 \alpha$  where  $k = \sin^4 \alpha/(4 + \pi \sin \alpha)$ . As in the case of the plate normal to the flow, we can find the forces acting on the plate. It can be found that the drag is  $D = \pi \sin^2 \alpha/(\pi \sin \alpha + 4)$  and the lift force is  $L = \pi \sin \alpha \cos \alpha/(\pi \sin \alpha + 4)$ .

Overall, we have summarised the method and results for the cavity of infinite extent. The conformal mappings and complex planes discussed here will appear again in the next section where we move to consider the open-wake model.

## 4.2 Cavity horizontal closure

### 4.2.1 Analytic method (reproduction)

Clearly, the fact that the free streamlines of the cavity of infinite extent asymptote to a parabola is an unphysical result for the flow far downstream. It is observable that, far downstream in a cavity or wake flow, there is dissipative mixing of the slowly-recirculating gas or fluid (respectively) with the stream, and then the flow returns to the undisturbed stream. Here, we modify the previous problem to now employ a closure model where the free streamlines bounding the cavity become horizontal downstream. The points at which the cavity boundaries become horizontal are unknown and will be referred to as the closure points. A solution to this problem is presented by Roshko [1954]. We follow a similar method here, with deviation occurring in the choice of conformal mappings.

The flow is as depicted in figure 71a: a cavity forms behind a finite-length, flat plate ( $BB'$ ) that is normal to the uniform horizontal stream of constant speed, with horizontal closure far downstream. As usual, we define  $z = x + iy$  and then we set the blade along the  $y$ -axis with the stagnation point set at  $z = 0$ . Note that we still have potential flow and neglect the effects of gravity. In the far-field, the pressure is denoted by  $p_\infty$ . Conversely, within and along the boundaries of the cavity, the pressure is constant and is denoted by  $p_c$ . Then, we know that we have constant speed  $Q_c$  along the free streamlines  $BC$  and  $B'C'$ . We non-dimensionalise with respect to the length  $l$  of the plate and the speed  $Q_c$ . We now use the lowercase notation — i.e.  $x$ ,  $y$ ,  $z$  and  $p$  (for the pressure) — to denote the non-dimensionalised variables in the physical plane. The Bernoulli condition along the free streamlines becomes

$$\frac{1}{2}\rho U^2 + p_\infty = \frac{1}{2}\rho + p_c, \quad (4.1)$$

where  $U$  is the (non-dimensionalised) speed of the undisturbed horizontal stream and  $\rho$  denotes the density. Note that the Bernoulli constant has been calculated by evaluating the Bernoulli

condition far upstream. By defining the dimensionless parameter

$$K = \frac{p_\infty - p_c}{\frac{1}{2}\rho U^2}, \quad (4.2)$$

we obtain that  $U = (K + 1)^{1/2}$ . Note that  $K$  is commonly referred to as the cavitation number and it determines the characteristics of the cavitating flow, e.g. whether we have numerous small bubbles of air or the formation of a large cavitation bubble.

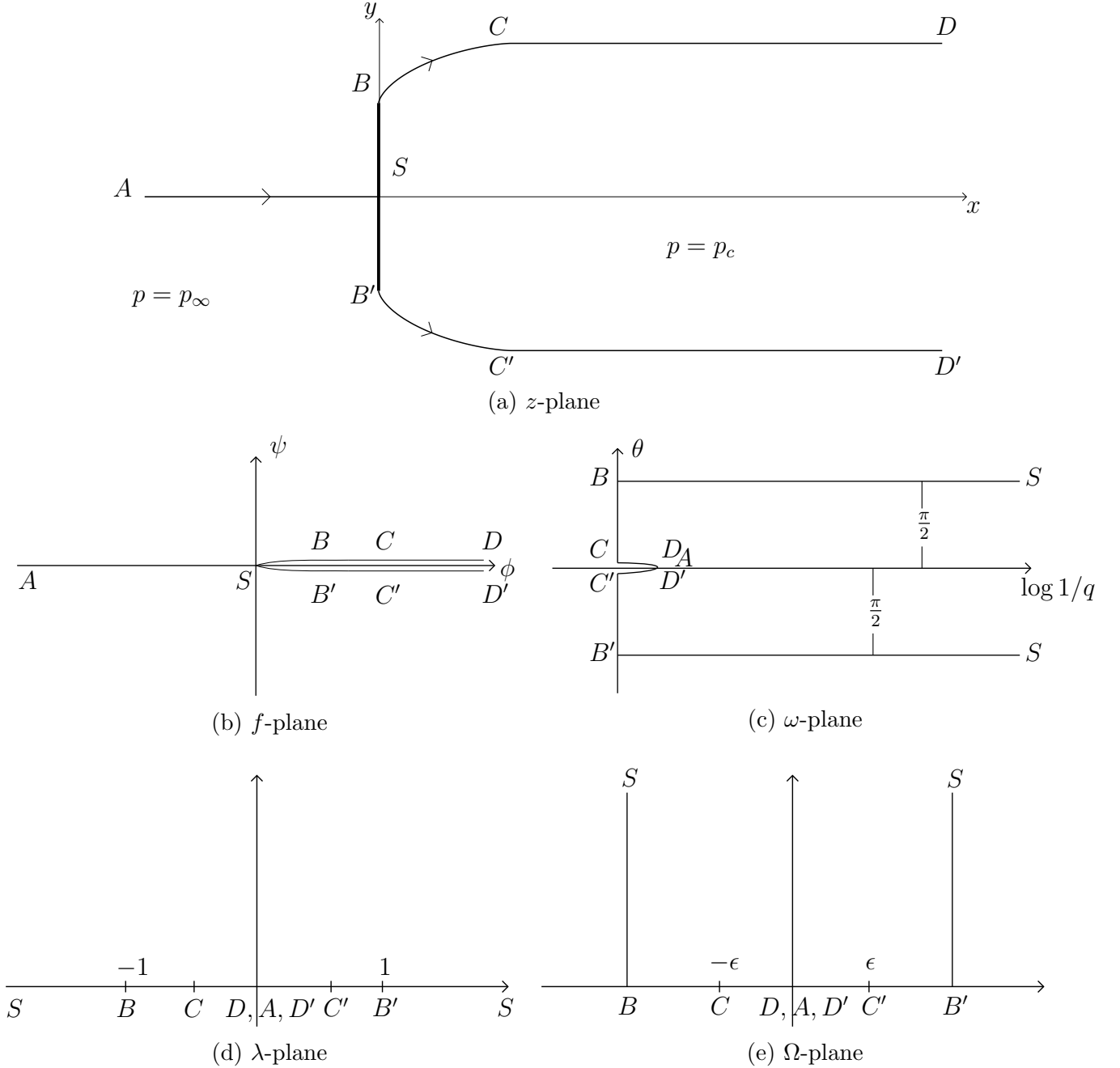


Figure 71: Complex planes for cavity forming behind a finite plate with horizontal wall closure.

The complex potential is denoted by  $f$ , as before, and we set  $\psi = 0$  along the dividing streamline and  $\phi = 0$  at the stagnation point  $S$ . We look to find  $z$  as a function of the complex potential. The  $f$ -plane is the same as in the previous case of the cavity of infinite extent (c.f. figure 71b); and we define  $\omega = \log(dz/df)$ , again as in the case of the infinite extent cavity. The  $\omega$ -plane is shown in figure 71c where the flow occupies a semi-infinite strip of width  $\pi$ . Two further intermediate complex planes are introduced:

$$\lambda = -\left(\frac{\phi_B}{f}\right)^{1/2} \quad \text{and} \quad \Omega = -(-\omega^2 + \epsilon^2)^{1/2}, \quad (4.3)$$

where  $\phi_B$  is an unknown constant and  $\epsilon = \log(1/U)$ . The Schwarz-Christoffel theorem can then be utilised to relate  $\lambda$  and  $\Omega$ . This gives

$$\lambda = -\cos\left(\frac{\pi}{2c}(\Omega + c)\right), \quad \text{where} \quad c = \left(\frac{\pi^2}{4} + \epsilon^2\right)^{1/2}. \quad (4.4)$$

We can then eliminate  $\lambda$  and  $\Omega$  from (4.3) and (4.4) to find that

$$\omega(f) = \left[ -\left(\frac{2c}{\pi} \arccos\left(\frac{\phi_A}{f}\right)^{1/2} - c\right)^2 + \epsilon^2 \right]^{1/2}. \quad (4.5)$$

Finally, we integrate  $\exp(\omega(f))$  with respect to  $f$  for  $z(f)$ . Recalling that we non-dimensionalise with respect to the length of the finite plate  $BB'$ , we solve to find the unknown constant  $\phi_B$  such that we have unit blade length. Therefore, the upper free streamline (and the lower free streamline, analogously) can be plotted via

$$z(\phi) = 0.5i + \int_{\phi_B}^{\phi} \exp(\omega(f)) df, \quad (4.6)$$

such that

$$\int_0^{\phi_B} \exp(\omega(f)) df = 0.5. \quad (4.7)$$

Free-streamline plots for various values of  $K$  are shown in figures 72 and 73.

The resulting drag coefficient for  $K = 0$  agrees with that obtained via the exact solution for

the cavity of infinite extent, i.e.  $c_D = \pi/(\pi + 4)$ . More generally, we note that, since we only specify the cavitation number and obtain the closure position of the cavity as part of the solution, we cannot specify  $p_c$  and  $x_C$  (the  $x$ -coordinate of the closure point) independently of each other. Table 5 lists, for a given cavitation number  $K$ , the resulting values of the  $x$ -coordinate of the closure point, the width of the cavitation bubble and the coefficient of drag. The results agree with those obtained by Roshko [1954] — comparison can be made with their figure 3 and noting that the value of  $U^{-1}$  here is equivalent to their parameter  $k$ . As  $K$  increases, the horizontal cavity closure approaches  $z = 0 \pm 0.5i$ , i.e. we approach having a submerged, semi-infinite, rectangular block instead of a cavitation bubble. This is then similar to the investigations into ploughing flows by Tuck and Vanden-Broeck [1998], but without a free surface bounding the stream above and with an infinite Froude number. Recall that the idea behind using closure models is to (hopefully) find a realistic description of the flow near the blade and sacrifice having such a realistic description far downstream. However, for large cavitation numbers, this closure model is not ideal since the closure mechanism is in the local neighbourhood of the blade.

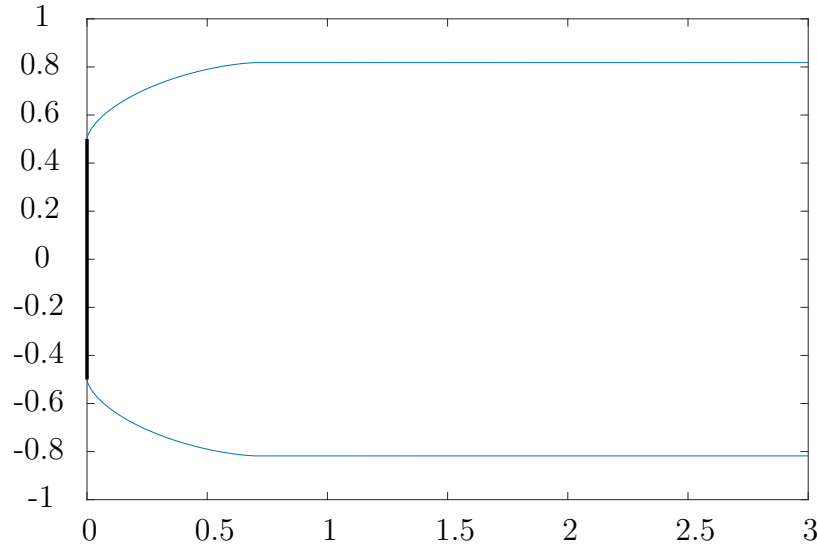


Figure 72: Free-streamline plot for cavity with horizontal wall closure  $K = 1.2$

As mentioned in the introduction, solutions can be obtained in a very similar way for a finite, flat plate or curved plate at an arbitrary angle of attack to the flow. The closure model employed is still such that the free streamlines become parallel to the undisturbed stream at some unknown closure points along these streamlines. Such solutions are presented by Wu [1956] and Mimura

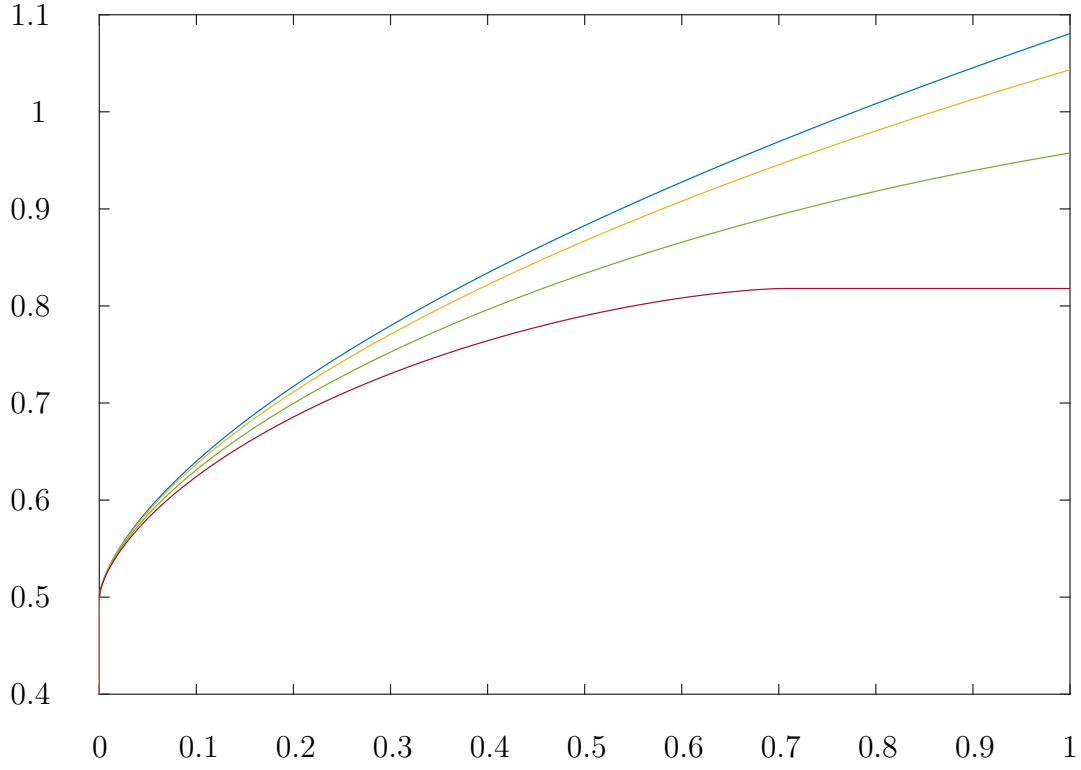


Figure 73: Free-streamline plots for cavity with horizontal wall closure. From top to bottom:  
 $K = 0, 0.4, 0.8, 1.2$ .

$K$	$U$	$\phi_B$	$x_C$	bubble width	drag coeff., $c_D$
0	1	0.140	$3.73 \times 10^{31}$	$3.05 \times 10^{15}$	0.880
0.4	0.845	0.138	4.64	3.09	1.24
0.8	0.745	0.134	1.38	2.00	1.60
1.2	0.674	0.130	0.70	1.64	1.96

Table 5: Results for cavity with horizontal wall closure

[1958]. Recall that it has also been discussed that an extra constraint is required. This is since there is an extra degree of freedom introduced due to the asymmetry of the problem, now that the plate is at an arbitrary angle of attack and so the position of the stagnation point along the plate is not known *a priori*. Wu [1956] and Mimura [1958] impose that the velocity potential is the same at both of the closure points. We will later move to include gravity in the problem and we will use this condition as one of the possibilities for the extra constraint required there — again, since it is an asymmetric problem but now this asymmetry arises from the inclusion of gravity. First, we will reconsider the zero-gravity case of the flat plate that is normal to the stream, but using alternative methods.

### 4.2.2 Finite Hilbert transform method

We consider the same problem as in the previous section, i.e. as depicted in figure 71a. However, for convenience of the method presented here, this time we non-dimensionalise such that we have unit incoming horizontal flow and unit plate length. We denote by  $q_c$  the (non-dimensional) flow speed along the free streamlines. We still retain the definition of the complex potential  $f$  as before with  $\psi = 0$  along the dividing streamline and  $\phi = 0$  at the stagnation point  $S$ . Then, we define  $\Omega = \tau - i\theta$  through  $u - iv = \exp(\tau - i\theta)$ , where  $u$  and  $v$  are the horizontal and vertical components of the velocity. It follows that, along the free streamlines, we have  $\tau = \log q_c$ . To find the free streamlines, it remains to solve for  $\theta$  along  $BC$  and  $B'C'$ .

We can write down the Bernoulli condition along the free streamlines as

$$q_c^2 = K + 1, \quad (4.8)$$

noting that the cavitation number  $K$  is as previously defined. This can be rewritten as

$$e^{2\tau} = K + 1, \quad (4.9)$$

along  $BC$  and  $B'C'$ . Now, we wish to obtain another expression for  $\tau$  along the free streamlines. The Cauchy integral formula will be of use and is stated below.

**Theorem 1** (*Cauchy Integral Formula*) *Let  $f(z)$  be a holomorphic function inside and on the closed contour  $\gamma$  oriented counterclockwise. Then, for every  $a$  in the interior of  $\gamma$ ,*

$$f(a) = \frac{1}{2\pi i} \oint_{\gamma} \frac{f(z)}{z - a} dz. \quad (4.10)$$

Since we have uniform horizontal flow in the far-field of unit speed, then we have that  $\tau - i\theta \rightarrow 0$  in the far-field. We apply the Cauchy integral formula to  $\Omega(\phi)$  for  $\phi \in \mathbb{R}$  in the  $f$ -plane with the contour  $\tilde{C} = [-R, \phi - \epsilon] \cup C_{\epsilon} \cup [\phi + \epsilon, R] \cup C_R$  as depicted in figure 74. The contour is traversed anti-clockwise and we consider the limit as  $R \rightarrow +\infty$  and  $\epsilon \rightarrow 0$ . Note that these calculations are



with reference to the upper free streamline  $BC$ . For  $\phi \in \mathbb{R}$ , on the contour  $\tilde{C}$ , we have

$$\begin{aligned}
(\tau - i\theta)(\phi) &= \frac{1}{2\pi i} \oint_{\tilde{C}} \frac{\tau(\varphi) - i\theta(\varphi)}{\varphi - \phi} d\varphi \\
&= \frac{1}{2\pi i} \lim_{R \rightarrow \infty} \left[ \text{P.V.} \int_{-R}^R \frac{\tau(\varphi) - i\theta(\varphi)}{\varphi - \phi} d\varphi + \int_{C_R} \frac{\tau(\varphi) - i\theta(\varphi)}{\varphi - \phi} d\varphi \right] \\
&\quad + \frac{1}{2\pi i} \lim_{\epsilon \rightarrow 0} \int_{-\pi}^0 \frac{(\tau - i\theta)(\phi + \epsilon e^{i\gamma})}{\phi + \epsilon e^{i\gamma} - \phi} i\epsilon e^{i\gamma} d\gamma \\
&= \frac{1}{2\pi i} \text{P.V.} \int_{-\infty}^{\infty} \frac{\tau(\varphi) - i\theta(\varphi)}{\varphi - \phi} d\varphi + \frac{i}{2\pi} \int_{-\pi}^0 (\tau - i\theta)(\phi) d\gamma \\
&= \frac{1}{2\pi i} \text{P.V.} \int_{-\infty}^{\infty} \frac{\tau(\varphi) - i\theta(\varphi)}{\varphi - \phi} d\varphi + \frac{1}{2} (\tau - i\theta)(\phi).
\end{aligned} \tag{4.11}$$

It follows that

$$\tau(\phi) - i\theta(\phi) = \frac{1}{\pi i} \text{P.V.} \int_{-\infty}^{\infty} \frac{\tau(\varphi) - i\theta(\varphi)}{\varphi - \phi} d\varphi. \tag{4.12}$$

Taking the real part of (4.12), we find

$$\tau(\phi) = -\frac{1}{\pi} \text{P.V.} \int_{-\infty}^{\infty} \frac{\theta(\varphi)}{\varphi - \phi} d\varphi. \tag{4.13}$$

Further to this, since  $\theta = 0$  for  $\phi \in (-\infty, 0]$  and  $[\phi_C, \infty)$ , and  $\theta = \pi/2$  on  $[0, \phi_B]$ , then we have

$$\tau(\phi) = -\frac{1}{\pi} \int_0^{\phi_B} \frac{\frac{\pi}{2}}{\varphi - \phi} d\varphi - \frac{1}{\pi} \text{P.V.} \int_{\phi_B}^{\phi_C} \frac{\theta(\varphi)}{\varphi - \phi} d\varphi, \tag{4.14}$$

along  $BC$ . Finally, the Bernoulli condition (4.9) along the upper free streamline for  $\phi_B < \phi < \phi_C$  becomes

$$\frac{1}{\pi} \text{P.V.} \int_{\phi_B}^{\phi_C} \frac{\theta(\varphi)}{\varphi - \phi} d\varphi = -\left[ \frac{1}{2} \log(K+1) + \frac{1}{2} \log\left(\frac{\phi - \phi_B}{\phi}\right) \right]. \tag{4.15}$$

Reordering the terms in the denominator of the integral on the left-hand side gives rise to

$$\frac{1}{\pi} \text{P.V.} \int_{\phi_B}^{\phi_C} \frac{\theta(\varphi)}{\phi - \varphi} d\varphi = \frac{1}{2} \log(K+1) + \frac{1}{2} \log\left(\frac{\phi - \phi_B}{\phi}\right). \tag{4.16}$$

The Bernoulli condition has been rewritten in this way to emphasise the fact that we have a finite Hilbert transform of  $\theta$  on the left-hand side. We now look to find  $\theta(\phi)$  through use of an inversion formula for the transform.

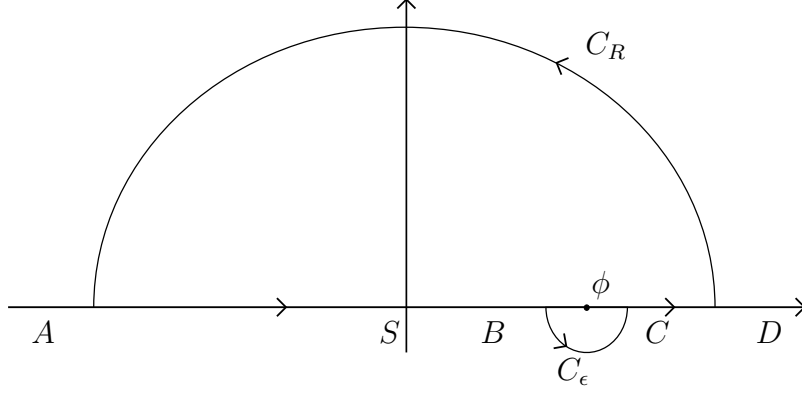


Figure 74:  $f$ -plane for lower free streamline

For ease of calculation, we first rescale by introducing variables  $\tilde{\varphi}$  and  $\tilde{\phi}$  and then setting  $\varphi = \phi_B + (\phi_C - \phi_B)\tilde{\varphi}$  and  $\phi = \phi_B + (\phi_C - \phi_B)\tilde{\phi}$ . We also define  $\theta(\phi) = \tilde{\theta}(\tilde{\phi})$ . Then, (4.16) becomes

$$\frac{1}{\pi} \text{P.V.} \int_0^1 \frac{\tilde{\theta}(\tilde{\varphi})}{\tilde{\phi} - \tilde{\varphi}} d\tilde{\varphi} = \frac{1}{2} \log(K+1) + \frac{1}{2} \log \left( \frac{R\tilde{\phi}}{1 + R\tilde{\phi}} \right), \quad (4.17)$$

where  $R = (\phi_C - \phi_B)/\phi_B$ . We denote by  $F(\tilde{\phi})$  the right-hand side of the integral equation (4.17), i.e.

$$F(\tilde{\phi}) = \frac{1}{2} \log(K+1) + \frac{1}{2} \log \left( \frac{R\tilde{\phi}}{1 + R\tilde{\phi}} \right). \quad (4.18)$$

Now, we look to solve this integral equation for  $\theta$  along the upper free streamline  $BC$  through use of the following inversion formula for the finite Hilbert transform provided by Tricomi [1985]. In its general form, Tricomi [1985] gives that for

$$Hf(s) = \frac{1}{\pi} \text{P.V.} \int_a^b \frac{f(t)}{s-t} dt, \quad (4.19)$$

we have

$$f(t) = \frac{1}{\pi \sqrt{(t-a)(b-t)}} \left( \int_a^b \frac{Hf(s)}{s-t} \sqrt{(s-a)(b-s)} ds + \int_a^b f(s) ds \right). \quad (4.20)$$

Therefore, in our case we have

$$\tilde{\theta}(\tilde{\phi}) = \frac{1}{\pi \sqrt{\tilde{\phi}(1-\tilde{\phi})}} \left( \int_0^1 \frac{F(s)}{s-\tilde{\phi}} \sqrt{s(1-s)} ds + c \right), \quad (4.21)$$

where  $c$  is an unknown constant.

We require that  $\tilde{\theta}$  is finite at  $\tilde{\phi} = 0$  and  $\tilde{\phi} = 1$ , so we can see from (4.21) that we need to set the expression within the bracket of (4.21) to zero at the two aforementioned values of  $\tilde{\phi}$ . It follows that we have

$$\int_0^1 F(s) \sqrt{\frac{1-s}{s}} ds + c = 0 \quad (4.22)$$

and

$$\int_0^1 F(s) \sqrt{\frac{s}{1-s}} ds - c = 0. \quad (4.23)$$

It follows that we can eliminate the constant  $c$  from (4.22) and (4.23) and, recalling the definition of the function  $F(\tilde{\phi})$  from (4.18), we obtain

$$\begin{aligned} \int_0^1 \left[ \frac{1}{2} \log(K+1) + \frac{1}{2} \log \left( \frac{Rs}{1+Rs} \right) \right] \sqrt{\frac{1-s}{s}} ds \\ + \int_0^1 \left[ \frac{1}{2} \log(K+1) + \frac{1}{2} \log \left( \frac{Rs}{1+Rs} \right) \right] \sqrt{\frac{s}{1-s}} ds = 0. \end{aligned} \quad (4.24)$$

Noting that  $\int_0^1 \sqrt{s/(1-s)} ds = \int_0^1 \sqrt{(1-s)/s} ds = \pi/2$ , then we find

$$\frac{\pi}{2} \log(K+1) = \int_0^1 \frac{1}{2} \log \left( 1 + \frac{1}{Rs} \right) \left[ \sqrt{\frac{1-s}{s}} + \sqrt{\frac{s}{1-s}} \right] ds. \quad (4.25)$$

By evaluating the integral above and simplifying, we obtain

$$\log(K+1) = 2 \log(1 + \sqrt{1+R}) - \log R, \quad (4.26)$$

which provides a relation between the constants  $R$  and  $K$ .

From (4.21), along with (4.22) and (4.23), we have

$$\tilde{\theta}(\tilde{\phi}) = \frac{1}{\pi} \sqrt{\frac{\tilde{\phi}}{1-\tilde{\phi}}} \text{P.V.} \int_0^1 \frac{\frac{1}{2} \log(K+1) + \frac{1}{2} \log \left( \frac{Rs}{1+Rs} \right)}{s - \tilde{\phi}} \sqrt{\frac{1-s}{s}} ds \quad (4.27)$$

and

$$\tilde{\theta}(\tilde{\phi}) = \frac{1}{\pi} \sqrt{\frac{1-\tilde{\phi}}{\tilde{\phi}}} \text{P.V.} \int_0^1 \frac{\frac{1}{2} \log(K+1) + \frac{1}{2} \log\left(\frac{Rs}{1+Rs}\right)}{s-\tilde{\phi}} \sqrt{\frac{s}{1-s}} ds. \quad (4.28)$$

Therefore, for a given value of  $K$ , using either (4.27) or (4.28) along with (4.26), we can obtain the values of  $\tilde{\theta}(\tilde{\phi})$  along the upper free streamline  $BC$ . To actually evaluate the principle value integral to obtain values of  $\tilde{\theta}$ , we can rewrite the integral as follows:

$$\begin{aligned} \tilde{\theta}(\tilde{\phi}) &= \frac{1}{\pi} \sqrt{\frac{\tilde{\phi}}{1-\tilde{\phi}}} \left[ \int_0^1 \frac{F(s) - F(\tilde{\phi})}{s-\tilde{\phi}} \sqrt{\frac{1-s}{s}} ds + \text{P.V.} \int_0^1 \frac{F(\tilde{\phi})}{s-\tilde{\phi}} \sqrt{\frac{1-s}{s}} ds \right] \\ &= \frac{1}{\pi} \sqrt{\frac{\tilde{\phi}}{1-\tilde{\phi}}} \int_0^1 \frac{1}{2} \frac{\log\left(1 + \frac{1}{R\tilde{\phi}}\right) - \log\left(1 + \frac{1}{Rs}\right)}{s-\tilde{\phi}} \sqrt{\frac{1-s}{s}} ds - F(\tilde{\phi}) \sqrt{\frac{\tilde{\phi}}{1-\tilde{\phi}}}. \end{aligned} \quad (4.29)$$

Using the fact that  $df/dz = u - iv = \exp(\tau - i\theta)$  and that  $\tau = \frac{1}{2} \log(K+1)$  along the free streamlines, we can then integrate to find the values of  $z$  along the free streamlines which we can subsequently plot. We also wish to normalise such that we have a plate of unit length. To achieve this, we note that from (4.14) and for  $0 < \phi < \phi_B$  (or  $0 < \tilde{\phi} < 1$ ) we have

$$\begin{aligned} \tau(\phi) &= -\frac{1}{2} \log \left| \frac{\phi_B - \phi}{\phi} \right| - \frac{1}{\pi} \int_{\phi_B}^{\phi_C} \frac{\theta(\varphi)}{\varphi - \phi} d\varphi \\ &= \frac{1}{\pi} \int_0^1 \frac{\tilde{\theta}(s)}{\tilde{\theta} - s} ds + \frac{1}{2} \log \left| 1 + \frac{1}{R\tilde{\phi}} \right|. \end{aligned} \quad (4.30)$$

This can then be used to set the scale in the physical  $z$ -plane by integrating  $dz/df$  along the plate section  $OB$  (again, noting that  $\theta = \pi/2$  here) to obtain the unscaled length of half of the plate. Hence, we can set the scale factor such that the plate is of unit length. Note that we can set  $K$  as the parameter and find the corresponding value of  $R$  by (4.26) to then be used in the expressions for  $\tau$  and  $\theta$  along the free streamline when evaluating to find  $z$  along  $BC$  and  $B'C'$ . The upper free streamline for  $K = 1$ , plotted using the method presented here, is shown figure 75.

The method of inverting the finite Hilbert transform is presented here not only to showcase an alternative method of solution for this particular problem, but also to possibly prompt the solution of other potential flow problems using this approach. However, most relevant to the current problem, an example of when this method of inverting the finite Hilbert transform may be

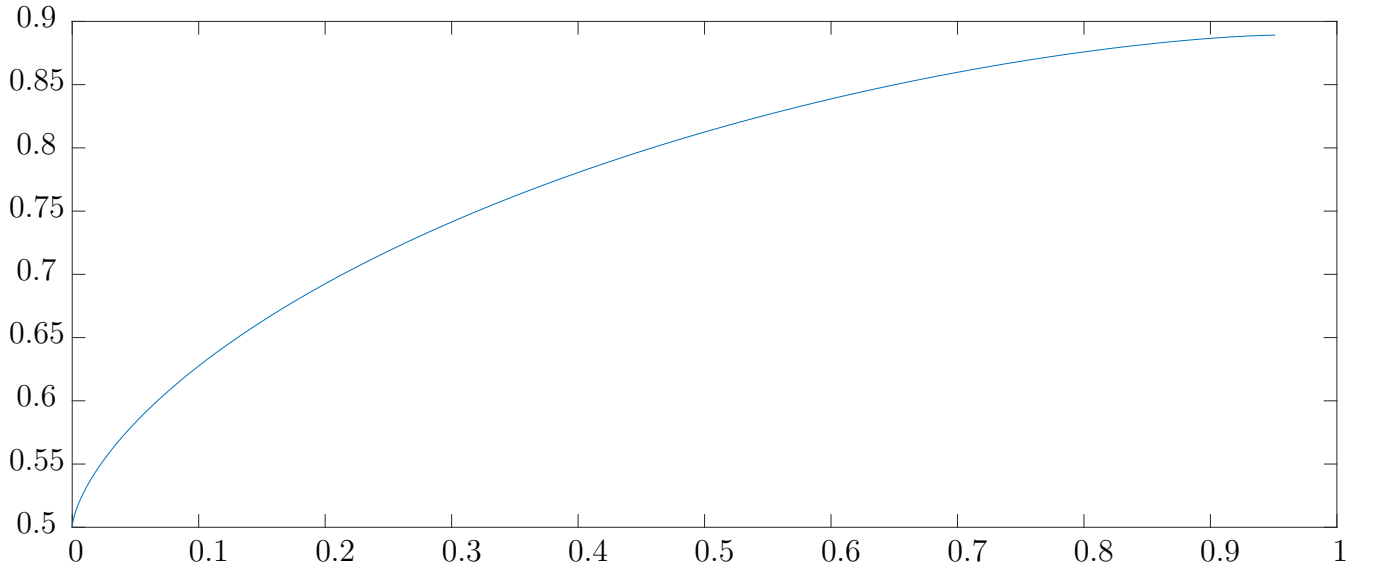


Figure 75: Profile of the upper free streamline for  $K = 1$ , obtained through the method of inverting the finite Hilbert transform.

useful is if a more generalised plate shape and/or angle of attack is involved. This would retain the assumptions and closure model taken for the far-field and so it would only be the known values of  $\theta$  along the finite-length plate that would change. This would affect the function of  $\phi$  on the right-hand side of (4.16). Whether an analytic solution exists will depend on the form of this function of  $\phi$ .

We will now consider the same zero-gravity problem of a finite-length plate normal to the stream yet again, but this time using a method that leads to a numerical solution. It is a modification to the approach used in the current section and so it could be used to obtain a numerical solution for a more generalised plate shape if an analytical solution is not attainable, as discussed above.

### 4.2.3 Matrix inversion method

Before moving on to develop the complexity of the problem of flow past the finite-length plate normal to the stream, we present a third method of solution for the zero-gravity case. As opposed to the conformal mappings method and the method of inverting the finite Hilbert transform, here we will obtain a numerical solution. Numerical methods will be necessary later where the assumptions will not allow for the utilisation of the analytic methods discussed so far. The approach begins as in the previous section, i.e. we use the Cauchy integral formula to integrate along a contour in the complex potential plane and, via the Bernoulli condition, obtain an integral equation to find  $\theta$  along the free streamlines. Therefore, we pick up the method from (4.17), repeated below for convenience:

$$\frac{1}{\pi} \text{P.V.} \int_0^1 \frac{\tilde{\theta}(s)}{\tilde{\phi} - s} ds = \frac{1}{2} \log(K+1) + \frac{1}{2} \log \left( \frac{R\tilde{\phi}}{1 + R\tilde{\phi}} \right), \quad (4.31)$$

where  $R = (\phi_C - \phi_B)/\phi_B$ . To solve for  $\theta$  along the free streamlines, we simply introduce  $N$  mesh points along  $BC$ . Note that we only discretise along the upper free streamline since the problem is symmetric. We let  $\tau_c = \frac{1}{2} \log(K+1)$  (c.f. (4.9)) and we leave this to be found as part of the solution, so we have  $N+1$  unknowns. Recall that, along the upper streamline, we have  $0 < \tilde{\phi} < 1$ , so we introduce the mesh points

$$\tilde{\phi}_i = \frac{i-1}{N-1}, \quad \text{where } i = 1, 2, \dots, N. \quad (4.32)$$

Corresponding to these points, we have the following unknown values of  $\theta$  along  $BC$ :  $\tilde{\theta}_i = \tilde{\theta}(\tilde{\phi}_i)$  for  $i = 1, 2, \dots, N$ . We also define the intermediate mesh points

$$\tilde{\phi}_i^{\text{inter}} = \frac{i - \frac{1}{2}}{N-1}, \quad \text{where } i = 1, 2, \dots, N-1, \quad (4.33)$$

at which we will satisfy the integral equation (4.31). On top of these  $N-1$  equations, we also have  $\tilde{\theta}_1 = \pi/2$  and  $\tilde{\theta}_N = 0$  due to the known values at the end of the plate at  $B$  and at the closure point  $C$ . Then, we have  $N+1$  equations. To form the matrix equation, we note that for

$j = 1, 2, \dots, N - 1$  we can first rewrite the integral of the (4.31) as

$$\begin{aligned} \frac{1}{\pi} \text{P.V.} \int_0^1 \frac{\tilde{\theta}(s)}{\tilde{\phi}_j^{\text{inter}} - s} ds &= \frac{1}{\pi} \sum_{i=2}^N \text{P.V.} \int_{\tilde{\phi}_{i-1}}^{\tilde{\phi}_i} \frac{\tilde{\theta}(s)}{\tilde{\phi}_j^{\text{inter}} - s} ds \\ &= \frac{1}{\pi} \left[ \tilde{\theta}_1(L_{1j} + A_{2j}) + \sum_{i=2}^{N-1} \tilde{\theta}_i(A_{i+1,j} - A_{ij}) + \tilde{\theta}_N(-(L_{Nj} + A_{Nj})) \right], \end{aligned} \quad (4.34)$$

where  $L_{ij} = \log |\tilde{\phi}_j^{\text{inter}} - \tilde{\phi}_i|$ ,  $N_{ij} = -(\tilde{\phi}_i - \tilde{\phi}_j^{\text{inter}}) \log |\tilde{\phi}_j^{\text{inter}} - \tilde{\phi}_i|$  and  $A_{ij} = \Delta N_{ij} / \Delta \tilde{\phi}_i + 1$ . Then, the matrix equation can be formed and the set of solution values is found simply by inverting the  $(N + 1) \times (N + 1)$  matrix and evaluating

$$\begin{pmatrix} \tilde{\theta}_1 \\ \tilde{\theta}_2 \\ \tilde{\theta}_3 \\ \vdots \\ \tilde{\theta}_N \\ \tau_c \end{pmatrix} = M^{-1} \begin{pmatrix} \frac{\pi}{2} \\ -\frac{1}{2} \log \left( 1 + \frac{1}{R\tilde{\phi}_1^{\text{inter}}} \right) \\ -\frac{1}{2} \log \left( 1 + \frac{1}{R\tilde{\phi}_2^{\text{inter}}} \right) \\ \vdots \\ -\frac{1}{2} \log \left( 1 + \frac{1}{R\tilde{\phi}_{N-1}^{\text{inter}}} \right) \\ 0 \end{pmatrix}, \quad (4.35)$$

where

$$M = \begin{pmatrix} 1 & 0 & \dots & 0 & 0 & 0 \\ \frac{1}{\pi}(L_{11} + A_{21}) & \frac{1}{\pi}(A_{31} - A_{21}) & \dots & \frac{1}{\pi}(A_{N1} - A_{N-1,1}) & -\frac{1}{\pi}(L_{N1} + A_{N1}) & -1 \\ \frac{1}{\pi}(L_{12} + A_{22}) & \frac{1}{\pi}(A_{32} - A_{22}) & \dots & \frac{1}{\pi}(A_{N2} - A_{N-1,2}) & -\frac{1}{\pi}(L_{N2} + A_{N2}) & -1 \\ \vdots & \vdots & \dots & \vdots & \vdots & \vdots \\ \frac{1}{\pi}(L_{1N} + A_{2N}) & \frac{1}{\pi}(A_{3N} - A_{2N}) & \dots & \frac{1}{\pi}(A_{NN} - A_{N-1,N}) & -\frac{1}{\pi}(L_{NN} + A_{NN}) & -1 \\ 0 & 0 & \dots & 0 & 1 & 0 \end{pmatrix}. \quad (4.36)$$

Note that, here, the parameter is  $R$  (instead of  $K$  as in the previous methods). The value of  $K$  can be obtained once the value of  $\tau_c$  is found through  $\tau_c = \frac{1}{2} \log(K + 1)$ .

Alternatively, we could pick up the method from (4.16), i.e. the integral equation before rescaling the variables. To solve for  $\theta$  along the free streamlines, we introduce  $N$  mesh points

along  $BC$ . We recall that, along this streamline we have  $\phi_B < \phi < \phi_C$ , so we introduce the mesh points

$$\phi_i = \phi_B + (\phi_C - \phi_B) \frac{i-1}{N-1}, \quad \text{where } i = 1, 2, \dots, N. \quad (4.37)$$

As before, we have  $N$  unknown values of  $\theta$  along  $BC$ , i.e.  $\theta_i = \theta(\phi_i)$  for  $i = 1, 2, \dots, N$ . Overall, with the addition of  $\phi_B$  and  $\phi_C$  to the list of unknowns, we have  $N+2$  unknowns. We also define the intermediate mesh points

$$\phi_i^{\text{inter}} = \phi_B + (\phi_C - \phi_B) \frac{i - \frac{1}{2}}{N-1}, \quad \text{where } i = 1, 2, \dots, N-1. \quad (4.38)$$

The integral equation for  $\theta$  is satisfied at these intermediate points. On top of these  $N-1$  equations, we also have  $\theta_1 = \pi/2$  and  $\theta_N = 0$ . Then, we have  $N+2$  equations with the inclusion of setting  $y_B = 0.5$  (due to the normalisation that gives a unit-length plate and since  $y_B$  denotes the value of  $y$  at  $B$ ). This system of  $N+2$  equations in  $N+2$  unknowns can simply be solved numerically with  $K$  being the parameter that we set. This approach is mentioned here since it will be utilised later in cases where the assumptions are not sufficiently simplified for the earlier methods to be employed. It is the easiest and quickest method to adapt for a flat plate at an arbitrary angle of attack. This method is also advantageous in terms of the minimal calculations required once the integral equation has been formed and extra scaling in post-processing is not required since the normalisation with respect to the plate length is included in the set of equations to be solved.

---

In this chapter, we have considered zero-gravity cavity and wake flows. Discussion in §4.1 of the method of solution in the case of the cavity of ambient pressure introduced the most basic form of the problem where conformal mappings are utilised to obtain the exact solution. In the following three subsections, the problem has been developed such that the cavity is no longer at ambient pressure and we have included an open-wake model. In each of the three subsections, this problem has been considered with a different method of solution. An analytic solution is obtainable, again by conformal mappings. An analytic solution has also been achieved through use of the Cauchy integral formula to reach a boundary integral equation that involves a finite Hilbert transform



of the flow angle. This finite Hilbert transform has then been inverted to obtain the flow angle along the cavity boundaries and hence, the solution. The applicability of this method to other similar problems has been discussed. The final method that has been presented is discretising the boundary integral equation and then solving for the unknown flow angles along the cavity boundaries by collocation, leading to a numerical solution. This approach will be used in the next chapter where gravity is introduced to the model.

## 5 Gravitational cavity and wake flows

In the final mathematical contribution of this thesis, we include the effects of gravity on the flows where we have a cavity or wake that forms behind a flat, finite-length plate that is either normal or oblique to a horizontal stream. First, in §5.1, we include gravity on the boundaries of the cavity or wake. Note that, in this case, we still consider an unbounded horizontal stream. Then, the problem is discussed in §5.2 where we have a submerged, finite-length plate that is normal to the horizontal stream which is bounded above by a free surface. We limit the model at this point to only consider the case of a wake (not a cavity) forming behind the plate.

### 5.1 Cavity horizontal closure

Here, we include gravity along the cavity or wake boundaries that form behind a flat, finite-length plate that is normal to (see §5.1.1) or at an arbitrary angle to (see §5.1.2) the unbounded, uniform, horizontal stream. As was the case in chapter 4, whilst the calculations of this section (§5.1) are applicable to both cases of a wake or cavity forming behind the plate, we will refer only to the cavity case. Conformal mappings and a boundary integral equation method are utilised here whilst in pursuit of a numerical solution. Due to the asymmetry of the problem, an extra condition on the flow will be required. Discussion will be presented for possible options for this condition. In particular, we propose using either a condition derived from imposing that the dividing streamline is horizontal far upstream, a condition to impose equal velocity potential at the closure points or an interpolation formula for the value at a collocation point on the cavity boundaries.

#### 5.1.1 Plate perpendicular to flow

The inclusion of the effects of gravity on the boundaries of the cavity means we are now considering a problem with asymmetry. As before, we set the horizontal stream to have speed  $U$  and we set the vertical, finite-length plate normal to the flow to be of length  $L$ . The open-wake model comprising of two horizontal walls (or streamlines) far downstream is employed, i.e. the open-wake closure model. This scenario is as depicted in figure 76a with the closure along  $CD$  and  $C'D'$ . Note that the stagnation point, at which the dividing streamline  $AS$  meets the plate  $BB'$ , is set at  $z = 0$ .

Along the free surfaces that bound the cavity, we have

$$\frac{1}{2}\rho q^2 + \rho g y + p_c = \frac{1}{2}\rho U^2 + p_\infty, \quad (5.1)$$

where  $\rho$  is the density,  $q$  is the magnitude of the (dimensional) velocity,  $g$  is the acceleration due to gravity and  $p_c$  is the pressure in the cavity. We also use  $p_\infty = \rho g y_0 + p_0$  to denote the pressure far upstream along the horizontal dividing streamline, where  $y_0$  and  $p_0$  are the constant values of  $y$  and pressure  $p$  along the dividing streamline far upstream. We non-dimensionalise the variables with respect to the speed  $U$  of the flow far upstream and the length  $L$  of the plate; and we define the Froude number  $F$  and cavitation number  $K$  by

$$F = \frac{U}{\sqrt{gL}} \quad \text{and} \quad K = \frac{p_\infty - p_c}{\frac{1}{2}\rho U^2}, \quad (5.2)$$

respectively. Then, the Bernoulli condition along the free surfaces bounding the cavity is

$$\frac{1}{2}q^2 + \frac{y}{F^2} = \frac{1}{2}(K + 1), \quad (5.3)$$

where  $q$  is the magnitude of velocity. Note that  $q = e^\tau$  and so we can write

$$\tau(w) = \frac{1}{2} \log \left( K + 1 - \frac{2}{F^2} y(w) \right). \quad (5.4)$$

As usual, we define the complex potential by  $f = \phi + i\psi$  and so we can sketch this plane as in figure 76b. The flow region is mapped to the whole  $f$ -plane with a branch cut along the positive real-axis. The values of the velocity potential  $\phi$  at the edges of the plate and the points of cavity closure ( $C$  and  $C'$ ) are unknowns to be found.

We introduce the  $w$ -plane (c.f. figure 76c), where  $w = f^{1/2}$ . Therefore, the flow region is mapped to the upper-half of the  $w$ -plane. The dividing streamline  $AS$  is mapped to the positive imaginary-axis; and the plate  $BB'$  and the cavity boundaries are mapped to the real axis.

Recall that we define  $u - iv = e^\Omega = e^{\tau - i\theta}$ . We then apply the Cauchy integral formula to  $\Omega(w)$  for  $w \in \mathbb{R}$  in the  $w$ -plane with the contour  $\tilde{C} = [-R, w - \epsilon] \cup C_\epsilon \cup [w + \epsilon, R] \cup C_R$ , consisting of

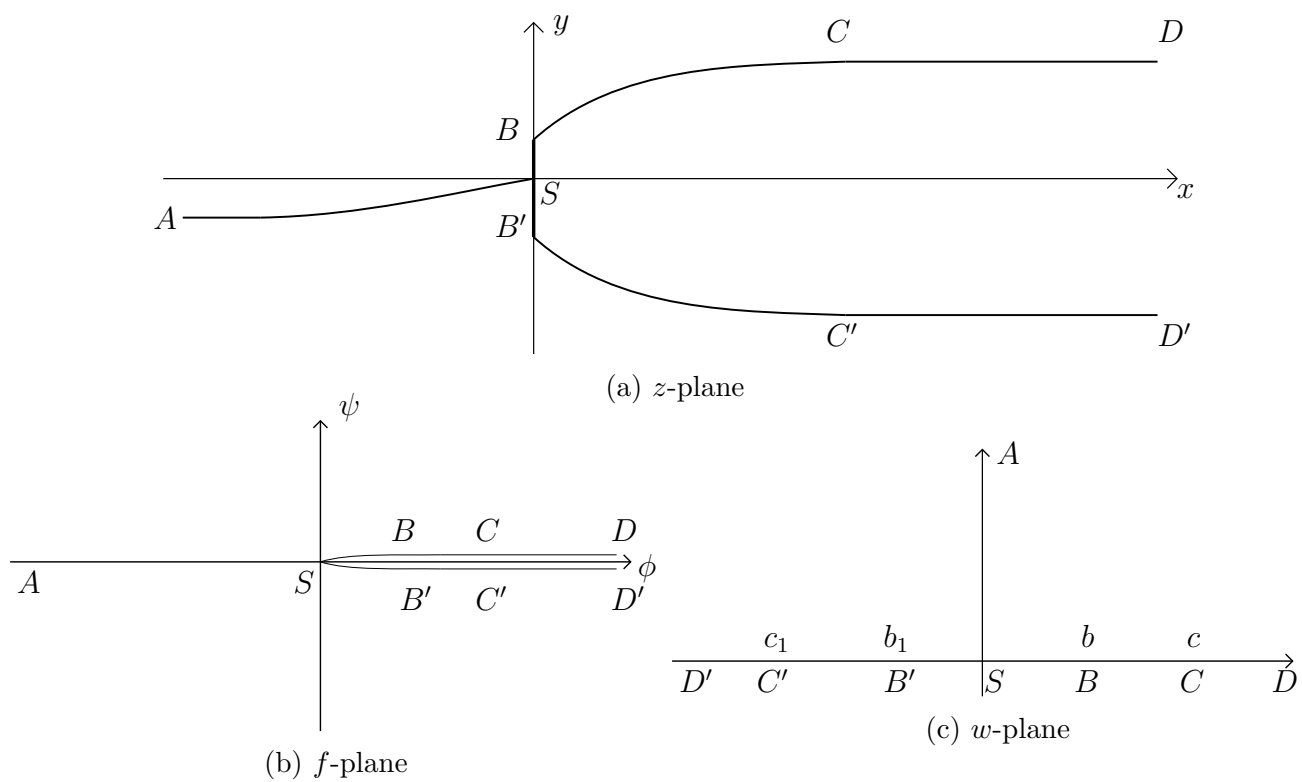


Figure 76: Complex planes for horizontal wall cavity closure with  $g \neq 0$ .

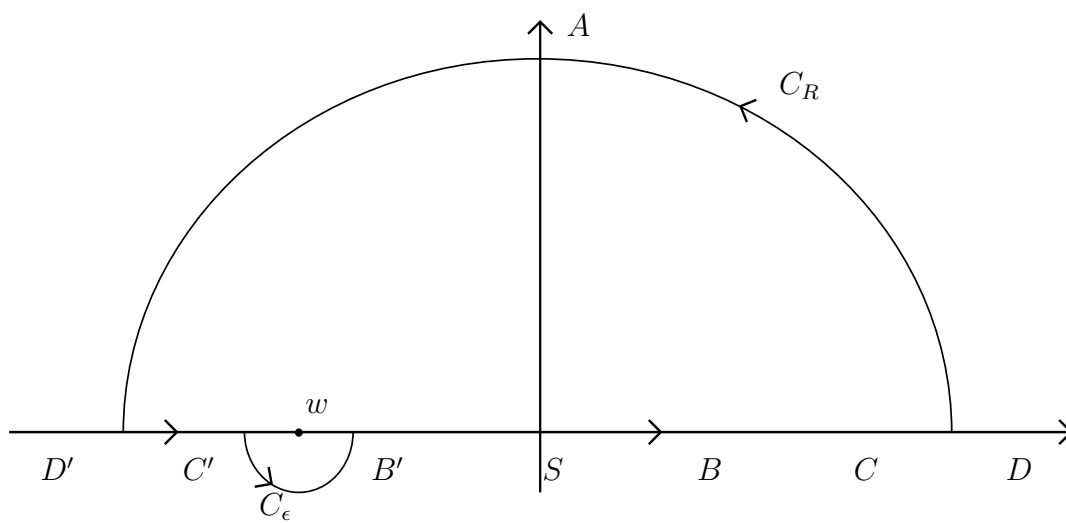


Figure 77:  $w$ -plane with contour  $\tilde{C} = [-R, w - \epsilon] \cup C_\epsilon \cup [w + \epsilon, R] \cup C_R$

semi-circular arcs  $C_R$  (of radius  $R$  centred at the origin) and  $C_\epsilon$  (of radius  $\epsilon$  centred at  $w$ ); and intervals  $[-R, w - \epsilon]$  and  $[w + \epsilon, R]$  along the real axis (c.f. figure 77). The contour is traversed anti-clockwise and we consider the limit as  $R \rightarrow \infty$ . Then, for  $w \in \mathbb{R}$ , on the contour  $\tilde{C}$ , we obtain that

$$(\tau - i\theta)(w) = \frac{1}{\pi i} P.V. \int_{-\infty}^{\infty} \frac{\tau(\sigma) - i\theta(\sigma)}{\sigma - w} d\sigma. \quad (5.5)$$

The calculation leading to this is very similar to that of (4.11) — recall that we use that the flow is horizontal and of unit speed in the far-field, hence  $\tau$  and  $\theta$  tend towards zero in the far-field. It follows that we have

$$\tau(w) = -\frac{1}{\pi} P.V. \int_{-\infty}^{\infty} \frac{\theta(\sigma)}{\sigma - w} d\sigma \quad (5.6)$$

along the boundaries of the cavity. We also recall that the angle of flow is zero along the horizontal closures  $CD$  and  $C'D'$ ;  $\frac{1}{2}\pi$  along the upper section  $OB$  of the plate; and  $-\frac{1}{2}\pi$  along  $OB'$ . Then, the integral expression for  $\tau$  can be simplified to

$$\begin{aligned} \tau(w) &= -\frac{1}{\pi} \left[ \int_{c_1}^{b_1} \frac{\theta(\sigma)}{\sigma - w} d\sigma + \int_b^c \frac{\theta(\sigma)}{\sigma - w} d\sigma \right] + \frac{1}{2} \int_{b_1}^0 \frac{1}{\sigma - w} d\sigma - \frac{1}{2} \int_0^b \frac{1}{\sigma - w} d\sigma \\ &= -\frac{1}{\pi} \left[ \int_{c_1}^{b_1} \frac{\theta(\sigma)}{\sigma - w} d\sigma + \int_b^c \frac{\theta(\sigma)}{\sigma - w} d\sigma \right] + \frac{1}{2} \log \left| \frac{w^2}{(b_1 - w)(b - w)} \right|, \end{aligned} \quad (5.7)$$

where  $b$ ,  $b_1$ ,  $c$  and  $c_1$  are the values of  $w$  corresponding to the points  $B$ ,  $B'$ ,  $C$  and  $C'$ , respectively. In (5.7),  $\theta$  is to be determined for  $c_1 < w < b_1$  and  $b < w < c$ , i.e. along the cavity boundaries. By equating (5.4) and (5.7), we obtain the following integral equation:

$$-\frac{1}{\pi} \left[ \int_{c_1}^{b_1} \frac{\theta(\sigma)}{\sigma - w} d\sigma + \int_b^c \frac{\theta(\sigma)}{\sigma - w} d\sigma \right] + \frac{1}{2} \log \left| \frac{w^2}{(b_1 - w)(b - w)} \right| = \frac{1}{2} \log \left( K + 1 - \frac{2}{F^2} y(w) \right), \quad (5.8)$$

for  $w \in \mathbb{R}$ . The values for  $y$  in (5.8) can found by evaluating

$$y(w) = \int_0^w 2\sigma e^{-\tau(\sigma)} \sin(\theta(\sigma)) d\sigma. \quad (5.9)$$

To determine  $\theta$  along the cavity boundaries, we introduce mesh points

$$w_j^U = b + \frac{c-b}{N-1}(j-1) \quad \text{and} \quad w_j^L = b_1 + \frac{c_1-b_1}{N-1}(j-1), \quad (5.10)$$

where  $j = 1, 2, \dots, N$ . Then, we look to determine  $\theta_j^U = \theta(w_j^U)$  and  $\theta_j^L = \theta(w_j^L)$  for  $j = 1, 2, \dots, N$ , i.e. the values of  $\theta$  at the mesh points. The other unknowns to be found are  $b$ ,  $b_1$ ,  $c$  and  $c_1$ , taking the total number of unknowns to  $2N + 4$ . Collocation points are now introduced, in order to discretise equation (5.8), as follows:

$$w_i^{U_{\text{inter}}} = b + \frac{c-b}{(N-1)}\left(i - \frac{1}{2}\right) \quad \text{and} \quad w_i^{L_{\text{inter}}} = b_1 + \frac{c_1-b_1}{(N-1)}\left(i - \frac{1}{2}\right), \quad (5.11)$$

for  $i = 1, 2, \dots, N-1$ . Satisfying equation (5.8) at these collocation points gives rise to  $2N-2$  equations. For the necessary number of equations for a square system to find the  $2N+4$  unknowns, the remaining six equations are comprised of

1. the known flow angles at the vertical plate ends, i.e.  $\theta(b) = \frac{1}{2}\pi$ ,  $\theta(b_1) = -\frac{1}{2}\pi$ ,  $\theta(c) = 0$  and  $\theta(c_1) = 0$ ; which can be rewritten as  $\theta_1^U = \frac{1}{2}\pi$ ,  $\theta_1^L = -\frac{1}{2}\pi$ ,  $\theta_N^U = 0$  and  $\theta_N^L = 0$ ;
2. the vertical plate is of unit length, i.e.  $y(b) - y(b_1) = 1$ , which can be rewritten as

$$\int_0^b 2\sigma e^{-\tau(\sigma)} d\sigma + \int_0^{b_1} 2\sigma e^{-\tau(\sigma)} d\sigma = 1; \quad (5.12)$$

3. and imposing either

$$\int_{c_1}^{b_1} \theta(\sigma) d\sigma + \int_b^c \theta(\sigma) d\sigma + \frac{\pi}{2}(b + b_1) = 0, \quad (5.13)$$

$$c = -c_1, \quad (5.14)$$

or

$$\theta_n^U = \frac{1}{2}(\theta_{n-1}^U + \theta_{n+1}^U), \quad \text{for some } n \in [1, N-1]. \quad (5.15)$$

We now discuss the three possible conditions (5.13), (5.14) and (5.15) that are stated above. The first option of imposing (5.13) is to ensure that the dividing streamline far upstream is indeed

horizontal and it is derived here. We can analyse the behaviour of  $\Omega(w)$  far upstream by considering the zero-gravity case of a submerged rectangular block that is semi-infinitely long in a uniform horizontal stream. Tuck and Vanden-Broeck [1998] obtain an analytic solution for this problem. However, the complex planes used in their calculation are different to those used in the present study, so we cannot simply quote the solution. Instead, by (5.6) and noting that here we are considering a solid, rectangular block, for  $w \in \mathbb{R}$  we obtain

$$\begin{aligned}\tau(w) &= -\frac{1}{\pi} P.V. \int_0^b \frac{\pi/2}{\sigma - w} d\sigma - \frac{1}{\pi} P.V. \int_{b_1}^0 \frac{-\pi/2}{\sigma - w} d\sigma \\ &= -\frac{1}{2} \log \left| \frac{b-w}{w} \right| + \frac{1}{2} \log \left| \frac{w}{b_1 - w} \right|.\end{aligned}\tag{5.16}$$

Then, a suitable form for  $\Omega$  for the whole flow is

$$\Omega(w) = \log w - \frac{1}{2} \log ((w-b)(w-b_1)),\tag{5.17}$$

which one can check satisfies the boundary conditions on the rectangular block and Laplace's equation. Then, for large  $|w|$  we have

$$\Omega(w) \sim \frac{\frac{1}{2}(b+b_1)}{w} + \mathcal{O}\left(\frac{1}{w^2}\right).\tag{5.18}$$

Therefore, in the present case with  $g \neq 0$  with flow past the plate normal to the stream, we take  $\Omega \sim \alpha/w$  for large  $|w|$  where  $\alpha$  is an unknown constant. We also obtain another expression for  $\Omega(w)$  for large  $|w|$ . Recall that the dividing streamline is mapped to the imaginary axis of the  $w$ -plane. Then, for  $w \notin \mathbb{R}$ , by applying the Cauchy integral formula to  $\Omega(w)$  in the  $w$ -plane with a contour in the upper half-plane comprising of the semi-circular arc  $C_R$  and interval  $[-R, R]$  traversed anticlockwise under the limit as  $R \rightarrow +\infty$ , we obtain

$$\Omega(w) = \frac{1}{2\pi i} \int_{-\infty}^{\infty} \frac{\Omega(\sigma)}{\sigma - w} d\sigma.\tag{5.19}$$

Along the dividing streamline  $AS$ , we write  $w = iW$  and then we take interest in  $\Omega(iW)$  as

$W \rightarrow +\infty$ . Let  $\Delta, W \in \mathbb{R}$  such that  $1 \ll \Delta \ll W$ . Then, we rewrite (5.19) as

$$\begin{aligned}
\Omega(iW) &= \frac{1}{2\pi i} \left[ \int_{-\infty}^{-\Delta} \frac{\Omega(\sigma)}{\sigma - iW} d\sigma + \int_{-\Delta}^{\Delta} \frac{\Omega(\sigma)}{\sigma - iW} d\sigma + \int_{\Delta}^{\infty} \frac{\Omega(\sigma)}{\sigma - iW} d\sigma \right] \\
&= \frac{1}{2\pi i} \left[ \int_{-\infty}^{-\Delta/W} \frac{\Omega(Wq)}{Wq - iW} W dq + \int_{-\Delta}^{\Delta} \frac{\Omega(\sigma)}{\sigma - iW} d\sigma + \int_{\Delta/W}^{\infty} \frac{\Omega(Wq)}{Wq - iW} W dq \right] \\
&= \frac{1}{2\pi i} \left[ \int_{-\infty}^{-\Delta/W} \frac{\alpha}{Wq} \frac{1}{q - i} dq + \int_{-\Delta}^{\Delta} \frac{i\Omega(\sigma)}{W} d\sigma + \int_{\Delta/W}^{\infty} \frac{\alpha}{Wq} \frac{1}{q - i} dq \right] + \mathcal{O}\left(\frac{1}{W^2}\right) \quad (5.20) \\
&= \frac{1}{2\pi i} \left[ \frac{\alpha}{W} P.V. \int_{-\infty}^{\infty} \frac{1}{q(q - i)} dq + \frac{i}{W} \int_{-\infty}^{\infty} \Omega(\sigma) d\sigma \right] + \mathcal{O}\left(\frac{1}{W^2}\right) \\
&= \frac{\alpha}{2iW} + \frac{1}{2\pi} \frac{1}{W} \int_{-\infty}^{\infty} \Omega(\sigma) d\sigma + \mathcal{O}\left(\frac{1}{W^2}\right).
\end{aligned}$$

Note that, in the final simplification step above, we use that

$$\begin{aligned}
P.V. \int_{-\infty}^{\infty} \frac{1}{q(q - i)} dq &= \lim_{a \rightarrow 0^+} \lim_{A \rightarrow \infty} \left( \int_a^A \frac{i}{q} - \frac{i}{q - i} dq + \int_{-A}^{-a} \frac{i}{q} - \frac{i}{q - i} dq \right) \\
&= \pi.
\end{aligned} \quad (5.21)$$

Using this along with (5.17) for  $w = iW$  where  $W \gg 1$ , we have that

$$\frac{\alpha}{iW} + \mathcal{O}\left(\frac{1}{W^2}\right) = \frac{\alpha}{2iW} + \frac{1}{2\pi} \frac{1}{W} \int_{-\infty}^{\infty} \Omega(\sigma) d\sigma + \mathcal{O}\left(\frac{1}{W^2}\right) \quad (5.22)$$

and so

$$\alpha = \frac{i}{\pi} \int_{-\infty}^{\infty} \Omega(\sigma) d\sigma. \quad (5.23)$$

It follows that, using the behaviour of  $\Omega(w)$  for large  $|w|$ , we have

$$\tau(iW) - i\theta(iW) \sim \frac{1}{\pi W} \int_{-\infty}^{\infty} \Omega(\sigma) d\sigma \quad \text{where } W \gg 1. \quad (5.24)$$

Since we require the dividing streamline to be horizontal far upstream, we deduce that

$$\frac{1}{\pi W} \int_{-\infty}^{\infty} \Im\left(\Omega(\sigma)\right) d\sigma = 0 \quad \Rightarrow \quad \int_{-\infty}^{\infty} \theta(\sigma) d\sigma = 0. \quad (5.25)$$



Hence, we have arrived at the first equation (5.13) of the possible conditions to be imposed.

Now, we discuss the remaining two possible conditions, (5.14) and (5.15). As stated in (5.14), we can set  $c = -c_1$  which imposes that the velocity potential is the same at  $C$  and  $C'$ , i.e. at the two closure points. This condition has been used in previous investigations where closure models have been employed, such as in the works of Wu [1956], Mimura [1958] and Faltinsen and Semenov [2008]. However, (5.14) may be considered to be an unnecessary, artificial addition to the model. Therefore, picking this particular solution (as opposed to a different solution that bears an alternative relation between the two closure points) is questionable. It imposes a symmetry on the solution of the non-zero gravity case that is not required by the theory. The final possible condition that we can impose is an interpolation formula, as given in (5.15). The justification for including this equation in the system to be solved is simply to ensure that it is square, without imposing another condition that could potentially restrict the solution. This would avoid the aforementioned potential issue of imposing (5.14). Furthermore, the condition (5.13) — which explicitly imposes that the dividing streamline is horizontal far upstream — may also be considered unnecessary since we utilise the upstream conditions on the flow when applying the Cauchy integral formula, i.e. that  $\Omega \rightarrow 0$  far upstream. Overall, the potential benefits of imposing the interpolation formula (5.15) are apparent. Results for imposing each of the three possible conditions (5.13)–(5.15) are presented later.

Once we have solved the  $2N + 4$  square system for the unknowns, we can plot the free surfaces using

$$z(w) = \int_0^w 2\sigma e^{-\tau(\sigma)} \cos(\theta(\sigma)) d\sigma + i \int_0^w 2\sigma e^{-\tau(\sigma)} \sin(\theta(\sigma)) d\sigma. \quad (5.26)$$

Also, note that, in order to plot the dividing streamline, we can write

$$\begin{aligned} z(iW_s) &= \int_0^{W_s} \frac{dz}{df} \frac{df}{dw} \frac{dw}{dW} dW \\ &= \int_0^{W_s} e^{-\tau(iW) + i\theta(iW)} 2iW i dW \\ &= - \int_0^{W_s} 2W e^{-\tau(iW)} \cos(\theta(iW)) dW - i \int_0^{W_s} 2W e^{-\tau(iW)} \sin(\theta(iW)) dW, \end{aligned} \quad (5.27)$$

where  $W_s \in \mathbb{R}$  is a point along the positive imaginary axis of the  $w$ -plane corresponding to dividing

streamline. Expressions for  $\tau$  and  $\theta$  along the positive imaginary axis of the  $w$ -plane, to be utilised in evaluating (5.27), can be obtained using equation (5.19). We find that, for  $W \in \mathbb{R}$ ,

$$\Omega(iW) = \frac{1}{2\pi i} \int_{-\infty}^{\infty} \frac{\sigma\tau(\sigma) + W\theta(\sigma) + i(W\tau(\sigma) - \sigma\theta(\sigma))}{\sigma^2 + W^2} d\sigma \quad (5.28)$$

and so we have

$$\begin{aligned} \tau(iW) &= \frac{1}{2\pi} \int_{-\infty}^{\infty} \frac{W\tau(\sigma) - \sigma\theta(\sigma)}{\sigma^2 + W^2} d\sigma \\ &= \frac{1}{2\pi} \left[ \int_{-\infty}^{\infty} \frac{W\tau(\sigma)}{\sigma^2 + W^2} d\sigma - \int_{c_1}^{b_1} \frac{\sigma\theta(\sigma)}{\sigma^2 + W^2} d\sigma - \int_b^c \frac{\sigma\theta(\sigma)}{\sigma^2 + W^2} d\sigma \right] + \frac{1}{8} \log \left( \frac{W^4}{(b_1^2 + W^2)(b^2 + W^2)} \right) \end{aligned} \quad (5.29)$$

along with

$$\begin{aligned} \theta(iW) &= \frac{1}{2\pi} \int_{-\infty}^{\infty} \frac{\sigma\tau(\sigma) + W\theta(\sigma)}{\sigma^2 + W^2} d\sigma \\ &= \frac{1}{2\pi} \left[ \int_{-\infty}^{\infty} \frac{\sigma\tau(\sigma)}{\sigma^2 + W^2} d\sigma + \int_{c_1}^{b_1} \frac{W\theta(\sigma)}{\sigma^2 + W^2} d\sigma + \int_b^c \frac{W\theta(\sigma)}{\sigma^2 + W^2} d\sigma \right] + \frac{1}{4} \arctan \frac{b_1}{W} + \frac{1}{4} \arctan \frac{b}{W}. \end{aligned} \quad (5.30)$$

In order to evaluate these functions for  $\tau$  and  $\theta$  along the positive imaginary axis, we need to calculate the integrals that run along the whole real axis in (5.29) and (5.30). To do so, we numerically evaluate a truncated integral on the interval  $[-L, L]$ , for some  $L > 0$ . Then, for the intervals  $(-\infty, -L]$  and  $[L, +\infty)$ , we will utilise an asymptote for  $\tau$ . To find this asymptote, we use (5.7), i.e. the expression for  $\tau(w)$  that is valid for  $w \in \mathbb{R}$ . For large  $|w|$ , this can then be rewritten as

$$\begin{aligned} \tau(w) &= \frac{1}{\pi} \left[ \int_{c_1}^{b_1} \theta(\sigma) \left( \frac{1}{w} + \frac{\sigma}{w^2} + \mathcal{O}\left(\frac{1}{w^3}\right) \right) d\sigma + \int_b^c \theta(\sigma) \left( \frac{1}{w} + \frac{\sigma}{w^2} + \mathcal{O}\left(\frac{1}{w^3}\right) \right) d\sigma \right] \\ &\quad + \frac{b + b_1}{2w} + \frac{b^2 + b_1^2}{4w^2} + \mathcal{O}\left(\frac{1}{w^3}\right) \\ &= \frac{1}{w} \left[ \frac{1}{\pi} \int_{c_1}^{b_1} \theta(\sigma) d\sigma + \frac{1}{\pi} \int_b^c \theta(\sigma) d\sigma + \frac{b + b_1}{2} \right] \\ &\quad + \frac{1}{w^2} \left[ \frac{1}{\pi} \int_{c_1}^{b_1} \sigma\theta(\sigma) d\sigma + \frac{1}{\pi} \int_b^c \sigma\theta(\sigma) d\sigma + \frac{b^2 + b_1^2}{4} \right] + \mathcal{O}\left(\frac{1}{w^3}\right). \end{aligned} \quad (5.31)$$

We can see that the coefficient of the  $w^{-1}$  term is the left-hand side of (5.13) divided by  $\pi$ . In

the earlier analysis of the flow upstream, (5.13) is obtained by noting that the dividing streamline should be horizontal far upstream due to the conditions of the undisturbed flow. Therefore, we know here that the coefficient of the  $w^{-1}$  term is zero and so the leading-order term for  $\tau(w)$  is instead  $w^{-2}$ . It follows that, for the asymptote, we can take

$$\tau(w) \sim \frac{1}{w^2} \left[ \frac{1}{\pi} \int_{c_1}^{b_1} \sigma \theta(\sigma) d\sigma + \frac{1}{\pi} \int_b^c \sigma \theta(\sigma) d\sigma + \frac{b^2 + b_1^2}{4} \right] \quad (5.32)$$

for large  $|w|$ .

Now, we look at the results obtained through solving the  $2N + 4$  square system. We first consider the solutions found when imposing (5.13), i.e. the condition that explicitly requires the dividing streamline to be horizontal upstream. Figure 78 shows several free-surface profiles for different Froude and cavitation numbers. For large  $F$  (e.g.  $F = 100$ , figures 78a–78c), we obtain very symmetrical results — as expected, since the plate is normal to the stream and the effect of gravity is very small. As  $F$  decreases, we find increased asymmetry, clear in both the cavity boundaries and the position of the stagnation point along the finite vertical plate (c.f. figures 78d–78f). In particular, the lower cavity boundary is shorter than the upper boundary. Figure 79 focuses on the dividing streamline near the stagnation point and figures 79a–79c demonstrate that as  $F$  decreases towards 1, the dividing streamline deviates further from the line  $y = 0$ .

We now look at the effect of the cavitation number and observe that, as  $K$  increases, we obtain a smaller cavitation bubble — the closure starts closer to the blade (c.f. figures 78a–78c). Increasing  $K$  also increases the symmetry, particularly evident in the position of the stagnation point along the plate (c.f. figures 78g–78i) and the straighter horizontal dividing streamline along  $y = 0$  (c.f. figures 79d–79f).

Figure 80 shows for which values of the cavitation and Froude numbers a converged solution can be reached when we discretise the integral equation with  $N = 40$  mesh points on each free surface. As the Froude number increases, the range of values of  $K$  for which a solution can be obtained increases. For small Froude numbers,  $K$  needs to be sufficiently large to obtain a solution. At this end of the range for the parameter  $F$ , achieving a converged solution becomes more sensitive to the initial guess — a resolution for which is to use the solution for a similar set of parameters as the

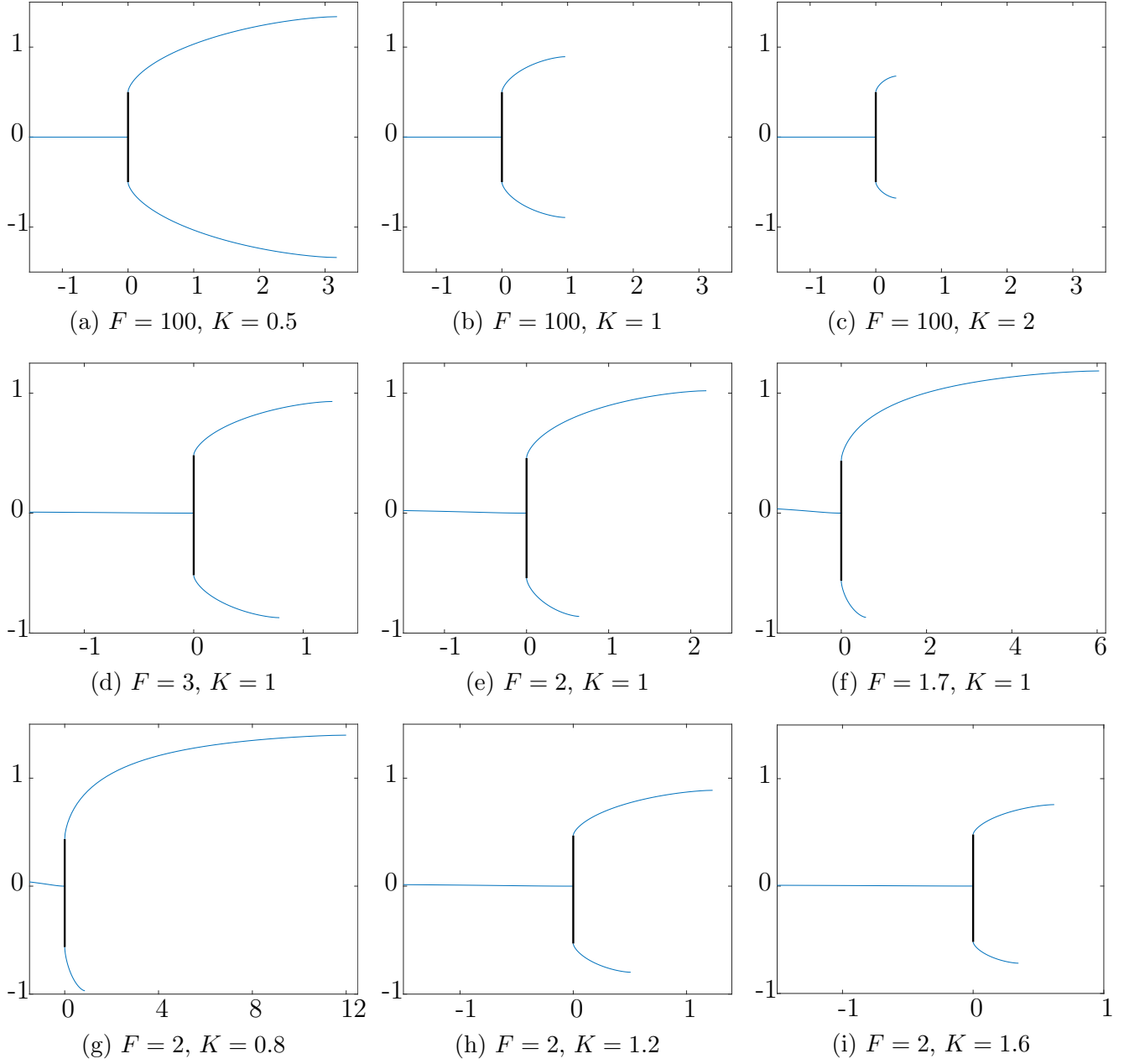


Figure 78: Free-surface profiles obtained by taking  $N = 40$  and imposing (5.13).

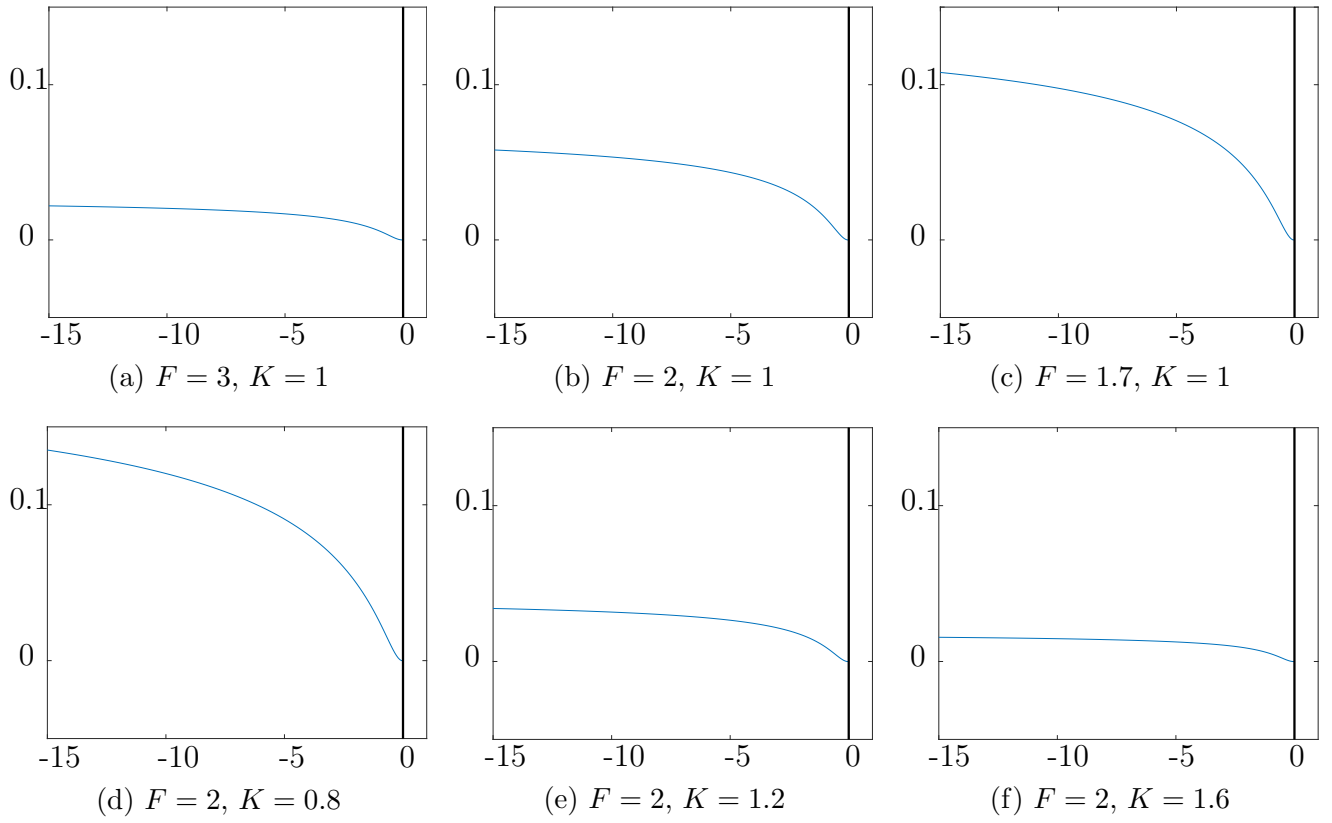


Figure 79: Focusing on the dividing streamline of free-surface profiles obtained by taking  $N = 40$  and imposing (5.13).

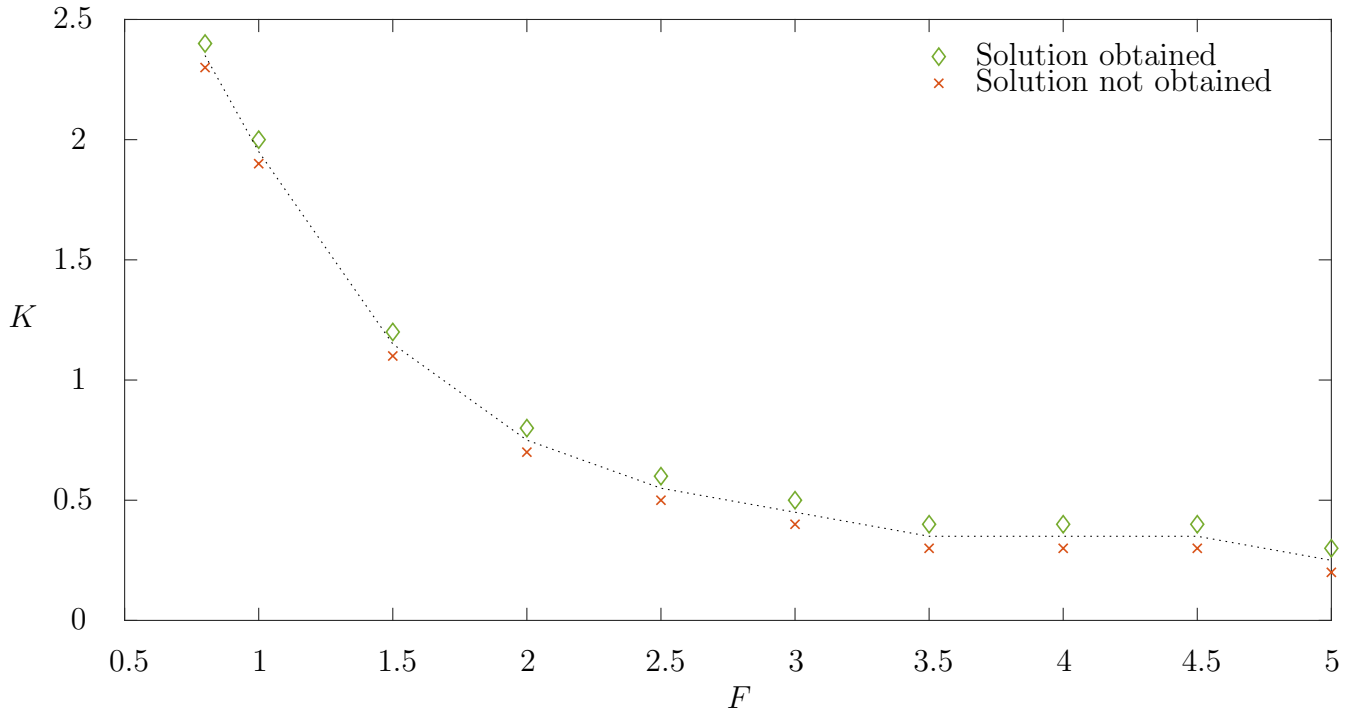


Figure 80:  $K$  against  $F$  to show which combinations of these parameters lead to a converged solution for  $N = 40$  and imposing (5.13).

initial guess. Faltinsen and Semenov [2008], in their work on the effect of gravity and cavitation on flow past a hydrofoil, investigate the limiting size of the cavitation bubble by setting  $K = 0$  and varying the Froude number. Figure 80 shows that the limiting size of the cavity here, for each Froude number, does not occur when  $K = 0$  since a converged solution cannot be obtained for this cavitation number. The open-wake closure model utilised here — in contrast to the complex, cusp-like closure model used by Faltinsen and Semenov [2008] — does not allow for a solution to be obtained as  $K \rightarrow 0$  for non-zero gravity. This is since, with the effect of gravity included, a small value for  $K$  forces the cavity closure too locally to the vertical plate. The closure model adopted here requires that the heights of the cavity boundaries remain constant along the closures  $CD$  and  $C'D'$  whilst the pressure gradient returns to that of the undisturbed stream and the flow speed returns to unity. However, the boundaries (in particular, the lower boundary) must be able to support the pressure within the cavitation bubble; and, with diminishing  $K$ , the boundaries are also diminishing, with the pressure along the lower boundary closure  $C'D'$  increasing back towards that of the undisturbed stream.

We now move on to consider the results if we instead impose (5.14), i.e. setting the velocity potential to be equal at both of the cavity closure points on the free surfaces. Figure 81 shows some resulting free-surface profiles for a variety of values of the parameters  $F$  and  $K$ . The same sets of parameters are taken here as earlier (c.f figure 78). For  $F = 100$ , we obtain very symmetric free-surface profiles (c.f. figures 81a–81c). This is to be expected since the condition of  $c = -c_1$  is complemented by very small gravity and hence, there is a lack of asymmetry. The result that we obtain symmetric solutions for large Froude numbers is as found earlier. Also, as before, we have that the bubble size decreases as  $K$  increases (c.f. figures 81g–81i). We find that decreasing the Froude number leads to more asymmetric results (c.f. figures 81d–81f) — again, another quality observed earlier. However, the asymmetry is now more evident in the shape of the dividing streamline rather than in any differences between the two cavity boundaries. This is to be expected since we impose some degree of symmetry specifically on the free surfaces by specifying that the velocity potential is equal at the closure points, but the asymmetric effect of gravity on the flow must be diverted elsewhere.

Figure 82 highlights a concern of these results: is it clear that the dividing streamline heads towards being horizontal far upstream? Even in the least extreme case given here (c.f. figure 82a), the streamline does not appear to be (or head towards) horizontal upstream. Whilst the condition that  $\theta = 0$  in the far-field is imposed implicitly (since it is used in deriving the integral equation for the flow), here it is not imposed explicitly far upstream. An issue of imposing  $c = -c_1$  is that it is not particularly well-justified. A cavity closure model is an artificial mechanism and, generally, focus is near to the object behind which the cavitation bubble forms, e.g. interest in forces acting on the body. However, whilst these closure models are accepted as not being particularly useful far downstream, it still calls into question whether it is reasonable to set the velocity potential equal at the closure points  $C$  and  $C'$ . As discussed earlier, Wu [1956] and Mimura [1958] use this condition for the zero-gravity problem, where it seems more reasonable to impose such symmetry on the flow. Faltinsen and Semenov [2008] also set the velocity potential equal at the closure points, but it is better justified to be used in their calculations due to the closed-cavity model that they employ, as opposed to the open-wake model used in the present study. Overall, there is evidence here to suggest that it is necessary to explicitly impose that the dividing streamline is horizontal upstream through use of (5.13).

Finally, we briefly discuss imposing the interpolation formula instead, i.e. setting (5.15). Many parameter combinations have been tested, but a converged solution has not been obtained. This suggests that an extra restriction on the flow is indeed necessary, whether that be requiring a flat dividing streamline far upstream or that the velocity potential is equal at the closure points, or another option altogether. It stands to reason that a condition other than the interpolation formula is required here since we obtained solutions both when setting (5.13) and when setting (5.14). This means that an extra restriction on the flow is needed in order to ‘pick’ the solution. The results presented here support the idea of imposing the condition on the flow angle far upstream and it is well-justified in its derivation. We will utilise this in the following section where we set the plate to be at an arbitrary angle of attack.

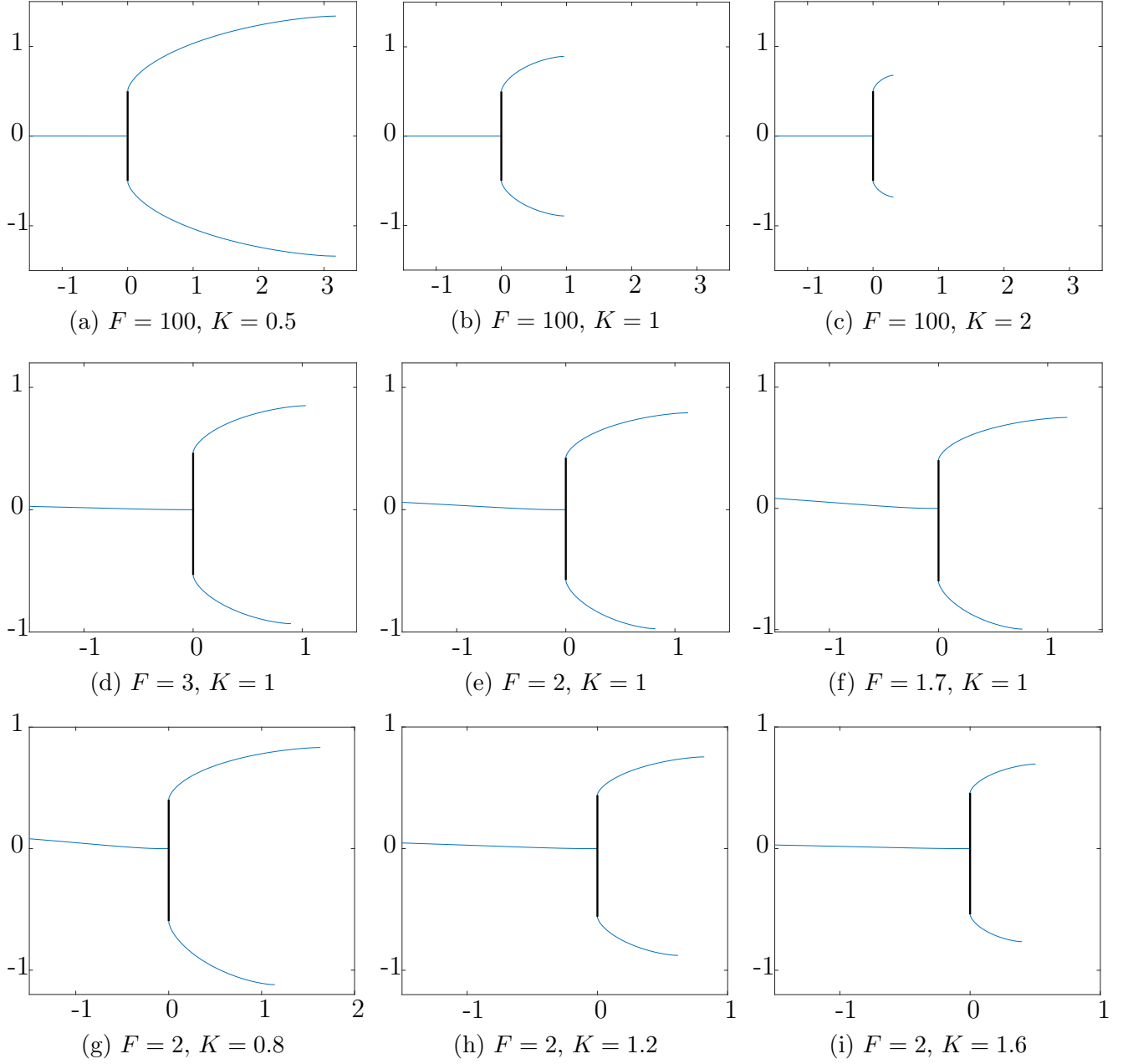


Figure 81: Free-surface profiles obtained by taking  $N = 40$  and imposing equal velocity potential at the closure points via (5.14).



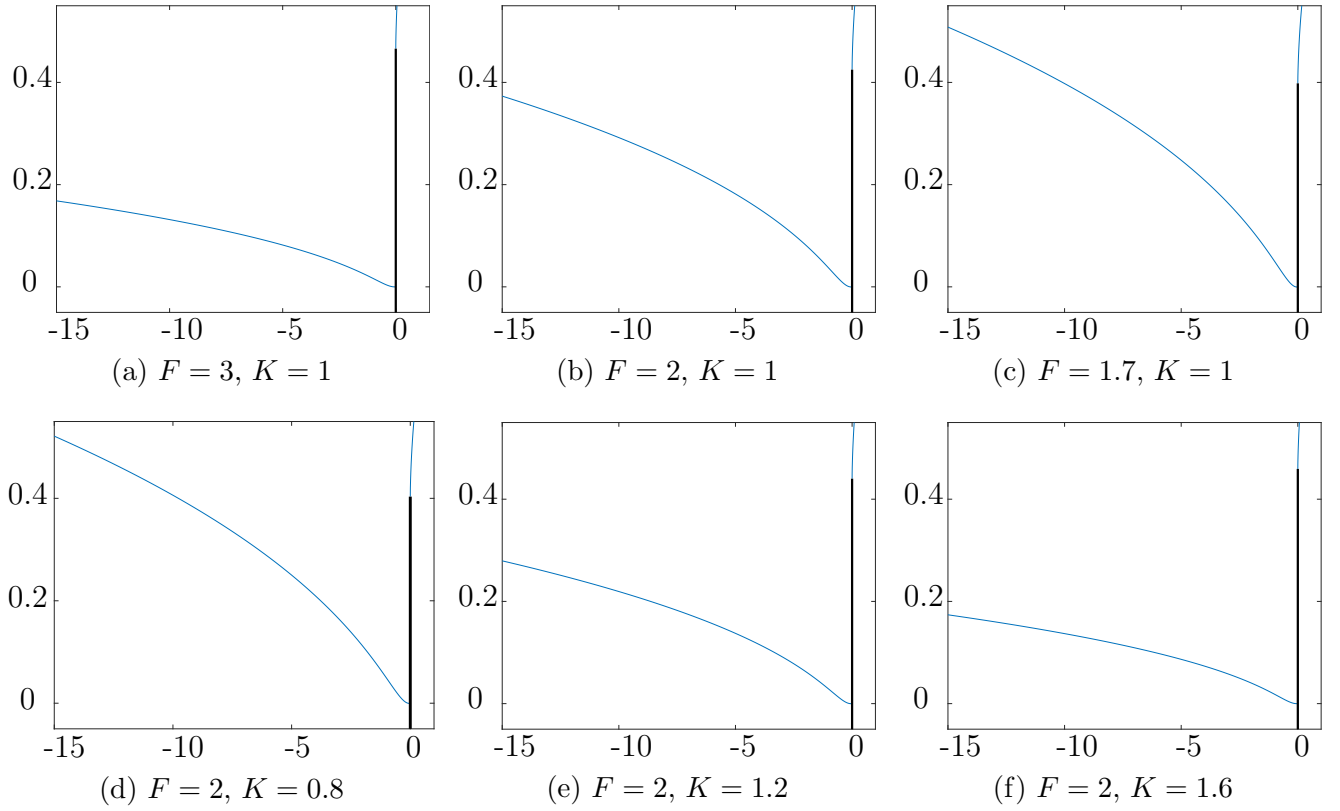


Figure 82: Focusing on the dividing streamline of free-surface profiles obtained by taking  $N = 40$  and imposing equal velocity potential at the closure points via (5.14).

### 5.1.2 Plate at arbitrary angle of attack

A small adjustment can be made to the formulation of the problem in order to allow for a specified angle of attack,  $\alpha \in (0, \pi)$ , other than just  $\pi/2$  as considered in the previous subsection. The model is as depicted in figure 76a with the origin of the  $z$ -plane still set at the stagnation point, but with the top section  $OB$  of the plate at an angle of  $\alpha$  to the  $x$ -axis (and the bottom section of the plate is at  $\alpha - \pi$  to the  $x$ -axis, i.e. we still have a flat plate  $BB'$ ). The plate is of unit length in a uniform, horizontal stream of unit velocity and we still employ the open-wake model downstream. It follows that the complex  $f$ - and  $w$ -planes remain the same as depicted in figures 76b–76c. The Cauchy integral formula can be applied to the  $w$ -plane and, since the far upstream and downstream conditions are as before, we arrive at the same expression for  $\tau(w)$ , i.e. (5.6). Using the known flow angles along the blade  $BB'$  and along the closures  $CD$  and  $C'D'$  we can rewrite this as

$$\begin{aligned}\tau(w) &= -\frac{1}{\pi} \left[ \int_{c_1}^{b_1} \frac{\theta(\sigma)}{\sigma - w} d\sigma + \int_b^c \frac{\theta(\sigma)}{\sigma - w} d\sigma + \int_{b_1}^0 \frac{\alpha - \pi}{\sigma - w} d\sigma + \int_0^b \frac{\alpha}{\sigma - w} d\sigma \right] \\ &= -\frac{1}{\pi} \left[ \int_{c_1}^{b_1} \frac{\theta(\sigma)}{\sigma - w} d\sigma + \int_b^c \frac{\theta(\sigma)}{\sigma - w} d\sigma \right] - \frac{\alpha}{\pi} \log \left| \frac{b - w}{b_1 - w} \right| + \log \left| \frac{w}{b_1 - w} \right|.\end{aligned}\tag{5.33}$$

Note that this is equivalent to (5.7) for  $\alpha = \pi/2$ , i.e. when the blade is perpendicular to the undisturbed flow. The Bernoulli condition (5.4) remains the same and so our integral equation becomes

$$-\frac{1}{\pi} \left[ \int_{c_1}^{b_1} \frac{\theta(\sigma)}{\sigma - w} d\sigma + \int_b^c \frac{\theta(\sigma)}{\sigma - w} d\sigma \right] - \frac{\alpha}{\pi} \log \left| \frac{b - w}{b_1 - w} \right| + \log \left| \frac{w}{b_1 - w} \right| = \frac{1}{2} \log \left( K + 1 - \frac{2}{F^2} y(w) \right),\tag{5.34}$$

for  $w \in \mathbb{R}$ .

We solve numerically by introducing  $N$  mesh points along each free surface as defined in (5.10) and we look to determine the values of  $\theta$  corresponding to each of the mesh points, i.e.  $\theta_j^U = \theta(w_j^U)$  and  $\theta_j^L = \theta(w_j^L)$  for  $j = 1, 2, \dots, N$ . We also leave  $b$ ,  $b_1$ ,  $c$  and  $c_1$  as unknowns to be found. Just as for the case of the plate normal to the flow, we have  $2N + 4$  unknowns. Discretising (5.34) using  $N - 1$  collocation points (as defined in (5.11)) along each cavity boundary, then we have  $2N - 2$

equations. The flow angles at the plate ends and at the cavity closure points are known, so we set  $\theta(b) = \alpha$ ,  $\theta(b_1) = \alpha - \pi$ ,  $\theta(c) = 0$  and  $\theta(c_1) = 0$ . These conditions can be rewritten as  $\theta_1^U = \alpha$ ,  $\theta_1^L = \alpha - \pi$ ,  $\theta_N^U = 0$  and  $\theta_N^L = 0$ . We also set unit length of the vertical plate via  $|z(b) - z(b_1)| = 1$ , i.e.

$$\left| \int_0^b 2\sigma e^{-\tau(\sigma)} e^{i\alpha} d\sigma - \int_0^{b_1} 2\sigma e^{-\tau(\sigma)} e^{i(\alpha-\pi)} d\sigma \right| = 1. \quad (5.35)$$

This can be simplified to

$$\int_0^b 2\sigma e^{-\tau(\sigma)} d\sigma + \int_0^{b_1} 2\sigma e^{-\tau(\sigma)} d\sigma = 1. \quad (5.36)$$

The final equation is chosen to be  $\int_{-\infty}^{\infty} \theta(\sigma) d\sigma = 0$ , i.e. imposing that the dividing streamline is horizontal far upstream. Utilising the known flow angles, this can be rewritten as

$$\int_{c_1}^{b_1} \theta(\sigma) d\sigma + \int_b^c \theta(\sigma) d\sigma + \alpha(b - b_1) + b_1\pi = 0. \quad (5.37)$$

Overall, we have  $2N + 4$  equations in  $2N + 4$  unknowns as before, to be solved numerically.

Some example free-surface profiles are presented here for various values taken for the parameters  $F$ ,  $K$  and  $\alpha$ . As seen in the case where  $\alpha = \pi/2$  (of the previous subsection), here we have that, for a given angle of attack, the bubble size increases as  $K$  decreases (c.f. figures 83d–83f). The cavitation number impacts the position of the stagnation point along the finite plate, but only to a very small degree. The Froude number also affects the stagnation point but, again, not greatly. The angle  $\alpha$  of attack clearly dominates the positioning of the stagnation point (c.f. figures 83a–83c). Another point to note is that, as the Froude number decreases, the bubble size increases. This is as seen in the previous subsection for  $\alpha = \pi/2$ . It has been checked that, if we set  $\alpha = \pi/2$ , then we recover the profiles and results as presented in the previous subsection. Another similarity is that a converged solution is not obtainable for every given set of the parameters (i.e.  $F$ ,  $K$  and  $\alpha$ ). However, it is left for future work to obtain a plot as shown in figure 80 to identify (for a given Froude number) the smallest cavitation number for which a solution can be achieved and how this depends on  $\alpha$ . For now, we move on to the final problem, where the flow is bounded above by a free surface.

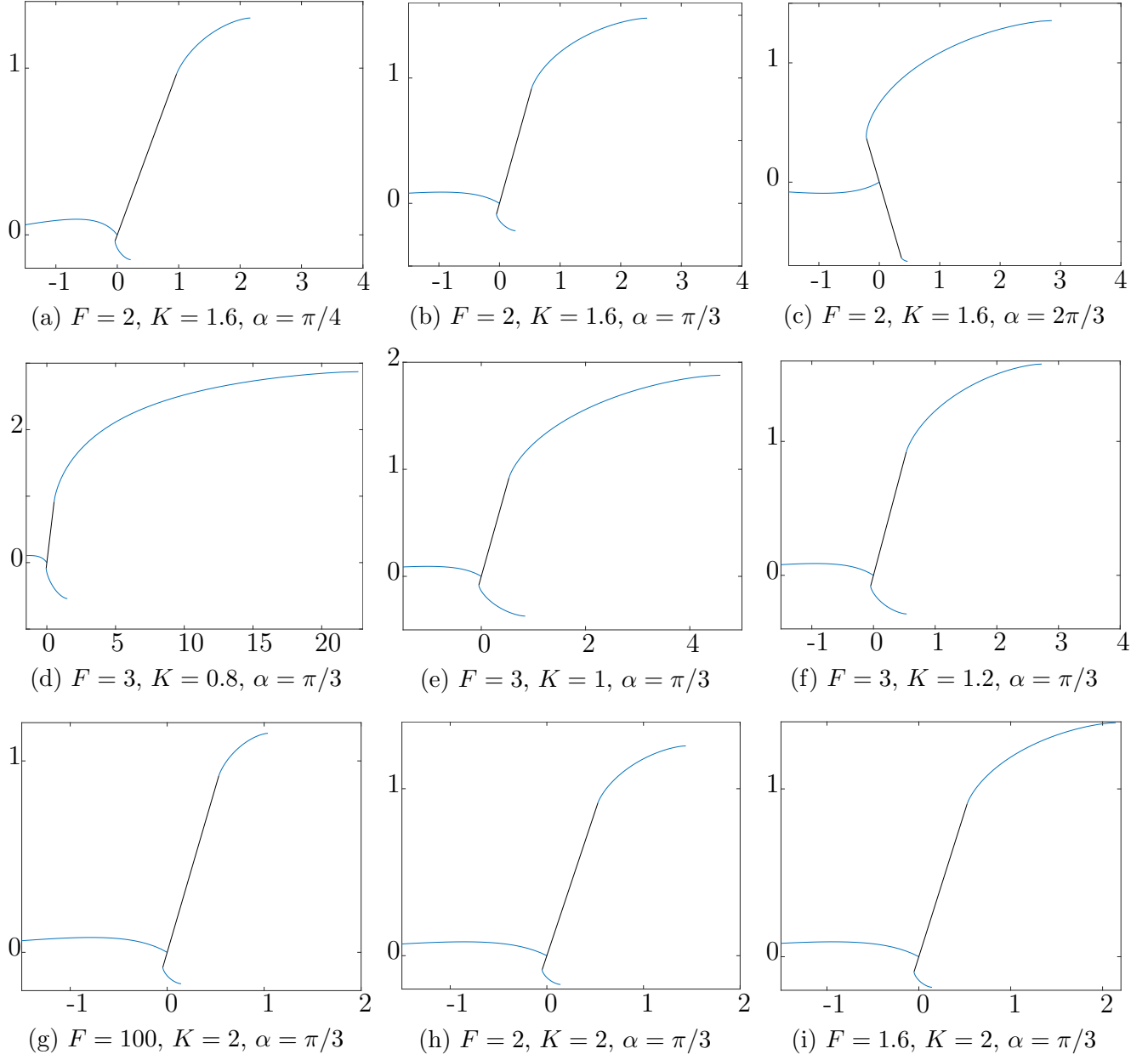


Figure 83: Free-surface profiles obtained by taking  $N = 40$  for the gravity flow past the plate at an angle  $\alpha$  of attack.

## 5.2 Wake horizontal closure with free surface

The final problem that is presented here now includes a free surface that bounds the flow from above. The flow is as depicted in figure 84a. We have a finite-length plate that is normal to a uniform, horizontal stream of speed  $U$ . The plate is submerged with the lower edge of the plate at  $B'$  at a distance  $\tilde{d}$  below the level of the free surface of the undisturbed stream. We will refer to  $\tilde{d}$  as the draft of the flow. The effects of gravity will be included and, again, we utilise the open-wake closure model. Recalling that the motivation for this problem here is interest in flow past rowing blades, it is sensible to limit the work in this section to wake-flow only. This leads to a useful simplification of the problem: whilst gravity is included here on the free surface, we will neglect the effects of gravity on the wake boundaries. This can be justified by noting that a wake contains fluid of the same density as that of the rest of the flow, but it is at rest and so we have hydrostatic pressure within the wake. The Bernoulli condition tells us that

$$p + \rho g y = p_c \quad (5.38)$$

within the wake, where  $p$  denotes that pressure,  $\rho$  is the density,  $g$  is the gravitational acceleration and  $p_c$  is a constant. Then, through use of (5.38) to eliminate the pressure  $p$  from the Bernoulli condition, along the wake boundaries we have

$$\frac{1}{2}\rho q^2 + p_c = C, \quad (5.39)$$

where  $C$  is a constant and  $q$  denotes the speed. Hence, gravity does not appear in this boundary condition and so it seems reasonable to neglect the effects of gravity along the boundaries of the wake.

We will now formulate the overall problem. The flow is as described above and shown in figure 84a where  $z = x + iy$  with the  $x$ -axis set along the level of the undisturbed free surface and the  $y$ -axis is set along the vertical plate  $BB'$ . We have an open-wake model, so the flow angle is zero along  $CD$  and  $C'D'$ . The effect of gravity is included on the free surface  $EF$  that bounds the flow above and we assume constant atmospheric pressure  $p = p_a$  along this free surface. On the

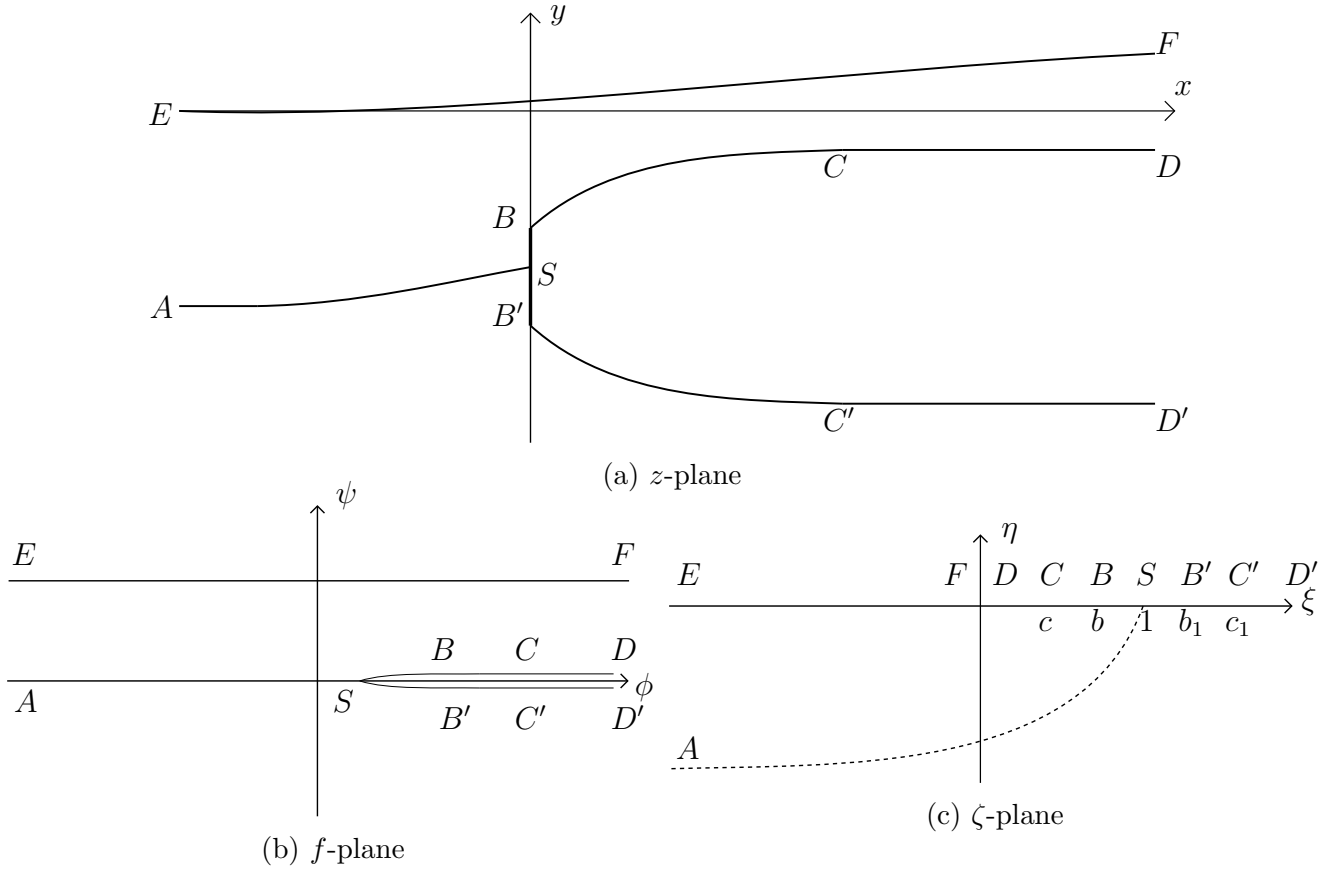


Figure 84: Complex planes for open-wake closure with a free surface bounding the flow above.

other hand, gravity is not included along the wake boundaries  $BC$  and  $B'C'$ ; and the pressure is taken to be constant (say,  $p = p_c$ ) along these boundaries. We normalise the velocity such that the uniform, horizontal stream is of unit speed and we normalise the distances such that  $\pi$  is the magnitude of the net volume flux of the flow above the plate. We denote the characteristic length for the latter normalisation by  $L$ ; and note that the normalised depth of the dividing streamline far-upstream is such that it lies along  $y = -\pi$ . Then, the Bernoulli condition on the free surface  $EF$  is

$$\frac{1}{2}q^2 + \frac{y}{F^2} = \frac{1}{2}, \quad (5.40)$$

where  $F = U/\sqrt{gL}$ . Along the wake boundaries we have

$$q^2 = K + 1, \quad (5.41)$$

where  $K = (p_\infty - p_c)/(\frac{1}{2}\rho U^2)$  is the wake underpressure coefficient and  $p_\infty$  denotes the pressure

of the stream in the far-field. As discussed in the introduction, the wake underpressure coefficient for wake flows is analogous to the cavitation number for cavity flows.

As usual, we let  $f$  denote the complex velocity for the flow. We set  $\psi = 0$  along the dividing streamline and  $\psi = \pi$  along the free surface (since we have a net volume flux of  $\pi$  for the flow between the dividing streamline and the free surface). We set the velocity potential at the stagnation point to be  $\phi = 1$ . Then, there is a branch cut along the positive  $\phi$ -axis for  $\phi > 1$ . The  $f$ -plane is as depicted in figure 84b. We also define an intermediate complex plane by  $\zeta = \xi + i\eta$  via

$$f = \zeta - \log \zeta. \quad (5.42)$$

Therefore, the flow region maps to the lower half of the  $\zeta$ -plane. In particular, the free surface  $EF$  maps to the negative  $\xi$ -axis; and the wake boundaries, along with the vertical plate, map to the positive  $\xi$ -axis. Also note that, by the given mapping,  $\zeta = 1$  corresponds to the stagnation point  $S$ . The positions in the  $\zeta$ -plane corresponding to the edges of the plate and the closure points are unknown and left to be determined. By  $b$ ,  $b_1$ ,  $c$  and  $c_1$  we denote these unknown positions corresponding to  $B$ ,  $B'$ ,  $C$  and  $C'$  in the  $\zeta$ -plane, respectively.

As was the case earlier, we define  $\Omega = \tau - i\theta = \log(df/dz)$ . Then, we apply the Cauchy integral formula to  $\Omega(\zeta)$  for  $\zeta \in \mathbb{R}$  with a semi-circular contour  $\tilde{C} = C_R \cup [R, \zeta + \epsilon] \cup C_\epsilon \cup [\zeta - \epsilon, -R]$  in the lower-half of the  $\zeta$ -plane, where  $C_R$  is the semi-circular arc of radius  $R$  centred at the origin,  $C_\epsilon$  is the semi-circular arc of radius  $\epsilon$  centred at  $\zeta$  and the intervals  $[R, \zeta + \epsilon]$  and  $[\zeta - \epsilon, -R]$  are along the real  $\zeta$ -axis. We obtain

$$\tau(\zeta) - i\theta(\zeta) = -\frac{1}{\pi i} P.V. \int_{-\infty}^{\infty} \frac{\tau(\sigma) - i\theta(\sigma)}{\sigma - \zeta} d\sigma \quad (5.43)$$

and in particular,

$$\tau(\zeta) = \frac{1}{\pi} P.V. \int_{-\infty}^{\infty} \frac{\theta(\sigma)}{\sigma - \zeta} d\sigma. \quad (5.44)$$

Then, by using the known flow angles along the vertical plate and the open-wake closure, the

expression can be rewritten as

$$\tau(\zeta) = \frac{1}{\pi} \left[ \int_{-\infty}^0 \frac{\theta(\sigma)}{\sigma - \zeta} d\sigma + \int_c^b \frac{\theta(\sigma)}{\sigma - \zeta} d\sigma + \int_{b_1}^{c_1} \frac{\theta(\sigma)}{\sigma - \zeta} d\sigma \right] + \frac{1}{2} \log \left| \frac{(1 - \zeta)^2}{(b - \zeta)(b_1 - \zeta)} \right|. \quad (5.45)$$

Recall that the speed of the flow can be expressed as  $q = \exp(\tau)$  and that the dynamic boundary condition along the wake boundaries is given by (5.41). It follows that, along  $BC$  and  $B'C'$  where  $\zeta \in \mathbb{R}$  such that  $c < \zeta < b$  or  $b_1 < \zeta < c_1$ , we have

$$\frac{1}{2} \log(K + 1) = \frac{1}{\pi} \left[ \int_{-\infty}^0 \frac{\theta(\sigma)}{\sigma - \zeta} d\sigma + \int_c^b \frac{\theta(\sigma)}{\sigma - \zeta} d\sigma + \int_{b_1}^{c_1} \frac{\theta(\sigma)}{\sigma - \zeta} d\sigma \right] + \frac{1}{2} \log \left| \frac{(1 - \zeta)^2}{(b - \zeta)(b_1 - \zeta)} \right|. \quad (5.46)$$

We also look to obtain an integral equation that is valid along the free surface  $EF$ . First, we differentiate the Bernoulli condition (5.40) along  $EF$  with respect to  $\zeta$  so we have

$$\frac{d\tau}{d\zeta} e^{2\tau} + \frac{1}{F^2} \frac{dy}{d\zeta} = 0. \quad (5.47)$$

Note that we can express the derivative that appears in the second term above as

$$\frac{dy}{d\zeta} = e^{-\tau(\zeta)} \left( 1 - \frac{1}{\zeta} \right) \sin(\theta(\zeta)). \quad (5.48)$$

Then, using this along with (5.47) and the fact that  $\tau \rightarrow 0$  as  $\xi \rightarrow -\infty$ , we find

$$\tau(\zeta) = \frac{1}{3} \log \left( 1 - \frac{3}{F^2} \int_{-\infty}^{\zeta} \left( 1 - \frac{1}{\xi} \right) \sin(\theta(\xi)) d\xi \right). \quad (5.49)$$

Finally, eliminating  $\tau$  between (5.45) and (5.49), then along  $EF$  where  $\zeta \in \mathbb{R}$  s.t.  $-\infty < \zeta < 0$ , we look to satisfy

$$\begin{aligned} \frac{1}{3} \log \left( 1 - \frac{3}{F^2} \int_{-\infty}^{\zeta} \left( 1 - \frac{1}{\xi} \right) \sin \theta(\xi) d\xi \right) &= \frac{1}{\pi} \left[ \int_{-\infty}^0 \frac{\theta(\sigma)}{\sigma - \zeta} d\sigma + \int_c^b \frac{\theta(\sigma)}{\sigma - \zeta} d\sigma \right. \\ &\quad \left. + \int_{b_1}^{c_1} \frac{\theta(\sigma)}{\sigma - \zeta} d\sigma \right] + \frac{1}{2} \log \left| \frac{(1 - \zeta)^2}{(b - \zeta)(b_1 - \zeta)} \right|. \end{aligned} \quad (5.50)$$

Before summarising the problem and discretising to obtain a numerical solution, we first discuss



the flow far upstream where, along the free surface, we have  $\xi \rightarrow -\infty$ . Considering (5.45) as  $\xi \rightarrow -\infty$ , we have that

$$\begin{aligned}\tau(\xi) &\sim \frac{1}{\xi} \left( -\frac{1}{\pi} \int_{-\infty}^{\infty} \theta(\sigma) d\sigma \right) + \dots \\ &\sim \frac{1}{\xi} \left[ -\frac{1}{\pi} \left( \int_{-\infty}^0 \theta(\xi) d\xi + \int_c^b \theta(\xi) d\xi + \int_{b_1}^{c_1} \theta(\xi) d\xi \right) - 1 + \frac{1}{2}(b + b_1) \right] + \dots \\ &\sim \frac{B}{\xi} + \dots,\end{aligned}\tag{5.51}$$

where we let  $B$  denote the constant coefficient of the  $\xi^{-1}$  term. From this behaviour of  $\tau$  far upstream, the Bernoulli condition (5.40) along the free surface and the fact that  $x \sim \xi$  as  $\xi \rightarrow -\infty$  (since we have unit horizontal velocity of the undisturbed flow), then we have

$$\frac{dy}{dx} \sim \frac{BF^2}{x^2} \text{ as } x \rightarrow -\infty\tag{5.52}$$

and hence

$$\theta(\xi) \sim \frac{BF^2}{\xi^2} \text{ as } \xi \rightarrow -\infty,\tag{5.53}$$

where  $B$  is the constant as defined above.

As in the previous cases, we discretise the problem by introducing  $N + 1$  mesh points along each of the wake boundaries and along the free surface, i.e. we have

$$\begin{aligned}\xi_j^U - \log \xi_j^U &= b - \log b + \frac{j-1}{N} \left( c - b + \log \frac{b}{c} \right), \text{ upper wake boundary } BC \\ \xi_j^L - \log \xi_j^L &= b_1 - \log b_1 + \frac{j-1}{N} \left( c_1 - b_1 + \log \frac{b_1}{c_1} \right), \text{ lower wake boundary } B'C' \\ \xi_j^{FS} - \log |\xi_j^{FS}| &= X_- + \frac{j-1}{N} (X_+ - X_-), \text{ free surface } EF\end{aligned}\tag{5.54}$$

where  $j = 1, 2, \dots, N + 1$  and where the finite range  $(X_-, X_+)$  is used to truncate the range  $(-\infty, \infty)$  of the velocity potential. Then, the unknowns of the problem are the values of the flow angle  $\theta$  at each of these mesh points, i.e. looking to find  $\theta_j^{FS} = \theta(\xi_j^{FS})$ ,  $\theta_j^U = \theta(\xi_j^U)$  and  $\theta_j^L = \theta(\xi_j^L)$  for  $j = 1, 2, \dots, N + 1$ . Recall that the positions corresponding to  $B$ ,  $B'$ ,  $C$  and  $C'$  in the  $\zeta$ -plane which are  $b$ ,  $b_1$ ,  $c$  and  $c_1$ , respectively, are unknowns. We also have the constant  $B$  of (5.51) to be

determined. Therefore, overall we have  $3N + 8$  unknowns.

For the equations in these unknowns, we introduce  $N$  collocation points along the free surface and wake boundaries defined by

$$\begin{aligned}\xi_j^{U_{\text{inter}}} - \log \xi_j^{U_{\text{inter}}} &= b - \log b + \frac{j - \frac{1}{2}}{N} \left( c - b + \log \frac{b}{c} \right), \text{ upper wake boundary} \\ \xi_j^{L_{\text{inter}}} - \log \xi_j^{L_{\text{inter}}} &= b_1 - \log b_1 + \frac{j - \frac{1}{2}}{N} \left( c_1 - b_1 + \log \frac{b_1}{c_1} \right), \text{ lower wake boundary,} \\ \xi_j^{FS_{\text{inter}}} - \log |\xi_j^{FS_{\text{inter}}}| &= X_- + \frac{j - \frac{1}{2}}{N} (X_+ - X_-), \text{ free surface,}\end{aligned}\tag{5.55}$$

for  $j = 1, 2, \dots, N$ . Satisfying the condition (5.50) at the collocation points along the free surface and the condition (5.46) at the collocation points along the upper and lower wake boundaries leads to  $3N$  equations. We also have several known values of the flow angle  $\theta$ . Along the upper wake boundary we know that

$$\theta(b) = \theta_1^U = \frac{\pi}{2} \quad \text{and} \quad \theta(c) = \theta_{N+1}^U = 0.\tag{5.56}$$

Along the lower wake boundary we have

$$\theta(b_1) = \theta_1^L = -\frac{\pi}{2} \quad \text{and} \quad \theta(c_1) = \theta_{N+1}^L = 0.\tag{5.57}$$

Along the free surface we take

$$\theta_1^{FS} = \frac{BF^2}{(\xi_1^{FS})^2} \quad \text{and} \quad \theta_{N+1}^{FS} = 0,\tag{5.58}$$

where the upstream asymptote for  $\tau$  is utilised in the first condition here. We also have that the constant  $B$  is constrained by

$$B = -\frac{1}{\pi} \left( \int_{-\infty}^0 \theta(\xi) d\xi + \int_c^b \theta(\xi) d\xi + \int_{b_1}^{c_1} \theta(\xi) d\xi \right) - 1 + \frac{1}{2}(b + b_1).\tag{5.59}$$

This is as derived earlier in (5.51). Finally, we set the (normalised) length  $H$  of the vertical plate by imposing

$$y_B - y_{B'} = H.\tag{5.60}$$

Hence, we have  $3N + 8$  equations. Note that we specify the values of the parameters  $F$ ,  $K$  and  $H$ . We can plot the profiles from a known vertical placement of the closure  $C'D'$  of the lower wake boundary: we have that  $y_{C'} = -\pi(1 + B)$ , where  $y_{C'}$  denotes the  $y$ -value at  $C'$ . This expression can be derived by noting that the depth of the dividing streamline far upstream (i.e. point  $A$  in figure 84a) is  $-\pi$ . Also, the  $\pi B$  contribution to the expression for  $y_{C'}$  can be obtained by finding the difference between the  $y$ -values far upstream at  $A$  and far downstream at  $D'$ . This is achieved by integrating around a large arc in the lower-half of the  $\zeta$ -plane, taking the limit as the radius of this arc tends to infinity and noting that  $\Omega \sim B/\zeta$  in the far-field. The (normalised) draft  $d$  of the plate can then be determined in post-processing (by integrating from the closure point  $C'$  on the lower wake boundary to the bottom  $B'$  of the plate). It is worth noting that, in the present study, the problem is posed with the wake underpressure coefficient  $K$  as a free parameter and the draft is obtained from the solution. This allows for convenient comparison of the results with those found by Tuck and Vanden-Broeck [1998]. However, the problem could (although it is not done here) be reworked so that the draft is prescribed and  $K$  is left to be found — this is a more natural way to consider the physical problem of the submerged plate placed at some given distance beneath the level of the undisturbed free surface. The results will be discussed with this in mind.

We begin analysis of the results by first looking solely at the wake boundaries. Figure 85 shows numerous plots of the wake boundaries obtained where we set  $K = 1$  and  $H = 0.2$ . We find that, as the Froude number  $F$  decreases, the upper wake boundary decreases in length and the lower wake boundary increases in length. Therefore, for large Froude numbers (above some value, say  $F_e$ ), the upper wake boundary is longer than the lower wake boundary; and for Froude numbers below  $F_e$ , the opposite is true. In the case presented in figure 85, we can see that the value for  $F_e$  lies between 4 and 5. The decrease in the upper wake boundary length is to be expected since the jet between the upper wake boundary and the free surface will have greater curvature due to the greater gravitational dominance and, therefore, obtain a zero flow-angle sooner, thereby shortening the boundary. As  $F \rightarrow \infty$ , there is a limiting size of the wake. We can see this from figure 86 which is a plot of the  $x$ -coordinate of the closure point on the upper free surface. Also, the resulting draft  $d$  increases as  $F$  decreases, i.e. with greater gravity, the vertical plate must be

submerged deeper to obtain the wave-free solution.

Further to this, still looking at just the wake boundaries, we have that, as  $K$  decreases, the size of the wake increases — this is qualitatively as seen in the earlier cavity and wake problems. This is clear in figure 87. Also, as  $K$  decreases, the draft  $d$  decreases. This is not visibly obvious from the plots of figure 87 since the differences in the draft are small. Therefore, we note that, for  $K = 1$  we have  $d = 3.23$  and for  $K = 0.6$  we have  $d = 3.18$ . Recall that earlier, it was discussed that it may be more natural to instead set the draft  $d$  and leave the wake underpressure coefficient to be found. In this light, it is worth restating the observation relating  $K$  and  $d$ : as  $d$  decreases,  $K$  decreases also.

Finally, we consider the effect of varying  $H$ . We find that, as the length  $H$  of the vertical plate decreases, the width of the wake obviously decreases and the length of the wake decreases also. This is evident in figure 88. However, as  $H$  decreases, the draft  $d$  also decreases. This is due to the vertical plate and wake becoming more slender as  $H$  decreases, and so the effect of the body and wake on the flow diminishes. Then, a wave-free solution can still be obtained when the draft of the plate is small.

We continue to analyse the results, but now we shift focus away from just the wake boundaries. Figures 89 and 90 show numerous examples of flow profiles: the parameters  $F$ ,  $K$  and  $H$  are varied and the effects on the wake boundaries and free surface are visible. Figures 89a and 89b demonstrate that a larger wake underpressure coefficient  $K$  results in smaller disturbance to the free surface. This is to be expected since a larger value of  $K$  leads to shortened wake boundaries, so the combined ‘obstacle’ of the vertical plate and the wake is smaller, hence the lesser effect on the free surface. Recall that the Froude number  $F$  is based on the characteristic length  $L$  which is the depth of the stagnation streamline far upstream. Figures 89c and 89d show how  $F$  affects the flow profiles. As discussed earlier, a larger Froude number results in a smaller draft and the visibly increased disturbance to the free surface is, therefore, to be expected. Similarly, the increased effect on the free surface of a longer plate (i.e. larger  $H$ ) is clear in figure 90. Furthermore, it is clear that the undisturbed level of the free surface (i.e.  $y = 0$ ) is not reached until very far upstream, due to the slow decay of  $\Omega$  far upstream. However, in the case shown in figure 90a

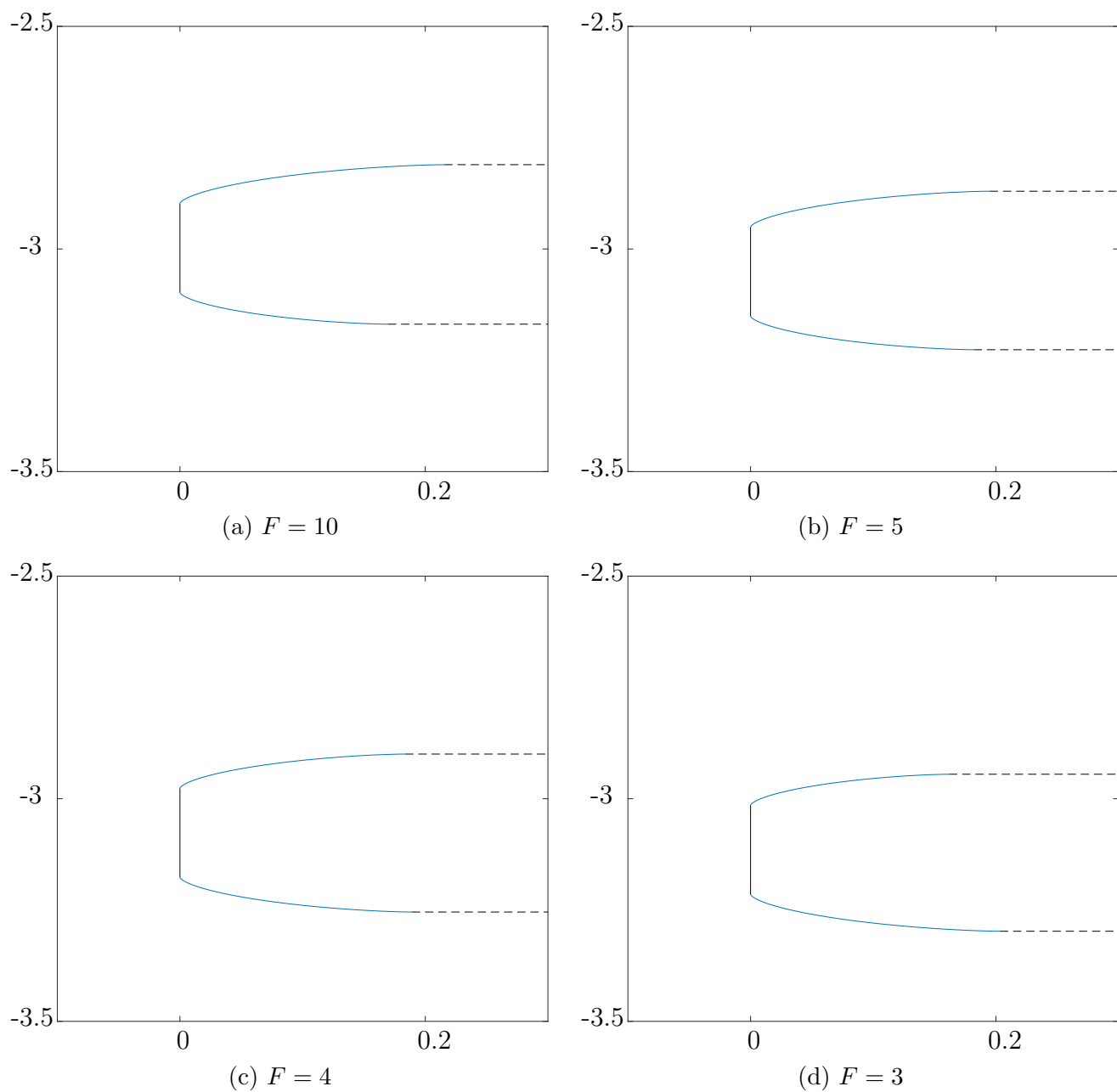


Figure 85: Profiles to show the wake boundaries for  $N = 200$ ,  $K = 1$  and  $H = 0.2$ . Note that the undisturbed free surface is set along  $y = 0$ . The dashed lines are the horizontal wake closures.

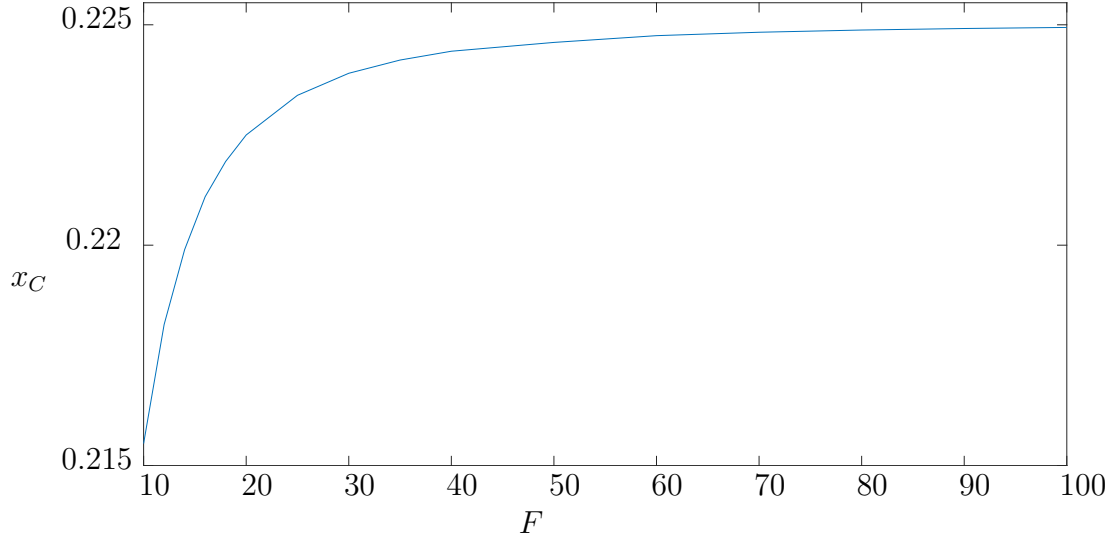


Figure 86: A plot of the  $x$ -coordinate  $x_C$  of the closure point on the upper wake boundary for  $N = 200$ ,  $K = 1$  and  $H = 0.2$ .

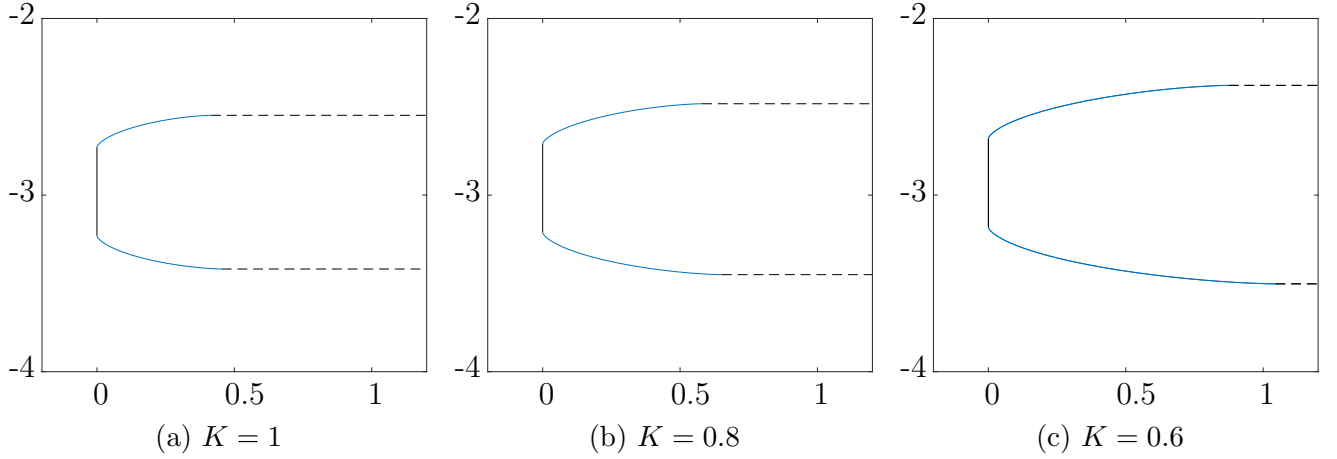


Figure 87: Profiles to show the wake boundaries for  $N = 200$ ,  $F = 4$  and  $H = 0.5$ . Note that the undisturbed free surface is set along  $y = 0$ . The dashed lines are the horizontal wake closures.

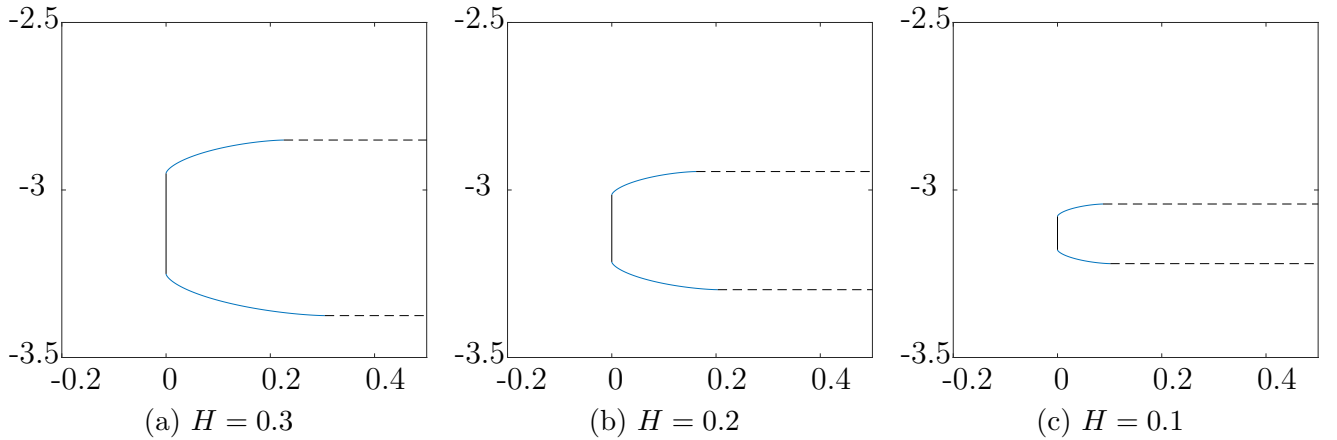
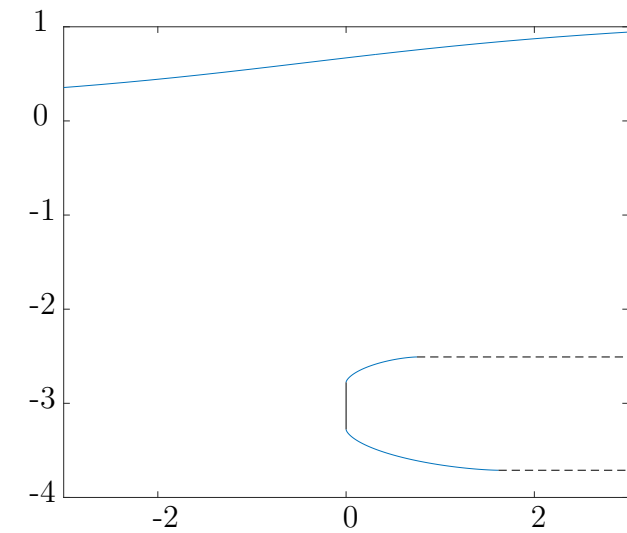
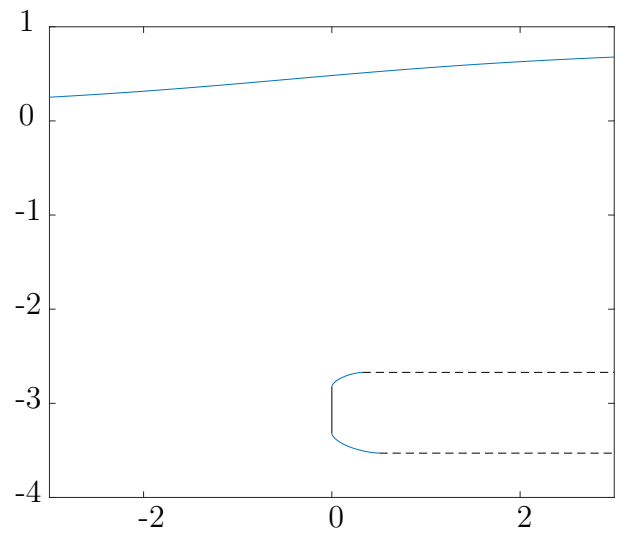


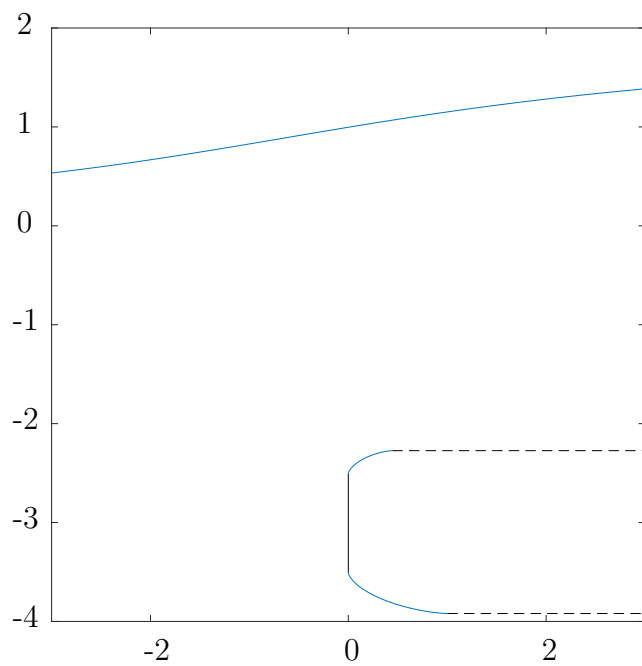
Figure 88: Profiles to show the wake boundaries for  $N = 200$ ,  $F = 3$  and  $K = 1$ . Note that the undisturbed free surface is set along  $y = 0$ . The dashed lines are the horizontal wake closures.



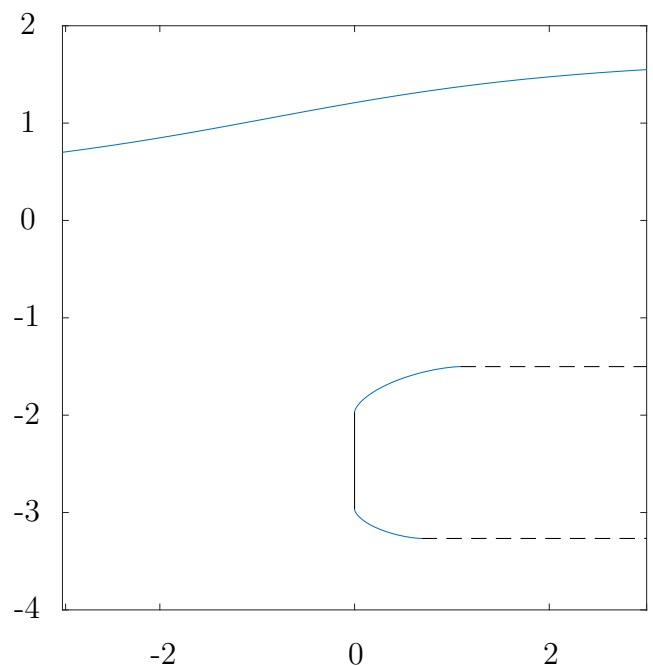
(a)  $F = 3$ ,  $K = 0.5$  and  $H = 0.5$



(b)  $F = 3$ ,  $K = 1$  and  $H = 0.5$



(c)  $F = 3$ ,  $K = 1$  and  $H = 1$



(d)  $F = 10$ ,  $K = 1$  and  $H = 1$

Figure 89: Profiles to show the wake boundaries and free surface for  $N = 200$ . Note that the undisturbed free surface is set along  $y = 0$ . The dashed lines are the horizontal wake closures.

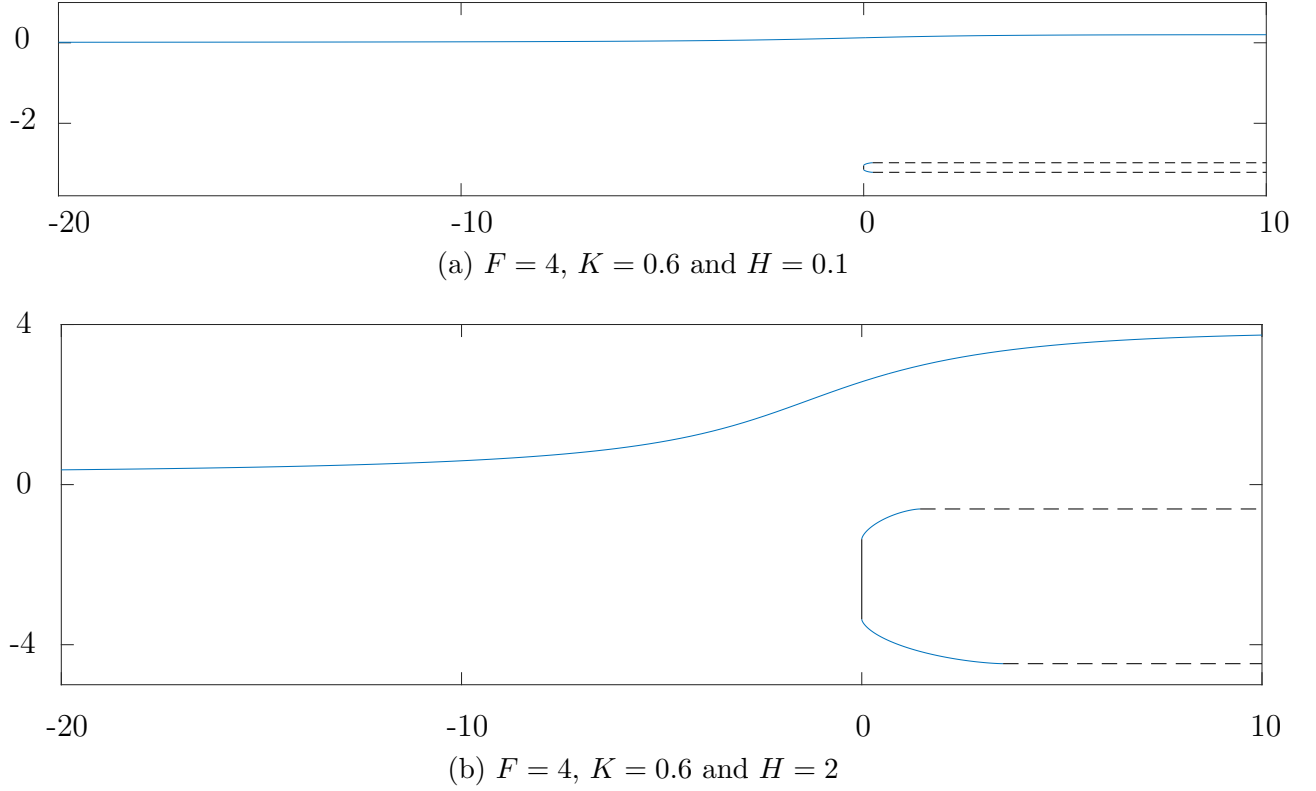


Figure 90: Further profiles to show the wake boundaries and free surface for  $N = 200$ . Note that the undisturbed free surface is set along  $y = 0$ . The dashed lines are the horizontal wake closures.

where the plate is small, we can observe the recovery of the undisturbed flow far upstream.

For a more quantitative examination of the results, we introduce Froude numbers based on the draft  $d$  of the plate and based on the flow quantities that characterise the channel between the free surface and the upper wake boundary. We let  $q_\infty$  and  $h_\infty$  denote the non-dimensional speed and width (respectively) of the channel that forms above the wake. Then, we let

$$F_d = \frac{F}{\sqrt{d}}, \quad (5.61)$$

which is a Froude number defined based on the draft; and we let

$$F_h = \frac{Fq_\infty}{\sqrt{h_\infty}}, \quad (5.62)$$

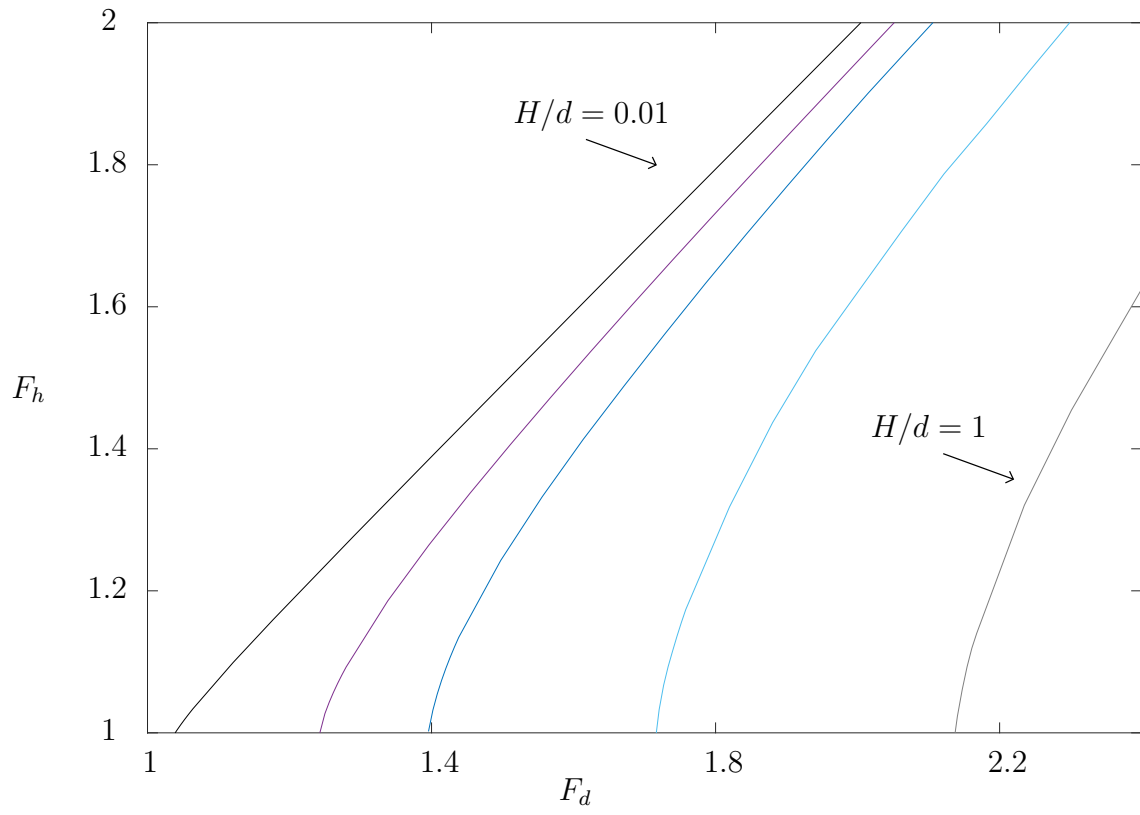
which is a Froude number defined based on the downstream channel above the wake. These Froude numbers are as utilised by Tuck and Vanden-Broeck [1998] in their work on the similar ploughing



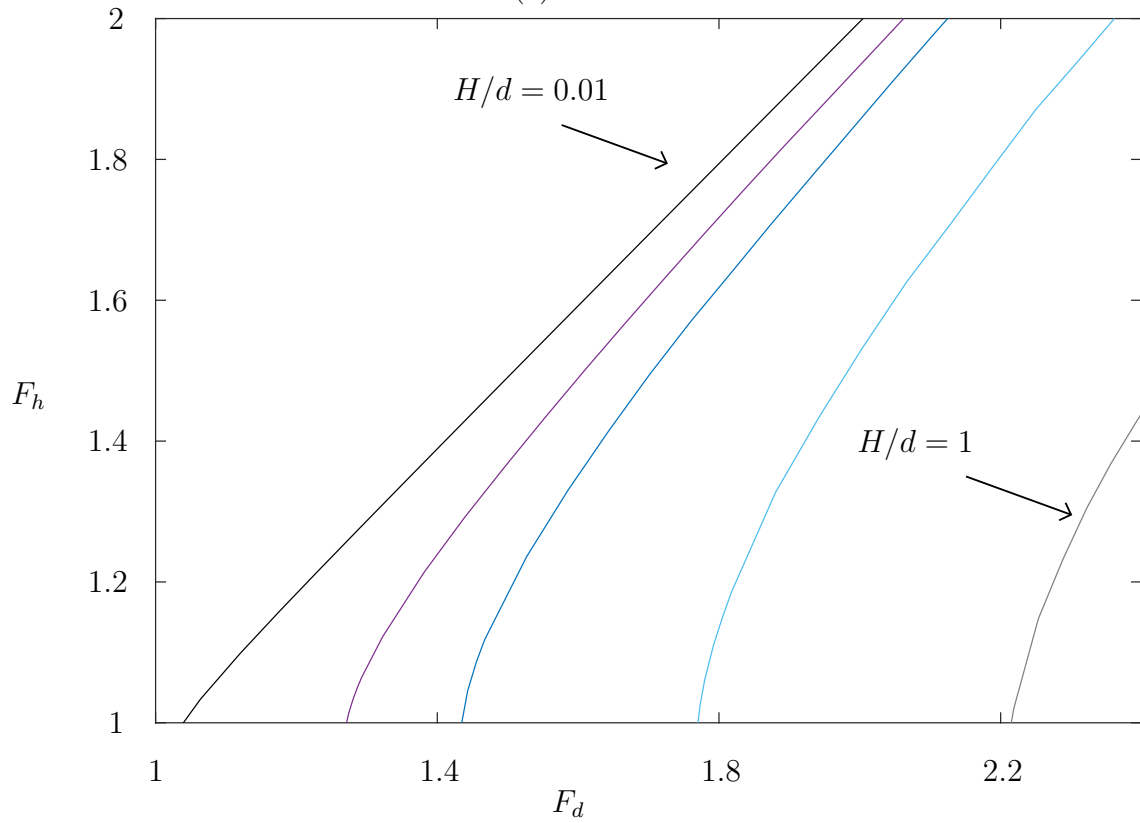
flows where the bluff body is a semi-infinite, rectangular block (instead of the plate and wake that we investigate in the present study). A small change to the problem can aid in discussing the results: instead of setting the plate length  $H$  we can instead impose a given value for the ratio between the plate length and draft of the body, i.e. we set  $H/d$  (instead of  $H$ ) to some given value and this does not change the number of unknowns or equations. It is worth noting that Tuck and Vanden-Broeck [1998] present their findings with respect to this  $H/d$  parameter.

Figure 91 shows plots of  $F_h$  against  $F_d$  for two different given values for the wake underpressure coefficient and for various given values of the ratio  $H/d$ . Note that these Froude numbers are determined here in post-processing once the solution has been obtained. These plots are similar to those presented by Tuck and Vanden-Broeck [1998]. In figure 91, as  $H/d \rightarrow 0$ ,  $F_h$  varies linearly with  $F_d$ . In the ploughing flows case of Tuck and Vanden-Broeck [1998], as  $H/d \rightarrow 0$ , it is found that  $F_h = F_d$  which is to be expected since it is the zero-disturbance limit. To recover these results in the model of the present study, the limit as  $K \rightarrow \infty$  is also required. This is apparent since, in figure 91, the plots of  $F_h$  against  $F_d$  (approximately) translate horizontally to the left as the wake underpressure coefficient increases; and since increasing  $K$  decreases the length of the wake boundaries then, as  $K \rightarrow \infty$ , we are left with a vertical plate and horizontal (closure) streamlines that begin at the plate corners — hence approaching a semi-infinite, rectangular block as studied by Tuck and Vanden-Broeck [1998]. We also approach a linear relationship between  $F_h$  and  $F_d$  in figure 91 for each value of  $H/d$  for large given values of  $F$ . Note that this corresponds to all of the Froude numbers tending towards infinity, i.e. for small gravity. Unlike the ploughing flows case of Tuck and Vanden-Broeck [1998], we do not simply obtain  $F_h \approx F_d$  for small gravity since the pressure difference between the stream and within the wake in our case means that the velocity upstream and the velocity downstream in the channel above the wake cannot be equal. Quantitatively, this is due to the wake underpressure coefficient being non-zero.

From figure 91, it is also clear that, for supercritical flow downstream, there is a minimum value for  $F_d$  (the Froude number based on the draft of the plate). We can obtain solutions where we find that  $F_h < 1$  and there appear to be small waves on the free surface. However, it should be noted that, by the truncation utilised in the numerical procedure — where we set  $\theta = 0$  close to



(a)  $K = 1$



(b)  $K = 0.7$

Figure 91: A plot of  $F_h$  against  $F_d$  for  $N = 200$  and various given values for  $H/d$ . From left to right, the lines correspond to setting  $H/d = 0.01, 0.1, 0.2, 0.5$  and  $1$ .

the origin in the  $\zeta$ -plane, i.e. for  $\xi$  between  $\xi_{N+1}^{FS}$  and zero — we suppress waves. In future work, the numerical procedure could be adapted to more-readily allow for wave solutions, similarly to calculations by Tuck and Vanden-Broeck [1998] for their ploughing flows.

The model and results presented here can be used to better understand the flow past a submerged, finite-length plate that is normal to the stream with a wake forming behind the object. The wake model presented here utilises a closure model that is relatively simple to implement, but it does lack use in terms of understanding the flow far downstream. However, the artificial nature of such a closure mechanism is discussed in the introduction of this thesis and its merits are highlighted — in particular, the resulting flow close to an object is largely unaffected by choice of closure model. Future work on this problem could involve solving with an alternative closure model that leads to a closed wake (as opposed to the open-wake closure model utilised in the present work) and so resulting in more physical flow far downstream.

---

In this chapter, we first considered the effect of gravity on the cavity or wake flow in an unbounded fluid. By obtaining a boundary integral equation and discretising, we have looked to numerically solve for the flow. We have considered three possible options for the extra equation in order to have a square system to be solved. We have considered using an equation derived from explicitly imposing horizontal flow far upstream, setting equal velocity potential at the closure points and imposing an interpolation formula. We concluded that a condition on the flow is required and that the interpolation formula is not sufficient. More specifically, we found that imposing that the dividing streamline is horizontal far upstream is the most suitable. This condition is then utilised in the subsequent iteration of the problem where the plate is at an arbitrary angle of attack. Overall, we found that (as usual), as the cavitation number decreases, the size of the cavity increases. Furthermore, for a given Froude number, there is a minimum cavitation number for which a solution can be obtained. We then moved to investigate (exclusively) wake flow past a submerged plate that is normal to the stream which is bounded above by a free surface (upon which gravity acts). Note that in this case we do not include the effects of gravity on the wake boundaries. Again, we have found that, as the wake underpressure coefficient decreases, the wake

size increases. Also, a solution cannot be obtained for every set of the parameters, i.e. the Froude number, wake underpressure coefficient and length of the plate. In particular, for supercritical flow downstream, there is a minimum value for the Froude number based on the draft of the plate. It has also been discussed that future work on this wake flow past a submerged plate normal to the stream would benefit from reformulating the problem to instead prescribe the draft to better reflect the physical problem.

## 6 Conclusions and future work

A wide variety of free-surface, potential flows have been investigated in this thesis. In particular, we have considered spillways, waterfalls and flows past submerged obstacles. Numerical approaches have been utilised to obtain solutions to these problems, but it should be noted that conformal mappings are at the centre of these approaches. Series truncation and collocation has been used for the spillways and waterfalls, including those cases that involve a submerged obstacle upstream; and a boundary integral method has been used for the problems concerning cavity and wake flows. The numerical methods utilised in this study are very powerful. The series truncation and collocation technique allows for a numerical solution to be obtained easily (since the code is simple to write) once a suitable complex velocity ansatz has been established, but arriving at such an ansatz can be difficult. On the other hand, it is quick to obtain the boundary integral equations via the Bernoulli condition and application of the Cauchy integral formula, but care must be taken in numerically evaluating the principal value integrals that are involved whilst taking note of the singularities in the flow (for example, at the ends of the plate in the cases considered in chapters 4 and 5).

It has been shown (in chapters 1 and 3) how conformal mappings coupled with series truncation and collocation can be applied to a greater range of scenarios than previously investigated, highlighting the use and flexibility of this approach as a tool for obtaining solutions to potential flow problems. Furthermore, when jets are involved and conformal mappings that involve logarithms are utilised, a limitation of the method is that a very large number of points are required to reach a reasonable distance downstream (if plotting using the mesh points utilised in solving for the unknowns). However, in the case of a free-falling gravity jet, we have shown that employing a three-term expansion for the jet singularity downstream enables the profiles to be extrapolated whilst still maintaining the expected parabolic nature of the jet downstream. The three-term expansion also allows for obtaining good solutions that we can extrapolate in more generalised cases than just the simple waterfall, i.e. cases where there is a free-falling jet downstream and an arbitrarily-shaped bed upstream.

Investigations into the numerical method used for flows involving jets (i.e. spillways and waterfalls) have led to the conclusion that, by smoothing the values of  $y$  at the collocation points

(which are then utilised in satisfying the dynamic boundary condition along the free surface(s)) and by employing the *A*-method (introduced in §2.4), we arrive at improved coefficient decay of the series representation for the complex velocity of the flow. Hence, we obtain improved numerical solutions.

In the cavity and wake flow problems discussed in chapters 4 and 5, we have employed the open-wake model. In the zero-gravity case, we have demonstrated three methods of solution: using only conformal mappings; forming a boundary integral equation and then inverting the finite Hilbert transform involved; and discretising the boundary integral equation to solve numerically. It has been discussed that the latter two approaches are suitable to be applied to other related zero-gravity cavity and wake flow problems. In the cavity and wake flows including the effects of gravity (chapter 5), we have obtained numerical solutions by using a boundary integral equation method. We have found that, for a given Froude number, a solution cannot be obtained for every cavitation number — more specifically, there is a minimum cavitation number that can be set for each Froude number. In §5.2, we restricted our investigation to just consider wake flow past a submerged plate that is normal to a uniform, horizontal stream. Again, we obtained numerical solutions through use of a boundary integral equation method and these solutions are dependent on a Froude number, wake underpressure coefficient and a prescribed length or ratio of lengths (i.e. setting either the length of the plate or the ratio of the length of the plate and the draft). The dependencies of the solution on these parameters have been investigated; and similarly to earlier wake and cavity cases, we have found that a solution cannot be achieved for every combination of the parameters. In particular, there is a minimum Froude number (based on the draft of the plate) for which solutions can be obtained that are supercritical downstream.

Whilst the investigations presented in this thesis answer many questions, there is certainly scope for future work on the flows discussed here. For example, in the interest of further validating the numerical results of the present study, comparisons could be made with experimental simulations. In particular, comparing numerical and experimental coefficients of drag and lift would be of use for investigations of wake flow past the submerged vertical plate. With reference to a motivation of this particular problem, these comparisons would be useful for research into the flow past a rowing

blade. Further to this, generalising the model to investigate the flow past an arbitrarily-shaped obstacle would clearly improve the applicability to the rowing scenario.

Specifically regarding problems that involve a free-falling jet, the improved numerical approach presented in chapter 2 can be applied to more related problems such as broad-crested weirs, breaking-wave flows and fluid expelled from a nozzle — all of which are clearly physical examples. Moreover, practical research interest in stepped spillways or waterfalls is often motivated by use of the steps in dissipating energy. Future investigations could include a dissipation factor in the calculations whilst still retaining the potential flow theory approach.

More broadly, we have exclusively sought wave-free solutions in the problems discussed throughout this work. However, wave solutions are also valid, realistic solutions and they are obtainable through the series truncation and collocation approach. Therefore, this is another direction of future work from the problems discussed here.

Overall, in this thesis, we present several improvements to methods and results for potential flow problems that have been investigated previously by other authors; we present solutions to many problems that have not been covered in the existing literature; and there are several avenues available to take this work further to improve our understanding of (and ability to calculate) jet, cavity and wake flows.

## References

- G. K. Batchelor. *An Introduction to Fluid Dynamics*. Cambridge University Press, 2010 (reprint).
- B. J. Binder, F. Dias, and J.-M. Vanden-Broeck. Influence of rapid changes in a channel bottom on free-surface flows. *IMA Journal of Applied Mathematics*, 73:254–273, 2008.
- J. Bonder. Sur un cas de mouvements plans à deux sillages. *Ann. Acad. Sci. Techn. Varsovie*, 3: 155–192, 1936.
- C. E. Brennen. *Cavitation and Bubble Dynamics*. Oxford University Press, 1995.
- H. Chanson. *Hydraulic Design of Stepped Cascades, Channels, Weirs, and Spillways*. Pergamon, 1994.
- W. L. Chow and T. Han. Inviscid solution for the problem of free overfall. *Journal of Applied Mechanics*, 46:1–5, 1979.
- P. Christodoulides, F. Dias, J.-M. Ghidaglia, and M. Kjerland. On the effect of compressibility on the impact of a falling jet. *Proceedings of the twentieth international offshore and polar engineering conference*, 3:53–61, 2010.
- N. S. Clarke. On two-dimensional inviscid flow in a waterfall. *Journal of Fluid Mechanics*, 22: 359–369, 1965.
- L. da Vinci. *Codex Arundel*. British Library: Arundel MS 263, 1478-1518.
- T. E. Dawson. *An experimental investigation of a fully cavitating two-dimensional flat plate hydrofoil near a free surface*. PhD thesis, California Institute of Technology, Pasadena, California, 1959.
- F. Dias and P. Christodoulides. Ideal jets falling under gravity. *Physics of Fluids A: Fluid Dynamics*, 3:1711–1717, 1991.
- F. Dias and E. O. Tuck. Weir flows and waterfalls. *Journal of Fluid Mechanics*, 230:525–539, 1991.



- F. Dias and E. O. Tuck. A steady breaking wave. *Physics of Fluids A: Fluid Dynamics*, 5:277–279, 1993.
- F. Dias and J.-M. Vanden-Broeck. Open channel flows with submerged obstructions. *Journal of Fluid Mechanics*, 206:155–170, 1989.
- F. Dias and J.-M. Vanden-Broeck. Nonlinear bow flows with spray. *Journal of Fluid Mechanics*, 255:91–102, 1993.
- A. Fage and F. C. Johansen. On the flow of air behind an inclined flat plate of infinite span. *Proceedings of the Royal Society A*, 116:170–197, 1927.
- O. M. Faltinsen and Y. A. Semenov. The effect of gravity and cavitation on a hydrofoil near the free surface. *Journal of Fluid Mechanics*, 597:371–394, 2008.
- J.-P. Franc and J.-M. Michel. *Fundamentals of Cavitation*. Kluwer Academic Publishers, 2004.
- K. H. M. Goh and E. O. Tuck. Thick waterfalls from horizontal slots. *Journal of Engineering Mathematics*, 19:341–349, 1985.
- M. I. Gurevich. *Theory of Jets in Ideal Fluids*. Academic Press, 1965.
- H. Helmholtz. Über diskontinuierliche flüssigkeitsbewegungen. *Monatbericht der königlich preussischen Akademie der Wissenschaften zu Berlin*, 23:215–28, 1868. Translated by F. Guthrie as XLIII. On discontinuous movements of fluids. *Philosophical Magazine and Journal of Science Series 4*, 36(244):337–346, 1868.
- F. M. Henderson. *Open Channel Flow*. MacMillan, 1966.
- N. E. Joukowski. I. A modification of Kirchhoff’s method of determining a two-dimensional motion of a fluid given a constant velocity along an unknown streamline. II. Determination of the motion of a fluid for any condition given on a streamline. *Rec. Math.*, 25, 1890. Also Collected works of N . E. Joukowski, vol. III: Issue 3, Trans. CAHI, 1930.
- J. B. Keller and J. Geer. Flows of thin streams with free boundaries. *Journal of Fluid Mechanics*, 59:417–432, 1973.

- J. B. Keller and M. L. Weitz. Upward ‘falling’ jets and surface tension. *Journal of Fluid Mechanics*, 2:201–203, 1957.
- A. C. King and M. I. G. Bloor. Free-surface flow over a step. *Journal of Fluid Mechanics*, 182:193–208, 1987.
- G. Kirchhoff. Zur theorie freier flüssigkeitsstrahlen. *Journal für die reine und angewandte Mathematik*, 70:289–298, 1869.
- S. F. Kistler and L. E. Scriven. The teapot effect: sheet-forming flows with deflection, wetting and hysteresis. *Journal of Fluid Mechanics*, 263:19–62, 1994.
- M. A. Lavrent’ev and B. V. Shabat. *Methoden der komplexen Funktionentheorie*. Deutscher Verlag der Wissenschaften, 1967.
- Lord Rayleigh. LIII. On the resistance of fluids. *Philosophical Magazine*, 2:430–441, 1876.
- E. McLean. Cavitation behind rowing blades. Unpublished MSci dissertation, University College London, 2018.
- E. McLean, R. Bowles, B. Scheichl, and J.-M. Vanden-Broeck. Improved calculations of waterfalls and weir flows. *Journal of Fluid Mechanics*, 941:A27, 2022.
- Y. Mimura. The flow with wake past an oblique plate. *Journal of the Physical Society of Japan*, 13:1048–1055, 1958.
- Z. Nehari. *Conformal Mapping*. McGraw Hill, 1952.
- B. R. Parkin. Experiments on circular-arc and flat-plate hydrofoils. *Journal of Ship Research*, 2:34–67, 1958.
- J. P. Richter. *The Literary Works of Leonardo da Vinci* (2nd edn.). Oxford University Press, 1939.
- A. Roshko. A new hodograph for free-streamline theory. Technical Note 3168, National Advisory Committee for Aeronautics, Washington, 1954.

- Y. A. Semenov and G. X. Wu. Free-surface gravity flow due to a submerged body in uniform current. *Journal of Fluid Mechanics*, 883:A60, 2020.
- E. Silberman. Experimental studies of supercavitating flow about simple two-dimensional bodies in a jet. *Journal of Fluid Mechanics*, 5:337–354, 1959.
- A. C. Smith and M. B. Abd-el-Malek. Hilbert’s method for numerical solution of flow from a uniform channel over a shelf. *Journal of Engineering Mathematics*, 17:27–39, 1983.
- F. G. Tricomi. *Integral Equations*. Dover Publications, Inc., 1985.
- E. O. Tuck and J.-M. Vanden-Broeck. Ploughing flows. *European Journal of Applied Mathematics*, 9:463–483, 1998.
- J.-M. Vanden-Broeck. *Gravity-Capillary Free-Surface Flows*. Cambridge University Press, 2010.
- J.-M. Vanden-Broeck and F. Dias. Nonlinear free-surface flows past a submerged inclined flat plate. *Physics of Fluids A: Fluid Dynamics*, 3:2995–3000, 1991.
- J.-M. Vanden-Broeck and J. B. Keller. Pouring flows. *The Physics of Fluids*, 29:3958–3961, 1986.
- J.-M. Vanden-Broeck and J. B. Keller. Weir flows. *Journal of Fluid Mechanics*, 176:283–293, 1987.
- J.-M. Vanden-Broeck and J. B. Keller. Pouring flows with separation. *Physics of Fluids A: Fluid Dynamics*, 1:156–158, 1989.
- T. Y. Wu. A free streamline theory for two-dimensional fully cavitated hydrofoils. *Journal of Mathematics and Physics*, 35:236–265, 1956.
- T. Y. Wu. A wake model for free-streamline flow theory Part 1. Fully and partially developed wake flows and cavity flows past an oblique flat plate. *Journal of Fluid Mechanics*, 13:161–181, 1962.
- T. Y. Wu. Cavity and wake flows. *Annual Review of Fluid Mechanics*, 4:243–284, 1972.
- B. Yoon and Y. Semenov. Separated inviscid sheet flows. *Journal of Fluid Mechanics*, 678:511–534, 2011.